

**Phenothiazine, thiazolium and sulfonic acid  
functionalized hybrid materials and their  
applications in electronics, optics and catalysis**

Dissertation zur Erlangung  
des Doktorgrades der Naturwissenschaften (Dr. rer. nat.)  
genehmigt vom Fachbereich Chemie  
der Technischen Universität Kaiserslautern  
(D 386)

vorgelegt von

**Zhou Zhou**

Betreuer der Arbeit: Prof. Dr. W. R. Thiel  
Tag der wissenschaftlichen Aussprache: 23.04.2009

Kaiserslautern 2009

Vom Fachbereich Chemie der Technischen Universität Kaiserslautern  
am 23.04.2009 als Dissertation angenommen.

Dekan: Prof. Dr. W. E. Trommer

Vorsitzender der Prüfungskommission: Prof. Dr. H. Sitzmann

1. Berichterstatter: Prof. Dr. W. R. Thiel

2. Berichterstatter: Prof. Dr. S. Ernst

Die vorliegende Arbeit wurde im Fachbereich Chemie Technischen  
Universität Kaiserslautern im Arbeitskreis von Prof. Dr. W. R. Thiel in  
der Zeit von Februar 2006 bis Februar 2009 angefertigt.

**To my parents**



## Abbreviations and indices

a.u	Arbitrary Units
BET	Brunauer-Emmet-Teller
BJH	Barrett-Joyner-Halenda
BTEB	1,4-bis(triethoxysilyl)benzene
CP MAS	Cross Polarization Magic Angle Spinning
CT	Charge Transfer
CTAB	Cetyltrimethylammonium bromide
CV	Cyclic Voltammetry
DFT	Density Functional Theory
EPR	Electron Paramagnetic Resonance
EtOH	Ethanol
EtOAc	Ethylacetate
FID	Flame Ionisation Detector
FT-IR	Fourier Transform Infrared Spectroscopy
GC	Gas Chromatography
LCT	Liquid Crystal Template
MCM	Mobil Crystalline Material
Me	Methyl
MeCN	Acetonitrile
NMR	Nuclear Magnetic Resonance
OTAB	Octadecyltrimethylammonium bromide
PMO	Periodic Mesoporous Organosilica
SBA	Santa Barbara Amorphous

SEM	Scanning Electron Microscopy
TEM	Transmission Electron Microscopy
TEOS	Tetraethyl Orthosilicate
TG-DTG	Thermogravimetric and Differential Thermogravimetric Analysis
THF	Tetrahydrofuran
UV-Vis	Ultraviolet Visible
XRD	X-ray diffraction

## Contents

Chapter 1. Introduction.....	1
1.1 Mesoporous materials .....	1
1.1.1 General introduction into the background .....	1
1.1.2 Periodic mesoporous silicas: synthesis and mechanisms .....	2
1.2 Hybrid mesoporous materials .....	10
1.2.1 General introduction into hybrid materials .....	10
1.2.2 Synthesis of mesoporous hybrid materials .....	11
1.2.3 Application of mesoporous hybrid materials .....	14
1.3 Phenothiazine and its derivatives .....	15
1.3.1 Properties of the phenothiazine molecule.....	15
1.3.2 Phenothiazine derived organic materials.....	17
1.3.3 Phenothiazine modified inorganic materials .....	19
1.4 Thiazolium salts as organo-catalysts and their heterogenization .....	21
1.5 Sulfonic acid functionalized mesoporous materials as catalysts .....	24
1.6 Motivation .....	26
1.6.1 The motivation for phenothiazine functionalized hybrid materials .....	26
1.6.2 The motivation for thiazolium salts and sulfonic acid functionalized hybrid materials .....	27
Chapter 2. Phenothiazine functionalized hybrid materials.....	28
2.1 Synthesis and characterization of carbamate-linked (oligo)phenothiazines in mesoporous silica materials by the post grafting method .....	28
State of the art .....	28
2.1.1 Synthesis of mesoporous hybrid materials .....	28
2.1.2 Structural properties of the hybrid materials .....	32
2.1.3 Characterization of the organic component in the hybrid materials.....	37
2.1.4 Photophysical properties .....	42
2.2 Synthesis and characterization of urea-linked (oligo)phenothiazines in mesoporous silica materials obtained by an in-situ one pot method .....	51

State of the art .....	51
2.2.1 Synthesis of the phenothiazine building blocks .....	52
2.2.2 Synthesis of the hybrid mesoporous materials.....	54
2.2.3 Structural properties of the hybrid materials .....	55
2.2.4 Hybrid material properties .....	81
2.2.6 Electronic and optical properties of the hybrid materials and the associated oxidized materials.....	97
2.3 Synthesis and characterization of triazole-linked (oligo)phenothiazines in mesoporous silica materials obtained by an in-situ one pot method .....	121
State of the art .....	121
2.3.1 Synthesis of hybrid mesoporous materials .....	122
2.3.2 Structural properties of the mesoporous materials.....	123
2.3.3 Spectroscopic properties of the hybrid materials.....	137
2.3.4 Optical properties of the hybrid materials and the associated oxidized materials .....	145
Chapter 3. Hybrid mesoporous materials containing covalently anchored <i>N</i> -phenylthiazolium salts as organo catalyst .....	155
State of the art .....	155
3.1 Silica MCM-41 supported <i>N</i> -phenylthiazolium salts as organo catalyst for benzoin condensation and cross-coupling reactions.....	156
3.1.1 Synthetic procedures.....	156
3.1.2 Structural characterization of the functionalized materials .....	157
3.1.3 Characterization of the functionalized materials by solid-state NMR and IR spectroscopy .....	161
3.1.4 Catalytic properties of the heterogenized thiazolium salts .....	164
3.2 One step co-condensation synthesis of <i>N</i> -phenylthiazolium salt functionalized silica SBA-15	169
State of the art .....	169
3.2.1 Synthetic procedures.....	169
3.2.2 Structural characterization of the functionalized materials .....	170
3.2.3 Characterization of the heterogenized catalyst by thermogravimetry, solid-state NMR and IR spectroscopy .....	173

---

3.2.4 Catalytic properties of the heterogenized thiazolium salts .....	179
3.3 Covalent anchoring of organic thiazolium salts on periodic mesoporous organosilicas as organo catalysts for cross-coupling of aldehydes with acylimines reaction .....	181
State of art.....	181
3.3.1 Synthetic procedures.....	182
3.3.2 Structural characterization of the functionalized materials .....	183
3.3.3 Characterization of the functionalized materials by solid-state NMR, FT-IR spectroscopy and thermogravimetric properties.....	187
3.4 Synthesis of a carbamate-linked thiazolium salt with a basic site in the same molecule covalently bonded on silica MCM-41 .....	191
3.4.1 Synthetic process.....	191
3.4.2 Information of the organic composition and the catalytic properties of the heterogenized catalyst. ....	192
Chapter 4. Sulfonic acid functionalized mesoporous materials.....	195
State of art.....	195
4.1 Synthetic procedure .....	197
4.2 Structural properties of the organic-acid functionalized silica materials .....	199
4.3 Characterization of the organic component in the hybrid materials.....	205
4.4 Application as catalysts .....	208
4.5 Arenesulfonic acid functionalized material as an ion exchanging support for application in catalysis .....	213
Conclusion .....	221
Outlook.....	223
Experimental section.....	225
4.1 General considerations .....	225
4.2 Characterization .....	225
4.3 Synthetic process.....	227
References.....	264

## Chapter 1. Introduction

### 1.1 Mesoporous materials

#### 1.1.1 General introduction into the background

Since the discovery of open-framework inorganic materials with well-defined geometry, the developments of such composite materials with precise and easily controlled pore shapes and sizes are of great importance in many areas of modern science and technology. According to the IUPAC definition, porous materials can be classified into three groups<sup>1</sup>. Microporous solids have pore diameters up to 2 nm with zeolites as the most prominent example, mesoporous solids have a pore size ranging from 2 to 50 nm, for example aerogels, pillared clays, M41S materials, and macroporous solids have pore diameters larger than 50 nm, such as glasses and foams. In addition, these materials can be distinguished by the arrangement of the pores (periodic or random), and the pore size distribution (narrow or broad).

The most important microporous material, containing a periodic arrangement of pores and a narrow pore size distribution, are the zeolites, which have the general molecular formula  $(M^+, M2^{+0.5})_x[(AlO_2)_x(SiO_2)_y]zH_2O$ <sup>2</sup>. The enormous interest in these materials is due to their wide catalytic applications within industrial areas such as oil refining, petrochemistry and synthesis of chemicals, or used as adsorbents<sup>3</sup>. Several superior properties of zeolites, such as various components, resistance towards heat, steam and chemical attacks, waste minimization, simple operation, and recyclability endue the good catalytic ability of this type of materials. However, one serious limitation is their small pore diameter. Hence they are not capable to efficiently process organic molecules having large kinetic diameters. Consequently, a considerable effort has been devoted in searching for methods that allow to increase the pore size.

In the early 1990s, Yanagisawa and Mobil researchers reported the first successful synthesis of novel periodic mesostructured materials<sup>4, 5</sup>, use long carbon chain molecules (such as cetyltrimethylammonium) as the structure directing agent, rather than the conventional single small amine molecules, which are widely used as templates in formation of microporous zeolite structures. This change raised strong research interest into the so-called M41S family of mesoporous materials<sup>6-8</sup>. Following this synthesis concept, different choices of inorganic precursors, organic templates, and reaction conditions have resulted in a variety of novel mesostructured materials, embracing silicates, organosilicas, metals, metal oxides, phosphates, sulfides, polymers, etc<sup>9, 10</sup>. The mesostructures include ordered two-dimensional hexagonal (2D,  $p6mm$ ) ordered three-dimensional hexagonal  $P6_3/mmc$ , 3D cubic, bicontinuous cubic, disordered and other structures. A derivative route called 'nanocasting' is performed through a replication process using ordered mesomaterials as the mold. This method is widely used for the synthesis of mesoporous carbons, metals, metal oxides and other inorganic materials<sup>11</sup>.

### **1.1.2 Periodic mesoporous silicas: synthesis and mechanisms**

#### 1.1.2.1 General synthesis method of mesoporous silica material

Mesoporous silicates are generally prepared under hydrothermal conditions, involving a sol-gel process. Normally, using water as medium, a homogenous solution of a dissolved surfactant is important to achieve an ordered mesoporous structure. Silicate precursors are then added into the mixture, followed by a hydrolysis of the silica species under acidic or base catalysis and the transformation to a sol of silicate oligomers<sup>12</sup>. The aggregations occur between these oligomers in combination with an interaction with surfactant micelles and a precipitate will form by the continuous condensation of silicate oligomers. Generally, the occurring of precipitation indicates the formation of mesostructure<sup>13</sup>. Subsequently,

hydrothermal treatment proceeds to a complete condensation and solidification of silica species and an improve of the organization of the ordered structure. The final pore free materials are obtained after the removal of the organic templates. Looking through this general process, some important issues should be pointed out, the properties of the silica precursor, the pH of the system, the type and the concentration of the surfactant, the temperature of the synthesis and the hydrothermal treatment, and even the way to eliminate the templates. Each of these factors can deduce dramatic influence on the ordering or the type of the mesostructure. To further understand the influence of these factors, informations about the synthesis mechanisms and pathways will be briefly introduced in the following section. Furthermore, the most important influence of these factors will be presented.

### 1.1.2.2 Synthesis mechanisms and pathways

The invention of the M41S family materials pops out a new methodology to achieve ordered mesoporous materials. As a following work, several mechanistic pathways of the formation of MCM-41 structure were proposed<sup>14</sup>. At the beginning, from the results of microscopy and X-ray diffraction comparing with those obtained from surfactant/water liquid crystals or micelle phases, Beck et al.<sup>7, 15</sup> proposed a liquid crystal templating (LCT) mechanism, illustrated in Figure 1. They described firstly the pre-existence of surfactant aggregates (rod-like micelles), which further produce hexagonally arrayed rods, followed by the migration and polymerization of the silicate anions around the rod-like structure. The second mechanistic pathway of LCT was vaguely postulated as a cooperative self-assembly of the surfactant cations and the silicate anions to form the liquid-crystal-like structures. However considering that the surfactant concentrations used in some conditions of the synthesis of MCM-41 are far below the critical micelle concentration (CMC) required for hexagonal LC formation, the first pathway seems not very accurate<sup>16</sup>. Moreover, Davis et al.<sup>17</sup>, by performing in situ <sup>14</sup>N NMR spectroscopy in the synthesis system, concluded that the



liquid crystalline phase is not present in the synthesis medium during the formation of MCM-41.

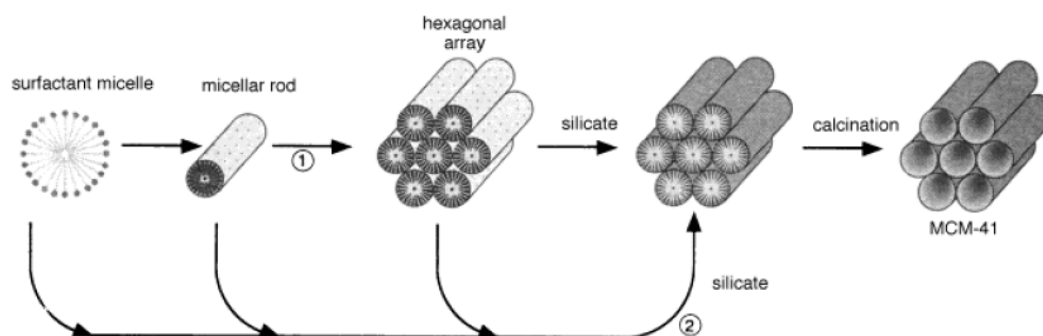


Figure 1. Two possible pathways for the LCT mechanism <sup>7</sup>.

A series subsequent research by different groups, using various method and techniques, such as changing the synthesis conditions (silica and surfactant concentration, temperature, and time) to form different structures <sup>18</sup>, <sup>1</sup>H and <sup>29</sup>Si NMR spectroscopy <sup>19</sup>, small angle neutron scattering <sup>20</sup>, low temperature transmission electron microscopy (TEM), and small-angle X-ray scattering <sup>21</sup> were performed to investigate the possible mechanism. Consequently, the results partially support the second pathway of LCT, but more in detail, especially the cooperative organization of inorganic and organic molecular LCT mechanism is more generally accepted by researchers (Figure 2). This was proposed by group Stucky and co-workers <sup>8, 22-24</sup>.

In this cooperative LCT mechanism, the charge density of the inorganic species decides how many surfactants are associated to each inorganic entity. Furthermore, it also directs the preferred orientation of the surfactant head groups relative to the inorganic species. In other words, the charge density matching determines the average distance between the surfactant head groups. Within this constraint and interactions between inorganic species, a preferred liquid crystalline-like morphology is formed. Generally, the syntheses were assumed to embrace the organization of hydrophobic and hydrophilic entities into a biphasic composite

material. Three types of interactions are involved in this cooperative process: inorganic-organic interactions, organic-organic interactions and inorganic-inorganic interactions.

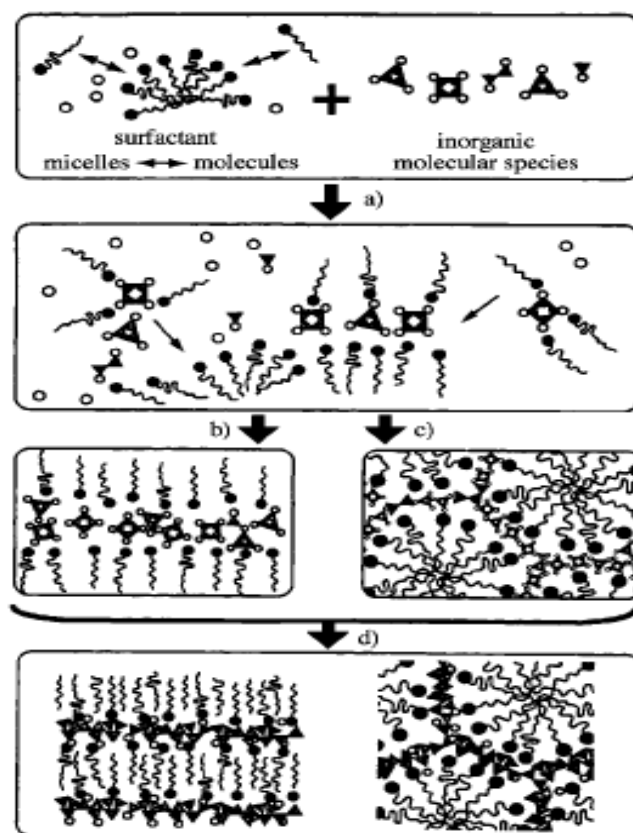


Figure 2. Cooperative organization of inorganic and organic molecules in the LCT mechanism <sup>22</sup> a) cooperative nucleation; b), c) liquid crystal formation with inorganic compounds; d) inorganic polymerization and condensation.

Table 1. Common synthesis pathway of silica mesoporous materials.

pathway	interactions	template	condition	classical products
$S^+I^-$	electrostatic coulomb force	ammonium surfactants	basic	MCM-41, MCM-48, MCM-50
$S^+X^-I^+$	electrostatic coulomb force	ammonium surfactants	acidic	SBA-1, 2, 3
$S^0H^+X^-I^+$	double layer H bond	nonionic surfactants	acidic	SBA-15, 16
$S^0I^0 (N^0I^0)$	H bond	nonionic surfactants	neutral	HMS, MSU

The key factor is the interaction between the surfactant and the inorganic species, such as the matching of charge density. Thus elaborate investigation on mesoporous materials have been focused on understanding and utilizing the inorganic-organic interactions. The most frequently used synthesis routes and the interaction of surfactants with inorganic species are illustrated in Figure 3 and indexed in Table 1. Huo et. al.<sup>8</sup> presented in detail four pathways for the synthesis of mesostructured surfactant-inorganic biphasic arrays, which are  $S^+I^-$ ,  $S^-I^+$ ,  $S^+X^-I^+$ , and  $S^-X^+I^-$  ( $S^+$  = surfactant cations,  $S^-$  = surfactant anions,  $I^+$  = inorganic precursor cations,  $I^-$  = inorganic precursor anions,  $X^+$  = cationic counterions, and  $X^-$  = anionic counterions). For example, the point of zero charge of silica is  $\text{pH} = 2$ , above this point the silica species are negatively charged, while below this point are positively charged. Therefore, to yield an ordered mesoporous structure, it is important to choose the suitable match pair of surfactant and inorganic component. Additionally to these four pathways where the components associate with electrostatic interactions, Tanev and Pinnavaia<sup>25</sup> also proposed an hydrogen-bonding interaction pathway (an alkylamine  $S^0$  head group, PEO  $N^0$  head group and hydroxylated TEOS  $I^0$  under neutral conditions). In this neutral system, only disordered worm-like mesoporous silicas were obtained. Later on, the synthesis of mesoporous silica SBA-15 was carried out under a strong acidic condition by using the triblock copolymer P123 as template<sup>26</sup>. It can be demonstrated as a double-layer hydrogen-bonding  $S^0H^+X^-I^+$  interaction (Figure 3c).

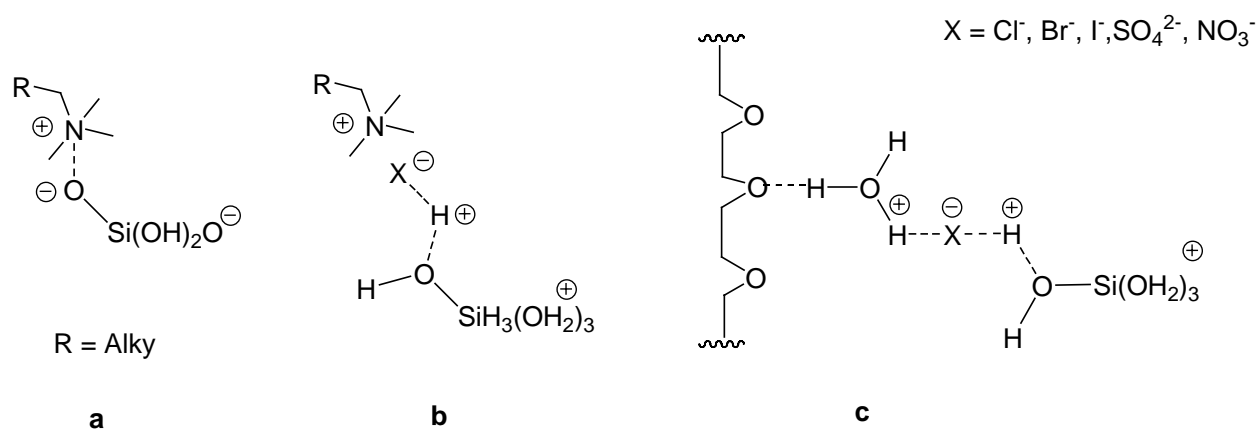


Figure 3. Illustration of three types of interaction between surfactant and silica species a) the most common ammonium cation surfactant head group with a negatively charged silica at  $\text{pH} > 2$  (typical material MCM-41). b) the most common ammonium cation surfactant head group with a positively charged silica at  $\text{pH} < 2$  (typical material SBA-1). c) nonionic surfactant (triblock copolymer) with positively charged silica at  $\text{pH} \sim 2$  (typical material SBA-15).

### 1.1.2.3 Factors influencing the silica mesostructure

The preparation of ordered mesoporous silica materials can be achieved by using various silica precursors, such as silica gel, colloidal sols, water glass (sodium silicates), silica aerogels, or tetraalkoxysilane (TEOS, TMOS, TPOS etc.)<sup>27, 28</sup>. Tetraalkoxysilanes are in small molecular size, while others have a high polymerization degree of the silicates. Thus, when the partially polymerized silicates are used as precursor, a hydrothermal treatment is required for a further cross-linkage to proceed highly ordered mesoporous structures. Among all, TEOS is the most convenient and efficient silicate precursor, due to its proper hydrolysis speed and the relatively cheap price. It also can perform in a lower temperature synthesis with controllable hydrolysis speed, thus the morphologies of products are diverse<sup>29</sup>.

The ordered silica mesoporous materials are normally synthesized in water solution either with alkali or acid as hydrolysis catalyst. Neutral conditions often offer disordered worm-like porous materials<sup>30</sup>. Under basic conditions, the pH range frequently is adjusted between 9.5 and 12.5 with different bases, which can be organic quaternary ammonium bases or inorganic bases<sup>12</sup>. Organic bases are often used to prepare other metal atom mixed silica hybrid materials, such as hydroxy-type mesoporous aluminosilicates<sup>31</sup>, and they also can avoid the introduction of other metal atoms into pure silica systems. Under acidic conditions, a strong acid and a low pH value ( $< 1$ ) is recommended to obtain highly ordered mesoporous structures, such as SBA-15 and SBA-16<sup>32</sup>. One of the benefits of acidic conditions is the products have

various morphologies<sup>33</sup>, since linear silicate oligomers can be formed under these conditions different to the network silicates under basic conditions<sup>34</sup>.

The accessibility of the pores can be achieved by the eliminating the templates from as-synthesized materials. The most often used method is calcination, and a totally remove of organic surfactants can be easy gained by a simple ‘burning’ process. Here a stepwise increase of the temperature is necessary to prevent a structural collapse. It is a fast and easy to handle way, but the drawback of the calcination is the sacrifice of surface hydroxyl groups by a further increase of cross-linkage in the framework<sup>35</sup>. Extraction is an alternative way to remove surfactants under mild conditions and without serious effects on the framework<sup>36</sup>. The common used solvents are methanol, ethanol and THF. In some occasions, a small amount of acid can help to remove surfactants in efficiency, especially, when the templates are ionic species. A novel method was developed by using supercritical fluids. It seems to be more favorable than the calcinations and normal solvent extraction<sup>37</sup>. It should be noticed that in the most cases, the extraction process can not achieve 100 % removing of the surfactants from the materials. Other methods are also invented to digestion surfactant and removing, such as microwave and ultraviolet irradiation<sup>38,39</sup>.

It is known that mesostructures can be obtained by rational design and control of organic-inorganic interaction and cooperative assembly of silica species with surfactants. Some of the resulting structures are illustrated in Figure 4, such as 2D hexagonal structure (p6mm, MCM-41, SBA-15), cubic (Ia3d, MCM-48), and cubic (Pm3n, SBA-1). In the ionic surfactant system, a concept of packing parameters is introduced to predict and explain the final mesostructure<sup>40</sup>. The packing parameter value is defined as,  $g = V/a_0l$ , where,  $V$  is the effective volume of the hydrophobic chain of the surfactant plus any cosolvent between the chains,  $a_0$  is the effective aggregate surface area of the hydrophilic head group at the aqueous-micelle surface, and  $l$  is the effective hydrophobic chain length. Table 2 presents the

relationship between the  $g$  value of cationic surfactants and the mesostructures<sup>6</sup>. The packing parameter function is simple, but it can explain many facts, such as the influence of organic-inorganic interaction, the occurring of phase transformation, and the impact of different structural template, organic additives etc.<sup>41-43</sup>. Based on these packing parameters, a more convenient concept named hydrophilic/hydrophobic volume ratios ( $V_H/V_L$ ) is suggested to account for the formation of different mesophases in the nonionic surfactant system (block copolymers)<sup>44</sup>, due to the hard definition of headgroup size of this type of surfactant.

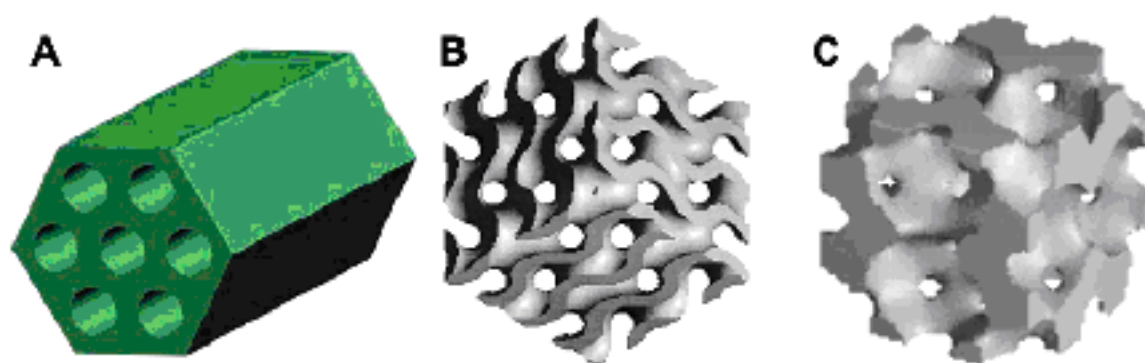


Figure 4. Pore structure of mesoporous materials with symmetries of A)  $p6mm$ , B)  $Ia3d$ , and C)  $Pm3n$ <sup>45</sup>.

Table 2. Relationship between the packing parameter of cationic surfactant and mesostructure

$g = V/a_0l$ ,	structure	classical material
$< 1/3$	cubic ( $Pm3n$ )	SBA-6, SBA-1
	3D hexagonal ( $P6_3/mmc$ )	SBA-7, SBA-2
$1/3 < 1/2$	2D hexagonal ( $p6mm$ )	MCM-41
	2D hexagonal ( $p6mmc$ )	SBA-3
$1/2 < 2/3$	cubic ( $Ia3d$ )	MCM-48
1	lamellar	MCM-50, SBA-4

## 1.2 Hybrid mesoporous materials

### 1.2.1 General introduction into hybrid materials

Hybrid materials have already been used by people from long time ago. The typical example is Maya blue with amazing vivid color surviving from long time exposure, found in ancient Maya fresco paintings<sup>46</sup>. It is not a copper mineral, nor any other natural ground mineral. It turned to be a hybrid organic-inorganic material with molecules of the natural blue dye indigo encapsulated within the channels of a clay mineral. This beautiful example of a man-made hybrid material tells us that combination of good properties from organic and inorganic components is the concept of hybrid materials. The final aim is serving for the application of these materials. Nowadays, hybrid materials are being expandingly developed by people from different aspects of organic and inorganic materials, and the variety embraces from the molecular scale to the polymer scale, such as donor-acceptor complexes, inorganic molecules doped polymers, organic molecule modified inorganic materials, polymer coated inorganic materials, biomineral type of composites and so on.

In recent years, mesoporous materials with an ordered mesostructure, large surface areas, good biocompatibility, and a tailorable size of the mesopores on the nanometer scale have attracted considerable interest as hosts for development of organic-inorganic hybrid materials. The most commonly used substrates are ordered siliceous mesoporous materials, due to their specific properties, such as the simple preparation, the high ordering, the facility for modification, the relatively high stability, the transparent walls etc. Considerable efforts have been undertaken to incorporate organic components within the silica framework or to trap them within the channels to achieve a symbiosis of the properties of both components<sup>47</sup>. The functionalized mesoporous materials have been effectively used as catalysts, sorbents, sensors, and drug delivering materials etc.<sup>48-50</sup>. This section briefly introduces into the

synthesis pathway to achieve ordered hybrid silica mesoporous materials and into some related application.

## **1.2.2 Synthesis of mesoporous hybrid materials**

### **1.2.2.1 Grafting Methods**

Grafting is a postsynthetic method and refers to a modification of prefabricated mesoporous materials. This methodology is based on the fact that not all  $\text{SiO}_4$  units in mesoporous silicates are four fold-connected, which generates a hydrophilic surface with hydroxyl groups (Si-OH) on the surface of these materials. This highly concentrated surface silanol groups can act as convenient anchoring points for organic functionalization (Figure 5). The process is performed primarily by reaction between the alkyoxysilane, chlorosilane, or silazanes and the free or geminal silanol groups<sup>51</sup>. The original mesostructure is usually retained after grafting, while a reduction in the porosity of the hybrid material is often observed due to the pore occupation and the molecular size of organic component<sup>52</sup>. A further modification can be realized by reaction between the target organic molecules and reactive functional groups on the surface, such as nucleophilic substitution of anchored amines and halides<sup>53</sup>. The post-synthesis grafting process is restricted by the fact that the functional groups may concentrate near the opening of the channels and by the limited diffusion into the pores. Additionally, the amount of loading is confined by the number of accessible and reactive surface silanol groups.



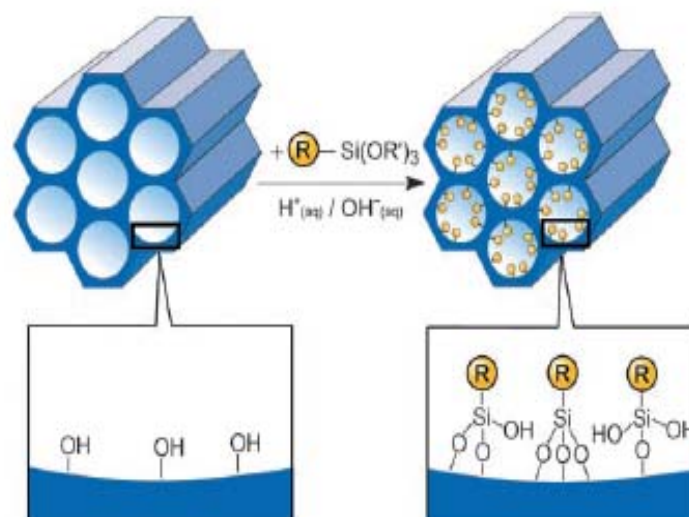


Figure 5. Grafting method for the organic modification of mesoporous silica materials with terminal organosilanes (*Source*: Ref. <sup>54</sup>).

#### 1.2.2.2 Co-condensation

Another pathway to synthesize organically functionalized mesoporous silica materials is the one-step co-condensation method (Figure 6). In this preparation, common silica precursors cross-link with terminal trialkoxysilanes in the presence of surfactants through cooperative organization to ordered hybrid mesoporous materials with the organic groups covalently bound to the pore walls <sup>55</sup>. The significant advantage of this method is higher organic loading and homogenous distribution of the organic groups in the pore channels, as well as a single step preparation procedure <sup>56</sup>. However, the degree of ordering in the mesostructure is usually decreased by increasing concentration of organosilane precursors in the reaction mixture <sup>57</sup>. Different mesoporous synthesis pathways have been used to generalize hybrid mesoporous materials (S<sup>+</sup>I<sup>-</sup>, S<sup>+</sup>XI<sup>+</sup>, S<sup>0</sup>I<sup>0</sup> and N<sup>0</sup>I<sup>0</sup>) <sup>58-60</sup>. It is easy to understand that the structural ordering of the final product might severely relate to the structure of the organosilane, since the organic groups certainly have some impact to the cooperative organization of the inorganic-organic interface. Thus a rational design of organosilane precursor is important. Attention should not only be paid on the functionality of the organic group, but also on the stability of the organic

group during the synthesis and the template extraction process, even on the effect of the cooperative assembling of inorganic-organic species.

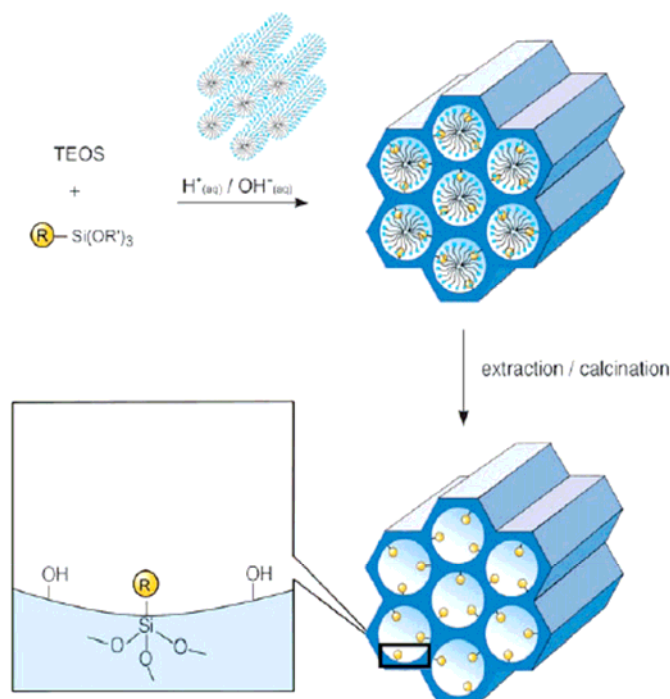


Figure 6. Co-condensation method for the organic modification of mesoporous silica material (Source: Ref. <sup>54</sup>).

### 1.2.2.3 Periodic mesoporous organosilicas (PMOs)

The preparation of periodic mesoporous organosilicas involves well-known bridged organosilica precursors, which have already been widely used in the fabrication of polymerized hybrid materials by sol-gel chemistry <sup>61, 62</sup>. Cooperating with surfactant, the (R'O)<sub>3</sub>Si-R-Si(OR')<sub>3</sub> type of precursors (with or without other silica sources) assemble to ordered hybrid mesoporous materials (Figure 7). Compared to the materials obtained by postsynthesis or direct synthesis, the organic units in PMOs are incorporated inside the framework <sup>63</sup>. The distribution of the organic units is normally homogenous throughout the pore wall, and the pore channels of these materials are unoccupied and show with large surface areas <sup>64</sup>. In some cases, the introduction of organic groups inside the wall provide a

high thermal and hydrothermal stability due to the molecular scaled ordering of the wall, as well as an increased hydrophobicity<sup>65</sup>.

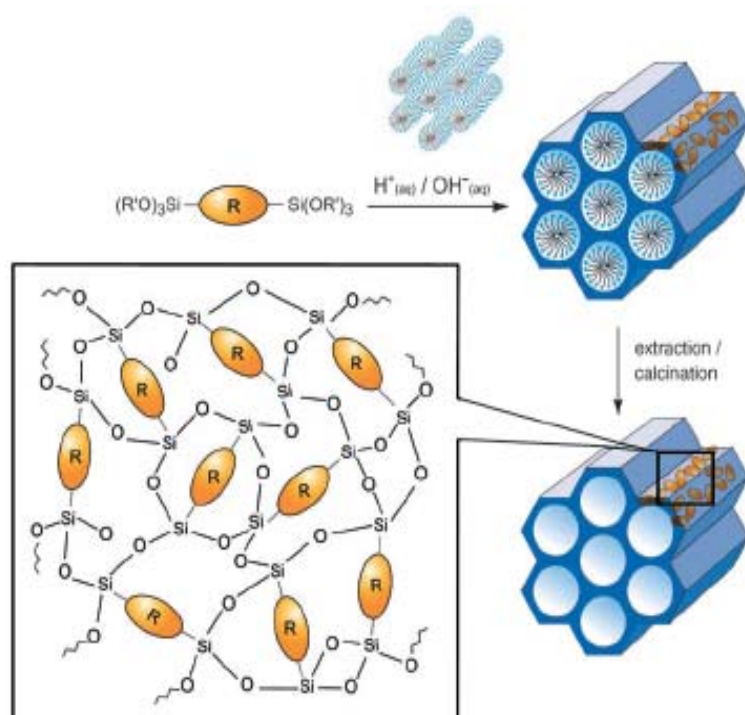


Figure 7. General synthetic pathway for PMOs (Source: Ref. <sup>54</sup>).

### 1.2.3 Application of mesoporous hybrid materials

The goal of the modification is functionalization, in other words, the application is important. The amorphous  $SiO_2$  framework decides the hydrophilic nature of this material, such as a poor stability in a humid atmosphere. To overcome this drawback is important for later applications. An excess of trimethylchlorosilane and hexamethyldisiloxane treated M41S family materials produces an enhanced surface hydrophobicity<sup>66</sup>. This process is well known as the silylation of mesoporous materials. Silylation agents have been expanded to other chlorosilanes such as triethyl-, tripropyl-, ethyldimethyl-, octyldimethyl-, or cyclohexyldimethylchlorosilane<sup>67</sup>.

In the early stages of surface studies the silylation modification discloses the surface properties of the silica mesoporous material. Consequently, new areas of functionalization of

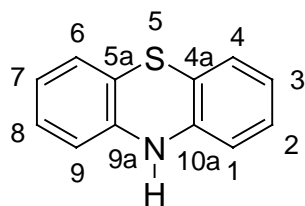
ordered mesoporous silica materials have been opened, since various applications are expected in many fields: optics <sup>48</sup>, electronics <sup>68</sup>, energy storage <sup>69</sup> and conversion <sup>70</sup>, membranes <sup>71</sup>, catalysis <sup>72,73</sup>, sensors <sup>74</sup>, biology <sup>75</sup>, etc.

From one point, we can see a small picture of this research area. For example, to tailor the material as an efficient absorbent, a thiol-functionalized MCM-41 can be invented to collect the heavy metal ions from water <sup>76</sup>. Selective absorption can also be achieved by amino groups modified mesoporous materials, to form complexes with metal ions or to remove acidic compounds <sup>77, 78</sup>. It thus is obvious that the specific absorption can be developed by functionalization with different organic groups. Furthermore, the thiol group can be further oxidized to a sulfonic acid, which can be used as heterogenized acid catalyst for a series of reactions (esterification, condensation, coupling, acylation, isomerization etc.) <sup>79</sup>. As an acid group, it can easily react with bases to anchor other functional groups. At the same time, this material also has the ability to act as a cation exchanging material <sup>80 81</sup>. Additionally, this material also presents promising proton conductivities for an application in fuel cell membranes <sup>82</sup>. Thus one simple example of modification (thiol group) extends to a broad variety of applications. Therefore, this research area is strongly interdisciplinary and expanding.

## **1.3 Phenothiazine and its derivatives**

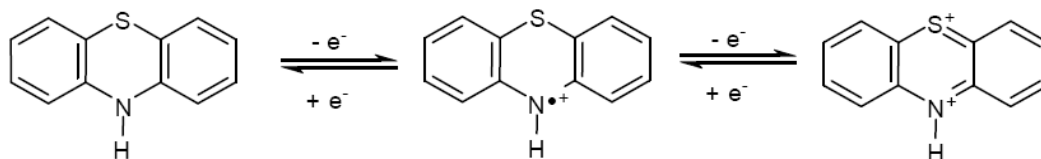
### **1.3.1 Properties of the phenothiazine molecule**

10*H*-phenothiazine is a nitrogen and sulfur containing, electron-rich, tricyclic molecule. The numbering of the skeleton atoms of the phenothiazine rings according to IUPAC is presented in Scheme 1. Phenothiazines have gained particular importance in pharmaceutical application <sup>83, 84</sup>.



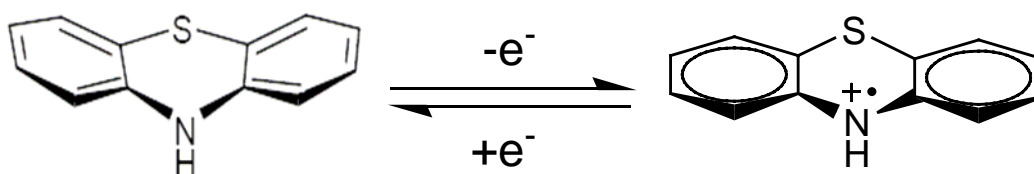
Scheme 1. Numbering of the skeleton atoms of phenothiazine ring.

Phenothiazines undergo reversible one-electron oxidation processes with low potentials which lead to stable and deeply colored radical cations<sup>85</sup>. A further one-electron oxidation will generalize the dicationic species<sup>86</sup> (Scheme 2). Both oxidation steps can be observed by cyclic voltammetric measurements ( $E_{1/2}^{0/+1} = 270$  mV and  $E_{1/2}^{+1/+2} = 770$  mV)<sup>87</sup>, and the existence of the radical cation can be determined by EPR<sup>88</sup>, UV-Vis<sup>89</sup> and Raman spectroscopy<sup>90</sup>. This redox behavior is not only responsible for the physiological properties of phenothiazines<sup>91</sup>, but also for their capability to cleave DNA upon photochemical excitation<sup>92</sup>. As a consequence, phenothiazine derivatives have found rising applications in material sciences as electrophoric sensors in supramolecular systems for photoinduced electron transfer (PET)<sup>93-95</sup> and as electron donors in electronically conducting charge-transfer composites<sup>96-98</sup>. Furthermore, phenothiazine polymers obtained by polycondensation play an important role, for example, as electrochromic materials for displays<sup>99</sup>. On the other hand, the low oxidation potential of polyphenothiazines is responsible for the capability of acting as an electron donor in fluorescent donor-acceptor chromophores, which are of special benefit as emitters in organic light-emitting diodes (OLED)<sup>100-102</sup>, as well as for nonlinear optical and electrooptical effects<sup>103</sup>.



Scheme 2. Two step one-electron oxidation of phenothiazine and the corresponding radical cation and dication.

An interesting geometry change can be observed from ground state to excited state of phenothiazine. The X-ray structure analysis shows that phenothiazine has a dihedral angle of  $153.3^\circ$  in the neutral state as illustrated in Scheme 3<sup>104, 105</sup>. However, the crystal structure of the phenothiazine radical cation discloses a planar structure, thus some  $\pi$ -delocalization will spread over the whole molecule of  $PT^{+\cdot}$  including the central ring<sup>106, 107</sup>. The occurring of a significant geometry change is also confirmed by the time-dependent DFT calculations<sup>108</sup>.



Scheme 3. The geometric changing from phenothiazine to its radical cation.

### 1.3.2 Phenothiazine derived organic materials

The reversible conformation and the low ionization potential give the phenothiazine derivatives wide applications in chromo-, fluoro-, and electrochromic materials. This work started with electrical resistivity measurements carried out to investigate the conducting properties of phenothiazine polycrystalline materials by Brown et. al.<sup>109</sup>. Furthermore pulsed light techniques have been applied to determine the charge carrier mobility in microcrystalline or amorphous phenothiazine layers<sup>110</sup>. In 1969, an early research of Sano's group correlates the extra absorption band in the near-infrared region ( $\sim 900 - 1100$  nm) of phenothiazine radical cation salts to the charge-transfer interaction between phenothiazine cation radicals in the solid<sup>111</sup>. The conclusion is also supported by the fact that the spin exchange coupling parameter for the salt is the largest in value. The authors propose that the charge-transfer rises from the stacking of phenothiazine radicals in a face-to-face manner, forming chain-like arrays of molecules. Thus, the charge-transfer is expressed as a transition of the type  $\langle \dots D^+ D^+ D^+ D^+ \dots \rangle \rightarrow \langle \dots D^+ D^{2+} D^0 D^+ \dots \rangle$ , where D denotes a phenothiazine molecule. Recently, intermolecular electron transfer (ET) between the free phenothiazine donor and its

radical cation (1:1) complex is observed for the first time by its diagnostic (charge-resonance) absorption band in the near-IR region <sup>112</sup>. These researches present that an electron transfer is permitted intermolecularly, between phenothiazine and its corresponding radical cation.

Following the research on the conductivity of organic substances, a series of phenothiazine-X systems [X = 7,7,8,8-tetracyanoquinodimethan (TCNQ), 1,3,5-trinitrobenzene (TNB), and pyromellitic dianhydride (PMDA) <sup>113</sup> etc.] were developed to investigate the intermolecular electronic transitions of phenothiazine containing donor-acceptor complexes. For example, research was devoted into the PTZ:PMDA (1:1 stoichiometry) system. The X-ray analysis discloses that the dihedral angle of phenothiazine is 176.4° in this structure, which compares with 153.3° in monoclinic phenothiazine and 158.5° in orthorhombic phenothiazine <sup>105</sup>. Contemporary, a lower ionization energy of the phenothiazine molecule in this complex (1.38 eV, absorption at 900±25 nm) than in the pure phenothiazine crystal can be observed, due to the increasing extension of the conjugated  $\pi$ -electron system. With these special properties, a series of phenothiazine molecules have been introduced into lithium-ion batteries to perform as stable redox shuttle additives for the protection of chemical overcharge and overdischarge <sup>114</sup>. The life of the battery can be extended, due to the addition of phenothiazines.

Phenothiazines are also used as building blocks to fashion conjugated polymers <sup>115</sup>, with applications in electronics and optoelectronics. Kong et al. applied two new soluble phenothiazine-based conjugated polymers (Figure 8 a (homopolymer), b (alternating copolymer)) into the generation of PLEDs with luminance of up to 320 cd/m<sup>2</sup>. The investigation of CV and adsorption/emission indicates that the phenothiazine ring is an excellent building block for lowering the IP of these conjugated copolymers and reveals that both polymers are promising as p-type (hole transport) semiconductor materials for LEDs and that they can be used effectively in multiplayer devices or as blends with electron transport materials. A further report from Hwang's group <sup>102</sup>, presents an EL device fabricated from a

random copolymer of phenothiazine-fluorene (Figure 8 c), which exhibits a high power efficiency and brightness ( $4200 \text{ cd/m}^2$  and  $2.08 \text{ cd/A}$ ). They also designed an organic field effect transistor (FET) from a phenothiazine homopolymer (Figure 8 d). Except the copolymer phenothiazine-fluorene system, phenothiazine containing polythiophene<sup>116</sup> and phenothiazinylene vinylene<sup>103</sup> conjugated copolymers were synthesized and applied for the fabrication of OLED and FET devices.

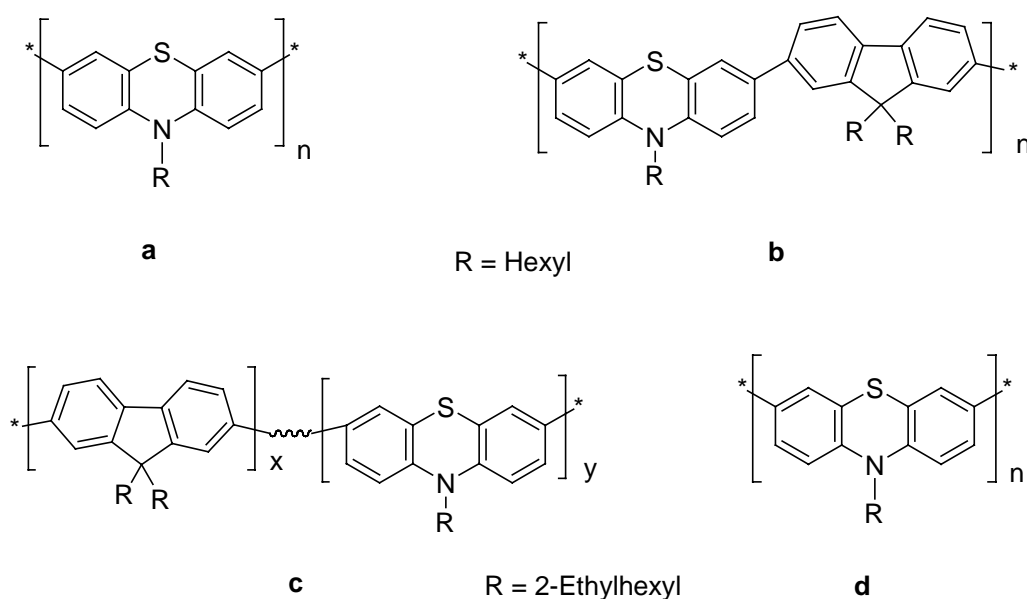


Figure 8. Conjugated polymers of phenothiazine and phenothiazine-fluorene.

### 1.3.3 Phenothiazine modified inorganic materials

The utilization of phenothiazine in hybrid organic/inorganic materials is not deeply developed up to now. In an early work from Meyer et. al. in 1994, a monolayer of a phenothiazine and a Ru (II) complex were attached to insulating or semiconducting substrates (antimony-doped tin dioxide, tin-doped indium oxide, or glass surfaces), based on the interaction between surface hydroxyls and carboxylic acid groups<sup>117</sup>, to investigate the potential of molecular-level devices. The electron or energy transfer between bound Ru(II) and phenothiazine (PTZ) can be observed with glass as substrate and demonstrates that lateral electron and energy transfer can occur across the surface. A further research discloses that a



remarkably long-living interfacial charge-separated pairs ( $\text{TiO}_2(\text{e}^-)\text{-Ru}^{\text{II}}\text{-PTZ}^+$ , Figure 9) can be created by visible light excitation of a ruthenium complex anchored on analogous colloidal  $\text{TiO}_2$  solutions and films <sup>118</sup>. Here, phenothiazine covalently bound to the ruthenium sensitizer, presents as an electron donor, and the rapid intramolecular electron transfer can occur from PTZ to the ruthenium metal center. The low oxidation potential and highly stability of the phenothiazine radical cation plays a key role to generate a hole, which is far away from the interface, thus a long-lived charge separation is created.

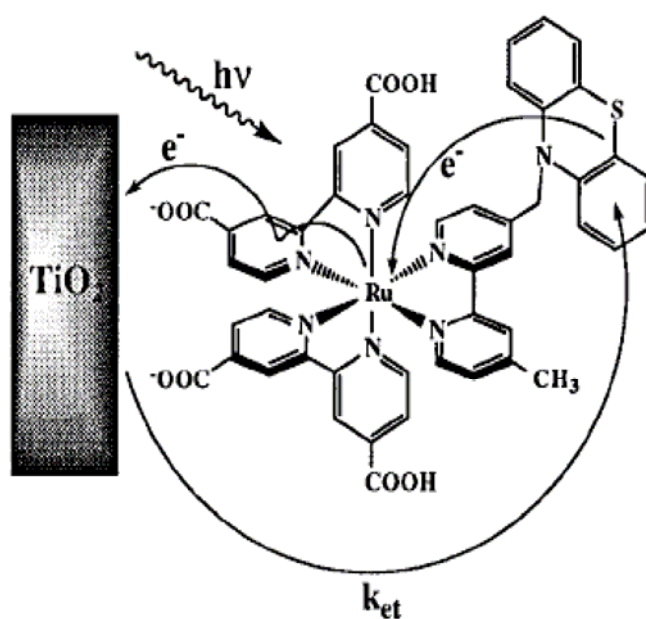


Figure 9. Visible light induced electron transfer in the ruthenium complex anchored  $\text{TiO}_2$  particles in the presence of phenothiazine donors <sup>118</sup>.

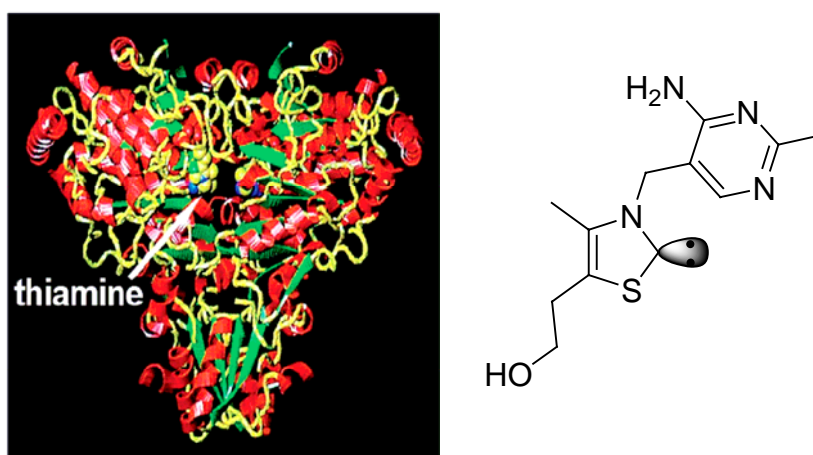
Phenothiazine is a good hole acceptor because of its low oxidation potential. Recently, based on this point, hole transfer from CdSe quantum dots to phenothiazine was investigated by time-resolved fluorescence and transient absorption spectroscopy by Lian's group <sup>119</sup>. This research is beneficial for understanding the dynamics of excitation dissociation in QDs, which is essential to their potential applications in many electronic devices such as solar cells.

To date, there are only a few reports on the physisorption of phenothiazines on mesoporous materials, which were reported by Kevan's group <sup>120, 121</sup>. They used MCM-41, SBA-15 and

MCM-48 as substrates, and the photoionized phenothiazine radical cations were characterized by EPR and Uv-vis spectroscopy. A series of researches disclose that porous silicas have been attributed for the stabilization of radical cations and that transition metal doped mesoporous materials facilitates the electron-transfer process. The silica network and the reducible transition metal ions probably act as electron acceptors <sup>122</sup>.

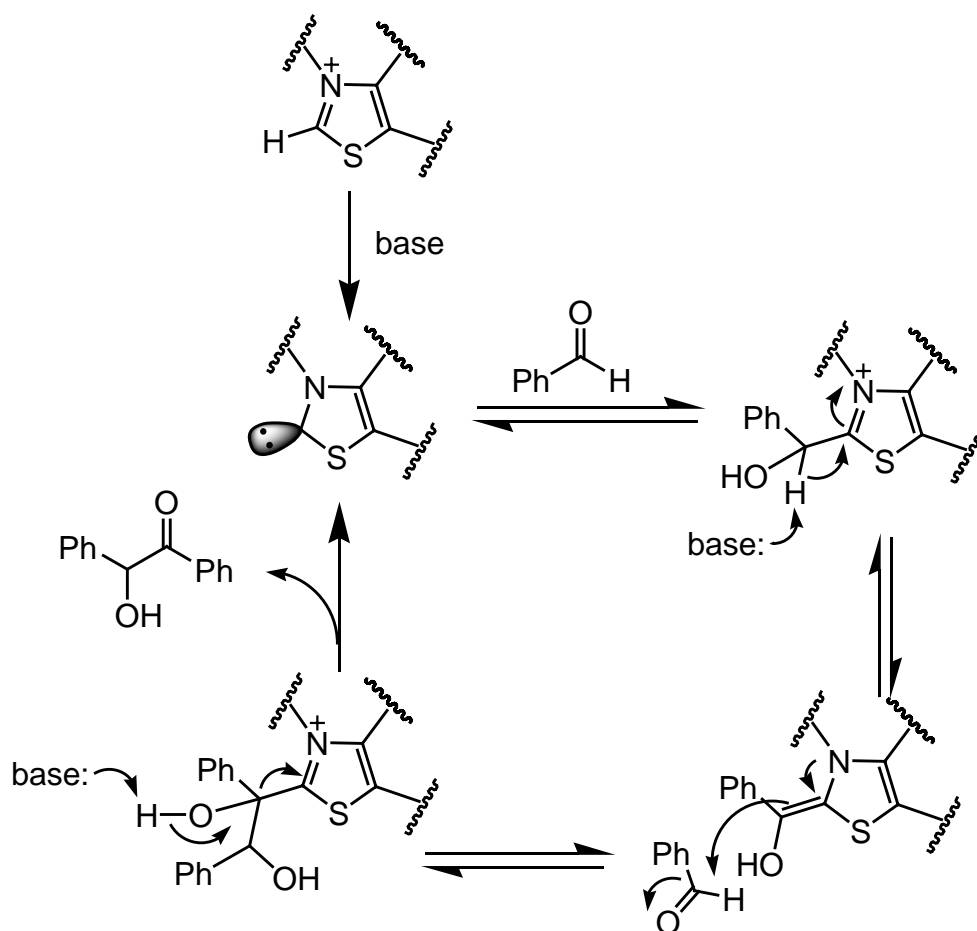
#### 1.4 Thiazolium salts as organo-catalysts and their heterogenization

The thiazolium motif comes from the thiamine (vitamin B<sub>1</sub>, see Scheme 4), the co-enzyme of series of enzymes catalyzing C-C coupling reactions in the fatty acid and carbohydrate metabolism <sup>123</sup>. A typical example for a thiamine depending reaction is the transketolase sequence, which converts hexoses into pentoses (via trioses, tetroses and heptoses). It therefore is essential for the generation of nucleotide building blocks as well as for the CO<sub>2</sub> fixation in plants. In the organocatalytic area, thiazolium catalysts have been applied for many coupling reactions, such as benzoin condensation <sup>124</sup>, the Stetter reaction <sup>125</sup>, Sila–Stetter reaction <sup>126</sup>,  $\alpha$ -amido ketones synthesis <sup>127</sup>, imidazole synthesis <sup>128</sup>, etc.

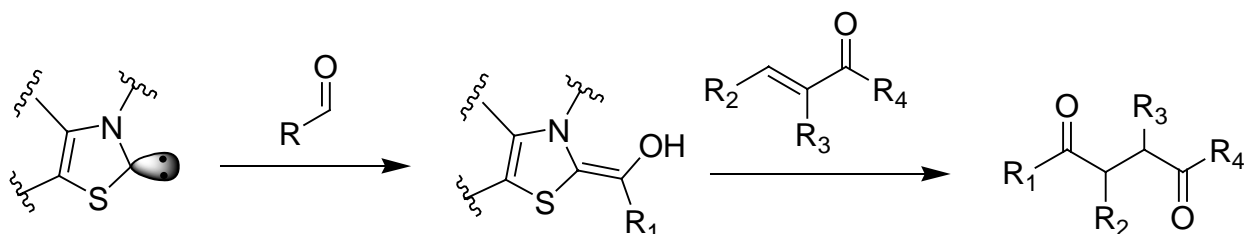


Scheme 4. Structure of the transketolase enzyme isolated from *Saccharomyces cerevisiae* and the molecular structure of the coenzyme thiamine (vitamin B<sub>1</sub>)

The reactions catalyzed by thiamine generally proceed via a nucleophilic carbene, generated by deprotonation of the C2 carbon atom of the thiazolium ring. A typical example is the mechanism of the benzoin condensation catalyzed by the thiazolium salts, which was first proposed by Breslow<sup>129</sup> (see Scheme 5). In this mechanism, the catalytically active species is thiazolin-2-ylidene, a carbene compound, which is formed in situ by deprotonation of the thiazolium salt. Nucleophilic attack on the carbonyl function of benzaldehyde then generates the thiazolium salt adduct. Deprotonation/reprotonation leads to the activated aldehyde in the form of a resonance-stabilized enaminol-type Breslow intermediate. This nucleophilic acylation reagent reacts again with a benzaldehyde molecule. Finally, the benzoin is eliminated and the original carbene catalyst is regenerated<sup>130</sup>. This protocol was not only limited to (asymmetric) benzoin condensations, but also extended to the cross-coupling of different aldehydes or of aldehydes and ketones<sup>131</sup>, as well as aldimines<sup>127</sup>, acylsilanes<sup>132</sup> etc.. Additionally, intramolecular cross-benzoin reactions were also performed by thiazolium salt catalysts<sup>133</sup>. Furthermore the thiazolium-catalyzed nucleophilic acylation was used for invention of the Stetter reaction<sup>134, 135</sup>, a catalytic 1,4-addition of aldehydes to an acceptor bearing an activated double bond (see Scheme 6). This branch is also widely developed from the respect of intermolecular and intramolecular Stetter reactions with special application in the synthesis of natural products<sup>136</sup>. This concept was also branched to the ring-opening polymerisation (ROP) reaction<sup>137</sup>.



Scheme 5. The mechanism of thiazolium salt catalyzed benzoin condensation



Scheme 6. Stetter reaction

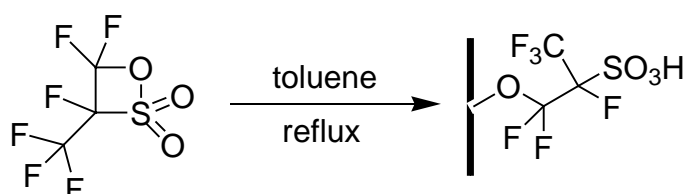
It is worth to notice that the thiamine cofactor is embedded in a narrow channel in the centre of the enzyme, which was disclosed from the X-ray structure analysis of a thiamine-dependent transketolase enzyme<sup>138</sup>. This structural property endows the high selectivities of related asymmetric chemical reactions. Thus the mimic of this enzymatic system is one of the aims of developing synthetic thiazolium salts catalysts. Many organic chemists are working

on the synthesis of chiral thiazolium salts to achieve high enantiomeric excesses. In this aspect, an alternative way probably is the modification of the reaction environment, which might also give an assistance for achieving high selectivity. A successful example was presented by Takagi et al.<sup>139</sup>, who used menthyl-substituted thiazolium salts to catalyzed the formation of benzoin in a micellar two-phase reaction system with an enhanced enantiomeric excess. Except changing the reaction phase, one further modification would be to transplante the active centre into some well designed materials. Up to now, thiazolium based catalysts have been fixed onto some supports, such as polymers, probably due to the molecular structure of the catalytically active system, which allows the simple introduction of linking blocks<sup>140</sup>. The other example is the adsorption of a thiazolium salt catalysts on the surface of calcium silicate<sup>141</sup>, alumina<sup>142</sup>, and resins<sup>143</sup>.

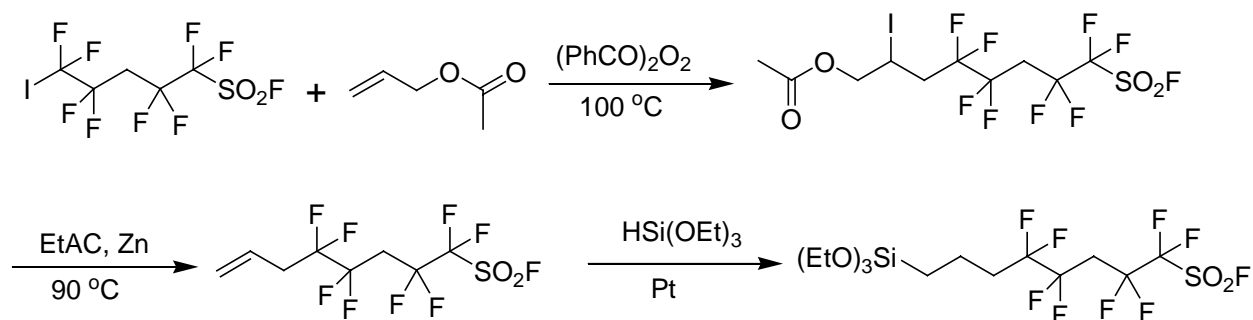
## 1.5 Sulfonic acid functionalized mesoporous materials as catalysts

The sulfonic acid functionalized mesoporous materials can be achieved by different synthesis pathways and by using various sulfonic groups containing organic moieties. The most commonly used precursor is 3-mercaptopropyltrimethoxysilane (MPTMS)<sup>144, 145</sup>. In this case, an oxidation treatment has to be taken to turn the thiol groups to sulfonic acid. To enhance the acid strength, arenesulfonic acid groups are employed. The introduction can be classified as indirect and direct method. The indirect way is first introducing the phenyl groups to the silica surface and subsequent sulfonation with chlorosulfuric acid. In general, this post treatment will damage the textural properties of the mesoporous material, leading to a clear reduction of the surface area. However, until the invention of the stabled periodic mesoporous benzene-silica with crystal-like pore wall by Inagaki et al., the sulfonation of phenylene groups of this material exhibits an ordered structure with high strength acid<sup>146</sup>. The direct way to achieve arenesulfonic acid founctionalized mesoporous material is first presented by Melero et al. used the similar route for the preparation of ordered SBA-15 with

2-(4-chlorosulfonylphenyl)-ethyltrimethoxy silane (CTPTMS) as the source of sulfonic group<sup>147</sup>. Additionally, some perfluorinated sulfonic-acid modified mesoporous materials were prepared by several groups. A successful and effective example was reported by Corma et al.<sup>148</sup>, who used a cyclic precursor (Scheme 7) the commercially available 1,2,2-trifluoro-2-hydroxy-1-trifluoromethyl ethane sulfonic acid sultone) reacting with the surface silanol groups and forming a covalent bond. Otherwise, a unique perfluorosulfonate silane was synthesized by Harmer's group (Scheme 8), subsequently, a series of hybrid sulfonic materials related with this precursor were prepared<sup>149, 150</sup>. These sulfonic acid functionalized solids have been widely applied as Brønsted acid catalysts in many types of reactions, such as esterification<sup>151</sup>, condensation<sup>152</sup>, Friedel-Crafts reactions<sup>144</sup>, rearrangement reactions<sup>153</sup>, etc..



Scheme 7. Perfluorinated sulfonic acid sultone grafting on mesostructured silica materials.



Scheme 8. Synthesis of a novel perfluorosulfonate silane by Harmer et. al..

## 1.6 Motivation

### 1.6.1 The motivation for phenothiazine functionalized hybrid materials

Our cooperate group has applied the Suzuki coupling reaction to straightforward achieve a series of soluble, monodisperse, and structurally well defined oligophenothiazines<sup>154</sup>. The inherent butterfly-shaped conformation of the phenothiazine structure multiplies and enhances helical and sigmoid oligomer conformations. Absorption and emission spectroscopy and cyclic voltammetry discloses that the effective conjugation length is already reached in the hexamer. Additionally, the oligophenothiaznes are both highly fluorescent with high fluorescence quantum yields and electroactive with low oxidation potentials. Therefore, their use as hole transporters and emitters in molecular electronic devices seems to be quit advantageous.

This work is to assemble (oligo)phenothiazine molecules into the channel or the framework of ordered mesoporous materials by stable covalent bonding. The strategy is to combine the properties of inorganic mesoporous materials (strong orientation of the pore system) and the phenothiazines (electrooptic features) for a rational design of one-dimensionally staked redox active molecules. By the assistance of the inorganic material, a manipulative intermolecular orientation of the  $\pi$ -conjugated systems is the main aim of our preparation. Thus, the existence of intermolecular charge transfer by electron hopping and even the generation of conducting hybrid materials are the final expectations. Additionally, the special electronic and optical properties of the modified phenothiazine molecules and a proper inorganic substrate might also provide an opportunity to design a sensor or an energy storage material.

### **1.6.2 The motivation for thiazolium salts and sulfonic acid functionalized hybrid materials**

The task of thiazolium salts and sulfonic acid functionalized hybrid materials is the heterogenization of these homogenous catalysts.

Before our research, there was no report about thiazolium modified mesoporous materials. Considering the structural properties of ordered mesoporous materials, they should be the suitable supports for organocatalysts to enhance the (stereo) selectivity and to allow recyclability. Additionally, the post synthetic modification of different surface parameters like hydrophobicity and basicity might provide a cooperative reaction environment.

Recently, a vast of investigations on sulfonic acid functionalized hybrid materials (especially the mesoporous materials) were published or applied as heterogenous catalysts. It is due to an increasing awareness of the environmental costs of traditional acid-catalyzed chemical processes and the various potential applications of this type of solid acid. Thus, a series of sulfonic acid functionalized silica materials will be synthesized by different methods, as well as their catalytic and ion exchange applications will be investigated. The acid strength and the structural properties of these materials are adjustable parameters, which should have some effect on the application.



## **Chapter 2. Phenothiazine functionalized hybrid materials**

### **2.1 Synthesis and characterization of carbamate-linked (oligo)phenothiazines in mesoporous silica materials by the post grafting method**

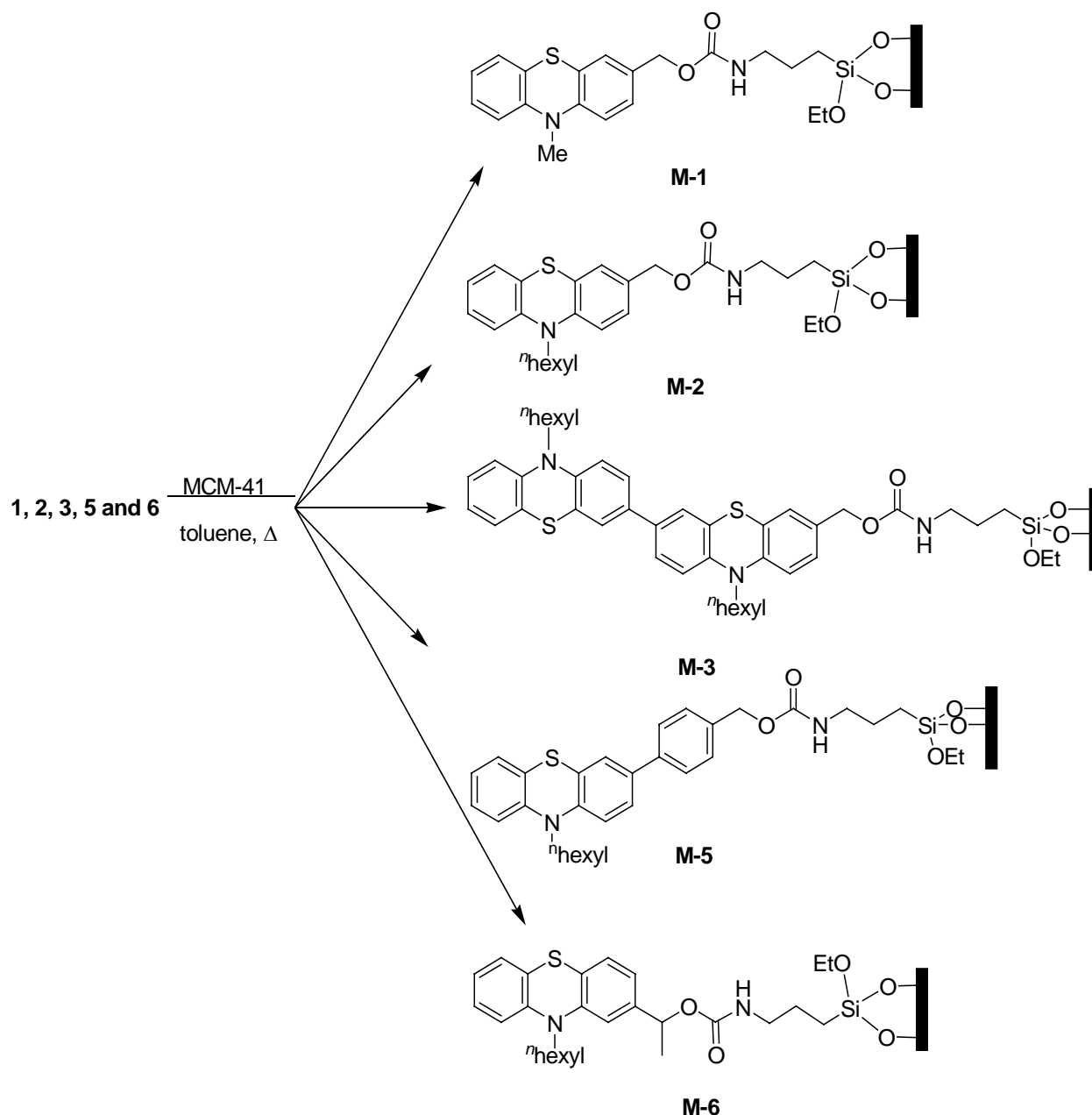
#### **State of the art**

Organic functionalization of the internal surface of a mesoporous silica host can be achieved by a grafting process after the formation of the neat support. This is also called post synthetic grafting. This approach has been widely employed to anchor specific organic groups onto diverse silica supports by using surface silanol groups. Typically, organochlorosilanes, organoalkoxysilanes or silazanes are used as precursors for this kind of surface modification. The concentration and the distribution of organic moieties in mesoporous materials by this method is constrained by the number of surface silanol groups and by their accessibility. Mesoporous silicas can be classed into amorphous materials due to the absence of a short ordered framework structure. However, this framework contains a considerable amount of surface silanol groups (Si-OH), which make it an attractive material to introduce organic compound by covalent bonding. Silylation generally occurs on free ( $\equiv\text{Si-OH}$ ) and geminal silanol ( $=\text{Si}(\text{OH})_2$ ) groups, while hydrogen-bonded silanol groups are less accessible to modification because they form hydrophilic networks among themselves<sup>51</sup>. The grafting rates depend on the reactivity of precursors, diffusion limitations, and steric factors<sup>155, 156</sup>.

#### **2.1.1 Synthesis of mesoporous hybrid materials**

The post synthetic grafting process, which follows the preparation of the neat silica materials is illustrated in Scheme 9 and Scheme 10. Two types of mesoporous materials were

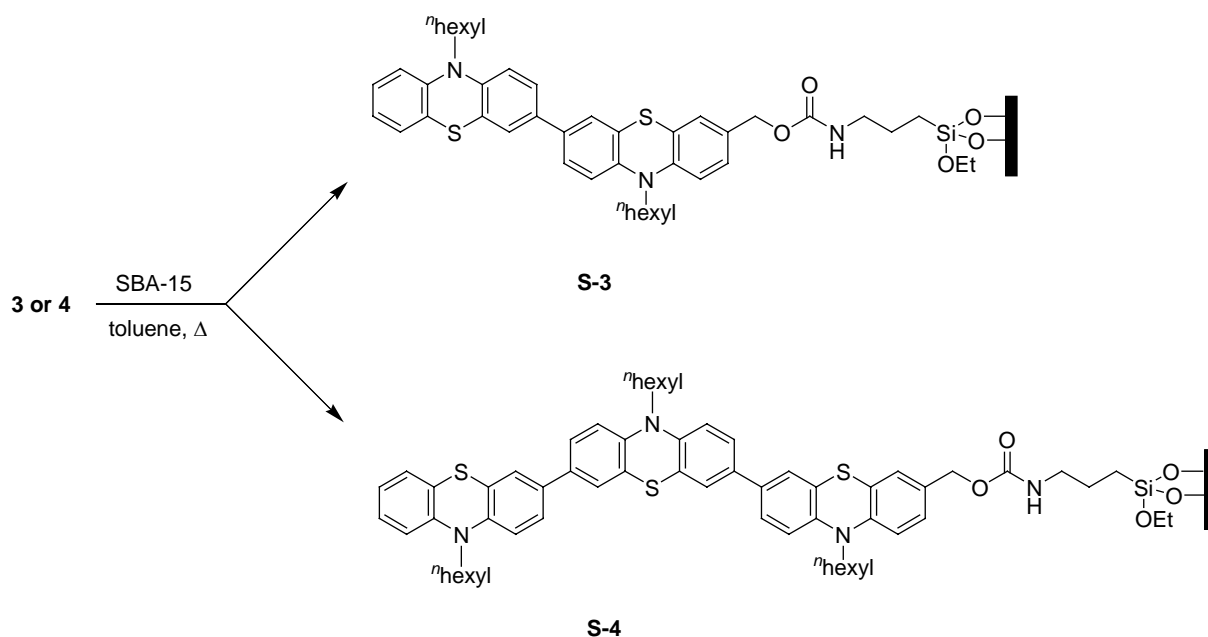
chosen, MCM-41 and SBA-15. Both of them have similar hexagonal mesostructures, but with large differences in the pore size. Before the grafting, the template has to be removed, which was performed by extraction with EtOH/HCl, to maximize the number of available surface silanol groups in purely siliceous MCM-41 and SBA-15<sup>157</sup>. The host materials were dried carefully prior to the addition of the precursors to avoid self-condensation of precursors in the presence of H<sub>2</sub>O adsorbed on the surface<sup>158</sup>. High temperature vacuum treatment is advantageous for more single silanol groups to be exposed on the surface of mesoporous materials, which facilitates the following reaction<sup>159</sup>. The carbamate linker is sufficiently stable to allow post-synthetic grafting of the electrophore units in toluene on MCM-41 or SBA-15. Unreacted precursors were removed by Soxhlet extraction with methylenechloride, and the collected organic/inorganic hybrid materials (oligo)phenothiazine@MCM-41 or (oligo)phenothiazine@SBA-15 were denoted as **M<sub>x</sub>**, and **S<sub>x</sub>**, respectively (**x** is the symbol of organic silaneprecursor, Scheme 9 and Scheme 10). It is known that the pore size of MCM-41 can be adjusted from 1.5 nm to 10 nm by modifying the conditions of the synthesis, such as the size of template, the temperature of hydrolysis, and the crystallization time or simply by adding an auxiliary organic agent<sup>160,161</sup>. Firstly we chose CTAB as surfactant, which contains sixteen carbon atoms in the alkyl chain, and can provide a hexagonal array of channels with a pore size of around 3 nm. This is almost the critical size of the biphenothiazines with the carbamate linker. One of our aims concerning the pore size control is to probe the size effect of different mono- and oligo-phenothiazine units in detail, therefore the same synthetic conditions were performed during the preparation of the functionalized MCM-41 materials **M1**, **M2**, **M3**, **M5** and **M6**.



Scheme 9. Synthesis of mesoporous hybrid materials **M-1**, **M-2**, and **M-3**, **M-5** and **M-6** by the post synthetic grafting method with MCM-41 as substrate.

The elemental analysis showed that the loading of the phenothiazine groups on MCM-41 varies (**M1** > **M2** > **M6** > **M5** > **M3**). Since the same amount of organic precursors and substrate material were used for all these modifications, we figure out that this discrepancy arises from the increasing molecular size of organic units. Especially, for biphenothiazine **M3**, only traces of nitrogen (< 0.1%) could be detected by elemental analysis. Additionally,

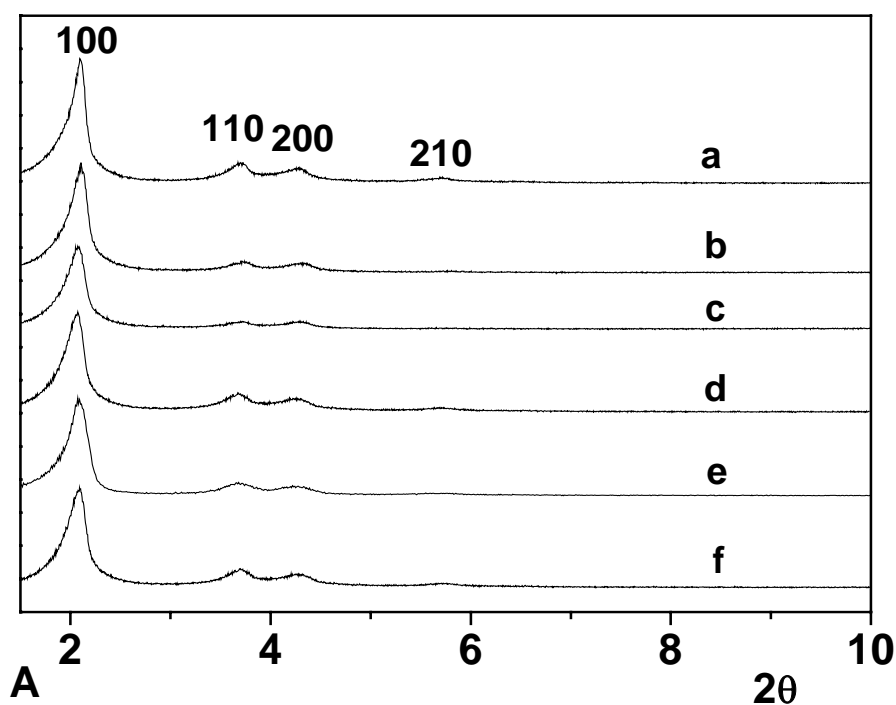
TG-DTG analysis exhibited only 1.8 % of mass loss from 300 to 600 °C which is assigned to the burning of the organic component. This corresponds to 0.03 mmol/g of **3** grafted on MCM-41. This extremely low amount of loading is due to the molecular size of **3** which is about 2.9 nm (Estimated by the Chem3D software), and thus larger than the main pore size of the substrate MCM-41 (2.8 nm). This size effect will hinder the diffusion of this compound inside the pore channels during the post-grafting process. We therefore changed the substrate to SBA-15 for the heterogenization of compound **S3** and **S4**. SBA-15 has the same two-dimensional hexagonal structure as MCM-41, but this material provides a relatively large pore size (from 5 nm to 30 nm based on the parameters of the synthesis). This should allow a rather large molecule to diffuse<sup>26</sup>. Consequently, a severe increase of loading can be observed with sample **S3** on SBA-15, we found 0.32 mmol/g of organic compound on the material, even though only 0.50 mmol of **3** was used for 1 g of SBA-15.



Scheme 10. Synthesis of mesoporous hybrid materials **S-3** and **S-4** by the post synthetic grafting method with SBA-15 as the substrate.

### 2.1.2 Structural properties of the hybrid materials

The powder XRD patterns of extracted neat MCM-41, **M1**, **M2**, **M3**, **M5** and **M6** are given in Figure 10A, those of the samples **S3** and **S4** together with **SBA-15** are presented in Figure 10B. Neat MCM-41 shows four Bragg reflexes for the (100), (110), (200) and (210) plane, which can be indexed to two-dimensional (2D) hexagonal  $p6mm$  symmetry, indicating a highly ordered hexagonal structure<sup>162</sup>. Similarly, neat SBA-15 can clearly be characterized by three reflections in the  $2\theta$  range of  $0.8-2^\circ$ , which can be indexed to a hexagonal cell as (100), (110), and (200)<sup>36</sup>, respectively. After modification by post synthetic grafting, the first-order (100) and the second-order reflections (110) and (200) are present for all samples, which suggests the structural preservation of the materials. The reduced intensity of the peaks of the modified samples in comparison with the parent materials is due to a slight reduction of ordering in the mesoporous material and/or a reduced scattering contrast between the silica wall and the porous system<sup>157, 163</sup>.



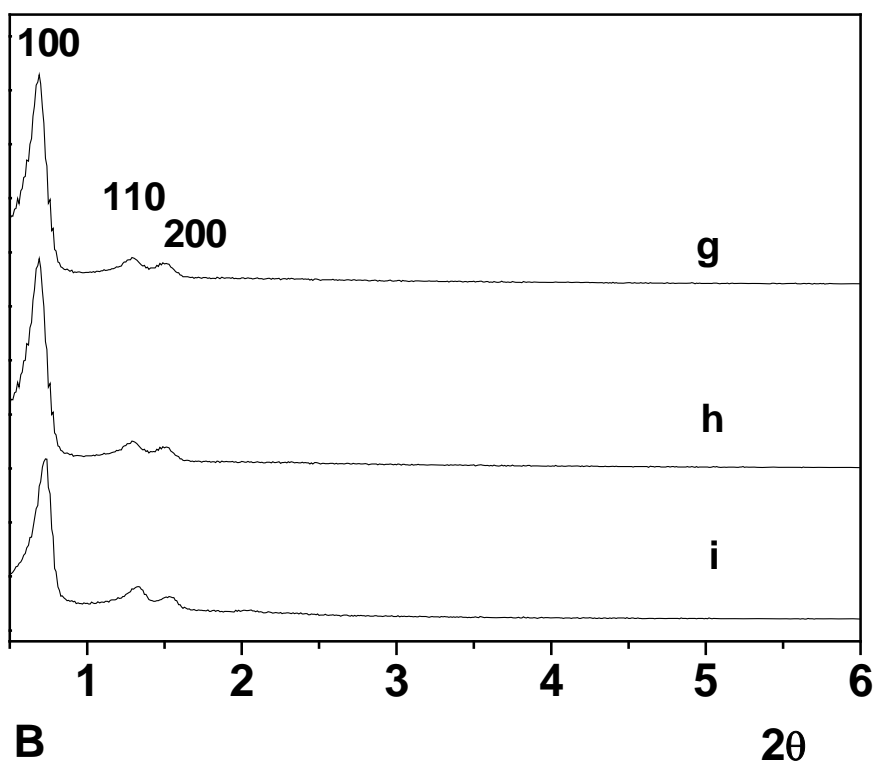
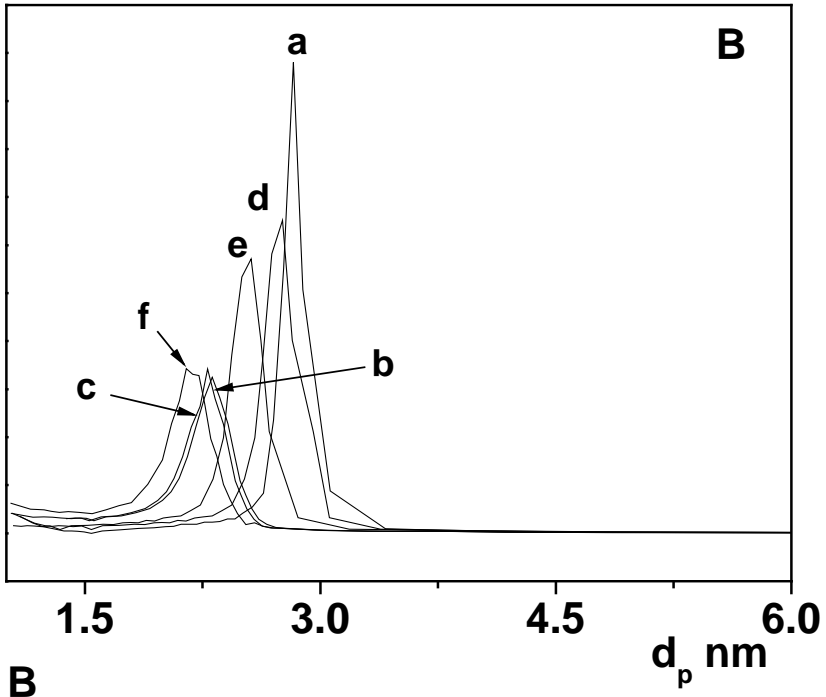
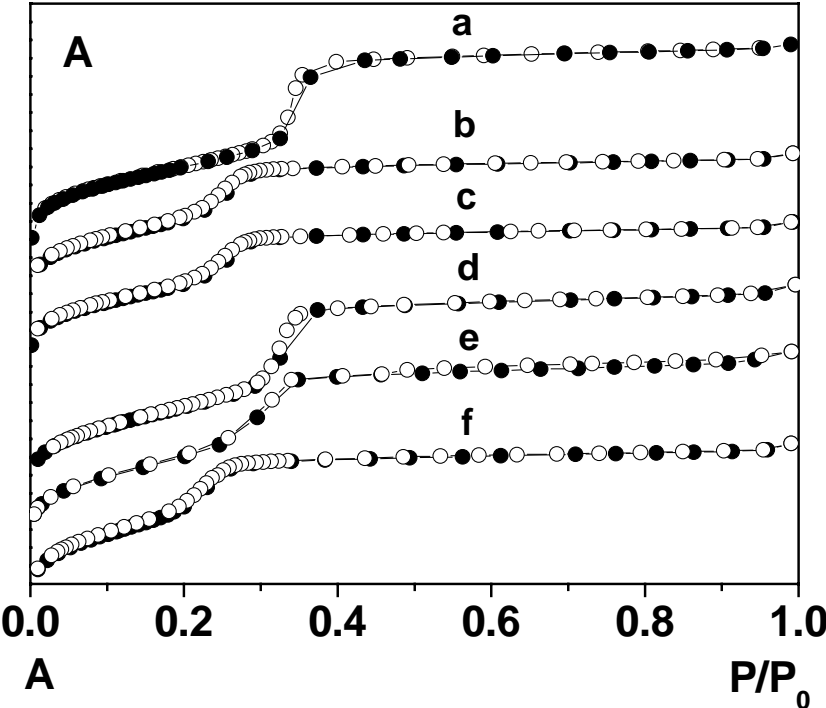


Figure 10. A: Powder XRD pattern of parent (a) **MCM-41**, (b) **M1**, (c) **M2**, (d) **M3**, (e) **M5**, and (f) **M6**; B: powder XRD pattern of parent (g) **SBA-15**, (h) **S3** and (i) **S4**.

Nitrogen sorption was used to follow the changes of the pore structures as a result of the organic modification in the channel. The specific surface areas and the textural properties of MCM-41, SBA-15 and all modified samples are summarized in Table 3. Both neat mesoporous substrates exhibit type IV isotherms, which is typical for periodic mesoporous materials, according to the IUPAC classification<sup>164</sup> (Figure 11C). The isotherm of MCM-41 shows no hysteresis, indicating a uniform pore size and ordered cylindrical channels<sup>165</sup>. SBA-15 displays a distinct hysteresis loop (type H1) and a sharp increase in adsorption at higher  $P/P_0$  value (0.65), indicating a relative large cylindrical pore<sup>166</sup>. Figure 11B and D illustrate the pore size distributions derived from the desorption data of the isotherms. This indicates uniform pore sizes to be present for all materials. Additionally a gradual decrease of the pore sizes after the modification can be observed.



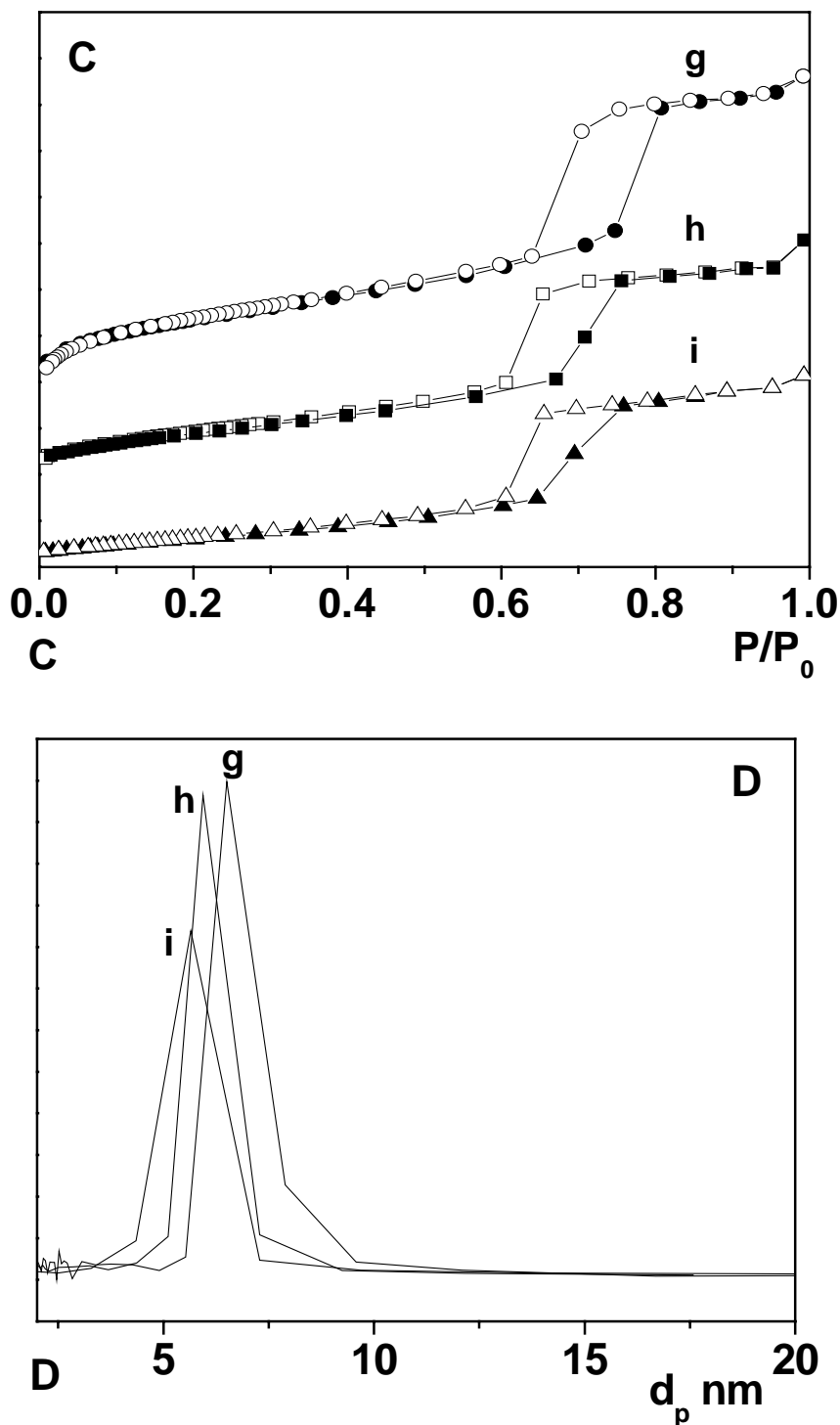


Figure 11. A: N<sub>2</sub> adsorption/desorption isotherms of (a) neat **MCM-41**, (b) **M1**, (c) **M2**, (d) **M3**, (e) **M5**, and (f) **M6**; B: pore size distribution of MCM-41 substrate samples B: N<sub>2</sub> adsorption/desorption isotherms of (g) neat **SBA-15**, (h) **S3** and (i) **S4**. D: pore size distribution of SBA-15 substrate samples (adsorption points are marked by solid circles and desorption points by empty circles).



The calculation of pore volume and pore size is estimated with the BJH method, the specific surface area was obtained from the BET treatment of the isotherm. Furthermore the contents of organic compounds in the materials are given in the Table 3. From the structural parameters of the materials, it was found that the specific surface area, the pore size and the pore volume of all the hybrid materials are decreased in comparison with the parent MCM-41 and SBA-15 supports. This is due to the presence of the organic fragments in the pore channels, but the maintenance of type IV isotherm and the narrow pore size distribution prove the preservation of ordered mesoporous structures after modification with different (oligo)phenothiazines.

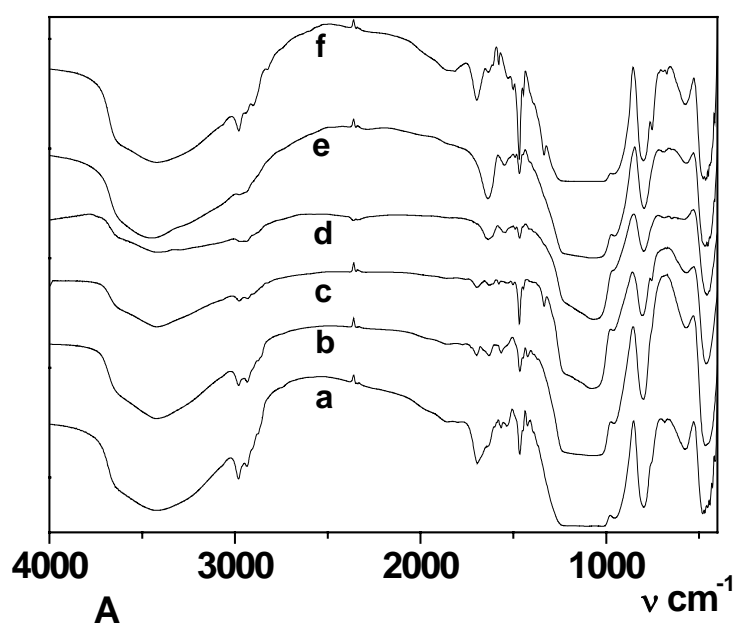
Table 3. The textural parameters of neat MCM-41, SBA-15 and **M-1**, **M-2**, **M-3**, **M-5**, **M-6**, **S-3**, and **S-4** derived from nitrogen-adsorption/desorption analysis and the content of the loading of phenothiazines on the hybrid materials.

sample	substrate	BET surface	pore volume	pore	content of phenothiazine <sup>a</sup>	
		area [m <sup>2</sup> g <sup>-1</sup> ]	[cm <sup>3</sup> g <sup>-1</sup> ]	diameter [Å]	[mmolg <sup>-1</sup> ]	[wt-%]
MCM-41	--	1092	0.95	28.3	--	--
SBA-15	--	1101	1.58	65.0	--	--
<b>M1</b>	MCM-41	814	0.62	23.1	0.41	15.5
<b>M2</b>	MCM-41	846	0.67	23.0	0.34	15.3
<b>M3</b>	MCM-41	996	0.90	27.6	0.03 <sup>b</sup>	1.8 <sup>b</sup>
<b>M5</b>	MCM-41	935	0.81	25.6	0.24	12.6
<b>M6</b>	MCM-41	903	0.72	22.6	0.30	13.9
<b>S3</b>	SBA-15	806	1.19	59.6	0.32	23.4
<b>S4</b>	SBA-15	716	0.96	56.4	0.17	17.2

<sup>a</sup> Calculated according to the content of nitrogen (CHN elemental analysis). <sup>b</sup> Calculated according to the data of TG-DTG analyses.

### 2.1.3 Characterization of the organic component in the hybrid materials

FT-IR spectroscopy was used to provide information with respect to the organic modification occurring in the silica system. The spectra of modified hybrid materials are shown in Figure 12A, except for sample **M3**. Due to the low concentration of organic material in this sample, the characteristic absorptions of the organic moieties are absent in this case. For comparison, the spectra of neat MCM-41 and SBA-15 are presented in Figure 12B. All materials show a broad band in the range of 3600-3200  $\text{cm}^{-1}$ , which can be assigned to the hydroxyl stretching vibration of hydrogen bonded internal silanol groups. The asymmetric Si-O-Si vibration appears at around 1100  $\text{cm}^{-1}$ , while the peak at 800  $\text{cm}^{-1}$  is attributed the symmetric Si-O-Si vibration. The bending vibrations of the surface silanol groups and Si-O are observed at 950 and 460  $\text{cm}^{-1}$ <sup>167</sup>, respectively. In addition to the characteristic bands of the SiO<sub>2</sub> framework, the anchored organic groups can be identified by peaks at 2700-3000 and 1470  $\text{cm}^{-1}$ , which are assigned to the aliphatic CH stretching and deformation vibrations, respectively. The C=O stretching vibration of the carbamate group can be observed at 1700  $\text{cm}^{-1}$  in the modified materials<sup>168</sup>. These results confirm the introduction of the carbamate linked phenothiazine molecules in the mesoporous materials.



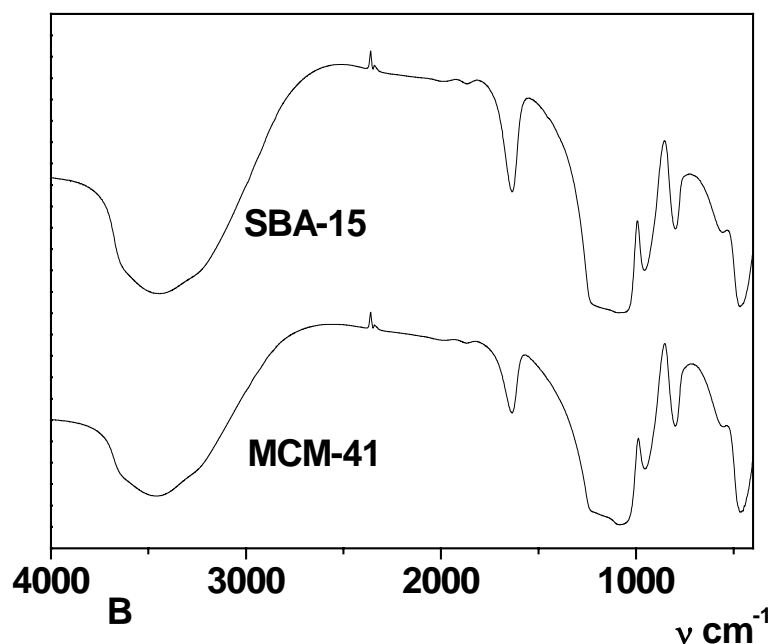


Figure 12. FT-IR spectra of A: (a) **M1**, (b) **M2**, (c) **S3**, (d) **S4**, (e) **M5**, and (f) **M6**; B: MCM-41 and SBA-15.

The successful grafting and the integrality of the organic components were additionally verified by solid-state  $^{13}\text{C}$  CP-MAS NMR spectroscopy. All samples present solid-state NMR spectra, that show resonances with chemical shifts, similar to those of the free compounds. This is exemplarily demonstrated for **M1** and **S3** in Figure 13 and Figure 14. The spectra of **M1** show two quite sharp signals at ca.  $\delta$  60 and 16 ppm, which are also present in the parent materials. They can be assigned to free ethanol formed as a side product of the grafting reaction or the remnant ethanol from the template extracting process. These signals overlap with the resonance of residual  $\text{Si-OCH}_2\text{CH}_3$  groups (see discussion of the  $^{29}\text{Si}$  NMR spectrum). The single peak at 8 ppm can be assigned to the carbon atom of the C-Si unit, which demonstrates that no cleavage of C-Si bond happens during the grafting process. A characteristic resonance at  $\delta$  35 ppm proves the preservation of the phenothiazine bound N- $\text{CH}_3$  group. The presence of carbon resonances of the phenothiazine moiety in the down field region ( $\sim$  114 ppm) is typical for an electronrich aromatic system. A small shift of the carbon

resonance of the C=O group ( $\sim 158$  ppm) for the hybrid material, compared to the solution data, is assigned an interaction of the carbonyl group with surface Si-OH units <sup>169</sup>.

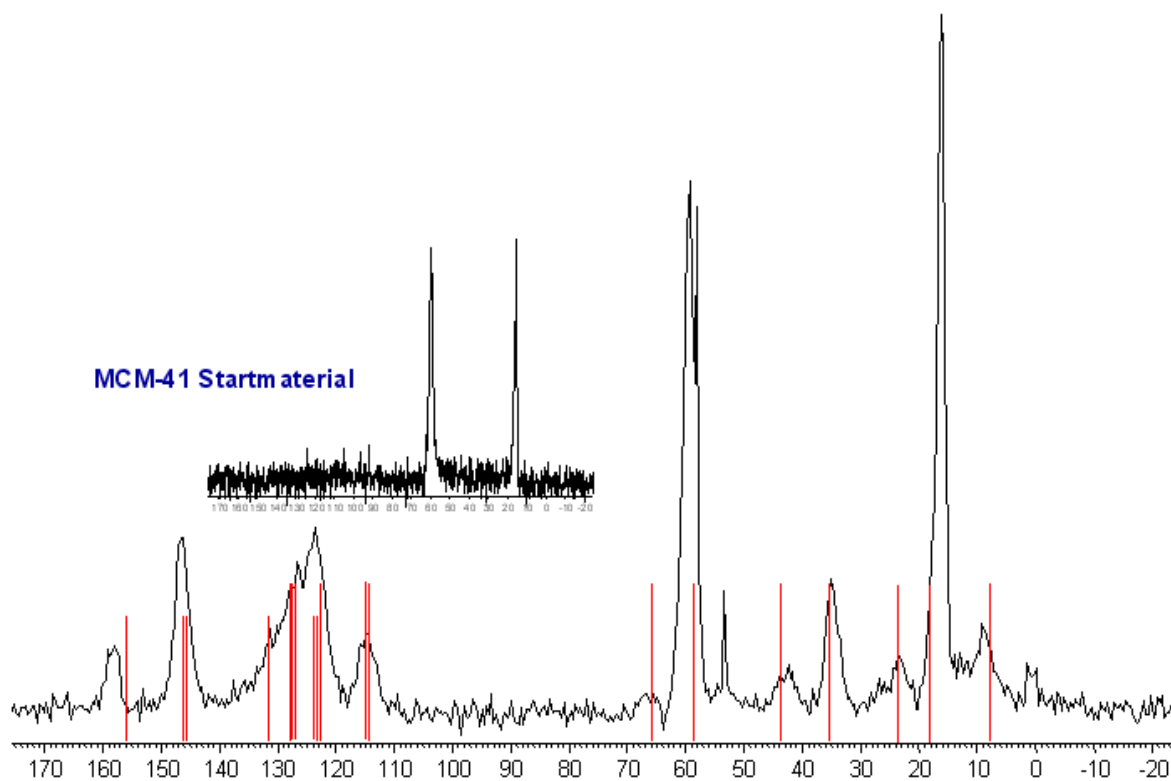


Figure 13.  $^{13}\text{C}$  CP-MAS NMR spectrum of **M1**; red lines give information on position and relative intensities in the solution NMR spectrum of **1**.

The biphenothiazine moiety **3** was introduced into SBA-15. The resulting solid state  $^{13}\text{C}$  spectra is presented in Figure 14. The overlapped resonances at high field (20-40 ppm) are assigned to the carbon atoms of the hexyl chains, while the peaks in the low field region can be assigned to the signals of biphenothiazine core. As discussed above, a shift for the resonance of the C=O group ( $\sim 158$  ppm) in the solid material system as compared to the solution NMR can be observed. It indicates again an interaction between the carbonyl group and surface silanol also occurred in the biphenothiazine modified SBA-15 system.

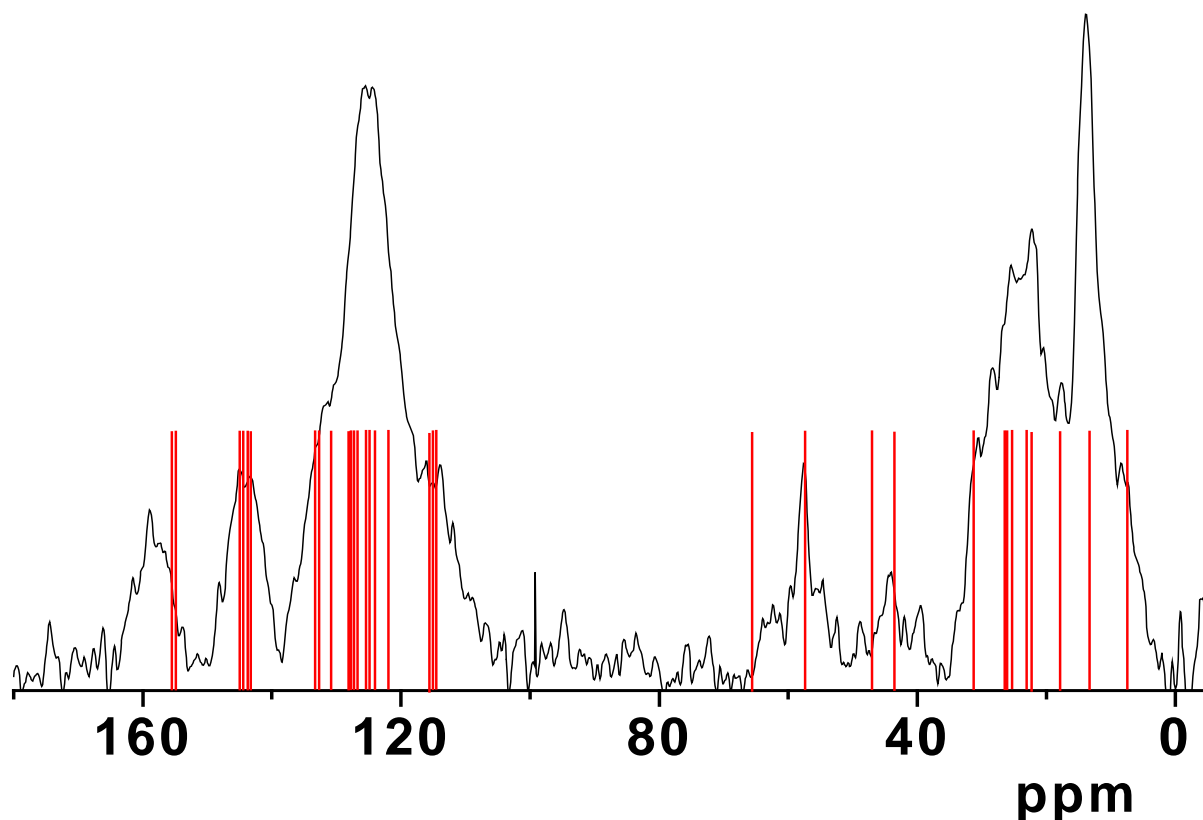


Figure 14.  $^{13}\text{C}$  CP-MAS NMR spectra of **S3**; red lines give information on the position in solution NMR spectra of **3**.

Modification of SBA-15 with the triphenothiazine compound **4** produces **S4**, which exhibits the  $^{13}\text{C}$  CP-MAS NMR spectrum shown in Figure 15. Two groups of overlapping strong resonances in the low field and high field region can be separately assigned to the carbon atoms of the electronrich aromatic system and aliphatic chains. The resonance of C=O group can be observed around 160 ppm. A little shift to low field is also due to the formation of hydrogen bonds between carbonyl group and the surface Si-OH units.

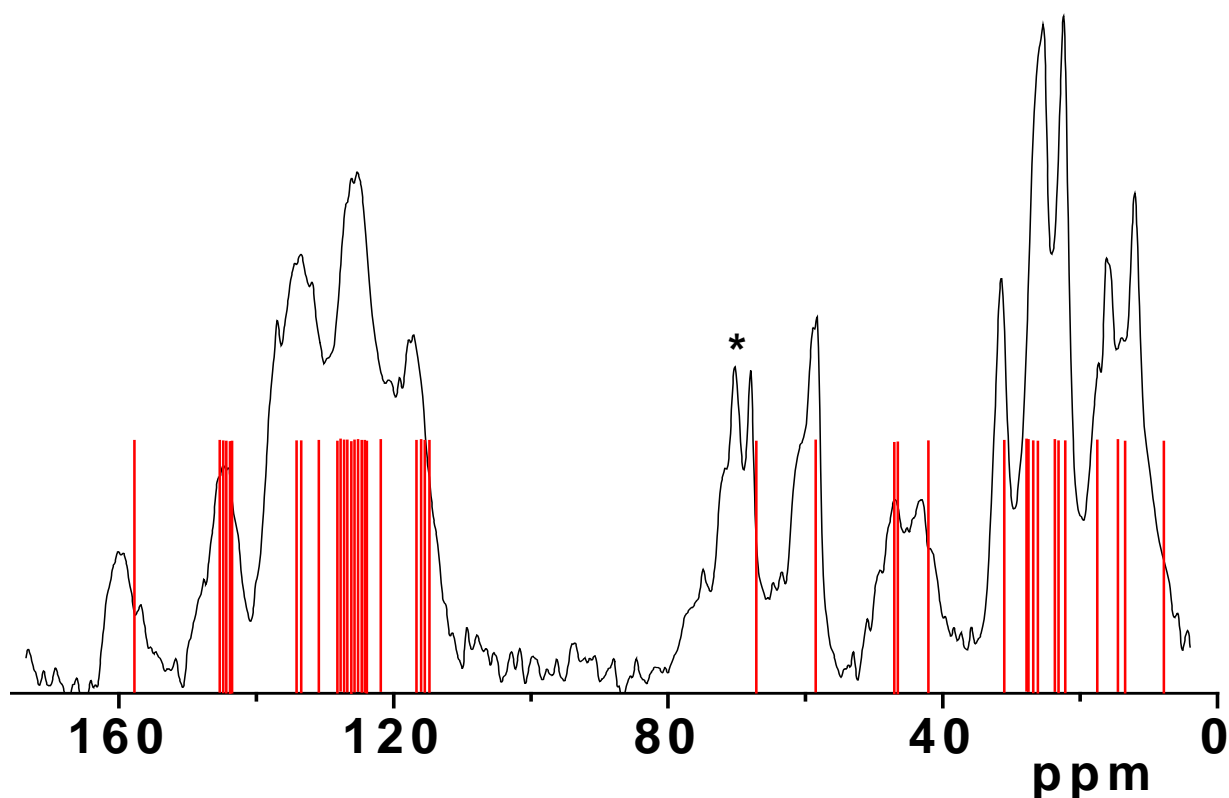
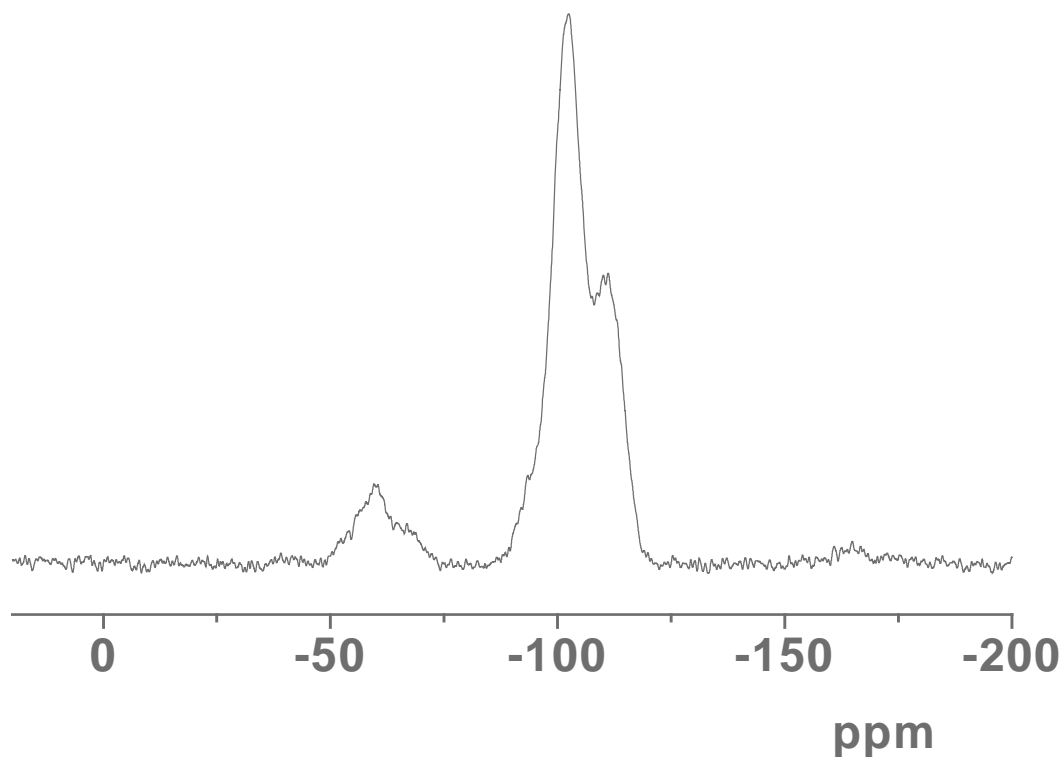


Figure 15.  $^{13}\text{C}$  CP-MAS NMR spectrum of **S4**; red lines give information on the position in solution NMR spectrum of **4**.

The covalent linkage of the phenothiazines in the mesostructured materials also can be monitored by means of  $^{29}\text{Si}$  CP-MAS NMR spectroscopy (shown exemplarily for **M1** in Figure 16). The spectrum of neat MCM-41 shows three signals at  $\delta$  -110, -101, and -92 corresponding to the  $\text{Si}(\text{OSi})_4$  ( $\text{Q}^4$ ),  $\text{HOSi}(\text{OSi})_3$  ( $\text{Q}^3$ ), and  $(\text{HO})_2\text{Si}(\text{OSi})_2$  ( $\text{Q}^2$ ) sites of the silica framework<sup>170</sup>. Covalently grafting of the phenothiazine onto the surface makes the  $\text{Q}^2$  signal disappear, decreases  $\text{Q}^3$ , and concomitantly increases the  $\text{Q}^4$  intensity, which is due to the consumption of isolated Si-OH groups and geminal silandiols during the reaction. For the modified materials, three additional broad and overlapping signals appear at  $\delta$  -49, -58, -67, which can be assigned to  $\text{R-Si}(\text{HO})_2(\text{OSi})$  ( $\text{T}^1$ ),  $\text{R-Si}(\text{HO})(\text{OSi})_2$  ( $\text{T}^2$ ), and  $\text{R-Si}(\text{OSi})_3$  ( $\text{T}^3$ ) organosiloxane species<sup>171</sup>.

Figure 16.  $^{29}\text{Si}$  CP-MAS NMR spectra of **M1**.

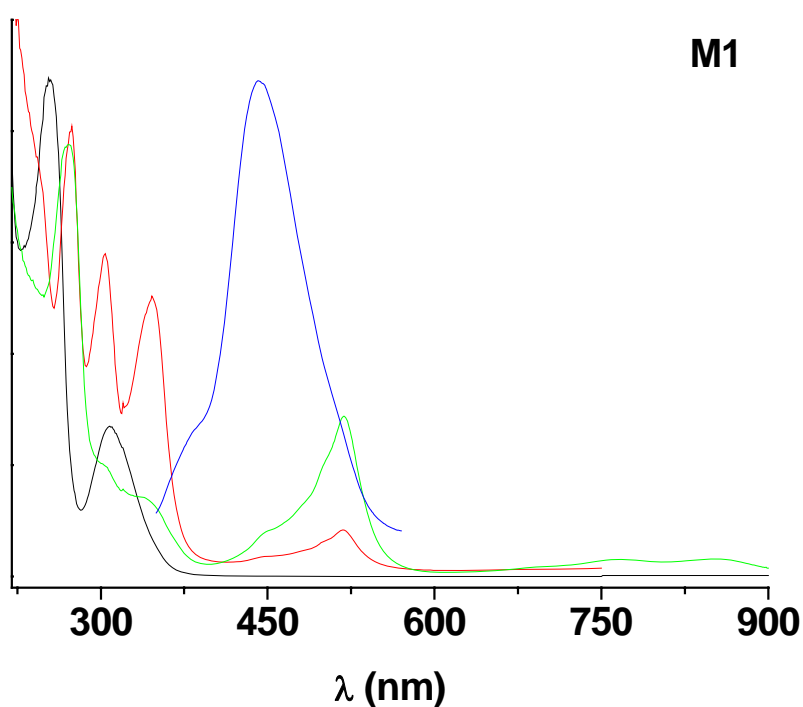
### 2.1.4 Photophysical properties

Table 4. Selected absorption and emission spectra data of the organic precursor molecules and the corresponding hybrid materials

sample	absorption $\lambda_{\text{max,abs}}$ [nm] ( $\epsilon$ )	emission $\lambda_{\text{max,em}}$ [nm]	hybrid sample	absorption $\lambda_{\text{max,abs}}$ [nm]	emission $\lambda_{\text{max,em}}$ [nm]
<b>1<sup>b</sup></b>	258 (42000), 290 (6300), 312 (7000)	465	<b>M1</b>	253, 308	442
<b>2<sup>b</sup></b>	260 (31100), 314 (5100)	441	<b>M2</b>	255, 312	386, 435
<b>3<sup>b</sup></b>	268, 322, 366 <sup>a</sup>	461	<b>M3</b>	267, 322, 363	391, 459
			<b>S3</b>	266, 323, 364	455
<b>4<sup>b</sup></b>	270 (9600), 324 (3900), 373 (3100)	474, 514 (sh)	<b>S4</b>	278, 324, 370	478
<b>5<sup>b</sup></b>	240 (144900), 322 (6400)	268 467	<b>M5</b>	268, 350	514
<b>6<sup>b</sup></b>	260 (28500), 312 (4400)	453	<b>M6</b>	246, 311	385, 441

<sup>a</sup> Extinction coefficients were not determined. <sup>b</sup> Data provided by the group of Prof. T. J. J. Müller (Univ. Düsseldorf).

All phenothiazine modified hybrid materials show several strong absorptions in the UV-region (Figure 17, Figure 18, Figure 19, and Table 4), which are similar to the absorptions of the pure organic compounds (see the absorption data of the precursors in Table 4). A slight red shift of the peak maxima can be observed when the number of the phenothiazine cores is increased or the phenothiazine is linked to a phenyl group. This is due to an extension of the  $\pi$ -electron system. The results on the solid hybrid materials indicate that there is no strong interaction between the phenothiazines and the framework silica of the channels in the ground state of the dye. They further prove the existence of phenothiazine molecules in the mesoporous materials. A band broadening in the spectra of incorporated phenothiazine molecules compared to the pure organic compounds in solution can be assigned to a  $\pi$ -electron interaction with surface hydroxyl groups. This phenomenon is often observed for aromatic chromophores adsorbed on silica materials<sup>172</sup>.





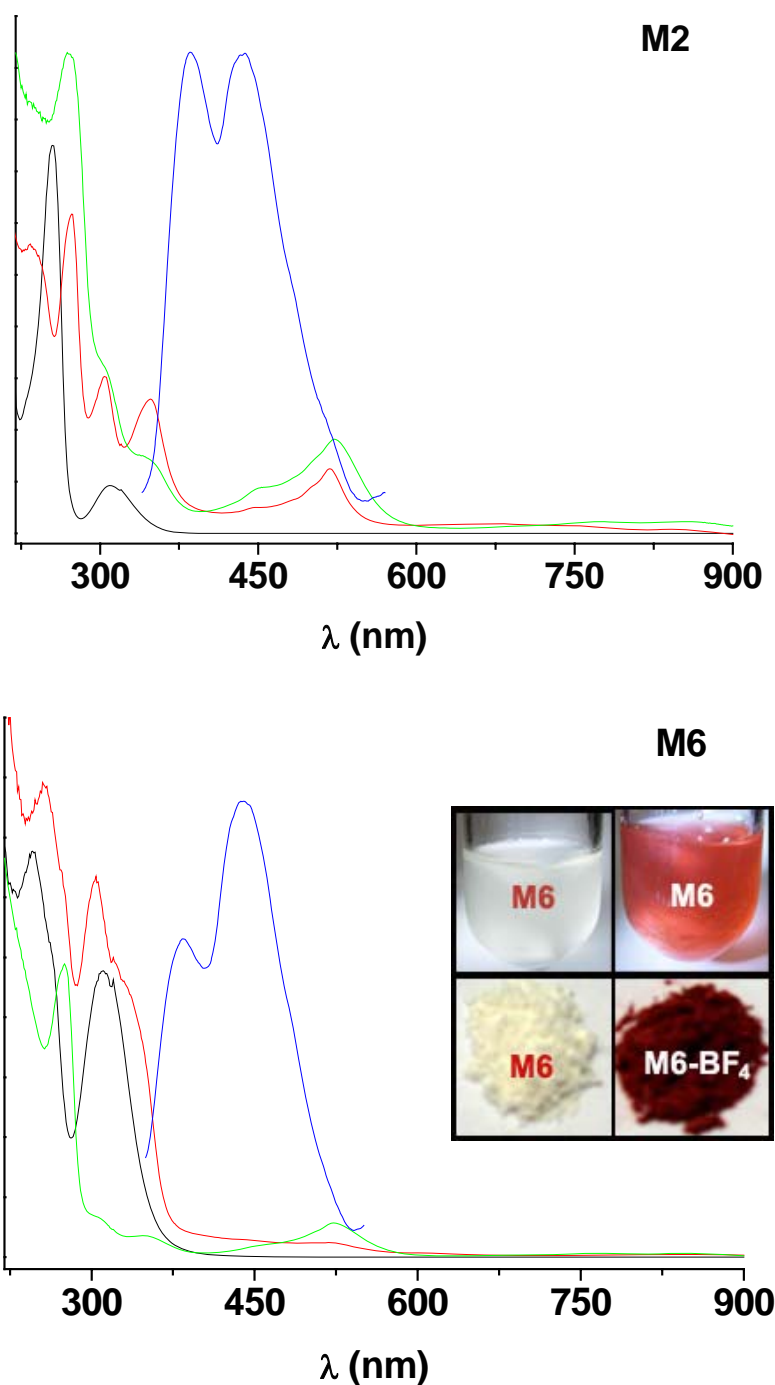
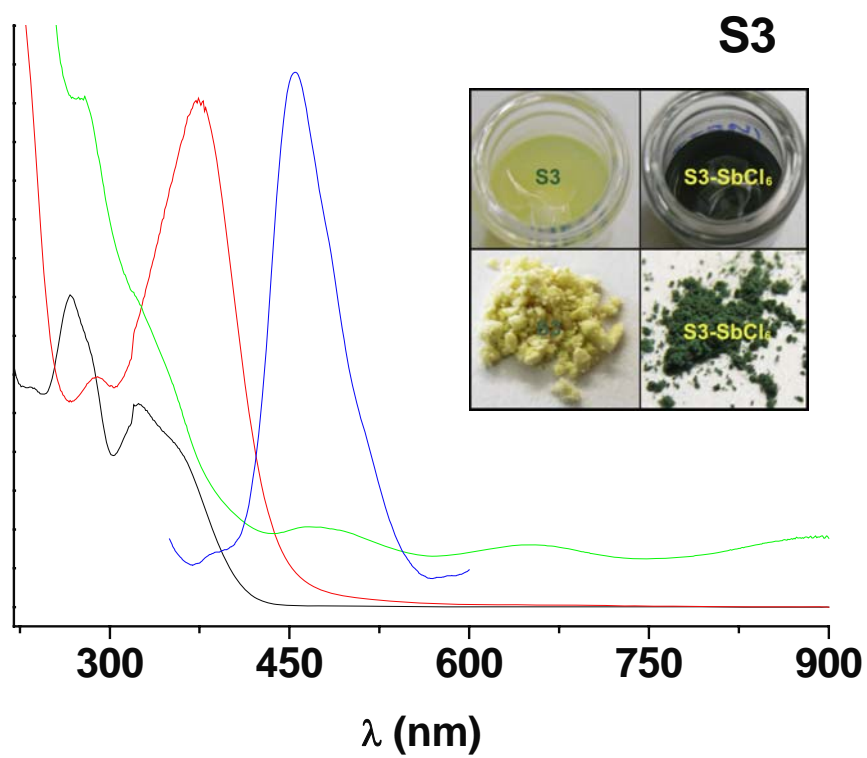
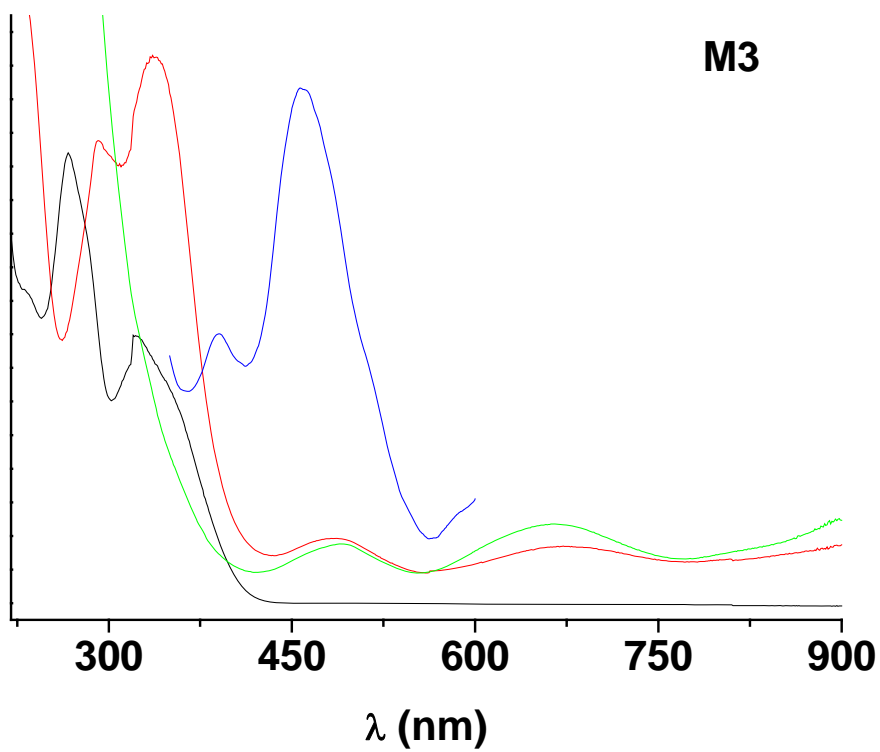


Figure 17. UV-Vis spectrum of the mono-phenothiazine modified samples **M1**, **M2**, **M6** (black lines), the absorptions of the corresponding radical cationic samples **M1-BF<sub>4</sub>**, **M2-BF<sub>4</sub>**, **M6-BF<sub>4</sub>** (red lines), **M1-SbCl<sub>6</sub>**, **M2-SbCl<sub>6</sub>**, **M6-SbCl<sub>6</sub>** (green lines), and the emission spectra of the modified samples **M1**, **M2**, **M6** (blue lines). The inset picture demonstrates the color change caused by the oxidation of **M6** using NOBF<sub>4</sub> in suspension and for the corresponding solid.



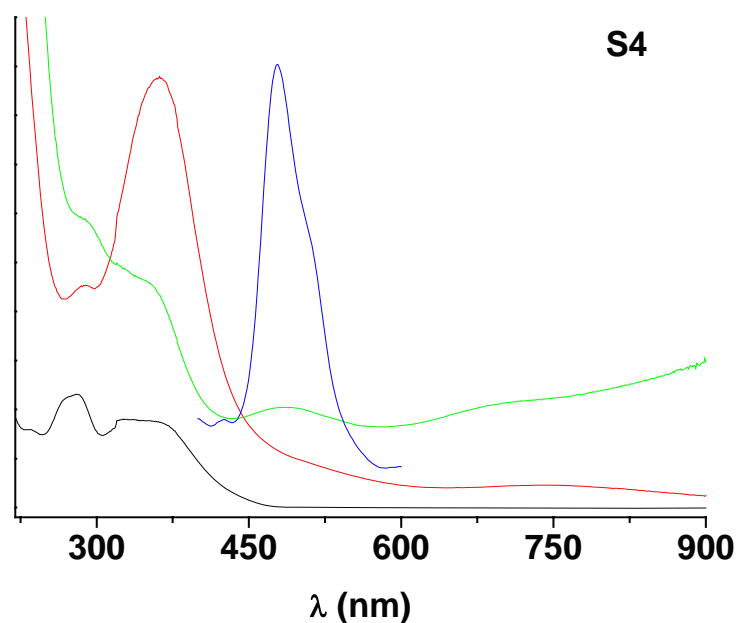


Figure 18. UV-Vis spectrum of the oligo-phenothiazine modified samples **M3**, **S3**, **S4** (black lines), the absorptions of the corresponding radical cationic samples **M3-BF<sub>4</sub>**, **S3-BF<sub>4</sub>**, **S4-BF<sub>4</sub>** (red lines), **M3-SbCl<sub>6</sub>**, **S3-SbCl<sub>6</sub>**, **S4-SbCl<sub>6</sub>** (green lines), and the emission spectra of the modified samples **M3**, **S3**, **S4** (blue lines). The inset picture demonstrates the color change caused by oxidation of **S3** using **SbCl<sub>5</sub>** in suspension and for the corresponding solid.

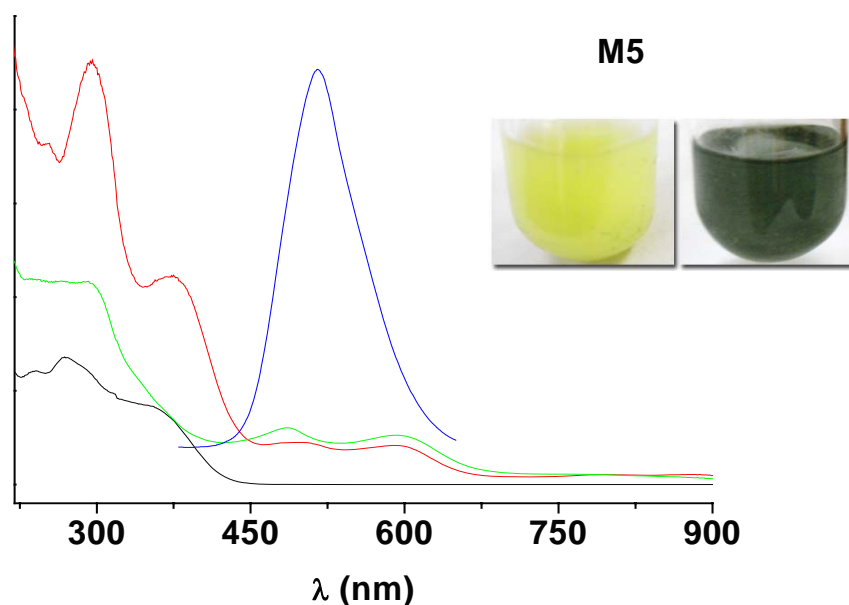
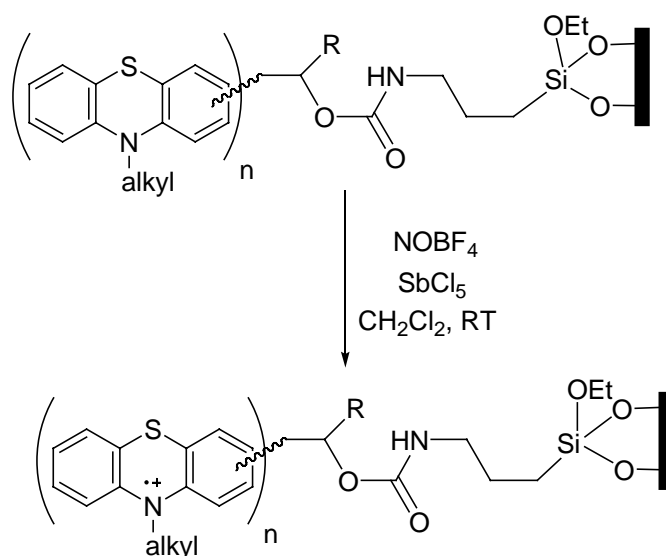


Figure 19. UV-Vis spectrum of the modified sample **M5** (black line), the absorption of corresponding radical cationic sample **M5-BF<sub>4</sub>** (red line), **M5-SbCl<sub>6</sub>** (green line), and the

emission spectrum of the modified sample **M5** (blue line). The inset picture demonstrates the color change caused by oxidation of **M5** using  $\text{NOBF}_4$  in suspension and for the corresponding solid.

The photo luminescence spectra of the hybrid materials are also shown as blue dashed lines. Similar to the corresponding pure organic precursors, the hybrid materials show an emission at about 440-470 nm. Only sample **M5** reveals a pronounced bathochromic shift of the emission maximum compared to its precursor **5**, a similar effect was found for the absorption spectra of **M5**. At the moment there is only speculation on this finding: **5** is the largest phenothiazine, which could be introduced in the narrow pores of MCM-41. Interaction of the  $\pi$ -system with the framework walls of the support may cause an increase of parallel orientation of the phenyl ring and the phenothiazine moiety and thus lead to a red shift of absorption and emission. Additionally, for **M2**, **M3**, and **M6**, besides the expected maxima around 430 nm additional maxima at 390 nm can be observed which are absent in the solution spectra of the precursor carbamates **2**, **3**, and **6**. This dual emission is either caused by conformational biases as a consequence of restricted molecular rotation and relaxation inside the pores or by population of TICT (twisted intramolecular charge transfer) states<sup>173</sup>.



Scheme 11. Oxidation of mesoporous phenothiazinyl hybrids

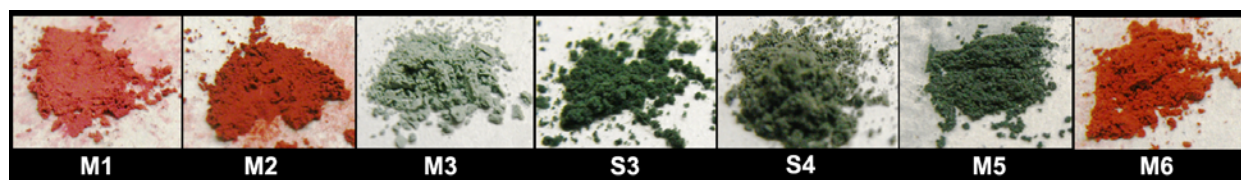


Figure 20. A photo series of hybrid materials containing stable phenothiazine radical cations.

All materials undergo the formation of surface bound radical cations when treated with oxidizing agents (Scheme 11 and Figure 20). We carried out the oxidation of the phenothiazine in dichloromethane solution with the one-electron acceptor  $\text{NOBF}_4$  or with antimonpentachloride, providing the corresponding radical cations as  $\text{BF}_4^-$  or  $\text{SbCl}_6^-$  salts<sup>174</sup>. For the mono-phenothiazine functionalized materials **M1**, **M2**, and **M6**, the color of all the solids changed from colorless to red after oxidation reaction with  $\text{NOBF}_4$  or  $\text{SbCl}_5$  (Figure 20 and the inset picture of Figure 17). All three samples show an intense absorption band around 520 nm, which is characteristic for phenothiazine radical cations<sup>89, 175</sup> (red lines and the green lines in Figure 17). This absorption becomes much stronger when  $\text{SbCl}_5$  is used as the oxidizer. Herefore we have two explanations: compared to  $\text{NOBF}_4$ ,  $\text{SbCl}_5$  is the stronger oxidant, thus it should provide more radical cations in the channels of the silica. Secondly, the formation of by-products is possible by the oxidation with  $\text{NOBF}_4$ . This could explain two peaks in the spectra around 300 and 345 nm. The oxidation of the (oligo)phenothiazine functionalized materials **M3**, **S3** and **S4** offered greenish products (see picture in Figure 18 and Figure 20), and thus different absorption spectra with respect to the mono-phenothiazine radical cations. This indicates a different electronic situation of the phenothiazine radical cations derived from bi- and trimeric structures<sup>176</sup>. They might be partially oxidized to  $(\text{PH}^+)_m(\text{PH})_{n-m}$  or totally oxidized to the bi- or trication  $(\text{PH})_n^{n+}$ <sup>112</sup>. Considering the distribution of phenothiazine in the materials pore system, also a mixture of these oxidized species should be considered. The broad absorption band in visible-NIR region, can be assigned to an intramolecular charge transfer (CT) band. It has been discussed that phenothiazines occupy a

butterfly configuration in the ground state. However, the structure of the phenothiazine radical cation is planar<sup>108</sup>, which brings a remarkable structural deformation, enhances intramolecular interaction, and thus provides intramolecular charge transfer. This intramolecular electronic communication had already been confirmed by cyclic voltammetry of the di- and trimeric precursors<sup>154</sup>, which have lower first oxidation potentials than monophenothiazine, suggesting a stabilizing interaction<sup>176</sup>. Furthermore, since the oxidation of phenothiazine moieties results in a considerable structural change from a butterfly conformation of the native neutral form to a planarized radical cation also intermolecular interactions of native and oxidized phenothiazine moieties within the pores can be expected. Hence, the observed solid state UV/Vis spectra of the oxidized materials **M3**, **S3**, **S4** represent a superposition of intra- and intermolecular electronic interactions and cause the formation of intensely colored materials. A special spectrum was also observed for sample **M5** possessing a phenyl group linked compound. Its color changes from yellow to dark green after treatment with  $\text{SbCl}_5$ . The radical cations show two new absorbances at 485 and 594 nm. This might also be because of the structure deformation. It is worth to notice that the resulting materials preserve their colors at ambient temperature for weeks when stored in the dark and under an atmosphere of nitrogen, indicating the persistence of stable phenothiazine radical cations in the mesoporous materials.

The existence of the distinguished stable phenothiazine radical cations in the hybrid materials, were additionally confirmed by EPR spectroscopy. The EPR spectrum of **M5-SbCl<sub>6</sub>** is exemplarily shown in Figure 21 (the spectra of **S3-SbCl<sub>6</sub>** and **S4-SbCl<sub>6</sub>** are shown in Figure 22 and Figure 23, respectively.) and reveals a g-value of 2.0051. Since the EPR signal is not resolved, hyperfine coupling constants and anisotropic g-tensors cannot be determined. However, the high symmetry of the EPR spectrum indicates that the phenothiazine radicals are in a quite isotropic environment in the hybrid materials.

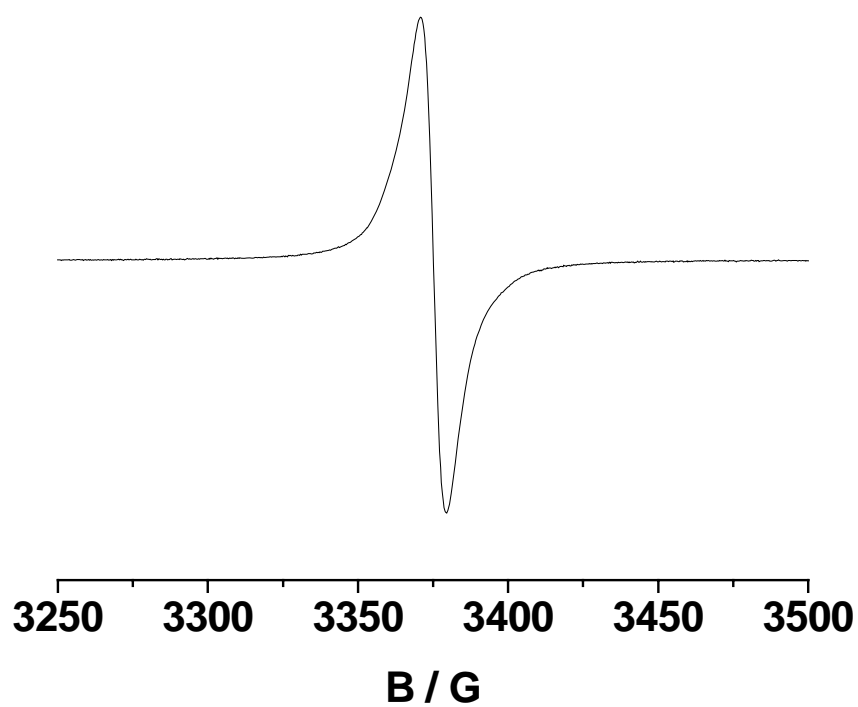


Figure 21. Q-band EPR spectrum of **M5-SbCl<sub>6</sub>** at 297 K.

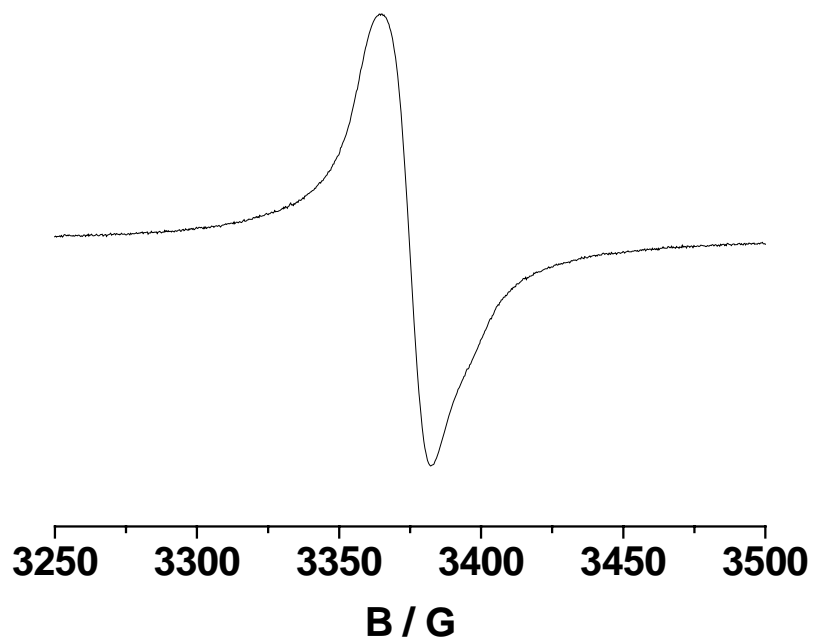


Figure 22. Q-band EPR spectrum of **S3-SbCl<sub>6</sub>** at 297 K. ( $g = 2.0054$ )

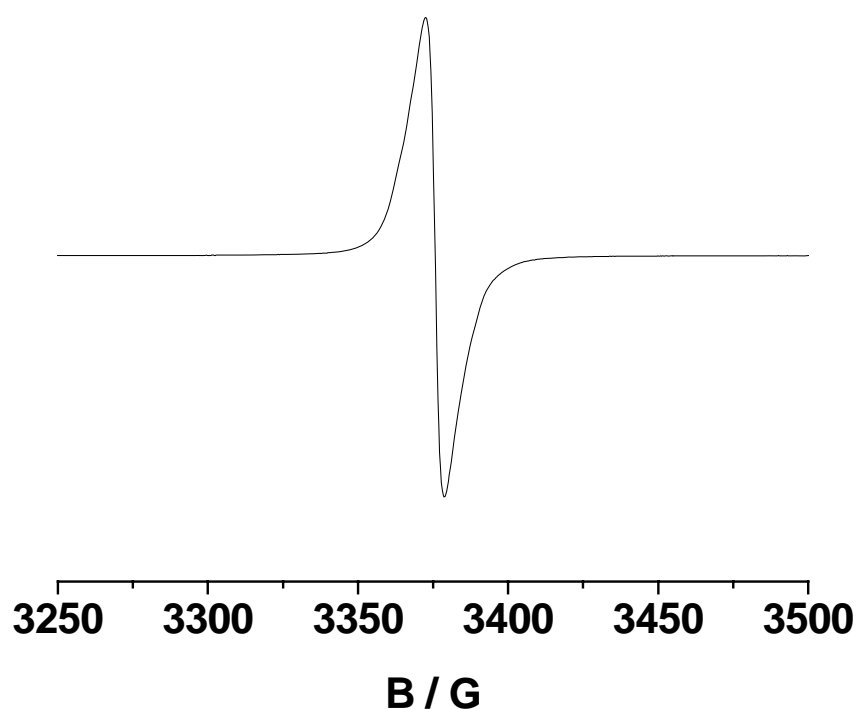


Figure 23. Q-band EPR spectrum of **S4-SbCl<sub>6</sub>** at 297 K. ( $g = 2.0051$ )

## **2.2 Synthesis and characterization of urea-linked (oligo)phenothiazines in mesoporous silica materials obtained by an in-situ one pot method**

### **State of the art**

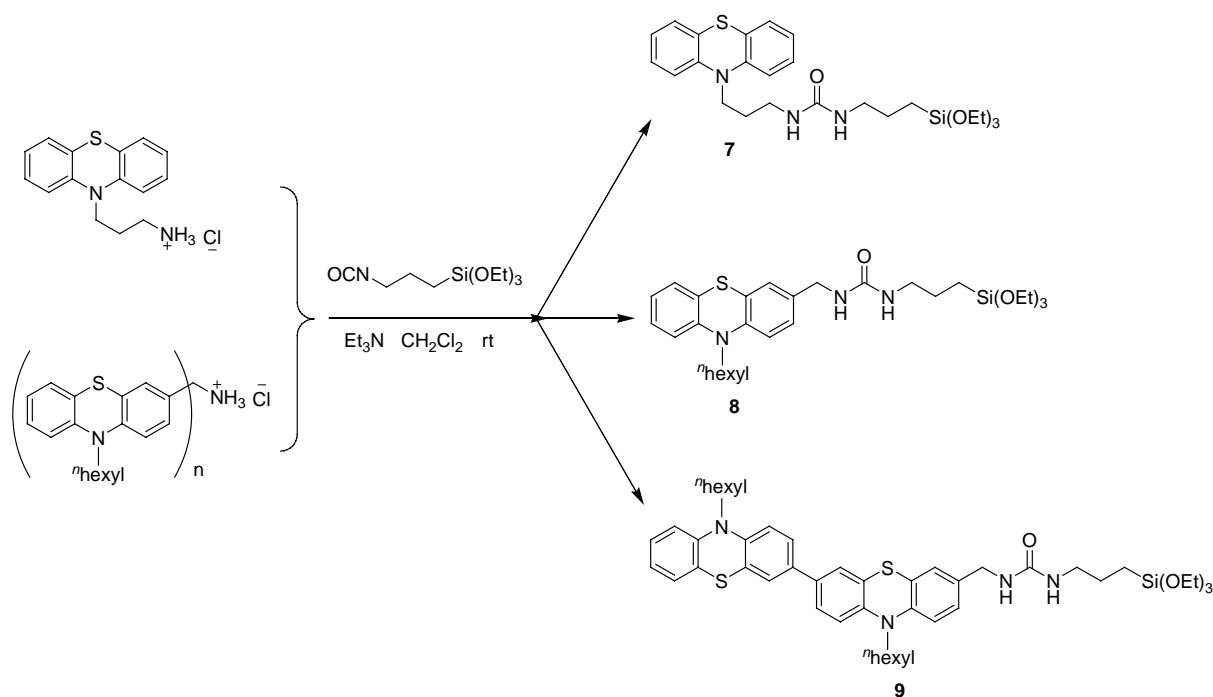
Although postsynthetic grafting is the most popular way to anchor organic groups in a specific manner to a silica surface, which finally results in hybrid organic-inorganic materials, there are still some drawbacks related to this procedure. (1) the distribution of the organic group is generally not uniform all over one channel, (2) the loading with larger and sterically demanding organic functionalities is often low, mainly constrained by diffusion limitations. Enhance our studies about the phenothiazine content in the pores and exploration of the materials properties, such as intermolecular charge transfer, interaction of phenothiazine molecules in an artificial restrictive spatiality and so on, an alternative method providing a



high content of the electrochromophore was developed. This is to prepare the hybrid mesoporous materials by a template-directed synthesis in the presence of the silylated phenothiazine. Here the siloxane precursors play a role as building blocks to construct the main framework, while the organosiloxanes contribute to both, framework silicate units and the organic surface functional groups. This single-step synthesis can produce mesoporous solids with a high loading of organic functional groups and a homogeneous surface coverage within the channel of the materials. It has to be mentioned here, that the organic groups of the silicon functionalized precursor molecules are supposed to stick into the micelle during the gelation process. Therefore, something like an intramolecular phase separation process takes place. Thus it is important for a successful in-situ synthesis to rationally design the organic precursors, which additionally must be stable under the conditions of the materials synthesis. Here we perform this process using urea linked phenothiazines.

### **2.2.1 Synthesis of the phenothiazine building blocks**

The precursors possessing phenothiazine and urea components as the functional unit were synthesized as shown in Scheme 12. All the compounds are synthetically accessible by a straightforward addition of an amine to a silylated isocyanate. After purification by chromatography, pure products can be afforded as precursors **7**, **8** (white waxy solids) and **9** (a yellow viscous oil).



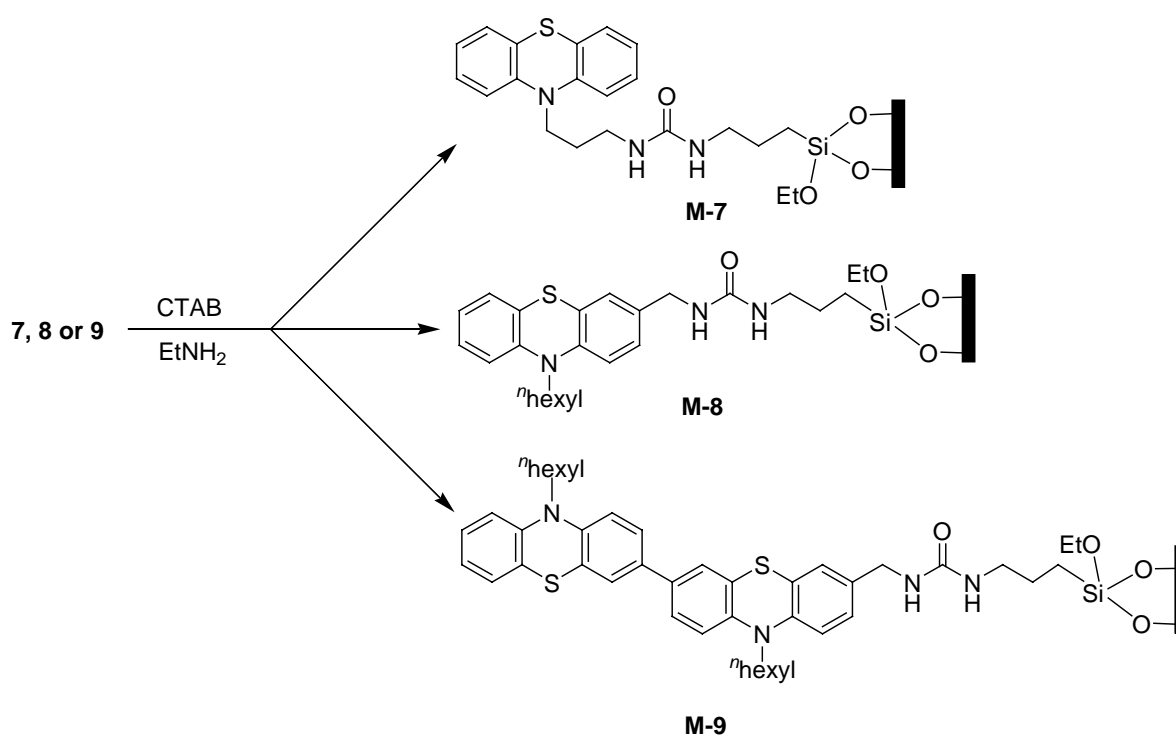
Scheme 12. Synthesis of triethoxysilyl functionalized (oligo)phenothiazine ureas.

The urea linked trialkoxysilyl functionalized compounds have some special properties. One of them is the capability to form H bonds between the urea groups. Some interesting work using this property is related to the assemblage of such molecules into well defined supramolecular architectures<sup>177</sup> or to the control of the morphology of hybrid materials<sup>178</sup>. Moreover, urea groups can interact effectively with anionic species by hydrogen bonding<sup>179</sup>. Based on this interaction, several sensors containing urea as the functional group have been reported<sup>179, 180</sup>. For example, if the urea group is linked to a fluorescent unit, such molecules can detect anionic species by reverse photoinduced electron transfer (PET) which decreases the fluorescence intensity. Another important property of the urea group is its chemical and thermal stability. As mentioned before, for the one-pot co-condensation synthesis of hybrid mesoporous materials, an essential term is a robust and firm organic precursor, which can sustain under strong acidic and basic conditions. The urea group is sufficiently stable to allow the co-condensation synthesis of phenothiazine units with TEOS in the presence of the base

EtNH<sub>2</sub> at 100 °C and long reaction times. After template extraction by EtOH/HCl under reflux conditions well ordered MCM-41 hybrid materials are obtained.

### 2.2.2 Synthesis of the hybrid mesoporous materials

The hybrid mesoporous products were obtained as outlined in Scheme 13. A main feature of this route is to use the organic base EtNH<sub>2</sub> instead of the conventionally applied strong base NaOH. This avoids the incorporation of Na<sup>+</sup> ions into the mesoporous materials. Our aim is to achieve a phenothiazine concentration as high as possible inside the pore channels in combination with a uniform pore distribution, in an ordered cylindrical pore arrangement. Thus, a delicate synthesis method had to be chosen. To fulfill a uniform distribution of the phenothiazines and to avoid phase separation during the formation of the mesoporous structure, TEOS and **7** (or **8**, **9**) were first dissolved in a small volume of methanol before adding this mixture to the surfactant solution. A slow dropping of this mixture into the surfactant solution is important. The addition of a certain amount of methanol in the synthesis of MCM-41 can increase the degree of ordering of the mesoporous structure compared with a purely aqueous system<sup>181, 182</sup>. For comparison, the same method was used for the synthesis of pure silica MCM-41. To determine how the concentration and the molecular structure of the phenothiazine influence the configuration of the hybrid mesoporous materials, various concentrations and well-designed phenothiazine moieties were employed. The structures, the optical and the electrochemical properties of these hybrid materials were then systematically investigated.



Scheme 13. Synthesis of the mesoporous hybrid materials **M7**, **M8**, and **M9** by the in-situ synthesis method with CTAB as the template

### 2.2.3 Structural properties of the hybrid materials

#### Powder X-ray diffraction

Powder XRD was carried out as a routine experiment to elucidate the structural ordering of the mesoporous materials. The patterns of as-synthesized MCM-41 and extracted MCM-41 are presented in Figure 24A. Both samples show four distinct peaks, which are due to the reflections of 100, 110, 200 and 210 planes<sup>7</sup> (the large angle signals are magnified in Figure 24B). This series of peaks can be indexed to a two-dimensional hexagonal  $p6mm$  symmetry, indicating a highly long-range ordered structure<sup>6</sup>. After the extraction treatment, the half width of (100) peak gets smaller, the intensities of the peaks increase, and a slight shift of the  $2\theta$  value to smaller angles with a corresponding increase in the  $d_{100}$  spacing from 4.27 nm to 4.30 nm, can be observed. This also demonstrates the homogeneously distributed and ordered pore structure of this material. The increasing intensity can be assigned to the elimination of

the organic surfactant from the pore. This enhances the contrast density between framework and pore channels<sup>163</sup>. Additionally, the differences in the unit cell values can be attributed to the further condensation of silicon species in the material framework during the extraction process<sup>183</sup>.

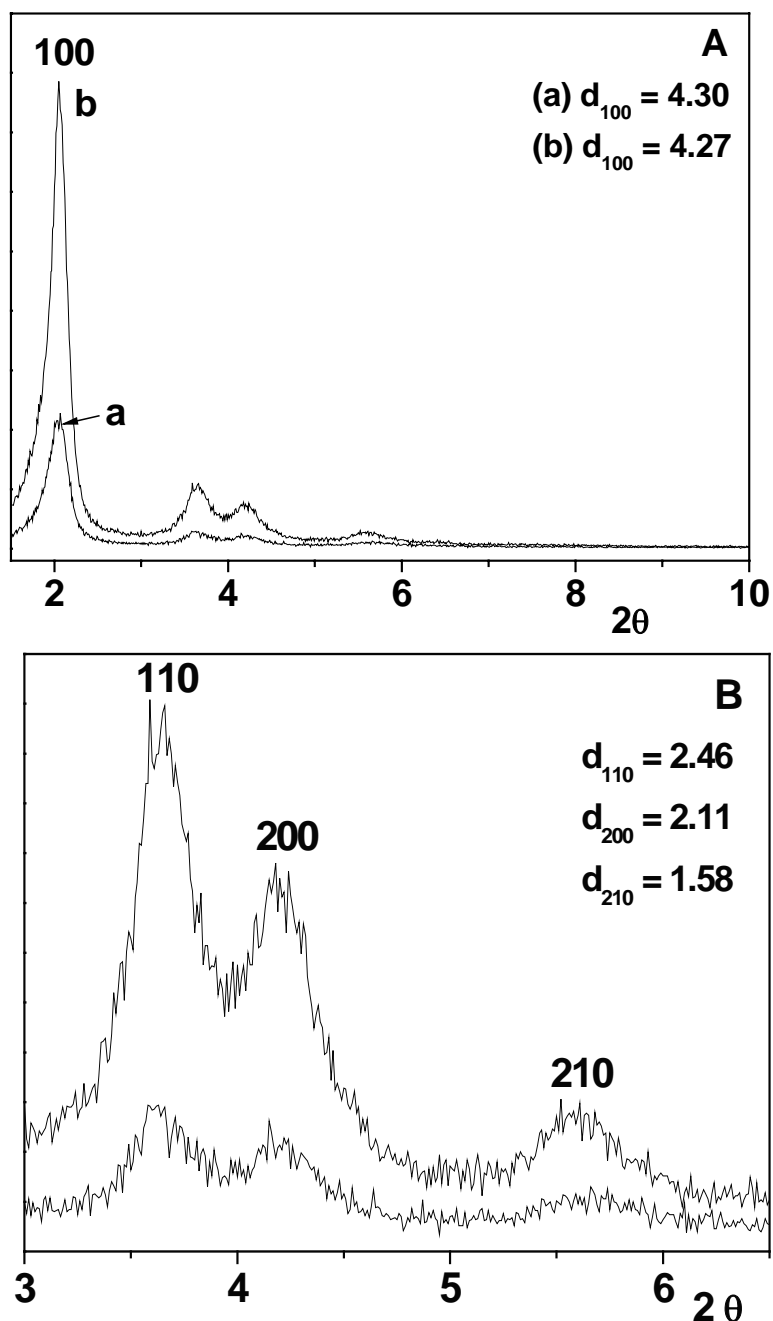


Figure 24. A: Powder XRD pattern of (a) as-synthesized MCM-41, and (b) template extracted MCM-41. B: magnified signals at higher angle of these two samples.

The patterns in Figure 25A are related to a series of **M7** samples with differ in the phenothiazine content. **M7-1** contains 0.33 mmol/g of organic moieties. It shows four Bragg diffraction peaks, and a pattern similar to MCM-41, which indicates a long-range ordered hexagonal mesostructure. The  $d_{100}$  value of **M7-1** is 4.38 nm, which is a slightly increased compared to neat MCM-41. This phenomenon may be due to the hydrophobic nature of the phenothiazine precursor **7**, which can partly locate in the bulk of the assembled organic surfactant leading to an increase of micelle size with respect to the micelles with the pure surfactant. As a result, an increase of the unit cell parameter can be observed. Additionally, a slight shift of the characteristic (100) peak to larger angle, with a corresponding linear decrease in the  $d$  spacing, is exhibited for **M7-2** ( $d_{100} = 4.23$  nm) and **M7-3** ( $d_{100} = 4.20$  nm). These two samples contain 0.54 mmol/g and 0.77 mmol/g phenothiazine, respectively. It seems that a higher concentration of phenothiazine precursor will not continue playing the role of a pore expander. The reason for this might be that precursor **7** has a rigid, relatively large, and horizontal head group (phenothiazine). In a lower concentration, it will not significantly disturb the surfactant during the formation the ordered cylindrical micelles. Due to the large molecular structure, it will extend the size of micelles and thus result in a larger unit cell<sup>157</sup>. However, increasing the amount of this precursor in the hydrophobic region of the micelles will exclude the normal surfactant molecules<sup>40</sup>. This will disturb the surfactant cooperation with inorganic species through balanced Coulombic interactions to form fully covered micelles with silica species, therefore the unit cell will contract after hydrothermal reaction<sup>184</sup>.

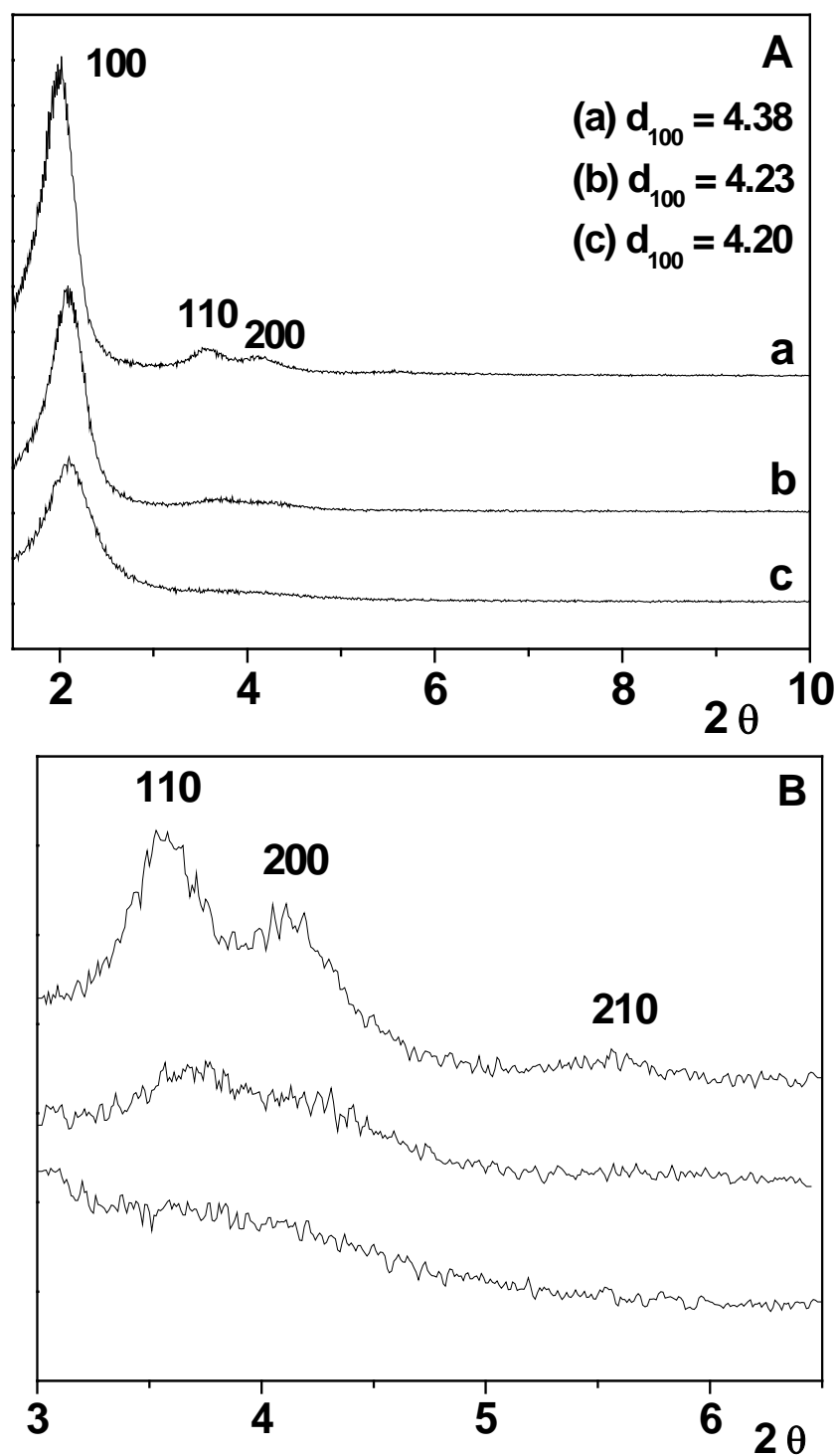


Figure 25. A: Powder XRD pattern of a group of M7 samples, (a) M7-1, (b) M7-2 and (c) M7-3. B: magnified signals at higher angles signals of these samples.

At the same time, the relative intensities of all diffraction peaks decrease as the concentration of phenothiazine groups increases. This is particular for the peaks at higher

angles, such as the Bragg diffraction peaks of the 200 and the 210 planes. For **M7-3** the sample with the highest concentration (0.77 mmol/g), the second order peaks (110) and (200) are overlapping and the peak of the 210 planes is nearly undetectable (see Figure 25B). The reduction may be partially attributed to a decrease in the mesoscopic order of the materials, and partly due to contrast matching between the amorphous silicate framework and organic moieties which are located inside the channels of these materials<sup>60, 157, 185</sup>. Since the diffraction peak (100) can be observed in all the samples, it confirms the presence of a periodic arrangement of pores in the materials<sup>25</sup>.

Figure 26A shows the XRD pattern of extracted hybrid mesoporous materials which are obtained from precursor **8**. Similar to the former results (**M7** and neat MCM-41), the sample **M8-1** with a lower phenothiazine concentration (0.26 mmol/g), shows four Bragg diffraction peaks, which can be indexed as the (100), (110), (200), and (210) reflections of the hexagonally symmetric lattice of the MCM-41 structural material. **M8-2** and **M8-3** contain an increased content of phenothiazine (0.40 mmol/g and 0.54 mmol/g). From the pattern it is clear that the intensities of the peaks in the range of higher angle are steadily decreased with the increase of organic content, but the prominent (100) plane diffraction is maintained for all the samples. These results suggest the presence of a periodic arrangement of channels in these hybrid materials. A decrease of the  $d_{100}$  spacing value can be observed in the order of **M8-3** < **M8-2** < **M8-1**, which is coherent with the trend of **M7**.



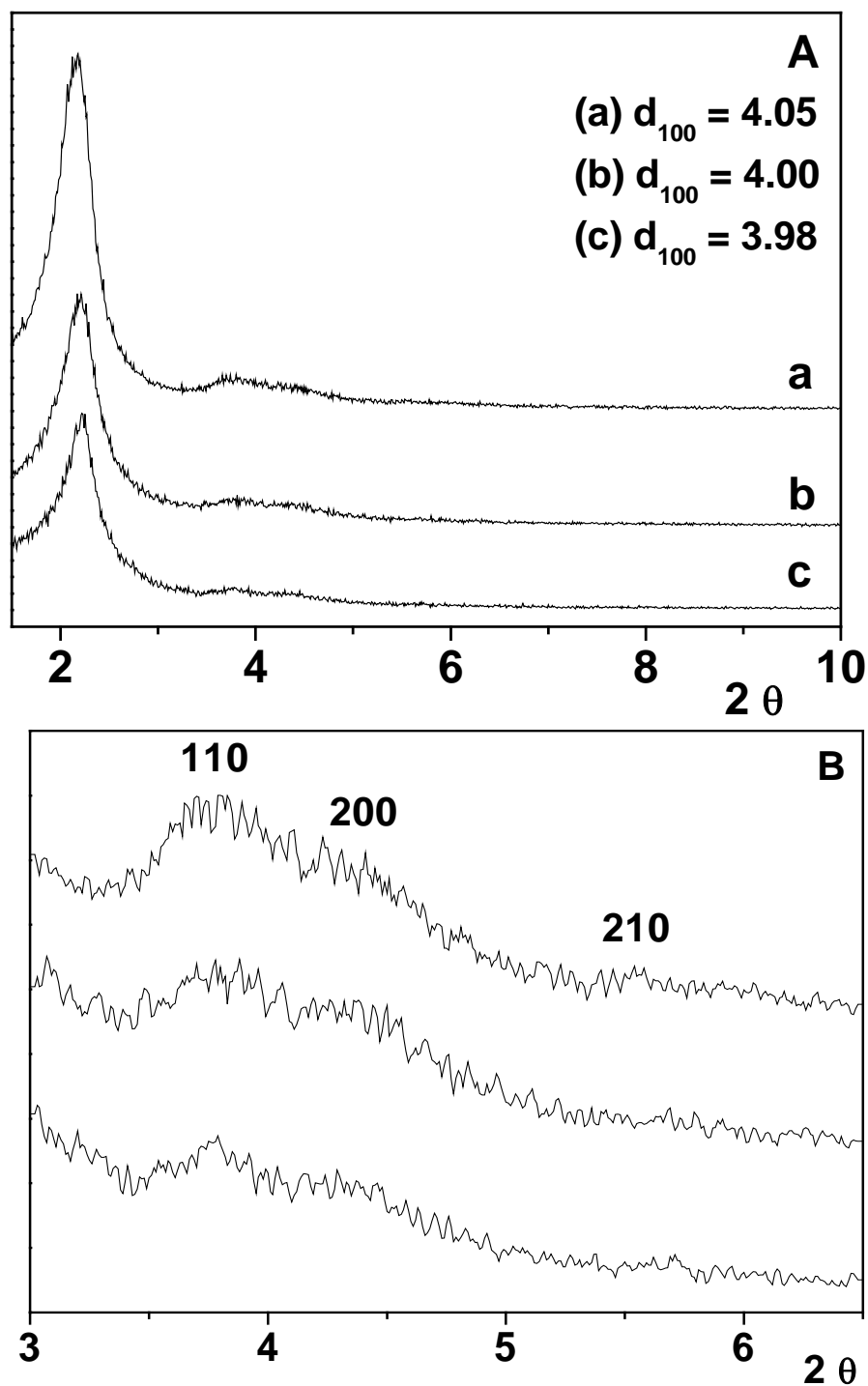


Figure 26. A: Powder XRD pattern of a group of **M8** samples, (a) **M8-1**, (b) **M8-2** and (c) **M8-3**, B: magnified signals at the higher angles of these samples.

The X-ray diffraction patterns of two samples **M9** are given in Figure 27. **M9-1** has a concentration of 0.28 mmol/g of the biphenothiazine moiety. The three significant (hkl) reflections of (100), (110) and (200) can be easily observed for **M9-1** in the  $2\theta$  range of 2 –

5°. Similarly, these peaks can be indexed to the two-dimensional (2D) hexagonal  $p6mm$  symmetry. The presence of a small broad signal around  $2\theta = 5.7^\circ$  attributes to the diffraction of (210) plane (Figure 27B), indicating a uniformly arranged hexagonal mesoporous structure.

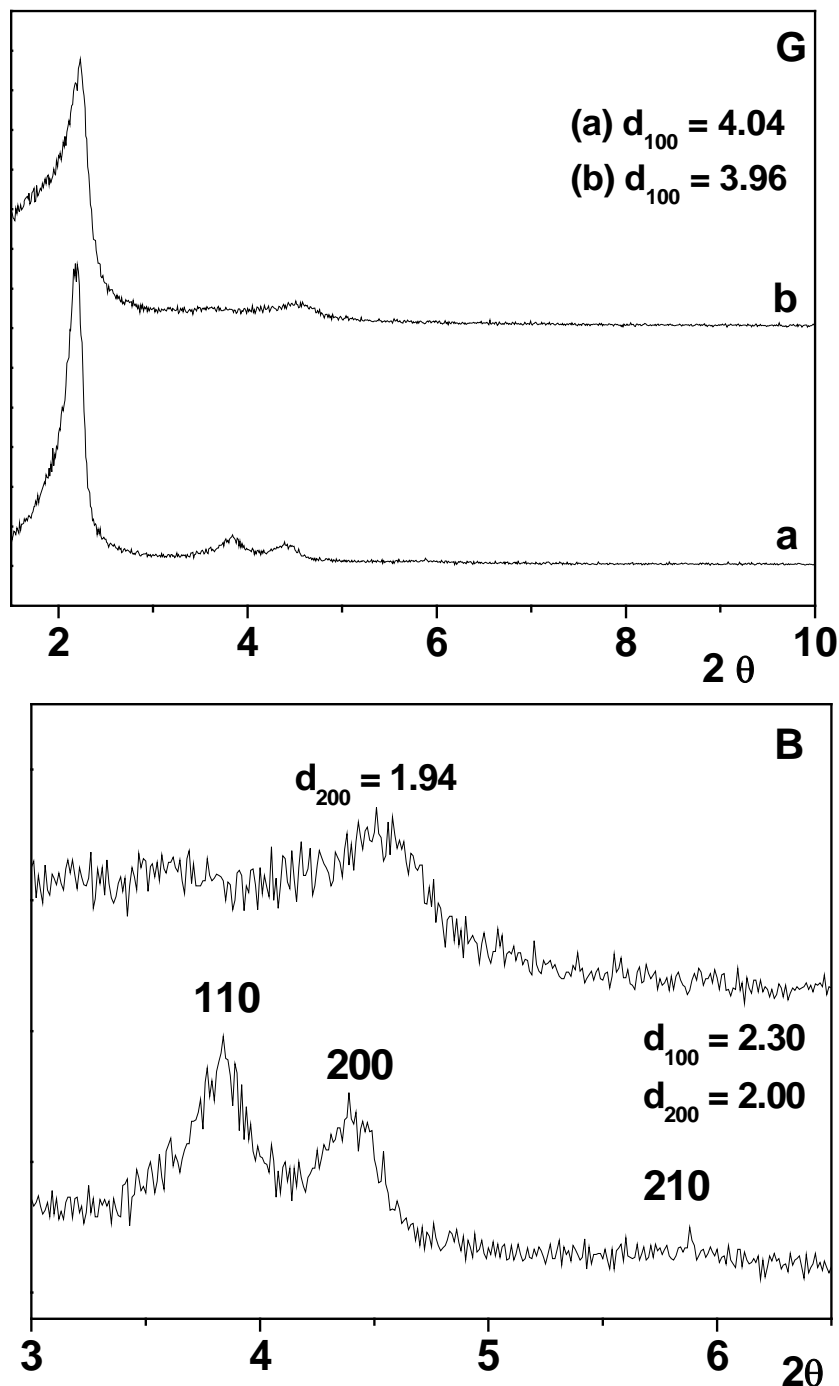


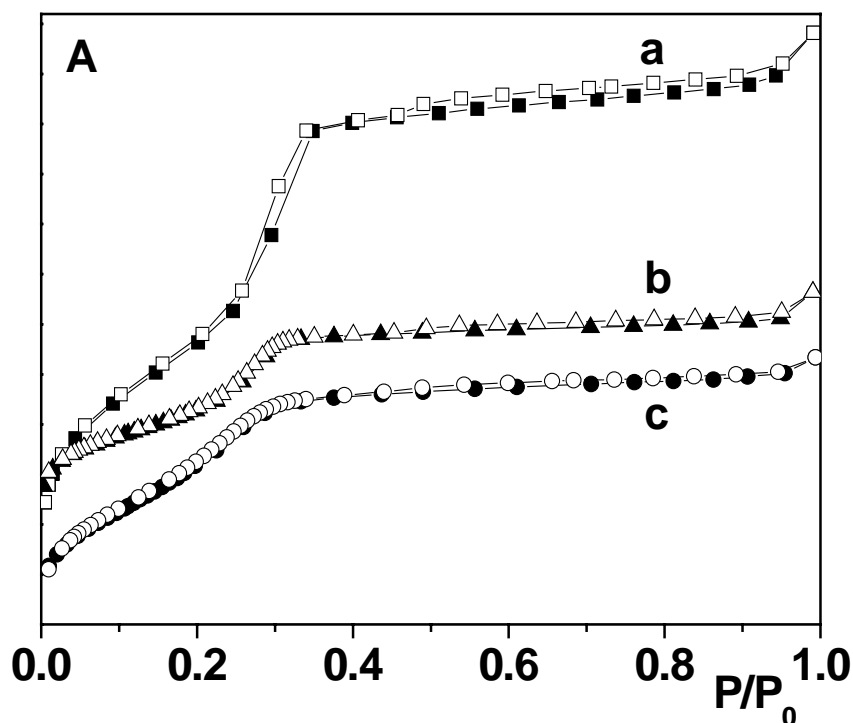
Figure 27. A: Powder XRD pattern of a group of **M9** samples, (a) **M9-1**, and (b) **M9-2**. B: magnified signals at higher angles of these samples.

The pattern of **M9-2** as usual presents an intense peak, which belongs to the (100) diffraction. However, a special (200) diffraction with relatively high intensity appears, which overlaps the (110) diffraction. This indicates the formation of a distorted hexagonal structure or an intermediate phase between hexagonal and lamellar configuration<sup>186, 187</sup>. This distorted hexagonal structure might be due to the amorphous nature of the mesoporous silica framework<sup>188</sup>. The silica species in this type of structural materials have a wide range of Si-O-Si bond angles, which are e.g. more flexible than in the crystallized zeolite walls<sup>189</sup>. Therefore, the motions of the big molecule **9** might twist the structure of the silica framework in some degree. The explanation of the presence of a transition phase can trace back to the classical surfactant pair packing parameter,  $g = V/a_0l$ , in which a variation of  $g$  can be indexed to phase transitions and different geometries of the mesophase products (see chapter 1 section 1.1.2.3)<sup>23</sup>. For sample **M9-2**, during the formation of the mesostructure, the large molecule **9** possessing two phenothiazine cores in combination with two hexyl chains, will dramatically increase the hydrophobic volume  $V$ , thus the value of  $g$  is increased. This will result in a decrease of surface curvature, so as to a mesophase transition between the hexagonal and the lamellar structure<sup>24, 190</sup>. While a normal lamellar structure will collapse after surfactant extraction, the existence of this XRD pattern could either be attributed to the presence of the distorted hexagonal structure, or to a stabilizing effect of the biphenothiazine in the material. Some reports had already pointed out that urea linked organic silanes can give self-structured lamellar hybrid materials, because of the presence of the intermolecular H-bonds<sup>191</sup>. Therefore, this XRD result shows that changing the ratio phenothiazine precursor **9**/surfactant will change the mesophase of the materials from an ordered hexagonal to an ordered lamellar phase. Nevertheless, also a lamellar structure, should be interesting in terms of the conduction properties for this type of hybrid material since it also will allow ordering of the assembled phenothiazine molecule through intermolecular hydrogen bonds and  $\pi$ - $\pi$  conjugation.

N<sub>2</sub> adsorption and desorption

It is known that N<sub>2</sub> physisorption analysis can be used to probe the structural ordering. If the material has a regular pore structure, it will show a step increase in adsorption isotherms due to the capillary condensation at a specific partial N<sub>2</sub> pressure. The nitrogen adsorption isotherms for the extracted phenothiazine-urea functionalized hybrid materials are presented in Figure 28-30, the structural parameters are listed in Table 5.

Figure 28A shows the isotherms of the group **M7** samples. The featured type of the isotherm and the capillary condensation step appear in all three samples. It confirms the ordered mesoporous structure of these materials. A narrow hysteresis loop on the steep low-pressure portion of the isotherm of **M7-1** may be due to nitrogen filling in the regions between adjacent organic groups and the silica wall<sup>183, 192</sup>. Another narrow H4 type of hysteresis loop on the horizontal portion (from  $p/p_0$  0.45-0.95) can be linked to uniform slit-shaped pores, which may indicate the presence of connections between cylindrical channels or due to aggregates of particles<sup>166, 193</sup>.



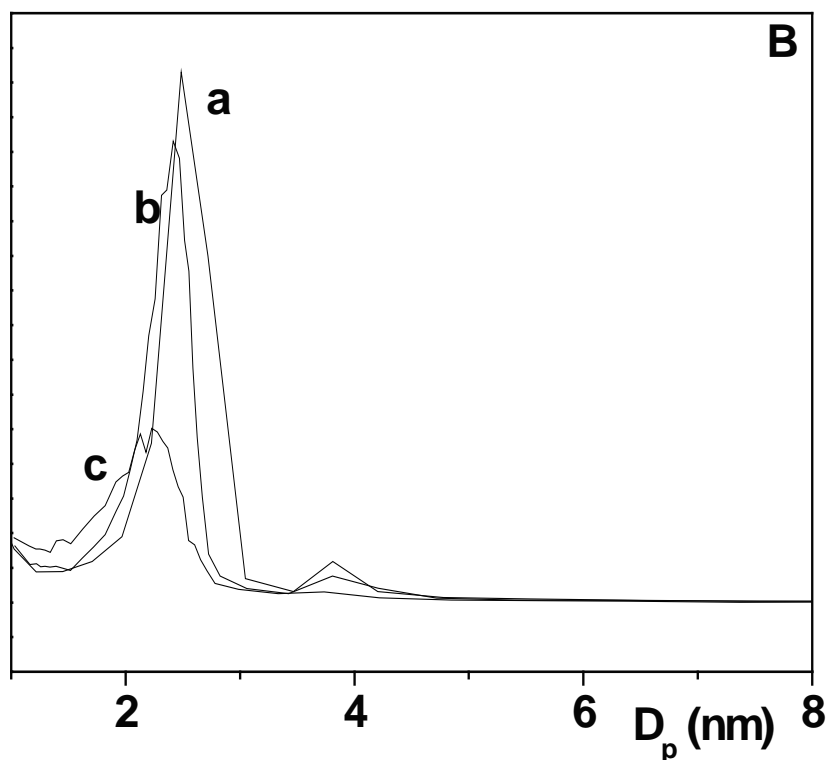
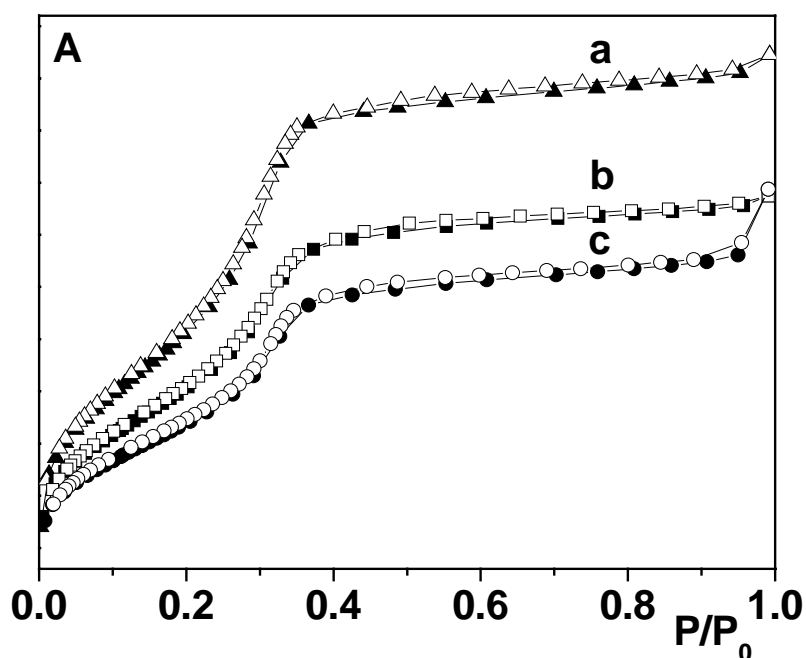


Figure 28. A:  $N_2$  adsorption/desorption isotherms of (a) **M7-1**, (b) **M7-2** and (c) **M7-3** (adsorption points are marked by solid items and desorption points by empty items). B: pore size distribution curves of (a) **M7-1**, (b) **M7-2**, and (c) **M7-3** (deduced from the desorption data of the isotherms).

The pore size distributions (PSD) of the **M7** were determined by the BJH method and are illustrated in Figure 28B. For these three samples, the PSD curve derives from the desorption branch of the gas isotherm. The small peak around 3.8 nm is related to narrow H4 type of hysteresis loop at high pressure. This type of hysteresis becomes narrow for **M7-2**, and is absent in the isotherm of **M7-3**. As the content of the phenothiazine precursor in the reaction mixture increases, the position of the capillary condensation step gradually shifts from a relative pressure of  $\sim 0.24$  to  $\sim 0.19$ . This shift indicates as expected a systematic pore size decrease<sup>161</sup>, which corroborates to the decrease of the  $d_{100}$  values and the unit cell parameters  $a_0$  of the samples, detected by XRD. The graph of the PSD apparently shows the stepwise decrease of the pore size, but a narrow pore size distribution is preserved for all these

samples, demonstrating the presence of uniform pores. In combination with the increase of organic material in the samples, the volume of total adsorption continuously decreases, which is attributed to a decline of the surface area and of the total pore volume.

The textural parameters of **M8** were also detected by  $N_2$  adsorption desorption measurements. The results are presented in Figure 29A and Table 5. All three samples display typical IV isotherms (definition by IUPAC)<sup>194</sup>, with a sharp capillary condensation step in the low  $P/P_0$  range of 0.2 to 0.4. The completely reversible isotherms and the absence of any hysteresis loops, indicates ordered mesoporous materials with uniform pore sizes and ordered arrangements of cylindrical channels without any intersecting disorder<sup>165</sup>. The isotherms show a gradually lower  $N_2$  uptake with the increase of organic loading, accounting for the decrease of surface area.



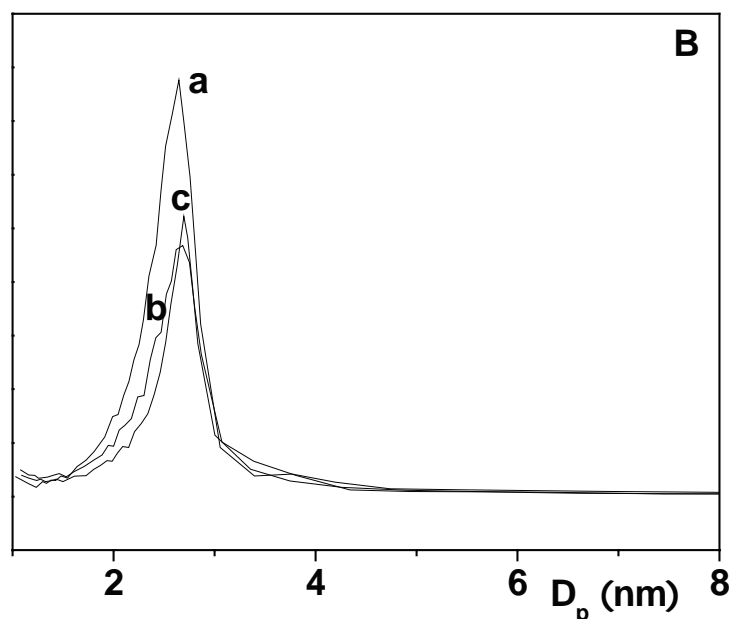


Figure 29. A: N<sub>2</sub> adsorption/desorption isotherms of (a) **M8-1**, (b) **M8-2** and (c) **M8-3** (adsorption points are marked by solid items and desorption points by empty items). B: pore size distribution curves of (a) **M8-1**, (b) **M8-2**, and (c) **M8-3** (deduced from the desorption data of the isotherms).

A shift of the capillary condensation points to higher relative pressure for the materials prepared with an increased organic loading (**M8-3** > **M8-2** > **M8-1**), indicates the filling of a larger pore. Moreover, the pore size distribution curves (Figure 29B), deduced from the desorption plot of the isotherms, visually prove just a slight increase of the pore size (see the data in Table 5). This phenomenon is opposite to the former samples **M7** and should be related to the process of the mesostructure formation. A detailed discussion will be presented later. Anyway, a reduction of the BET surface area and the total pore volume from **M8-1** to **M8-3** is apparent, due to the introduction of more organic groups inside the channels of the materials.

The N<sub>2</sub> isotherms of the **M9** samples in Figure 30A, which can also be grouped to type IV adsorption curve with inflections at  $P/P_0$  of  $\sim 0.25$  for **M9-1** and  $\sim 0.22$  for **M9-2**, indicate uniform channels with pore sizes around 2.6 nm. A second inflection appears at  $P/P_0$  close to

0.42 until 1, which displays a type H4 hysteresis loop in the desorption branch of the isotherm. This latter feature is characteristic of a slit-like pore, which may be due to a textural porosity within the particles of the materials or an intersecting disorder of the materials<sup>192</sup>. From the isotherm data, rather high surface areas (761 and 632 m<sup>2</sup>g<sup>-1</sup>) and pore volumina (0.65 and 0.57 cm<sup>3</sup>g<sup>-1</sup>) were determined. As usual, an increase of organic loading deduces these two values.

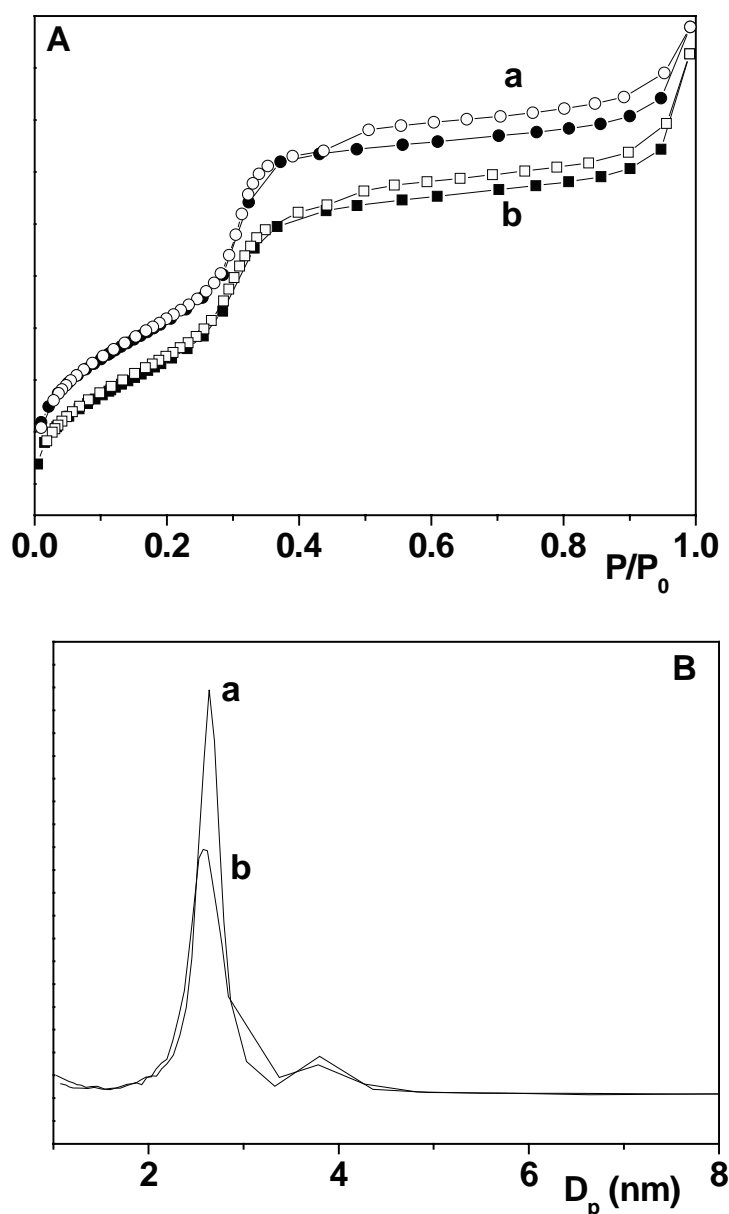


Figure 30. A: N<sub>2</sub> adsorption/desorption isotherms of (a) M9-1, and (b) M9-2 (adsorption points are marked by solid items and desorption points by empty items). B: Pore size



distribution curves of (a) **M9-1**, and (b) **M9-2** (deduced from the desorption data of the isotherm).

Table 5. Textural parameters of **M-7**, **M-8** and **M-9** derived from nitrogen adsorption-desorption analysis or powder X-ray diffraction and loading of phenothiazines in the hybrid materials

sample	$d_{100}^a$ (nm)	$a_0^b$ (nm)	$S_{BET}^c$ ( $m^2 g^{-1}$ )	$V_p^d$ ( $cm^3 g^{-1}$ )	$D_p^e$ (nm)	$w_t^f$ (nm)	$C^g$ (mol%)	content of phenothiazine <sup>h</sup>	
								( $mmol g^{-1}$ )	(wt %)
MCM-41	4.30	4.96	1123	0.98	2.83	2.14	--	--	--
M7-1	4.38	5.06	1040	0.85	2.48	2.58	17.8	0.33	13.0
M7-2	4.23	4.88	914	0.69	2.41	2.48	35.0	0.54	21.2
M7-3	4.20	4.85	700	0.42	2.25	2.60	53.6	0.77	30.2
M8-1	4.05	4.68	991	0.78	2.65	2.02	15.7	0.26	11.7
M8-2	4.00	4.62	766	0.58	2.68	1.94	26.4	0.40	17.9
M8-3	3.98	4.60	638	0.51	2.69	1.90	37.1	0.54	24.2
M9-1	4.04	4.66	761	0.65	2.64	2.02	18.6	0.28	20.4
M9-2	3.96	4.57	632	0.57	2.58	1.98	25.7	0.35	25.2

<sup>a</sup>  $d_{100}$  is the  $d(100)$  spacing; <sup>b</sup>  $a_0$  the cell parameter ( $a_0=2d_{100}/\sqrt{3}$ ); <sup>c</sup>  $S_{BET}$  is the BET surface area; <sup>d</sup>  $V_p$  = pore volume; <sup>e</sup>  $D_p$  = pore diameter; <sup>f</sup>  $w_t$  is the wall thickness  $a_0-D_p$ ; <sup>g</sup> the molar ratio of precursor/CTAB; <sup>h</sup> calculated according to the content of nitrogen (CHN element analysis).

By an analysis of this group of textural parameters in Table 5, a general conclusion can be deduced: The  $d_{100}$  spacings, the specific BET surface areas and the pore volumina are reduced by increasing amounts of organic silane in the reaction mixture. A similar behavior was observed by others, who investigated the loading with pendent organic groups by applying the co-condensation method. The size of the organic component ranges from small molecules

(vinyl, thiol, and amino group etc.)<sup>55, 195, 196</sup> to large chromophore molecules<sup>197</sup> and catalytic species<sup>198</sup>.

The increase of the pore filling organic content, naturally, will decrease the pore volume and surface areas. These effects are quite easy to understand. While the reason of the decrease of the  $d_{100}$  spacings by increasing the organic precursor concentration is not so easy to illuminate. Some studies ascribe this trend to different interactions between the cationic surfactant molecules and the silicate or organosilicate precursors during the hydrothermal reaction<sup>157, 199</sup>. To understand the effect of the organosilicates, which contain differently structured phenothiazine molecules, the process of the mesophase formation has to be considered in detail. It is well known that the formation of mesostructures is associated with an interaction of inorganic species and organic molecules. The interface curvature can be changed by changing charge repulsion, van der Waals interactions, hydrogen bonds, and covalent bounds between inorganic/organic molecular units<sup>184, 200</sup>. In our system, the synthesis was performed under basic conditions (pH  $\sim$  13). The aqueous isoelectric point (IEP) of the silica species is at about pH  $\sim$  2. Here the silica species have a surface charge of zero<sup>34</sup>. This means that during the synthesis, the silicate species are negatively charged, they can interact with the positively charged surfactant head groups through electrostatical forces. The formation of this inorganic species/organic surfactant interface will definitely be influenced by the location and concentration of the phenothiazine precursor. Because the molecular size and shape of the phenothiazinyl substituted silanes may decide the location, they are also important terms, which will have an effect on the formation of the mesophase configurations.

Combining these effectors with data obtained from the experiment, some units on the influence of different phenothiazines in the formation of MCM-41 type hybrid materials, can be deduced and may help for the further research in this field.

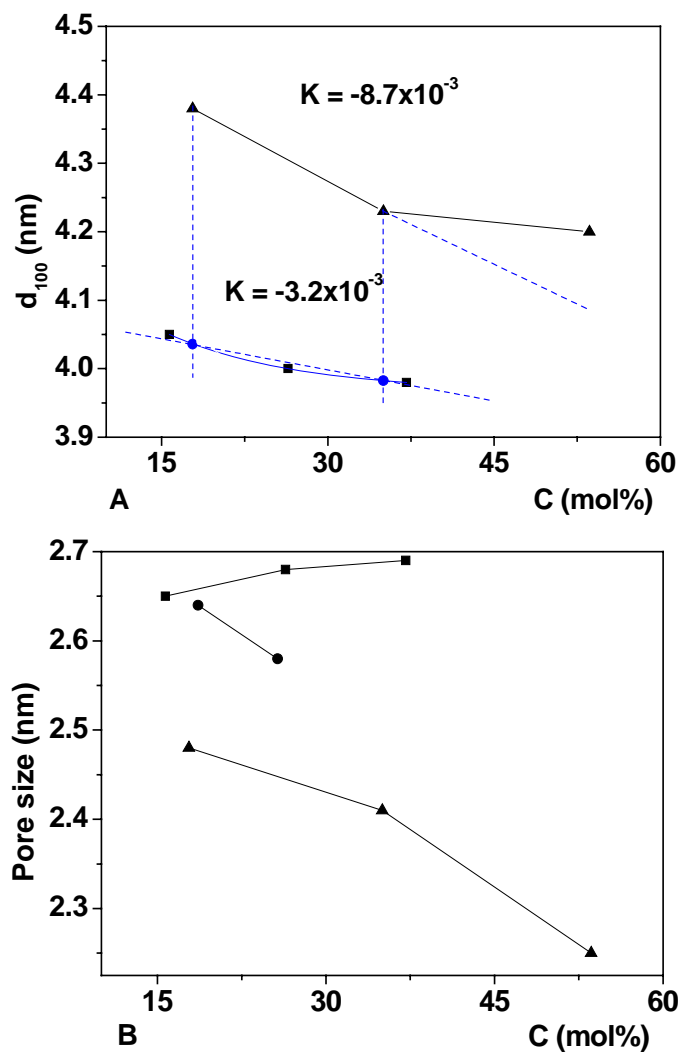


Figure 31. A:  $d_{100}$  spacings as a function of percentage of organic precursor input (with respect to the total surfactant content) (▲) M7 and (■) M8; B: pore size as a function of organic phenothiazine loading in the hybrid materials (▲) M7, (■) M8, and (●) M9.

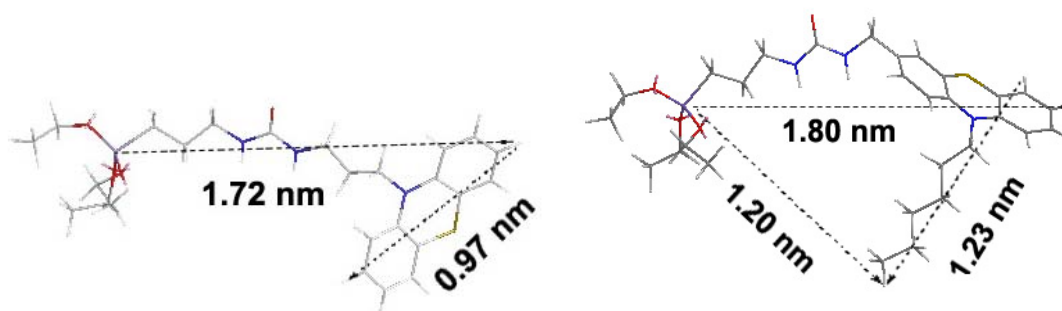


Figure 32. Molecular structures of the precursors 7 (left) and 8 (right), calculated with Chem 3D (MM2).

As shown in Figure 31, a plot of the phenothiazine/CTAB molar ratio versus  $d_{100}$ , which is determined by X-ray diffraction, results in a decreasing curve for both the **M7** and the **M8** materials. In the concentration range of 17.8 to 35% (between the two blue dotted lines), **M7** (slope:  $-0.87 \times 10^{-3}$ ) apparently has a sharper decreasing trend than **M8** (slope:  $-0.32 \times 10^{-3}$ ). The main difference of these two precursors is their molecular structure, thus it should be a key issue. During the formation of the ordered micelles, the siloxane group of the precursor will be embedded in the inorganic species layer, while the phenothiazine group might be located near this interface or reach the internal core, due to the molecular property of the precursor<sup>200</sup>.

It seems that for **7** (Figure 32), due to the flexibly linked chain and the possibility of hydrogen bond formation between the urea groups and the oxygen of silica, the phenothiazine core of this precursor should be more located nearer to the interface of the micelles. As a result, the density of silanol groups in this region will decrease, and due to the charge compensation, fewer surfactant molecules are required for charge balance. This leads to a remarkable contraction of the cylindrical micelle size in the hybrid materials with increasing concentrations of organic precursor. In contrast **8** (Figure 32), has a urea linker in the 3-position and hexyl chain in the 10-position. This type of molecular structure should be favorable to cooperate with the template molecules through stronger hydrophobic interactions, thus the phenothiazine group can be drawn further into the inner part of the surfactant micelles. As a result, there are no bulky phenothiazine cores hanging around near the inorganic species/organic surfactant interface. The influence of the concentration of **8** on the interface layer should not be such significant as in the former situation with **7**. Therefore, it leads to a less pronounced contraction of the micelle size. This explains the slow decrease of  $d_{100}$  with increasing concentrations of precursor **8**.

The relationship between the pore size and the precursor can provide further proof for this explanation. Figure 31B shows a plot of the phenothiazine precursor/CTAB molar ratio versus the pore sizes, which were obtained from the nitrogen physisorption measurements. It shows a slight increase of pore size with an increasing concentration of precursor **8**, while a decreasing trend appears for **M7** and **M9**. Normally, to extend the pore size, one will input some auxiliary organic compounds, such as hexane, mesitylene, etc in to the reaction mixture<sup>201, 202</sup>. Based on their liquid crystalline phases of surfactants are capable to solubilize organic molecules within their hydrophobic interiors. Considering a proportional increase of pore size with incremental addition of precursor **8**, it means that this precursor with its hexyl chain, can reach the interiors of the surfactant micelles, to enlarge the size of micelles, thus play a role of a pore expanding agent. In contrast, the precursor **7** due to its molecular geometry with the horizontal phenothiazine core can not reach the interior of surfactant micelles, makes the curvature of the micelles increase, and thus leads to a fast decreasing of the pore size. In the case of precursor **9**, although it has two hexyl chains and double hydrophobic phenothiazine cores, the large molecular size might not allow totally to immerge in the surfactant. This will perturb the micelles in the aspect of the size and even the structure (phase transfer or distorted channel).

In summary, since the molecular structure of the precursor can decide the location of phenothiazine groups, it thus can influence the structure and physical parameters of the products. Until now, it seems that precursor **8** has the best capability to cooperate with CTAB in a sense to form relatively ordered materials with high organic content.

### Electron microscopy

Transmission electron microscopy (TEM) can be used as an indispensable tool for the characterization of the hybrid materials. It can provide a direct evidence for the structural ordering of the materials in the form of images and a direct discovery of the intrinsic pore

structures of the hybrid materials. Figure 33a shows the [10] direction image of hybrid material **M7-1**. The bright dots are corresponding to the straight channels of the hexagonally structured mesoporous material and the uniform arrangement of these dots indicates a highly ordered structure. The brightness and the shape of the channel differ slightly from place to place, due to slight changes in diffraction conditions, which show a domain character<sup>203</sup>. Image Figure 33b is obtained when the incident electron beam is perpendicular to the pore. Large domains of typically ordered stripe-like arrangements of the long parallel cylindrical channels along the [11] direction, demonstrate a highly ordered pore structure. In an image of a large area (Figure 33c), the uniformity is still preserving, implying the long-range highly ordered mesoporous structure of this material. Image Figure 33d and Figure 33e are the TEM images of samples **M7-2** and **M7-3**. Although the overall order is slightly reduced, the pore channels of these two samples still appear to be uniform at the mesoscale. This is consistent with the XRD results: all these three hybrid materials with different concentrations of phenothiazine preserve their mesoporous structure.

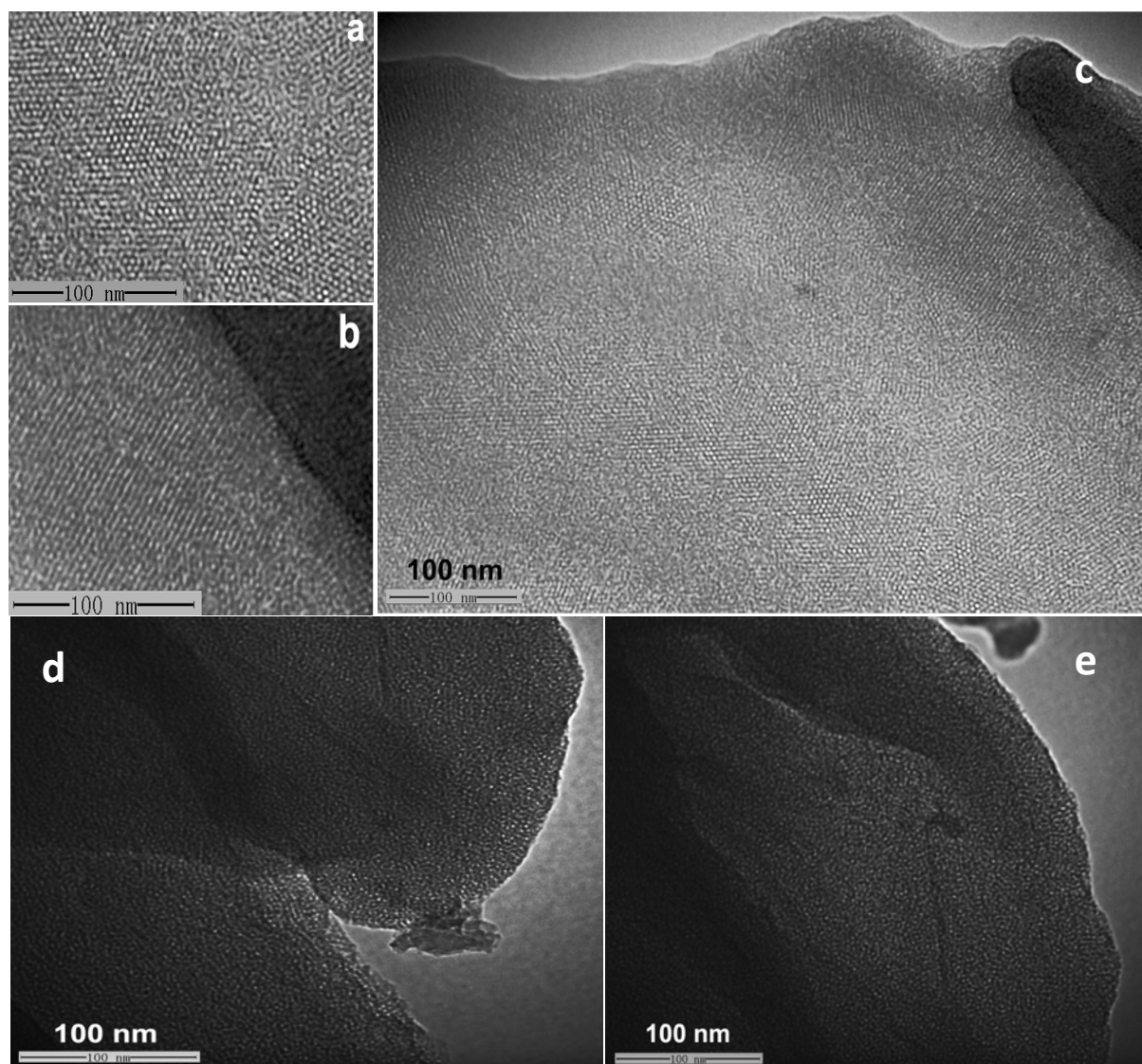


Figure 33. Transmission electron microscopy images of hybrid mesoporous materials, (a) **M7-1** along the channel direction, (b) **M7-1** perpendicular to the channel direction, (c) **M7-1** large scale image (d) **M7-2** (e) **M7-3**.

Figure 34 shows the TEM image of a series of material **M8**. The selected area images Figure 34b and Figure 34c show the ordering of the mesostructure in two directions, the electron beam parallel to the pore or perpendicular to the pore. Image Figure 34a is covering a large area and demonstrates the highly uniform pore structure. After increasing the organic content, a decrease in the channel ordering is observed in images Figure 34d and Figure 34e,

which are obtained from **M8-2** and **M8-3** respectively. It is interesting to see an aggregation of small rods in the thin section of **M8-3**.

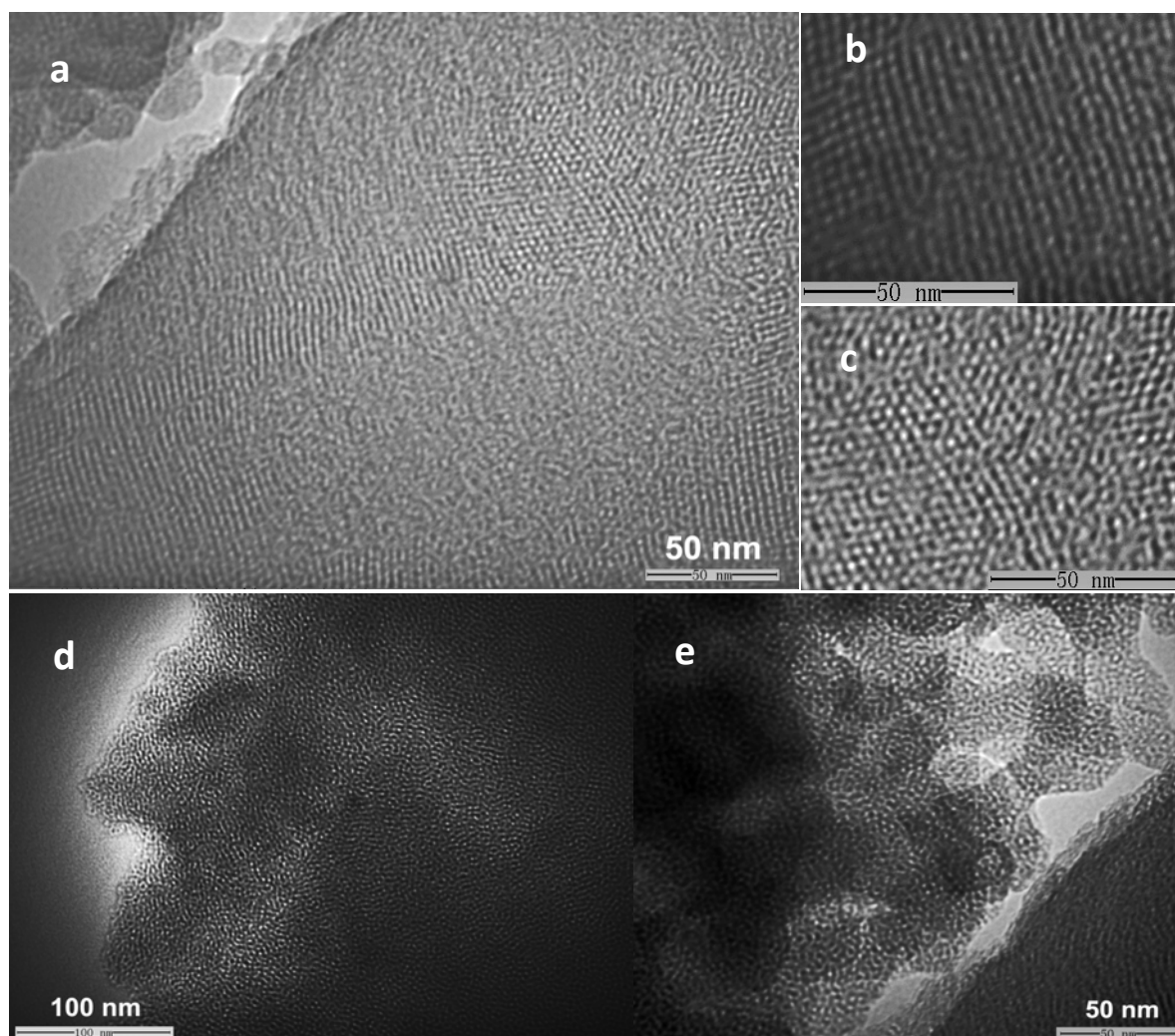


Figure 34. Transmission electron microscopy images of hybrid mesoporous materials, (a) **M8-1**, (b) **M8-1** perpendicular to the channel direction, (c) **M8-1** along the channel direction, (d) **M8-2** and (e) **M8-3**.

Figure 35 shows several TEM images of **M9-1**. This sample also exhibits hexagonally arranged pore channels, when viewed along the pore direction (Figure 35c), and on a side view analysis, which is vertical to the pore channels, the presence of parallel lattice fringes are clear (Figure 35b). The large scale image proves the formation of a long-range ordered mesoporous structure in this material (Figure 35a).



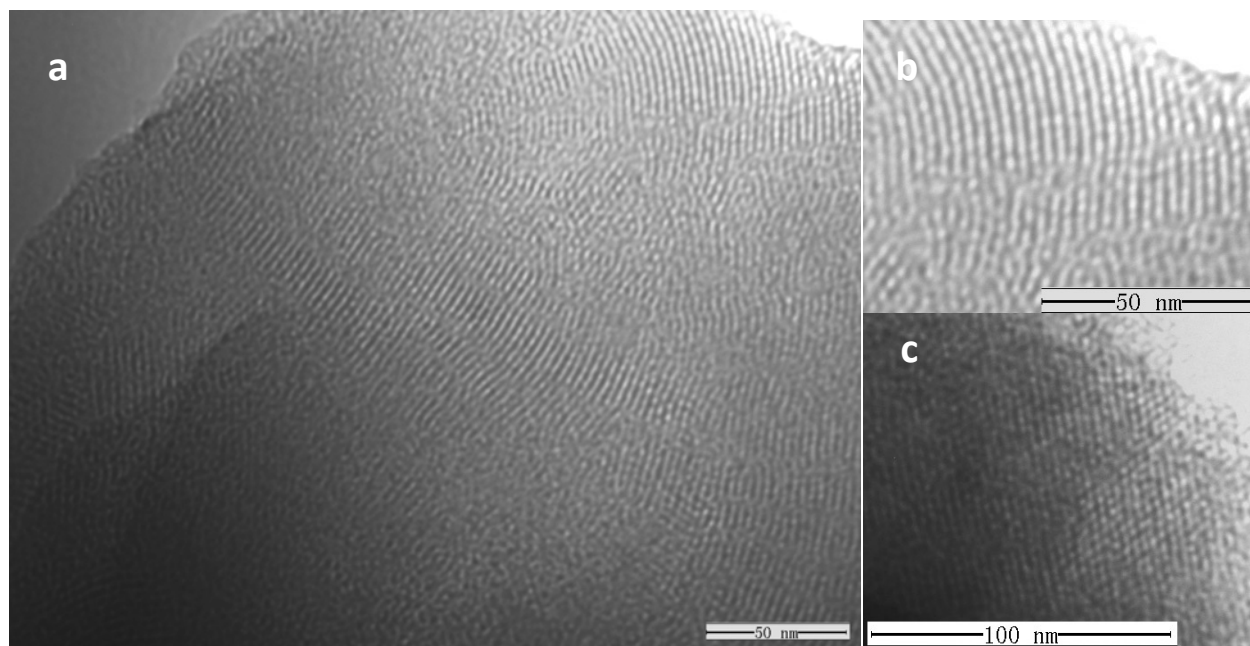


Figure 35. Transmission electron microscopy images of hybrid mesoporous materials (a) **M9-1**, (b) **M9-1** perpendicular to the channel direction, (c) **M9-1** along the channel direction.

Transmission electron micrographs of thin sections of extracted **M9-2** are presented in Figure 36. It presents a type of nanofilaments elongated specifically along the channel direction of the hybrid mesostructure. Based on the results of TEM and XRD, a hypothesis explaining of the formation of this structure can be proposed basing on the well-known mechanism of the formation of MCM-41<sup>6, 204</sup>. The large and hydrophobic molecules of the biphenothiazine precursor **9** can form the  $\pi$ - $\pi$  interaction. This will stabilize the micelles, thus quite long micelles can be obtained which are observed in TEM and a distorted transform structure can be predicted from the results of XRD.

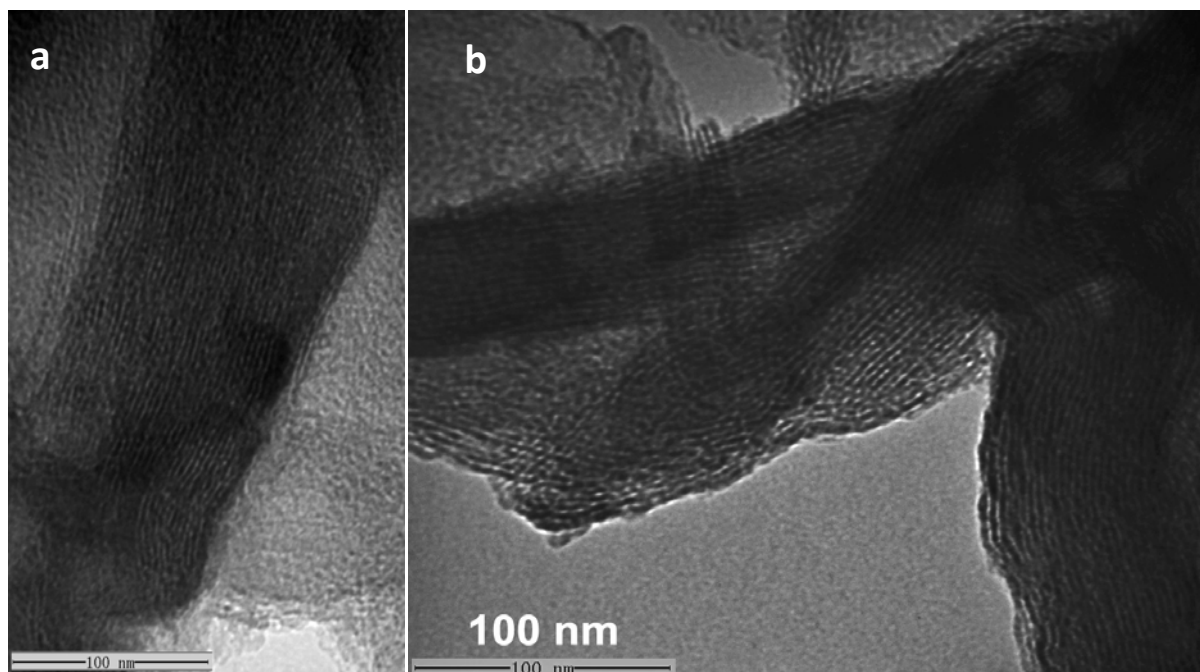
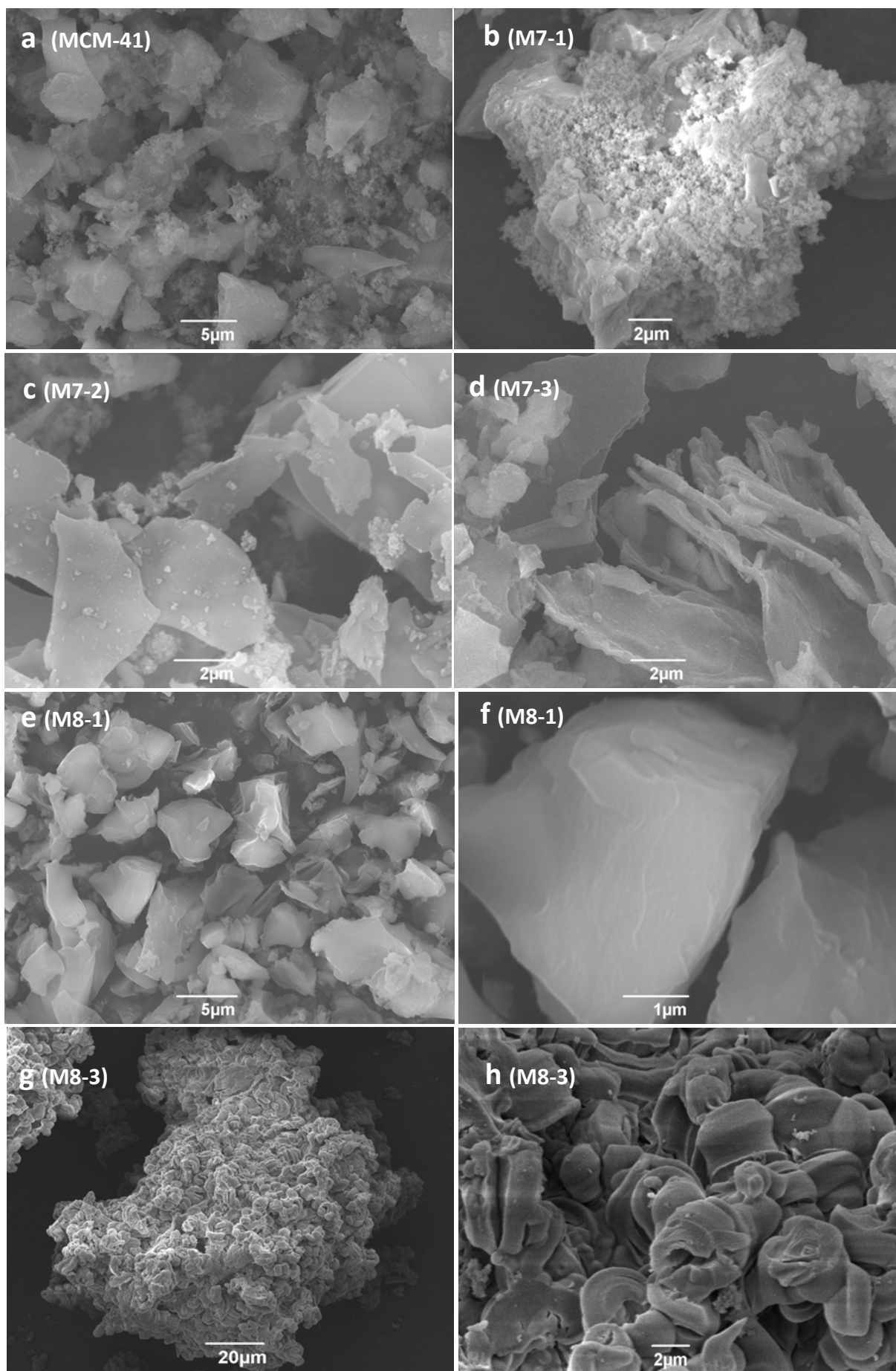


Figure 36. Transmission electron microscopy images of hybrid mesoporous material **M9-2**.

The co-condensation of silicate with different organoalkoxysilanes has shown a great influence on the morphology of the final products. By changing the precursor or its concentration, the particle morphology was tuned to various shapes including spheres, tubes and rods of various dimensions<sup>205,206</sup>. Such an interesting phenomenon also can be observed for our phenothiazine organosilanes when different concentration of the co-condensation products are involved. Most of the morphologies are not as uniform as in the particular reports. This is due to our synthetic process, which includes a long time hydrothermal treatment. However, this is favorable for the total hydrolysis of the silica species to achieve high loading of organic moieties under these conditions, powderous bulk materials are obtained, rather than a morphological uniform nanoscale material. Anyhow, the influence of the phenothiazine precursors for the material morphology can be tracked down in some extent. Since all the approaches are similar except the molecular structure and the concentration of phenothiazine precursor, the following discussion will focus on the relation between the resulting morphology and these two parameters.

A series of SEM pictures are presented in Figure 37. Image Figure 37a shows neat MCM-41, which is built up from irregular blocks and most of these block have a smooth surface. The growth of the mesoporous materials is similar to the growth of zeolites using a hydrothermal sol-gel method, occurring from the sub-micro size to the macroscopic size. The agglomeration of small fragments always happens. In our MCM-41 product, the bulk structure with a smooth surface indicates that the hydrolysis and cross-linking of the silica species is relatively complete. The image of **M7-1** (Figure 37b) shows a similar irregular bulk with a coarse surface. The surface covered by small particles and flakes is due to an incomplete hydrolysis and contraction. The pictures of **M7-2** and **M7-3** (Figure 37c and d) exhibit flake-like structures as the primary composition and an absence of big bulks generated by aggregating of these small flakes. This group of images implies that the concentration of the organic precursor has an important influence on the hydrolysis speed of the silica species and thus has an impact on the morphology of the final product. The same phenomena can be observed in the images related to the **M8** and **M9** samples. In sample **M8-1** with a low concentration of phenothiazine, the material presents a disordered bulk of different sizes (ca. 3 $\mu$ m-10  $\mu$ m) (see Figure 37e and Figure 37f), with rather smooth surfaces. For the sample **M8-2** (Figure 37g and Figure 37h), it is interesting to see an aggregation of a large amount of uniformly curved rods. The formation of these uniform rods is only present, when high concentrations of precursor **8** are involved in the synthesis. This means that molecular structure of the phenothiazine precursor also has an important influence on the morphology of the material. The same influence is displayed in **M9-1** (Figure 37i and Figure 37j), and **M9-2** (Figure 37k and Figure 37l). The introduction of more organic compound is attributed to a very thin flake shaped material (**M9-2**). Additionally, in Figure 37l, a layer by layer assembly of these thin flakes can clearly be observed.



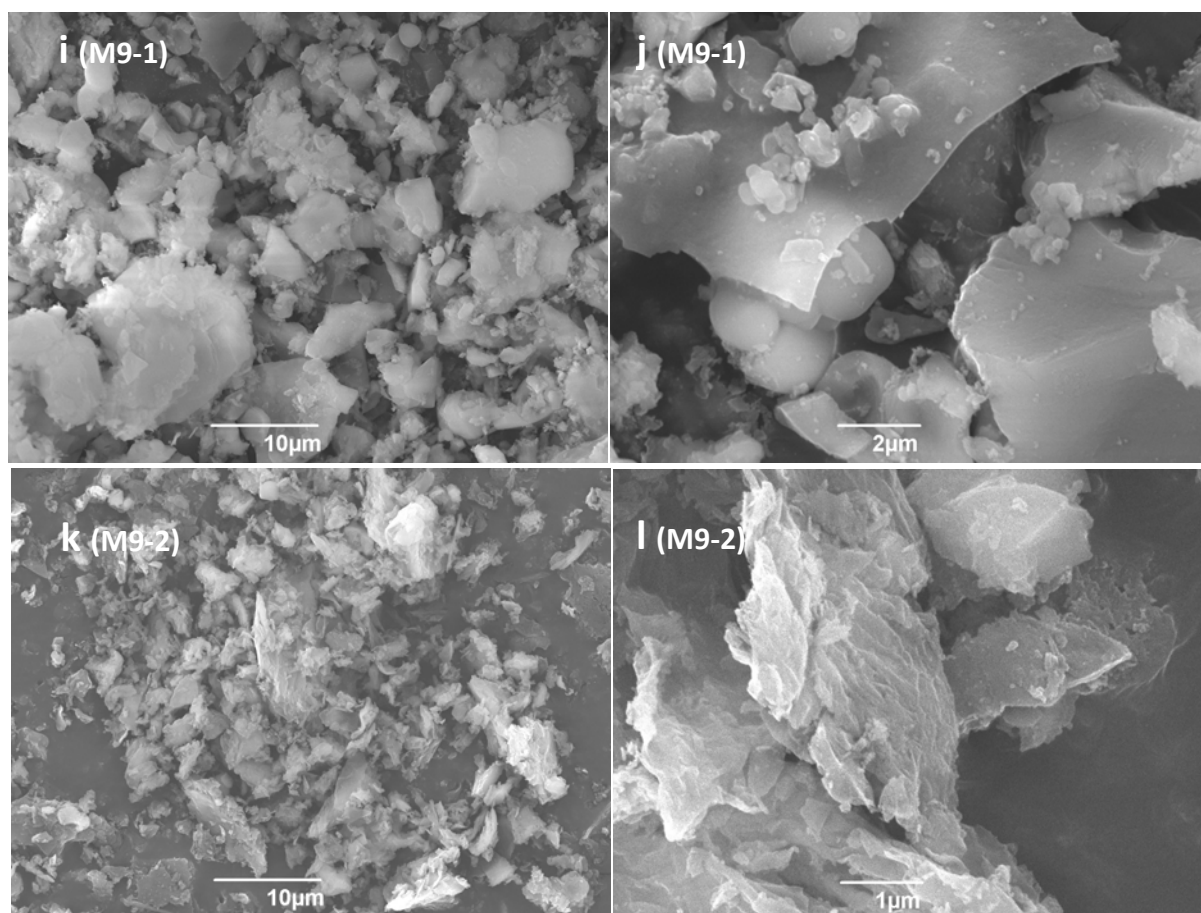


Figure 37. SEM image of extracted pure silica MCM-41, and hybrid mesoporous materials (a) MCM-41 (b) **M7-1**, (c) **M7-2**, (d) M7-3 (e, f) **M8-2**, (g, h) **M8-3**, (i, j) **M9-1**, and (k, l) **M9-2**.

Although, the exact relationship between the morphology and the structure of the organic precursor is hard to explain, it is clear that the hydrolysis properties, the concentration, and the structure of the precursor affect the final morphology of the materials. Because of the +I effect of the alkyl group of  $R-Si(OMe)_3$ , the phenothiazine precursor hydrolyzes and condenses slower than TEOS. Thus with an increased concentration of the phenothiazine precursor, there is less cross-link in the materials, and the size of the particle becomes smaller and exhibits a more uniform morphology.

## 2.2.4 Hybrid material properties

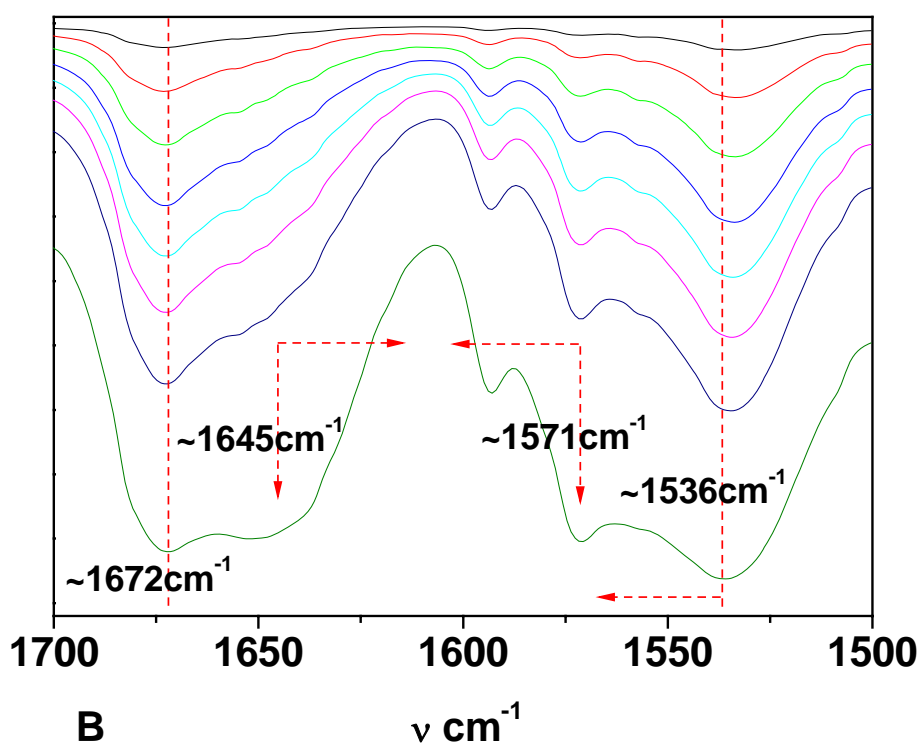
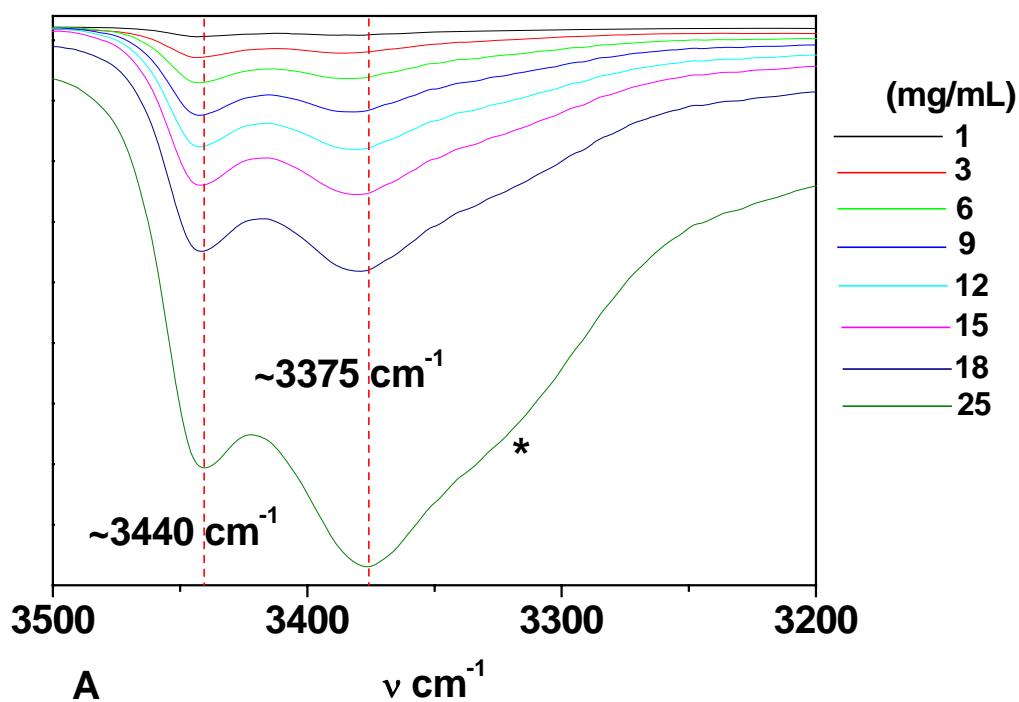
### FT-IR spectra

Normally, the position of N-H and C=O absorptions are very sensitive to hydrogen bonding<sup>168</sup>. Intermolecular hydrogen bonding is strongly concentration dependent: the higher concentrated the sample, the more pronounced is the hydrogen bonding<sup>207</sup>. Here in this section, we first discuss the data of measurements in solution. For this, different concentrations of **7** dissolved in CH<sub>2</sub>Cl<sub>2</sub> were investigated. These data will further be compared with the solid pure precursor **7** as well as with the hybrid solid materials **M7**.

Figure 38A presents the concentration dependence of the NH stretching vibration of precursor **7** at different concentrations in CH<sub>2</sub>Cl<sub>2</sub>. The band at 3440 cm<sup>-1</sup> is a typical for free urea groups, the absorption around 3375 cm<sup>-1</sup> can be assigned to urea groups involved in H-bonding. The shift to lower energy is due to weakening of the N-H bonds<sup>168</sup>. It can be observed that the band associated with H-bonding urea groups become more and more prominent with increasing concentrations of **7**. In parallel, the peak maximum of this band is slight shifted to the lower wavenumbers. An additional shoulder at around 3325 cm<sup>-1</sup> can be observed in the most concentration solution.

Figure 38B shows the two important absorption bands of the amide unit at different concentrations of **7** in CH<sub>2</sub>Cl<sub>2</sub>. These two bands are named as amide I (the carbonyl band) and the amide II (bending vibration of N-H) in the literature<sup>168</sup>. It is known that hydrogen bonding will weaken the C=O bond, and thus lead to a decrease of the stretching frequency. Therefore, the adsorption at 1672 cm<sup>-1</sup> can be assigned to the  $\nu_{\text{CO}}$  of non-hydrogen-bonding urea groups, and the adsorption at 1645 cm<sup>-1</sup> is typical for urea groups involved in intermolecular hydrogen bonds. Similarly, the  $\delta_{\text{N-H}}$  absorption is also observed as two bands at 1536 cm<sup>-1</sup> and 1571 cm<sup>-1</sup>. The signal at the lower wavenumber is corresponding to non-hydrogen-bonded urea groups, the  $\delta_{\text{N-H}}$  of the hydrogen-bonded urea groups appears at the

higher wavenumber. The band of H-bonded amide I and amide II absorptions becomes distinct by increasing of the precursor concentration.



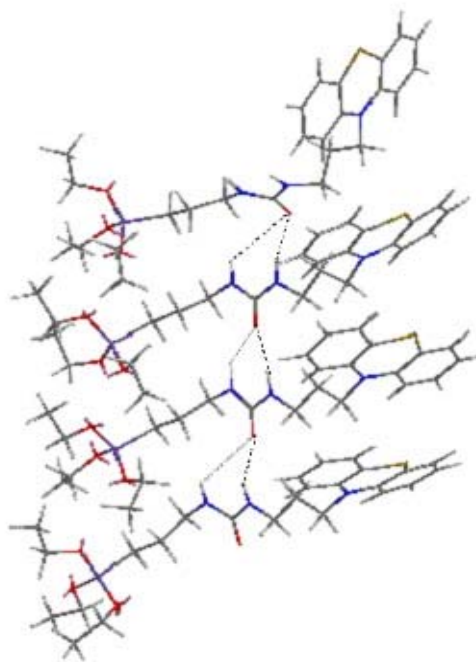


Figure 38. FT-IR spectra of different concentration of **7**/ $\text{CH}_2\text{Cl}_2$  solution, A: in the wavenumber range of  $3700\text{--}3200\text{ cm}^{-1}$ . B: in the wavenumber range of  $1700\text{--}1500\text{ cm}^{-1}$ ; the graph on the right is the illustration of intermolecular hydrogen bond of precursor **7**.

Figure 39a shows the IR-spectrum of the powdered pure precursor **7**. An important double peak band can be observed in the range of  $\nu_{\text{N-H}}$  ( $3354$  and  $3308\text{ cm}^{-1}$ ). Compared to the result in solution, the absence of the peak at  $3440\text{ cm}^{-1}$  indicates the absence of free urea groups, all urea units are involved in H-bonding. A significant shift can be observed for the NH absorption of hydrogen-bonded urea groups from  $3375\text{ cm}^{-1}$  in solution to  $3354$  and  $3308\text{ cm}^{-1}$ . This is due to a generally stronger  $\text{NH}\cdots\text{H}$  interaction in the solid state, which strongly weakens the N-H bond and lowers the energy of the NH vibration<sup>168</sup>. The double band can either be indicative for two different types of N-H bonds, or the symmetric and asymmetric NH vibration of the urea. A further important strong absorption band is observed in the signal region of the amide I and amide II vibration. In the pure solid sample **7**, amide I appears at  $1625\text{ cm}^{-1}$  and amide II at  $1580\text{ cm}^{-1}$ . Both bands are shifted compared to the solution data, due to the stronger intermolecular hydrogen bond in the solid state. The  $\Delta\nu$  (amide I – amide



II) is  $45\text{ cm}^{-1}$ , which is much smaller than the  $\Delta\nu$  value of free urea groups ( $120\text{ cm}^{-1}$ )<sup>208</sup> and even smaller than  $\Delta\nu$  ( $74\text{ cm}^{-1}$ ) of **7** solution. This result indicates a strong association of the urea groups by hydrogen bonds in the neat solid precursor **7**.

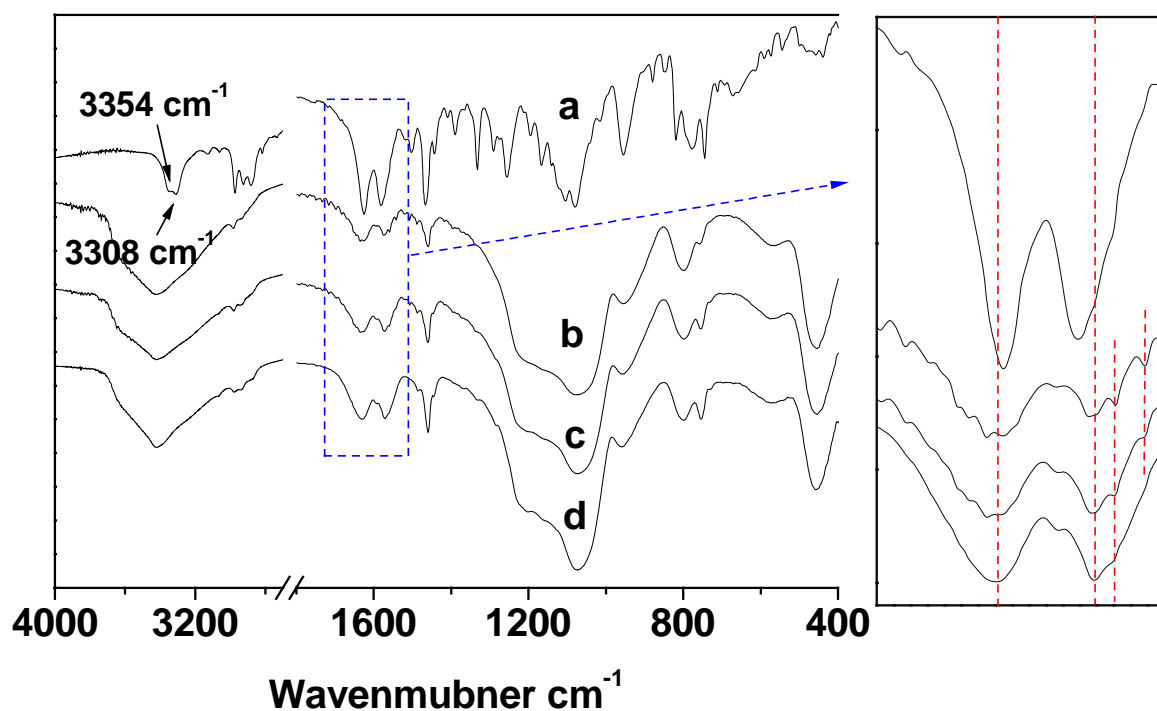


Figure 39. FT-IR spectra of the solid samples (a) **7**, (b) **M7-1**, (c) **M7-2** and (d) **M7-3**

Additionally, some other significant signals which are also characteristic for this molecule, are observed: Peaks around  $3000\text{--}2800\text{ cm}^{-1}$ , can be assigned to the CH vibration. In the fingerprint region, several strong absorptions can be figured out, such as CH deformation ( $1467\text{ cm}^{-1}$ ), C–O stretching vibration of the ester group ( $1250\text{ cm}^{-1}$ ) (this band may also cover the signal of the Si–C vibration). The asymmetric vibration of  $\nu_{\text{as}}(\text{Si–O–CH}_2)$  locates around  $1080\text{ cm}^{-1}$ . The signal at  $778\text{ cm}^{-1}$  is due to the symmetric Si–O–CH<sub>2</sub> stretching vibration<sup>209</sup> and the peak at  $740\text{ cm}^{-1}$  is assigned to the out-of-plane bending vibrations of the C–H bonds in aromatic rings.

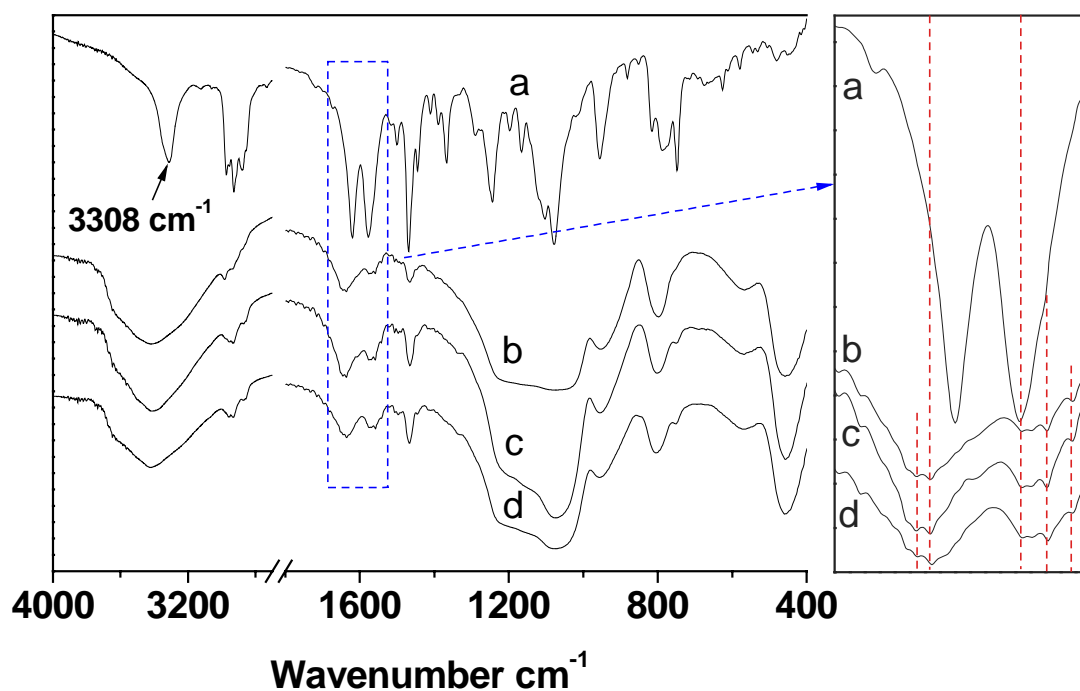
FT–IR was also carried out to detect the introduction of the organic groups into the inorganic materials. The spectra of group **M7** samples are shown in Figure 39 (b–d), and

zoomed spectra from 1700 to 1530  $\text{cm}^{-1}$  are placed on right side. The spectra of all these hybrid materials show a broad band in the range of 3600–3200  $\text{cm}^{-1}$ , which can be assigned to the  $\nu_{\text{OH}}$  stretching vibration of the hydrogen bonded internal silanol groups<sup>170</sup>. The broad bands at 1300 to 1100  $\text{cm}^{-1}$  are attributed to the asymmetric stretching vibration of various Si–O–Si bonds of the silica network. The band at 955  $\text{cm}^{-1}$  is attributed to the stretching vibration of surface Si–O<sup>-</sup> groups and the peak at 800  $\text{cm}^{-1}$  is assigned to the symmetric vibration of Si–O–Si. The strong peak at 460  $\text{cm}^{-1}$  can be assigned to the bending band of Si–O–Si<sup>210</sup>. It is worth to notice that this bending band is absent in the spectrum of precursor **7**.

Additional to these general characteristic signals of bulk SiO<sub>2</sub>, the spectra of all these samples also present some peaks, which can be assigned to the organic moieties. The stretching vibrations of saturated C–H groups is identified by peaks around 2980–2850  $\text{cm}^{-1}$ , and the band at 1470  $\text{cm}^{-1}$  is due to C–H deformations. Unfortunately, the broad absorption of H-bonded silanols just covers the position of the NH stretching vibration, but the significant two peaks  $\nu_{\text{C=O}}$  and  $\delta_{\text{N-H}}$  of the urea groups can be observed at ~1629  $\text{cm}^{-1}$  and ~1572  $\text{cm}^{-1}$ , respectively. The corresponding  $\Delta\nu$  is 55  $\text{cm}^{-1}$ , which is a little bit larger than for the neat precursor **7** ( $\Delta\nu = 45 \text{ cm}^{-1}$ ), but still much smaller than for the free urea ( $\Delta\nu = 120 \text{ cm}^{-1}$ ). It indicates the presence of hydrogen bonded urea groups in these hybrid materials. Furthermore, the low loading sample **M7-1** (0.33 mmol/g) and **M7-2** (0.54 mmol/g) show two small peaks at around 1542 and 1558  $\text{cm}^{-1}$ , which disappear in the high loading sample **M7-3** (0.77 mmol/g). This phenomenon implies the existence of a majority of hydrogen bonding species in the higher loading sample, and thus this type of hydrogen bonding should be assigned to the intermolecular hydrogen bonding formed between the urea groups. In summary, these results prove the introduction of urea functionalized phenothiazine groups into the silica materials, as well as the existence of a large amount of phenothiazine urea species associated

by hydrogen bonds. In other words, the phenothiazine molecules are mainly aggregated in the pore channels of this mesoporous hybrid materials, due to intermolecular hydrogen bonds.

Figure 40 shows the spectra of precursor **8** and of the corresponding hybrid mesoporous materials **M8**. Similar to **7**, **8** also exhibits a series of characteristic peaks. The stretching vibration of N-H is observed at  $3308\text{ cm}^{-1}$  indicating that a strong hydrogen-bonding interaction is present. A rather strong triple peak around  $2980\text{-}2880\text{ cm}^{-1}$  is representative for the alkyl CH vibrations. The high intensity of these peaks is due the presence of the long hexyl chain in precursor **8**. The sharp signals of amide I and amide II can be easily observed at  $1620\text{ cm}^{-1}$  and  $1577\text{ cm}^{-1}$ , respectively. A small  $\Delta\nu = 43\text{ cm}^{-1}$  is in agreement with the low frequency of the  $\nu_{\text{N-H}}$  vibration and indicates again a strong intermolecular hydrogen-bonding interaction. Compared to the data of precursor **7**, it seems that **8** presents a even stronger hydrogen-bonding. **8** not only has the aromatic phenothiazine core, which can undergo  $\pi\text{-}\pi$  interactions, but also contain a hexyl chain, which can provide a special association by van der Waals forces. As usual, a series of peaks in the fingerprint region, can be assigned to the other part of the molecule as already discussed for **7**.



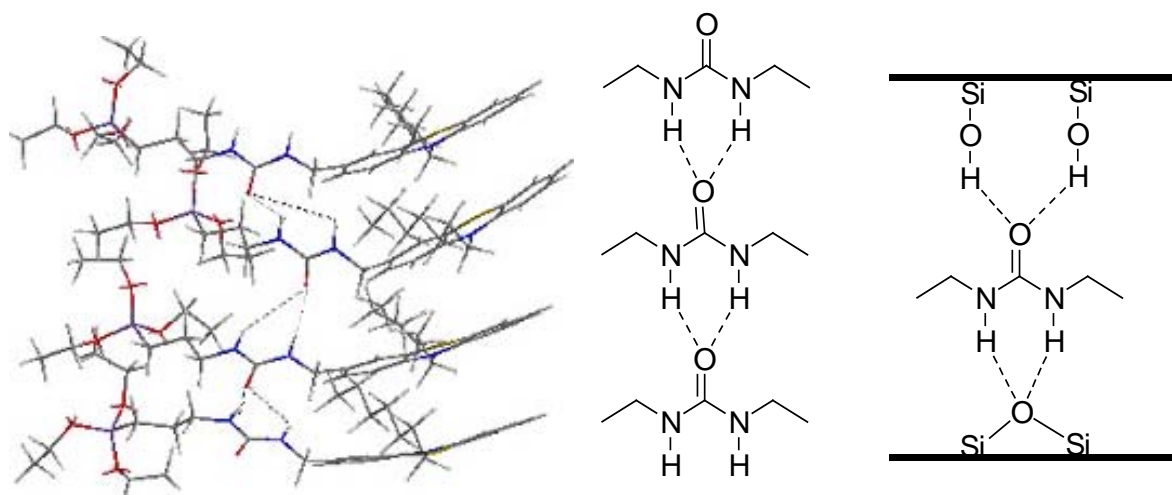


Figure 40. FT-IR spectra of (a) **8**, (b) **M8-1**, (c) **M8-2**, and (d) **M8-3**; the graphic illustrates the intermolecular hydrogen bonding of precursor **8** and the different types of hydrogen bonding of urea groups associated in the hybrid materials.

The infrared spectrum (KBr) of the **M8** samples are also presented in Figure 40. As usual, a broad band around  $3700\text{--}3100\text{ cm}^{-1}$  is observed (H-bonded silanol groups), which covers the MH stretching vibration. However the presence of hydrogen bonds is proved by the vibrations of the urea units  $\nu_{\text{C=O}}$  and  $\delta_{\text{N-H}}$ . Here several signals (marked in the right spectrum of Figure 40) are detected, which imply the presence of different types of H-bonded urea groups. Two of these alternatives are illustrated in Figure 40 (bottom). The positions of the peaks do not change significantly with an increasing organic loading, which indicates that only a limited amount of intermolecular H-bond attributes to these bands. The main reason for this is the molecular structure of precursor **8**, which can cooperate with the template molecules through van der Waals interactions by the alkyl chain. This phenomenon is consistent to the results deduced from the material structure analysis (XRD and TEM). This type of association allows the organic moiety of **8** to distribute homogeneously in the pore of materials. Seldomly, any high concentrated organic clusters are found in this material. On the assumption that the distribution of all the phenothiazine molecules is uniform, the average phenothiazine–phenothiazine distances for all hybrid materials are illustrated in Table 6. The mean distances

between the phenothiazine molecules in this series of hybrid materials (**M8**) should be more close to the calculation values. These values are relatively large, therefore the intermolecular H-bonding, should not be the major interaction, even at the highest loading of 0.54 mmol/g (**M8-3**).

The infrared spectrum of precursor **9** is shown in Figure 41 a. Similar to the former samples, a band at  $3358\text{ cm}^{-1}$  can be assigned to the NH stretching vibration. The position of this peak indicates hydrogen bond formation through the N-H moiety of the urea group. The amide I and amid II bands further prove this result. They are observed at  $1633$  and  $1575\text{ cm}^{-1}$ , respectively. The difference value ( $\Delta\nu$ ) is  $58\text{ cm}^{-1}$  and implies the existence of H-bonds by the urea group. This value is larger than the values found for precursor **7** ( $44\text{ cm}^{-1}$ ) and **8** ( $43\text{ cm}^{-1}$ ). It might be attributed to the two phenothiazine cores of this molecule which will enlarge the mean distance of two molecules.

The infrared spectra of hybrid materials **M9** recorded with the conventional KBr pellet technique are also depicted in Figure 41. The C=O absorption of this two materials arise at  $1645$  and  $1636\text{ cm}^{-1}$ . The two values possibly indicate the presence of a secondary C=O...H-X type interaction (where X is N or OSi). The bending vibration of the NH group presents multiple signals, a shoulder peak with a maximum wavenumber of  $1564\text{ cm}^{-1}$ , a strongest peak at  $1559\text{ cm}^{-1}$ , and a minimum wavenumber peak at  $1542\text{ cm}^{-1}$ . This result confirms with the two values of  $\nu_{\text{C=O}}$ , indicating different types of H-bonded urea groups in these two materials.

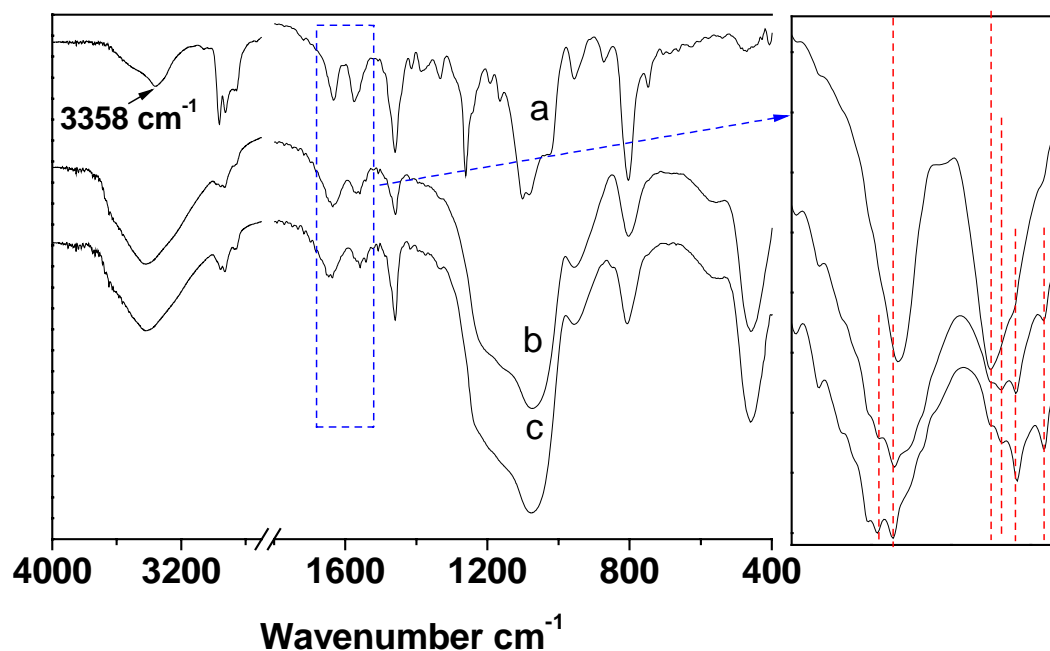


Figure 41. FT-IR spectra of (a) **9**, (b) **M9-1**, and (c) **M9-2**.

In summary, the IR bands having relation with the urea groups in the precursors and in the hybrid materials are collected in Table 6. Looking in detail to these data, it can be recognized that the value of  $\Delta\nu$  increases in the order of **8** < **7** < **9**, which is obviously related to the structure of the molecules. Intermolecular  $\pi$ - $\pi$  and van der Waals interactions significantly will shrink the distance of molecules, and thus stabilize the H-bonds between the urea groups **8**. Another evidence to prove that there are strong intermolecular H-bonds in **7** and **8** is the fact that both of them are solid, while **9** is a yellow oil. The large phenothiazine core of molecule **9** would be the main hamper for the formation of intermolecular H-bonds by urea groups, due to the non-planar structure (butterfly) of phenothiazine molecular in its ground state.

After assembling these phenothiazine molecules into the hybrid mesoporous materials with template by the co-condensation method, the final product present larger values of  $\Delta\nu$  than the pure precursors, and in a different order (**M7** < **M8** < **M9**). This result indicates that intermolecular H-bonds in hybrid materials are not as popular as in the pure precursors.

Additionally, various type of H-bonds can be assigned from the presence of multiplex absorptions. This phenomenon can easy be understood, since the average distance of the molecules in the hybrid materials should be much larger than in pure precursor.

Table 6. IR bands of urea groups obtained for organic precursor and hybrid materials.

sample	$\nu_{\text{N-H}}$	$\nu_{\text{C=O}}$	$\delta_{\text{N-H}}$	$\Delta \nu_{(\text{min, max})}^a$	$n/\text{nm}^2$	$d$ (nm)
<b>7</b>	3354, 3308	1625	1580	45	-	-
<b>M7-1</b>	--	1628	1573, 1558	55, 70	0.19	2.27
<b>M7-2</b>	--	1628	1573, 1558	55, 70	0.36	1.68
<b>M7-3</b>	--	1628	1573	55	0.66	1.23
<b>8</b>	3308	1620	1577	43	-	-
<b>M8-1</b>	--	1645, 1636	1576, 1559, 1543	60, 102	0.16	2.51
<b>M8-2</b>	--	1645, 1636	1576, 1559, 1543	60, 102	0.31	1.80
<b>M8-3</b>	--	1645, 1636	1576, 1559, 1543	60, 102	0.51	1.40
<b>9</b>	3358	1633	1575	58	-	-
<b>M9-1</b>	--	1645, 1636	1574 (sh), 1568, 1559, 1542	62, 103	0.22	2.12
<b>M9-2</b>	--	1645, 1636	1574 (sh), 1568, 1559, 1542	62, 103	0.33	1.73

<sup>a</sup>  $\Delta \nu = \text{amide I} - \text{amide II}$  ( $\Delta \nu_{\text{min}} = \text{amide I}_{\text{min}} - \text{amide II}_{\text{max}}$ , and  $\Delta \nu_{\text{max}} = \text{amide I}_{\text{max}} - \text{amide II}_{\text{min}}$ ).

### <sup>13</sup>C CP MAS NMR spectra

To detect the integrality of the organic compound in the solid inorganic materials, solid state <sup>13</sup>C CP-MAS NMR spectra were recorded from these hybrid phenothiazine functionalized materials. The exemplified result of **M7-2** is presented in Figure 42, the red lines represent the resonances of the organic precursor **7** in solution. It can be seen that the solid state <sup>13</sup>C NMR spectrum shows resonances with chemical shifts similar to the free compound. The subsistent signal at 7.6 ppm corresponds to C-Si, confirming that cleavage of

the C-Si bond did not occur during the hydrothermal synthesis. Two sharp peaks at ca.  $\delta$  60 and 16 ppm are due to remnant ethanol from the template extracting process. Additionally, these signals overlap with the resonance of small amounts of residual Si-OCH<sub>2</sub>CH<sub>3</sub> groups. The resonance  $\sim$ 40 ppm can be assigned to the alkyl carbons atoms next to the urea group, demonstrating the stability of the urea group under the co-condensation condition. Several signals in the low field region ( $\sim$ 114 to  $\sim$ 130 ppm) are typical for an electronrich aromatic system as it is the phenothiazine core. Compared to the spectrum in solution, a small shift of the resonance of the C=O group ( $\sim$ 158 ppm) for the hybrid materials is ascribed to the hydrogen bonding urea groups, and it is consistent with the results of the FT-IR spectroscopy.

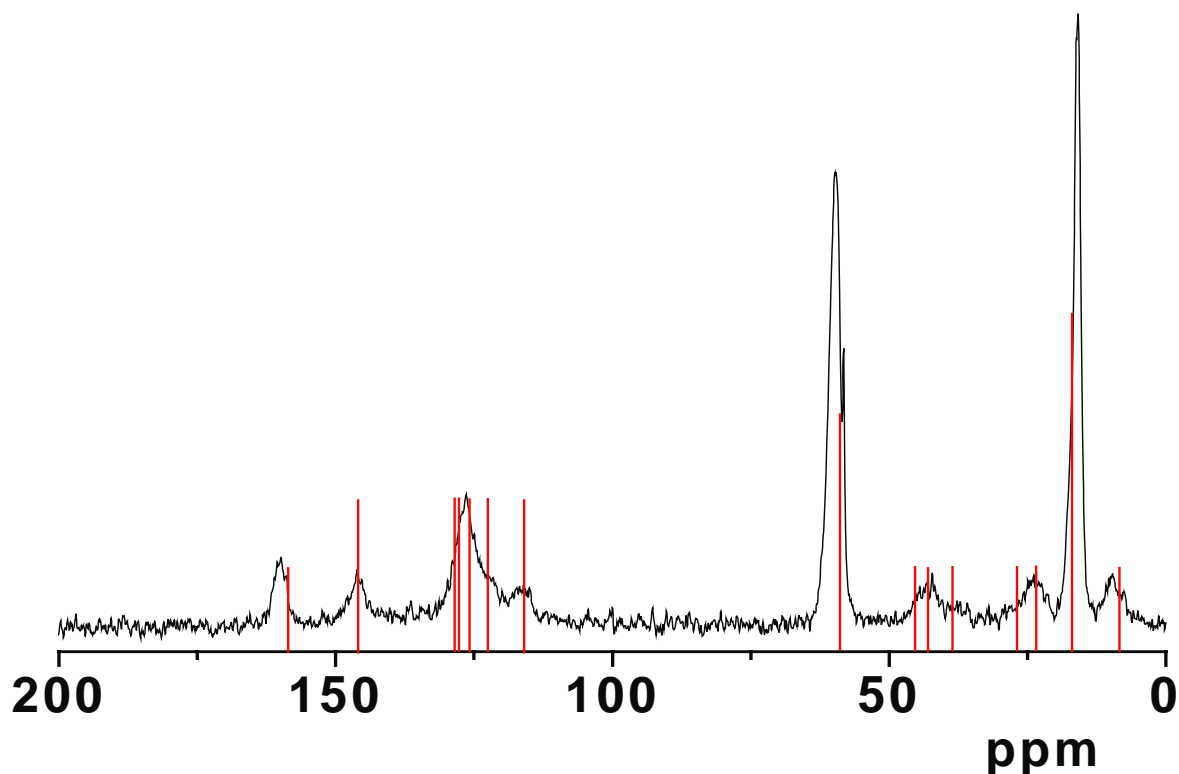


Figure 42. <sup>13</sup>C CP-MAS NMR spectrum of **M7-2**; the red lines give information on the position and the relative intensities in the solution NMR spectrum of **7**.

Figure 43 shows the <sup>13</sup>C MAS NMR spectra of **M8-3** and organic compound **8** (red lines). The matching of the solid state NMR resonances with the result of free compound in solution, demonstrates the conservation of the phenothiazine moiety in the hybrid material. The intense



resonances in the high field region are mainly due to the hexyl chain (14 - 30 ppm). The alkyl carbon atoms at the urea group are present around  $\delta$  43 ppm. A group of peaks at lower field is attributed to the characteristic signals of the phenothiazine core (116 - 145 ppm). Similarly to **7**, a shift for the resonance of C=O group to lower field can be observed for the hybrid material, compared to the data in solution.

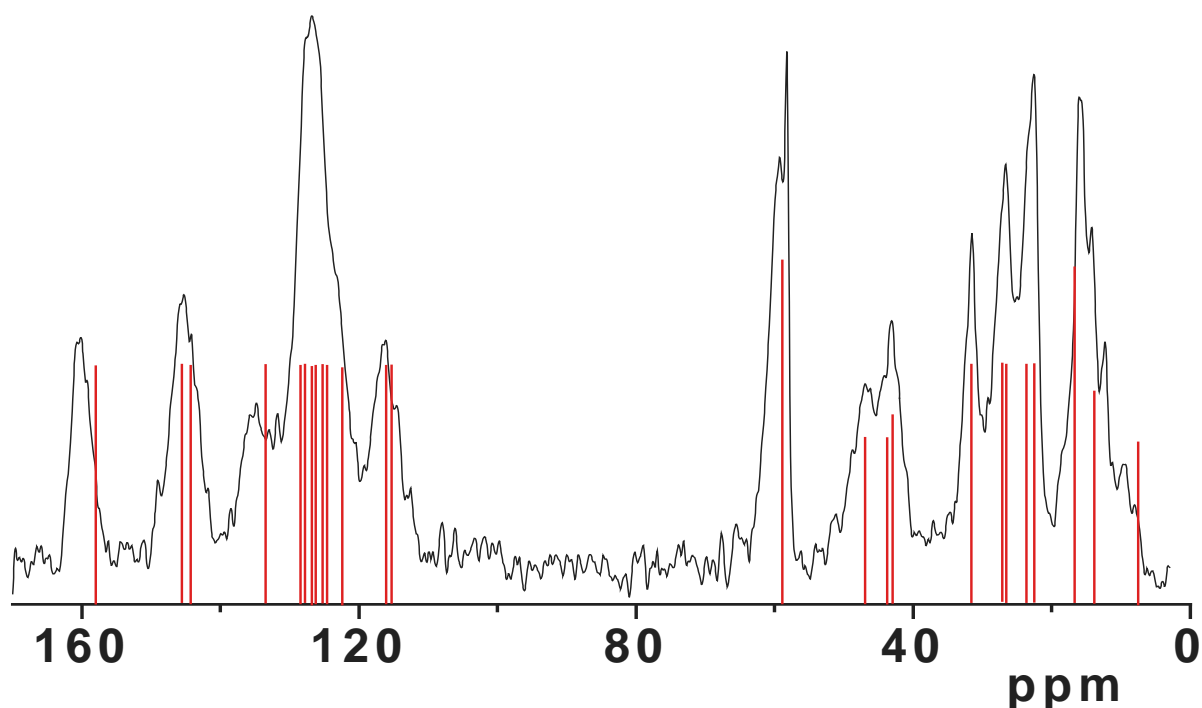


Figure 43.  $^{13}\text{C}$  CP-MAS NMR spectrum of **M8-3**; the red lines give information on the position and the relative intensities in the solution NMR spectrum of **8**.

The  $^{13}\text{C}$  CP MAS NMR spectrum of **M9-2** is presented in Figure 44. At higher field, a group of peaks can be assigned to the carbon atoms of the hexyl chains and urea side chain. At lower field the resonances appearing in the aromatic region are due to the phenothiazine cores. The matching of the spectrum of the hybrid material with the pure organic precursor implies the introduction and the stability of the organic molecule **9**. Similar to the results of two hybrid samples discussed before, a shift to lower field can be observed for the resonance of the C=O group in the solid state compared to the solution data.

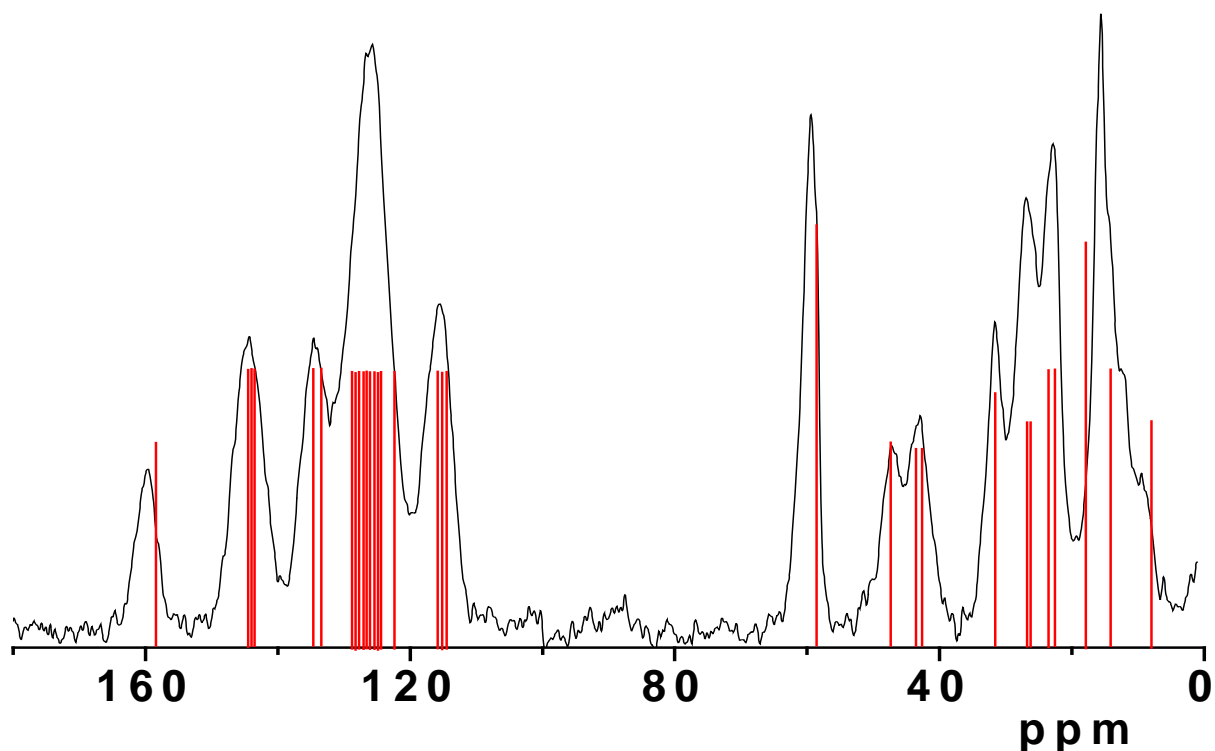


Figure 44.  $^{13}\text{C}$  CP-MAS NMR spectrum of **M9-2**; the red lines give information on the position and the relative intensities in the solution NMR spectrum of **9**.

#### $^1\text{H}$ CP MAS NMR spectra

Figure 45 presents the solid state  $^1\text{H}$  MAS NMR spectrum of **M7-2**. The red lines represent the resonances from the NMR experiment in solution with precursor **7**. A sharp signal centers at  $\sim 1.0$  ppm, which is due to residual ethanol from template extracting process. Additionally, this strong signal is overlapping with the peak of remaining  $-\text{Si}-\text{OCH}_2\text{CH}_3$  groups and the resonance of  $-\text{Si}-\text{CH}_2-$  unit. A small peak can be observed at  $\delta$  1.85 ppm. It is attributed to the proton of the silanol groups on the surface of the material. Another strong peak present at  $\delta$  3.55 ppm is also due to the remnant ethanol, and this broad band also covers several proton resonances of the urea side chain and residual  $-\text{Si}-\text{OCH}_2\text{CH}_3$ . The protons of the phenothiazine ring resonate in the low field region with an overlapping peak centering at 6.90 ppm.

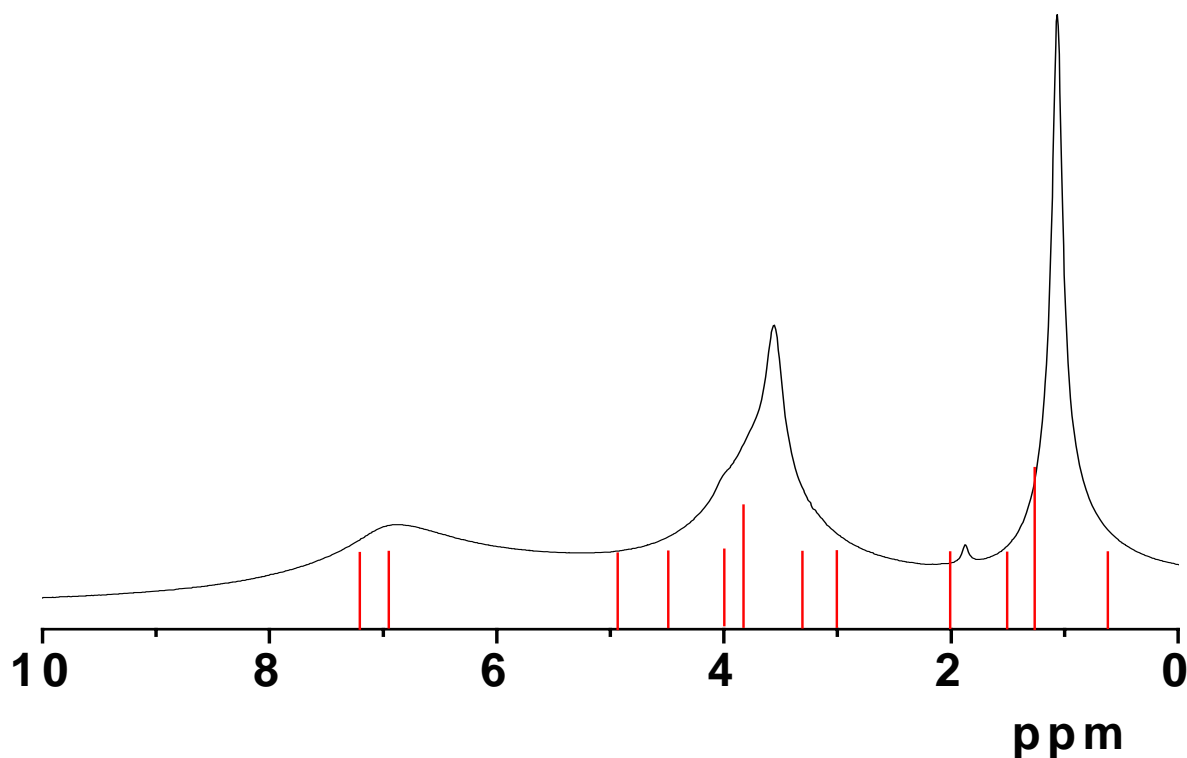


Figure 45.  $^1\text{H}$  MAS NMR spectrum of **M7-2**

#### $^{29}\text{Si}$ CP MAS NMR spectra

Solid state  $^{29}\text{Si}$  CP MAS NMR provides information about the silicon environment and the degree of organic functionalization. Figure 46 shows the  $^{29}\text{Si}$  CP MAS NMR spectrum of hybrid material **M7-2**. The low-intensity peaks at  $-92$  ppm correspond to silicon atoms with two siloxane bonds and two silanol groups, i.e., geminal silanol sites,  $(\text{OH})_2\text{Si}(\text{SiO})_2$  ( $\text{Q}^2$ ). The resonance at  $-101$  ppm is attributed to silicon atoms with three siloxane bonds and one silanol group, such as isolated silanol sites,  $(\text{OH})\text{Si}(\text{SiO})_3$  ( $\text{Q}^3$ ), while the resonance at  $-110$  ppm is ascribed to the four siloxane bonding silicon atoms  $\text{Si}(\text{SiO})_4$  ( $\text{Q}^4$ )<sup>211</sup>. The signals from  $-50$  ppm to  $-70$  ppm are due to the introduction of organo silicon species. Normally, three signals at  $-49$ ,  $-58$  and  $-67$  ppm can be assigned to  $\text{R-Si}(\text{HO})_2(\text{OSi})$  ( $\text{T}^1$ ),  $\text{R-Si}(\text{HO})(\text{OSi})_2$  ( $\text{T}^2$ ), and  $\text{RSi}-(\text{OSi})_3$  ( $\text{T}^3$ ), respectively<sup>212</sup>. In this spectra, a broad band having a center at  $-65$  ppm can be observed, which means that the major species is  $\text{T}^3$ . It indicates that a relative

complete cross-linking reaction occurred between the phenothiazine precursor **7** and TEOS during the co-condensation process<sup>213</sup>.

Figure 47 gives as an example the spectrum of **M8-3**. It is almost analogous to the spectrum shown in Figure 46 with a slightly more intense  $Q^2$  peak. A similar type of pattern is observed in Figure 48 showing the  $^{29}\text{Si}$  CP-MAS NMR spectrum of **M9-2**.

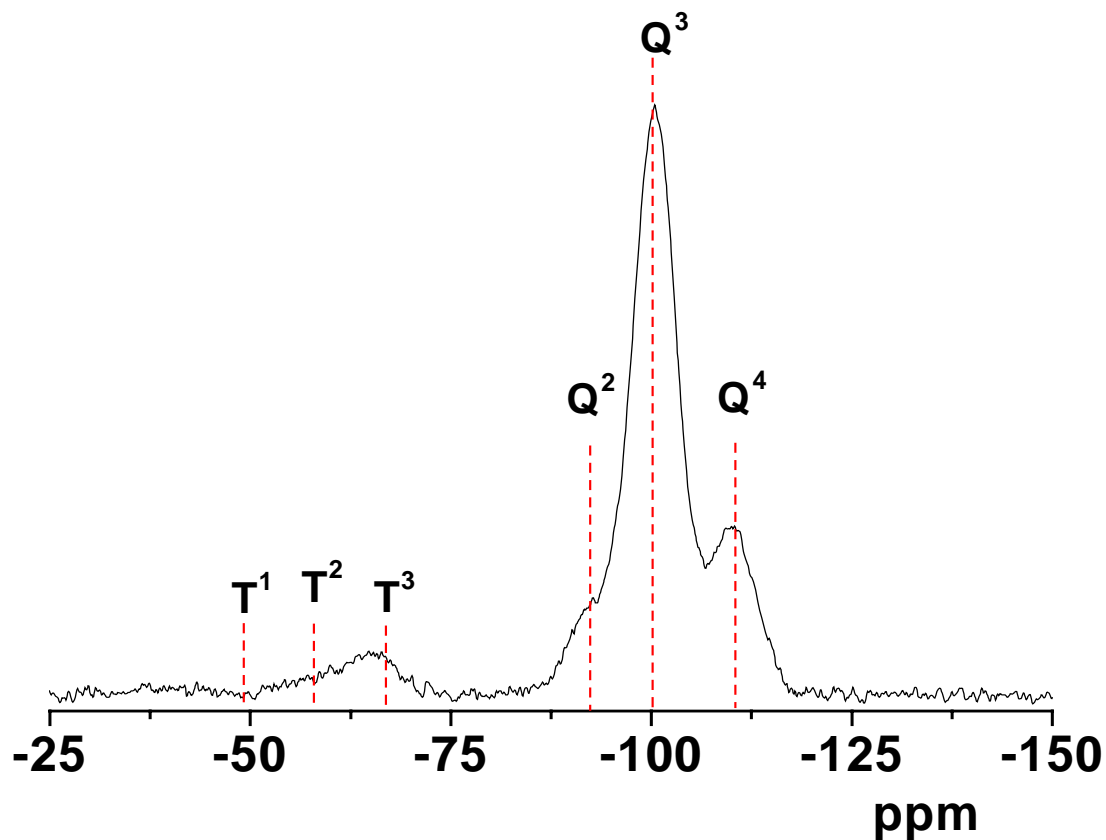


Figure 46.  $^{29}\text{Si}$  CP-MAS NMR spectrum of **M7-2**.

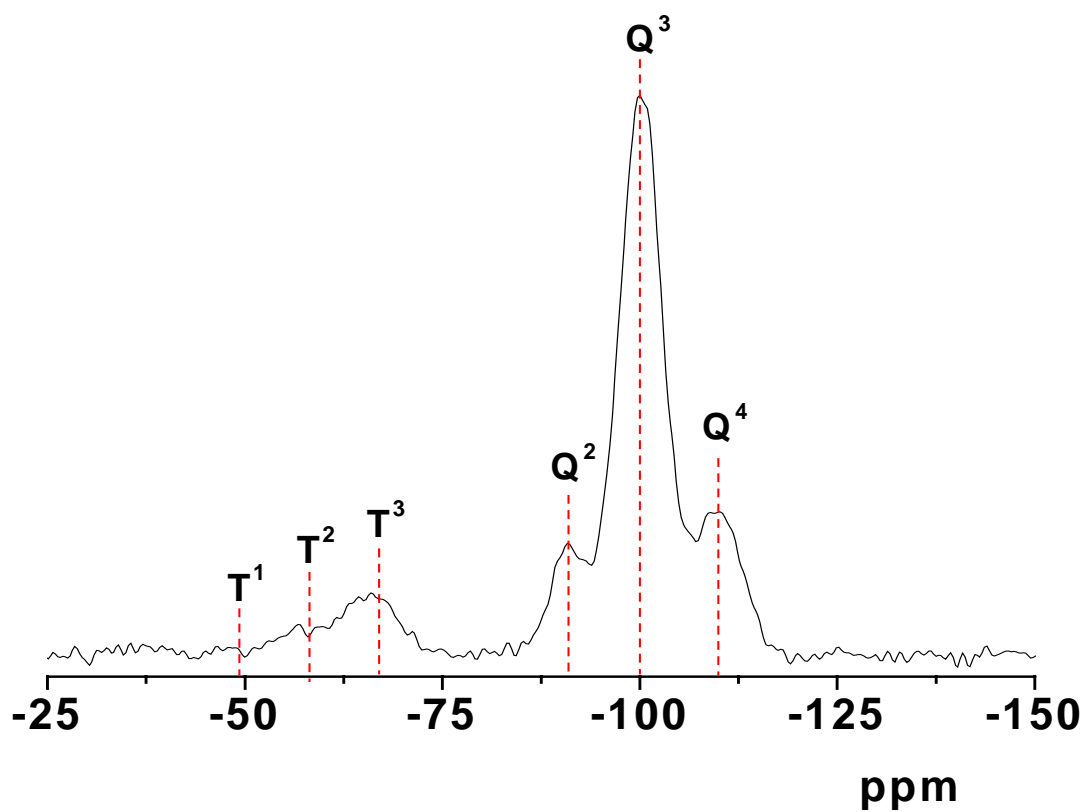


Figure 47.  $^{29}\text{Si}$  CP-MAS NMR spectra of M8-3.

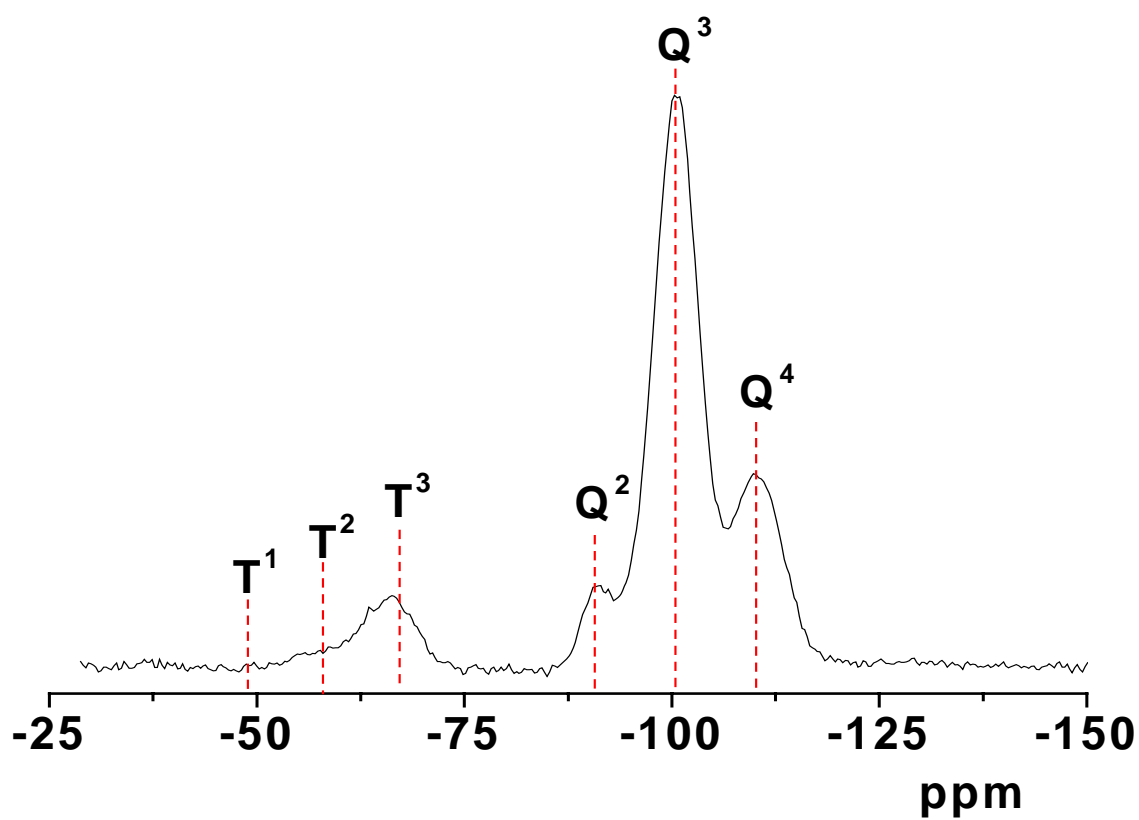
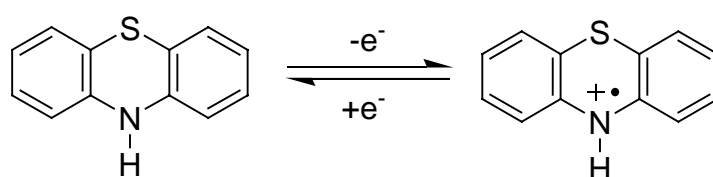


Figure 48.  $^{29}\text{Si}$  CP-MAS NMR spectra of M9-2.

## 2.2.6 Electronic and optical properties of the hybrid materials and the associated oxidized materials

As mentioned before, phenothiazines are structurally well defined redox active molecules, exhibiting a one-electron oxidation processes at relatively low potentials (Scheme 14). Thus to determine the electrochemical and optical properties of the phenothiazines in this hybrid materials will provide some useful information about the molecule and its surroundings. Herefore absorption and emission spectroscopy and cyclic voltammetry were carried out.



Scheme 14. The oxidation of 10H-phenothiazine.

### Electrochemical and optical properties of the organic precursors

The spectroscopic data of precursors **7** and **8** are illustrated in Table 7. Both have two absorption bands in the UV region, accompanied by an intense blue to greenish blue fluorescence. The emission maxima lie at 449 and 459 nm, respectively. The Stokes shifts are quite remarkable and range from  $\Delta\nu = 9990$  to  $10060 \text{ cm}^{-1}$ . Substantial Stokes shifts have also been observed for many phenothiazine derivatives<sup>214-216</sup> and can be attributed to significant geometrical changes upon excitation from a highly nonplanar ground-state to a largely planarized excited state<sup>217, 218</sup>.

Table 7. Selected absorption emission spectra and CV data

compound	$\lambda_{\text{max,abs}}$ (nm) ( $\epsilon$ )	$\lambda_{\text{max,em}}$ (nm)	Stokes-shift ( $\text{cm}^{-1}$ )	$E_{1/2}^{0/+1}$ (mV)
<b>7</b>	257 (47131), 310 (7189) <sup>a</sup>	449, 511 (sh.) <sup>a</sup>	9990	690 <sup>a</sup>
<b>M7-1</b>	250, 304	436	9960	-- <sup>b</sup>

<b>M7-2</b>	251, 307	438	9740	671 <sup>c</sup>
<b>M7-3</b>	248, 305	388 (sh), 437	9900	720 <sup>c</sup>
<b>8</b>	260 (20303), 314 (3067) <sup>a</sup>	459 <sup>a</sup>	10060	669 <sup>a</sup>
<b>M8-1</b>	256, 308	388 (sh), 450	10250	
<b>M8-2</b>	255, 311	456	10220	
<b>M8-3</b>	255, 310	436	9930	
<b>M9-1</b>	268, 324	467, 512 (sh)	9450	
<b>M9-2</b>	268, 329	461, 504 (sh)	8700	

<sup>a</sup> CH<sub>2</sub>Cl<sub>2</sub> as the solvent. <sup>b</sup> UV-Vis diffuse reflectance. <sup>b</sup> undecidable due to the unclear E<sub>pc</sub>. <sup>c</sup> CH<sub>3</sub>CN as the medium.

Electrochemical data for these two phenothiazine precursors were obtained by cyclic voltammetry in the anodic region (up to 1.2 V). A representative reversible oxidation steps are found reflecting the phenothiazine core in the individual molecules (Figure 49). The half wave potentials of these two samples stem at 690 mV for **7**, and 669 mV for **8**.

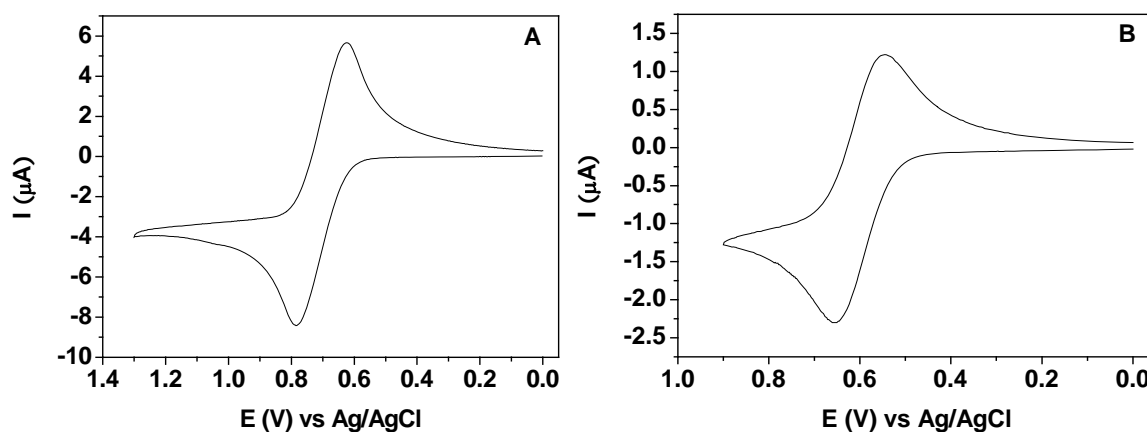


Figure 49. Cyclic voltammograms of (A) precursor **7**, and (B) precursor **8** (<sup>n</sup>Bu<sub>4</sub>N<sup>+</sup>PF<sub>6</sub><sup>-</sup>/CH<sub>2</sub>Cl<sub>2</sub>, 20 °C,  $\nu = 100$  mV/s, Pt-working electrode, Pt-counter electrode, Ag/AgCl reference electrode).

## Electrochemical properties of hybrid materials

The solid state electrochemical characterization of sample **M7** was carried out by Dr. Markus Pagels (Schlumberger Cambridge Research). The powdered hybrid materials were abrasively immobilized on a glassy carbon electrode. The cyclic voltammograms (CVs) of these samples were measured in acetonitrile solution with  ${}^n\text{Bu}_4\text{N}^+\text{PF}_6^-$  (0.1 M) as supporting electrolyte.

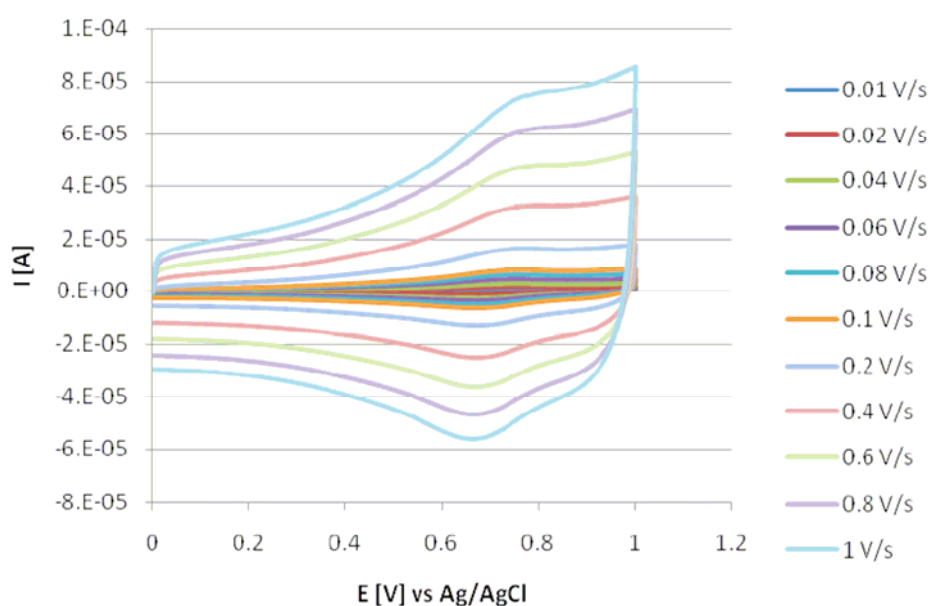


Figure 50. Cyclic voltammograms of a **M7-3** modified electrode in  ${}^n\text{Bu}_4\text{N}^+\text{PF}_6^-/\text{CH}_3\text{CN}$  at RT with varying scan rates.

The cyclic voltammogram of sample **M7-3** (0.77 mmol/g loading of phenothiazine) is shown in Figure 50. A potential sweep with a **M7-3** modified GC electrode with a scan rate of 0.1 V/s reveals an oxidation wave at a potential of 762 mV against Ag/AgCl, and a reduction wave at a potential of 678 mV against Ag/AgCl. The half wave potential of this reversible one electron transfer is 720 mV, with a peak separation of 84 mV. When the scan rate is varied between 0.01 V/s and 1.0 V/s the voltammograms still show a reversible redox signal with the peak potentials being fairly constant, and the peak currents increasing with increasing scan rate. How can the electron transfer from electrochemically active species to the electrode?



In general, there are two major pathways to realize the electron transfer for the hybrid mesoporous silica materials<sup>219</sup>. One is direct electron transfer from the conductive electrode surface to the electrochemically active species. For this pathway the redox sites have to be mobile. This type of electron transfer normally is present in the case of a physical absorption of an organic moiety in the mesoporous materials<sup>220</sup>. Another propagation of the charge pathway is a long-range electron transfer from the electrode surface through the immobilized redox centers via electron exchange between the adjacent redox centers (electron hopping)<sup>221, 222</sup>. Considering the situation of the hybrid material **M7-3**, the electrochemical active centers (phenothiazine) are covalently fixed in the pore of the mesoporous silica matrix. Thus, the charge pathway of this material should be the electron hopping between the adjacent phenothiazines, which are assembled in a limited interspace of pore with a rather short distance (Table 6).

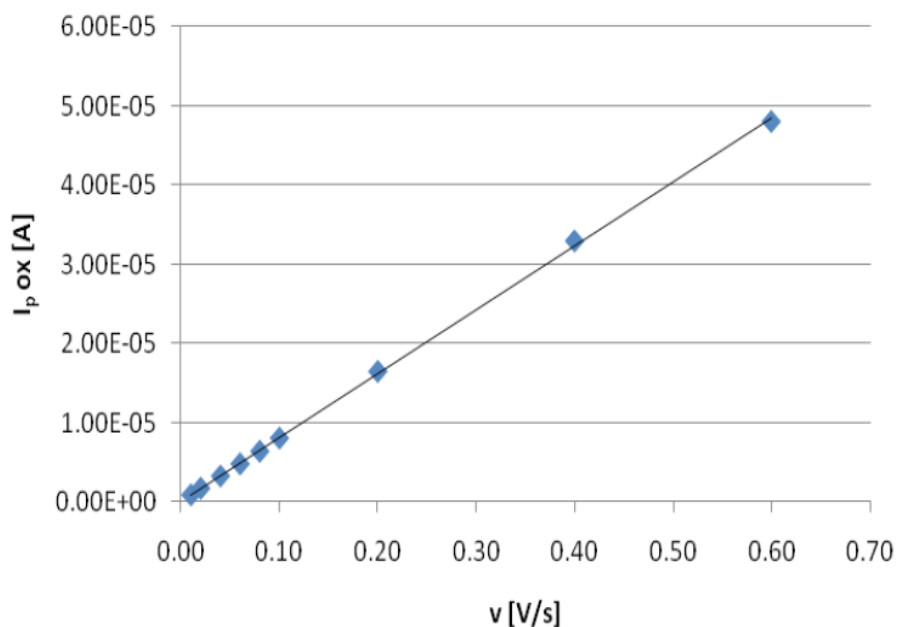


Figure 51. Plot of the oxidation peak potentials at varying scan rates against the scan rate.

A further evidence for the electron hopping transfer is presented in Figure 51, which is a plot of the oxidation peak currents against the scan rate giving a straight line. The peak

current scan rate is linearly proportional to the scan rate, which indicates surface bound redox centers<sup>219</sup>. Additionally, a multi-cycle voltammogram of **M7-3** is presented in Figure 52. After 100 times scans, the overall current just shows a slight decrease, which is due to the loss of the redox active powdered material from the electrode over time. This is different to the situation of diffusion-controlled electrochemical reactions in electrode supporting materials for which in this case the detected signal should fail quickly, due to diffusion of electroactive species to the electrolyte<sup>219, 223</sup>. Thus, the redox active phenothiazine molecules are immobilized on the silica pore walls of this material, and the electron propagation in this insulating silica matrix should take place via self-exchange between the phenothazines (electron hopping).

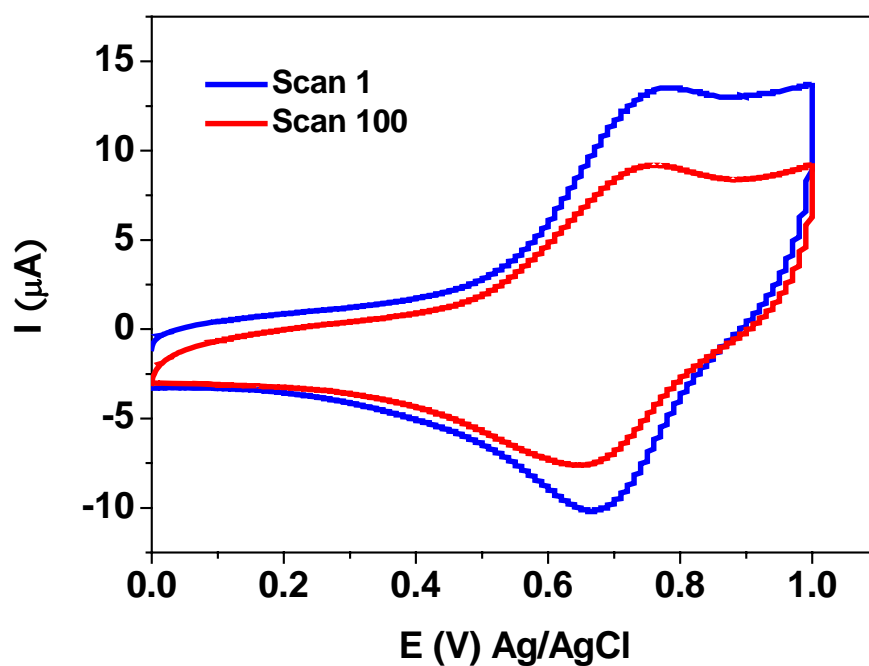


Figure 52. Multi-cycle voltammogram of a **M7-3** modified GC electrode in  ${}^n\text{Bu}_4\text{N}^+\text{PF}_6^-$  / $\text{CH}_3\text{CN}$  at RT,  $v = 100 \text{ mV /s}$ .

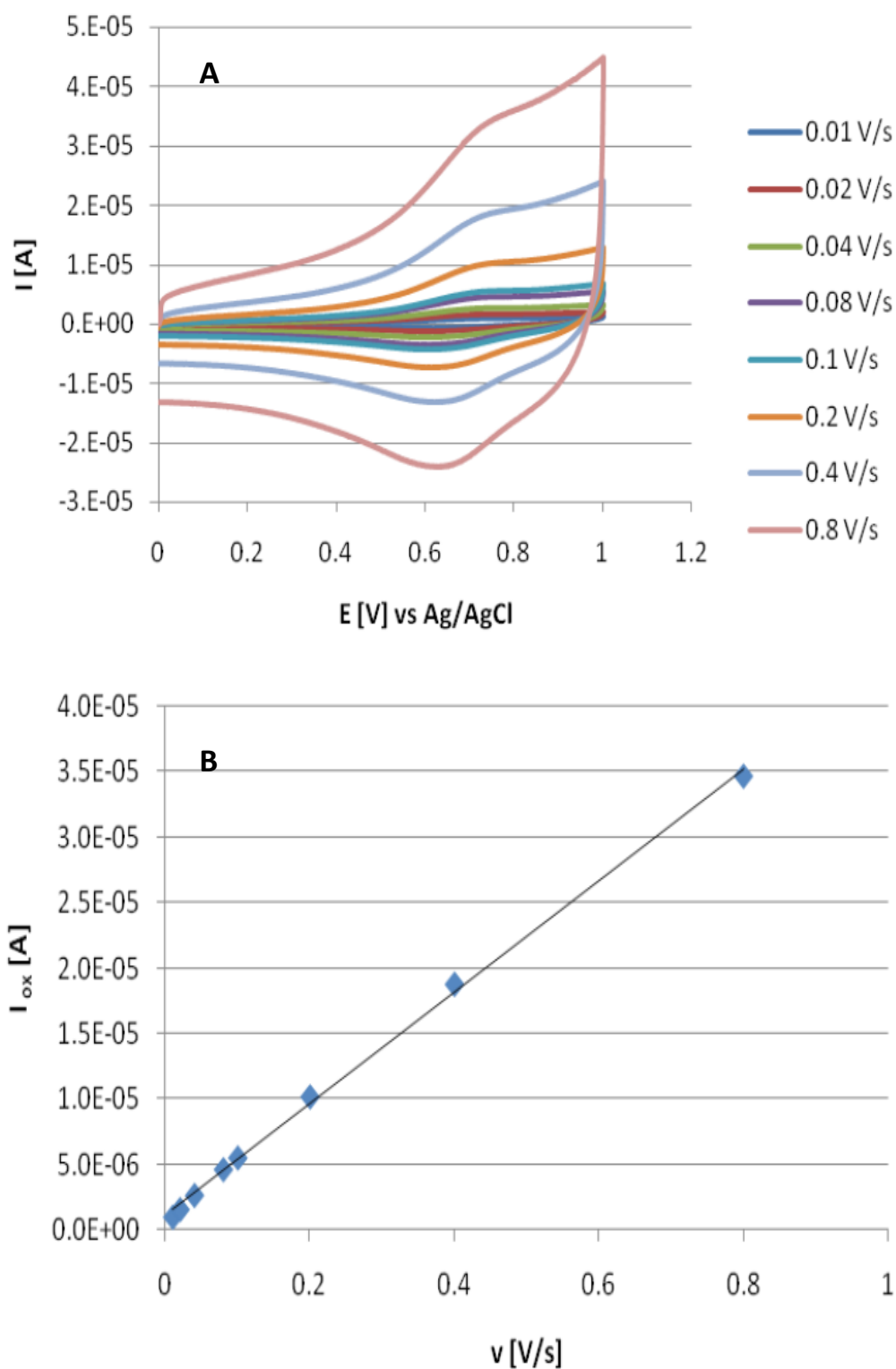


Figure 53. (A) Cyclic voltammograms of a **M7-2** modified electrode in  $n\text{Bu}_4\text{N}^+\text{PF}_6^-/\text{CH}_3\text{CN}$  at RT with varying scan rates. (B) Plot of the oxidation peak potentials at varying scan rates against the scan rate of **M7-2**.

The cyclic voltammogram of **M7-2** is presented in Figure 53, showing an oxidation wave at a potential of 726 mV against Ag/AgCl and a reduction wave at a potential of 616 mV against Ag/AgCl. The half wave potential of this reversible one electron transfer is 671 mV, with a peak separation of 110 mV. The difference of oxidation and reduction peak potential of **M7-2** is larger than for **M7-3** (85 mV). This means that the lower loaded sample has a deceleration of the electrode kinetics (slower charge transfer speed), which should be attributed to the decrease of redox centers in the pore channels and relatively large intermolecular distances (Table 6). For the sample **M7-1** with the lowest loading of phenothiazine (0.33 mmol/g), the cyclic voltammogram is shown in Figure 54. A reduction wave at a potential of 582 mV can be observed, while the  $E_{pc}$  of oxidation wave is not clear. However, **M7-1** and **M7-2** have a redox behaviour largely similar to **M7-3** with reduced current peak heights. Additionally, the plot of the redox peak currents against the scan rates results in a straight line, which implies the existence of grafted redox active phenothiazine centers in these two hybrid materials.

In summary, the solid state cyclic voltammetric results show that all three samples **M7** present a series of reversible one electron redox curves in the potential range 0-1.0V, which is a typical redox behaviour of a monophenothiazine compound<sup>224</sup>. It further proves the introduction of phenothiazine moiety in the pores of the silica materials by the in-situ method. Contemporarily, the electronic activity of this organic precursor is well preserved. Additionally, the presence of a well reversible electron transfer proves the advantages of the mesoporous materials to build up an appropriate host matrix, which can not only provide mechanical stability, but also can serve as a structural materials to arrange the phenothiazine molecules without hindering the charge transfer to the internal redox sites.

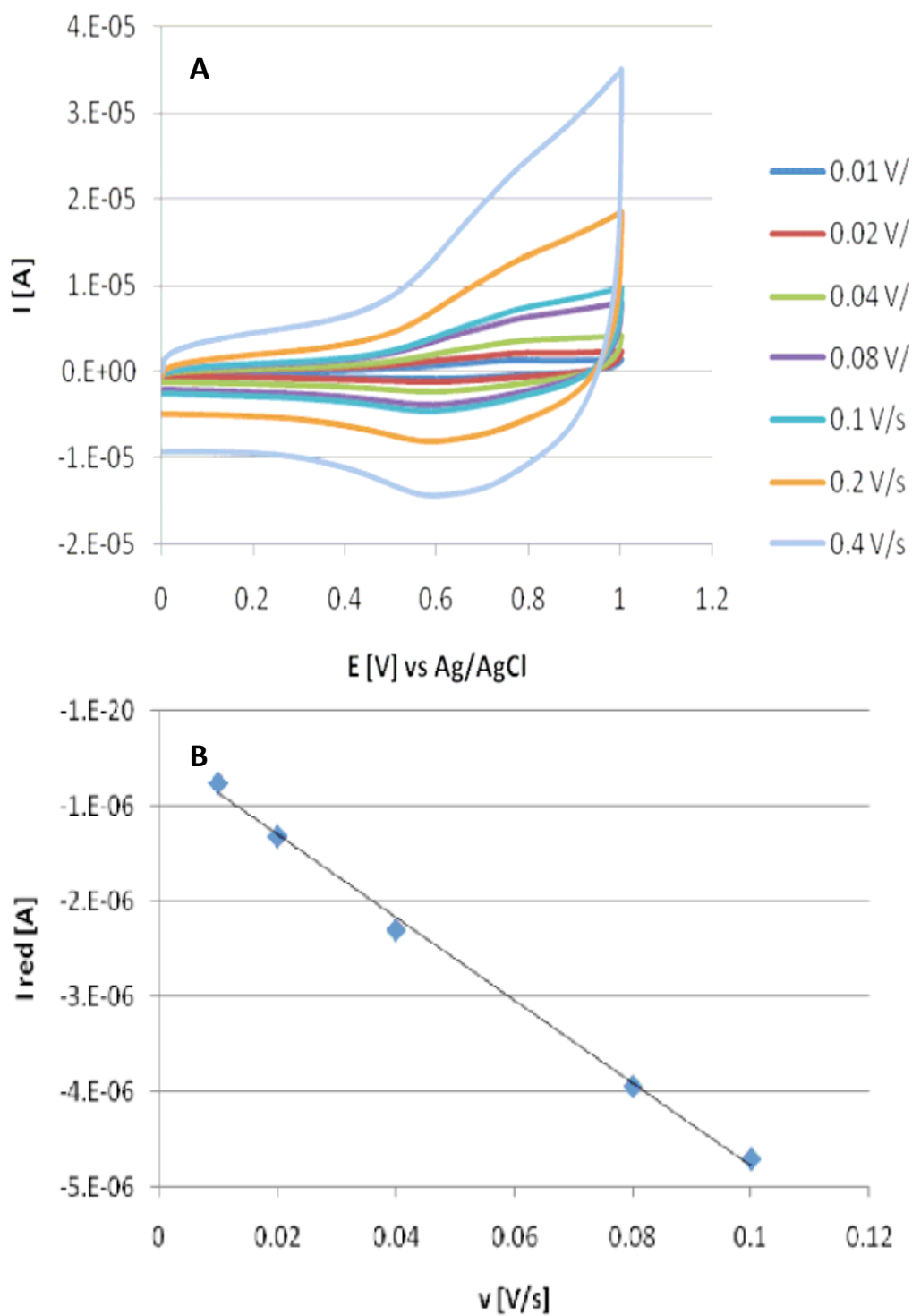


Figure 54. (A) Cyclic voltammogram of a **M7-1** modified electrode in  $n\text{Bu}_4\text{N}^+\text{PF}_6^-/\text{CH}_3\text{CN}$  at RT with varying scan rates. (B) Plot of the reduction peak potentials at varying scan rates against the scan rate.

## Absorption and emission spectroscopy of hybrid materials

The absorption spectra of the **M7** samples are illustrated in Figure 55 (black lines). All the samples present two absorptions in the ultraviolet region, which are similar to the absorption of the pure organic compound. Compared to the result of precursor **7** in CH<sub>2</sub>Cl<sub>2</sub> (Table 7), a slight blue shift of the peak maxima can be observed for the hybrid materials. This hypsochromic shift might be due to the existence of H-bonds between the N or S atom of phenothiazine core and the silanol of material's surface, or be attributed to the one-dimensional array of phenothiazine molecules in the channel of mesoporous material having a H-type of aggregation (H-aggregate, or face-to-face arrangement)<sup>225, 226</sup>. Additionally, for easier comparison, these two absorption bands of the hybrid materials are normalized to the maximum absorbance (Figure 56), which demonstrates that no shift can be observed by changing the amount of phenothiazine in this hybrid materials. Only a little broadening occurs by increasing the loading of phenothiazine, which may be attributed to weak  $\pi$ -electron interactions with surface hydroxyl groups of silica material<sup>172</sup>, or as a result of H-aggregation, which normally, leads to a relatively broadened blue-shifted band<sup>225, 227</sup>. However, there is no  $\pi$ - $\pi$  conjugation, or a large extending  $\pi$  electron delocalization even in the sample with the highest loading. This is mainly due to the fact that the phenothiazine ring is highly nonplanar in the ground state (butterfly structure), preventing sufficiently close intermolecular interactions which are essential for the formation of aggregates<sup>108, 228</sup>.

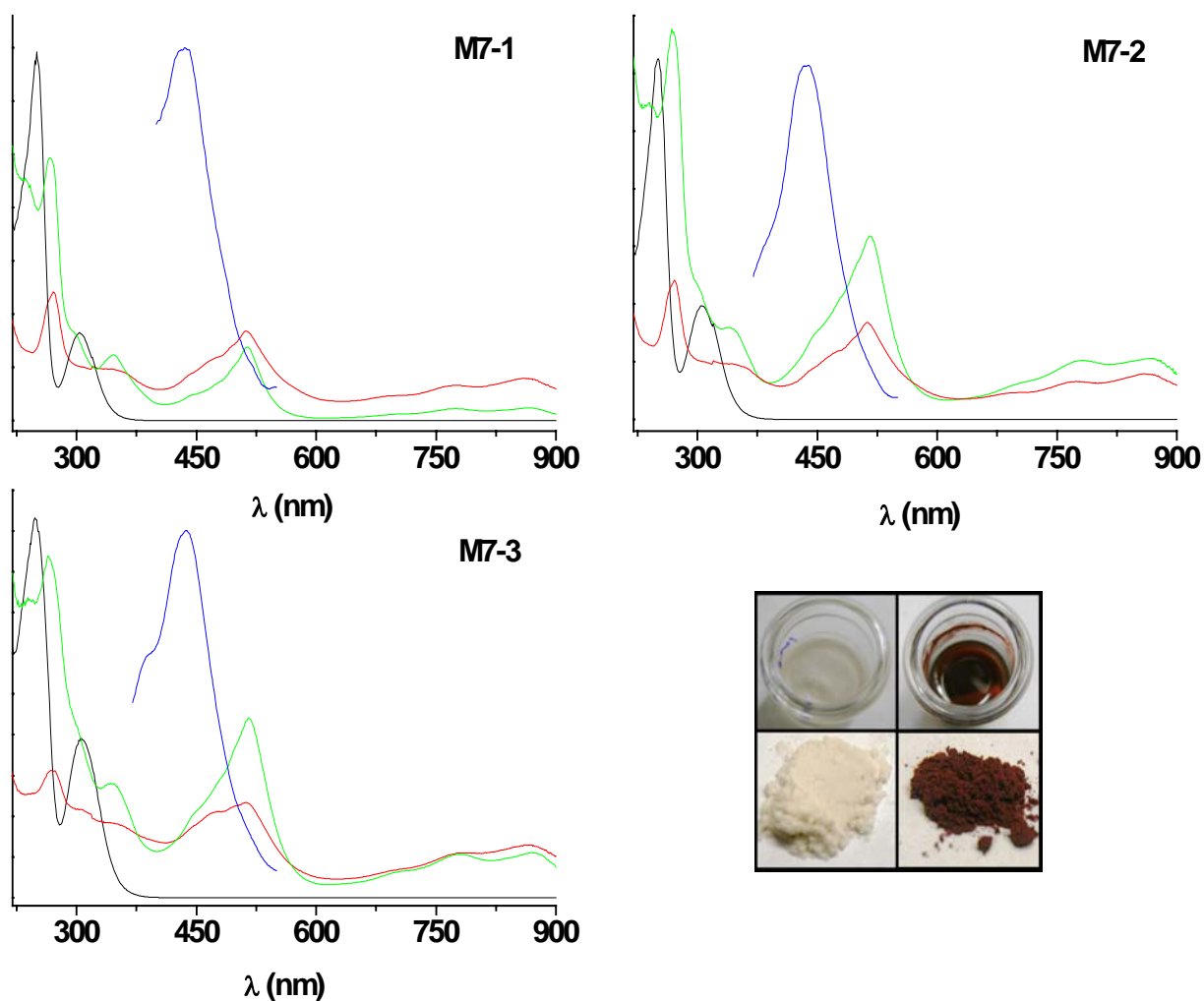


Figure 55. UV-Vis spectra of the hybrid mesoporous materials **M7-1**, **M7-2**, **M7-3** (black lines), the absorptions of the corresponding radical cationic samples **M7-1-BF<sub>4</sub>**, **M7-2-BF<sub>4</sub>**, **M7-3-BF<sub>4</sub>** (red lines), **M7-1-SbCl<sub>6</sub>**, **M7-2-SbCl<sub>6</sub>**, **M7-3-SbCl<sub>6</sub>** (green lines), and the emission spectra of the modified samples **M7-1**, **M7-2**, **M7-3** (blue lines). The inset picture demonstrates the color change caused by the oxidation of **M7-1** using NOBF<sub>4</sub> in suspension and for the corresponding solid.

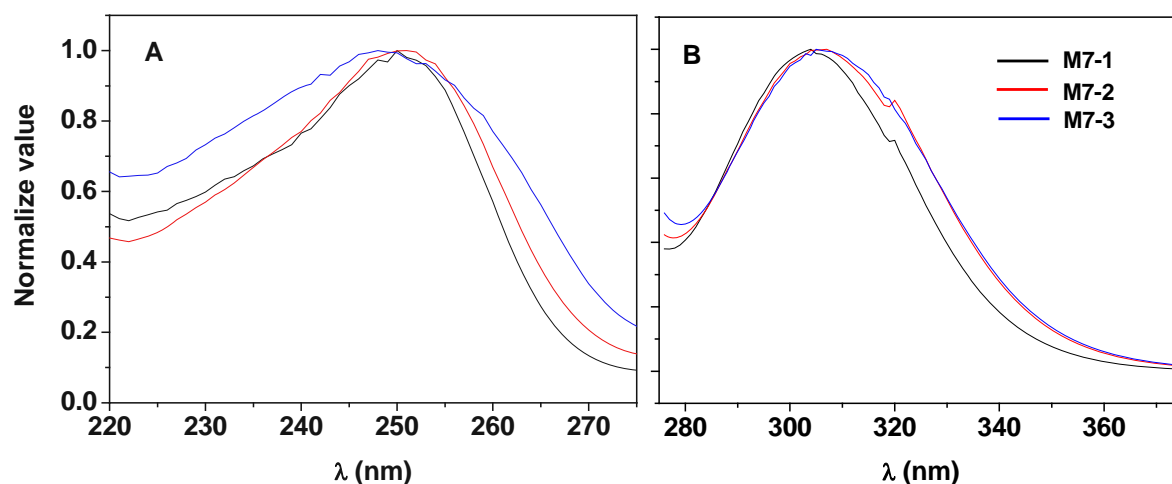


Figure 56. Normalized absorption of **M7** (A) at around 250 nm, and (B) at around 305 nm.

The emission spectra of **M7** are also shown in Figure 55 (blue lines). The blue emission is located with a peak maximum at  $\sim 437$  nm, and is blue shifted, compared to the data of precursor **7** in  $\text{CH}_2\text{Cl}_2$  solution (peak maximum at 449 nm, and a shoulder at 511 nm), and with a similar Stokes-shift of around  $10000\text{ cm}^{-1}$ . For better comparison, the normalized emission spectra are presented in Figure 57. The peak maximum position does not change for all three samples. Interestingly a second emission peak can be observed in the spectra of the high loading samples: a small shoulder for **M7-2** and a more pronounced shoulder for **M7-3** at 388 nm, instead of the shoulder of precursor **7** at 511 nm (Table 7). This emission result is either caused by conformational biases as a consequence of restricted molecular rotation and relaxation inside the pores or by population of a TICT (twisted intramolecular charge transfer) states<sup>173</sup>. The twisted intramolecular charge transfer in some case is very sensitive to the microenvironment and in particular on its polarity<sup>173</sup>. Thus, we propose that the silanol groups on the surface of materials should also play an important role for such TICT states.



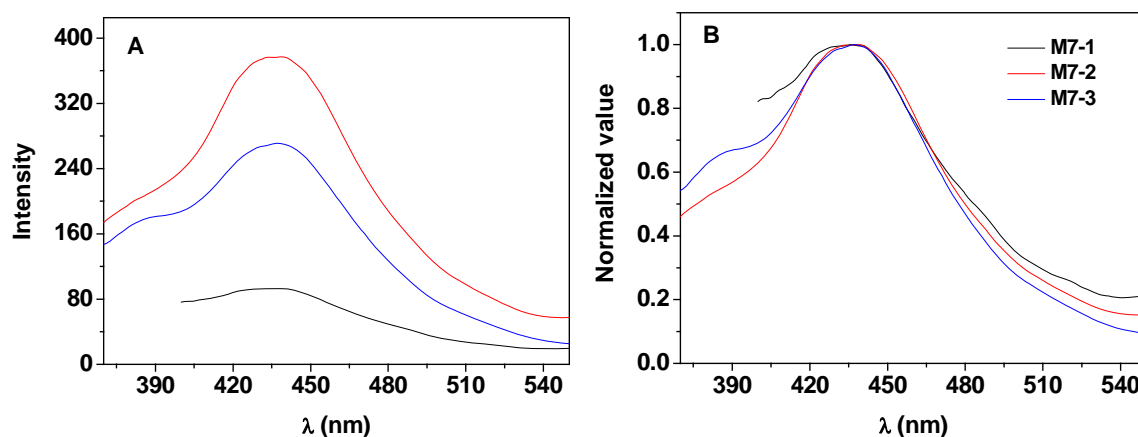
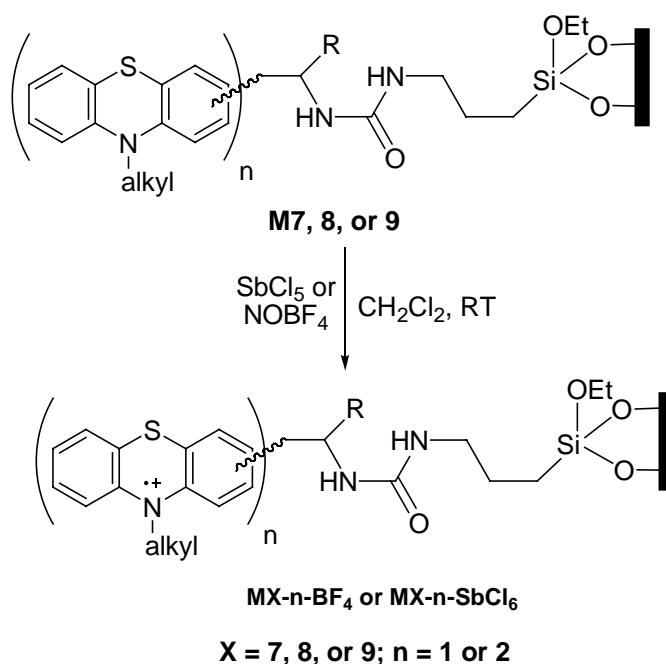


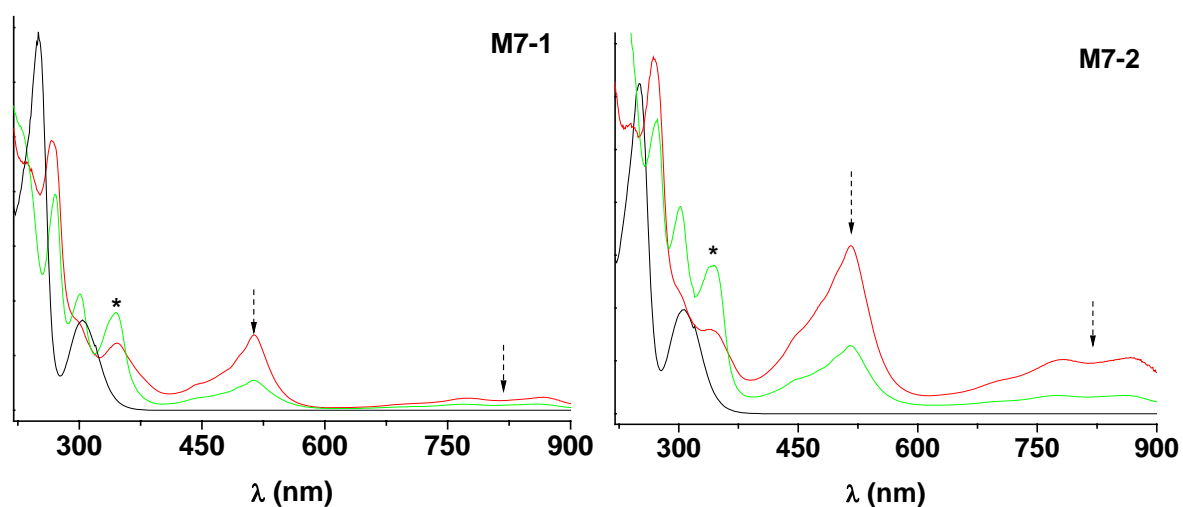
Figure 57. (A) The emission spectra of **M7**, and (B) normalized emission spectra of **M7**.

The materials undergo the formation of surface bound radical cations when treated with oxidizing agents (Scheme 15). Here oxidation was carried out with the one-electron acceptors antimony pentachloride or  $\text{NOBF}_4$  in dichloromethane suspension, leaving  $\text{SbCl}_6^-$  or  $\text{BF}_4^-$  as the counter ions. For the materials **M7**, functionalized with monophenothiazine a color change to red was observed during the oxidation reaction (Figure 55, picture in the bottom section). This color change is manifested by an absorption band at around 515 nm, which is typical for a phenothiazine radical cation (Figure 55 red lines and green lines). Additionally, a broad absorption band in the visible-NIR region can be observed for all materials and this band becomes more significant by increasing the concentration of phenothiazine. Such a near-IR band has often been associated with a charge resonance transition of cofacially oriented aromatic donor/acceptor dyads<sup>229-231</sup>. It is also well known that the electron can be transferred between the free phenothiazine donor and its cation radical<sup>112</sup>. Furthermore, this kind of broad band is absent in the mono-phenothiazine modified mesoporous materials, obtained by the post grafting method (see Chapter 2, section 2.1). The co-condensation method can provide a high concentration of phenothiazine in the material, which are just located inside the pore channels, as well as a uniform distribution. The considerable structural change from a butterfly conformation of the native neutral form to a planarized radical cation affords a vast opportunity to form intermolecular interactions of the native and the oxidized moieties within

the pores. Thus, we assign this broad band to intermolecular charge transfer bands (CT). Moreover, an increase of phenothiazine loading improves the intensity of this band, which further proves that this band is raised by intermolecular charge transfer. This result demonstrates that the co-condensation method is an appropriated way to achieve the intervention of strongly coupled complexes. Additionally, the ordered mesoporous material with a narrow pore size distribution is a proper substrate to confine the phenothiazine molecules in a beneficial orientation.



Scheme 15. Oxidation of mesoporous phenothiazinyl hybrid materials.



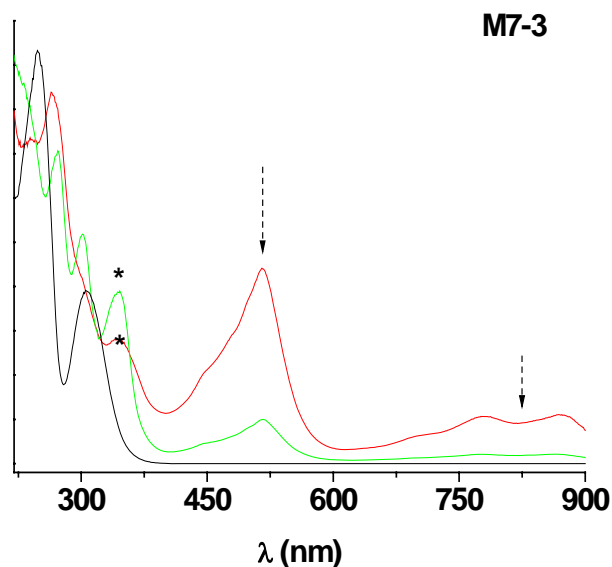


Figure 58. UV-Vis spectra of the hybrid mesoporous materials **M7-1**, **M7-2**, **M7-3** (black lines), the absorptions of the corresponding freshly synthesized radical cationic samples **M7-1-SbCl<sub>6</sub>**, **M7-2-SbCl<sub>6</sub>**, **M7-3-SbCl<sub>6</sub>** (red lines), and the radical cationic samples after three days exposed to air (green lines).

It is worth to mention that the resulting deeply colored materials containing phenothiazine radical cation preserve their color under ambient temperature for weeks when stored under an atmosphere of nitrogen. Thus, the radical cations in these mesoporous structured hybrid materials are very stable. By exposing these materials to air at room temperature for three days, the color fades to pink. The absorption spectra of these exposed materials are shown in Figure 58, as green lines. It can be seen that the typical absorption of the phenothiazine radical cation is still persevered for all samples, but with a decrease in intensity. Compared to the freshly generated materials (red lines) and the neutral materials (black lines), there is an intense peak at 344 nm, which can be observed for the exposed sample, and which might be associated with a new compound obtained from a phenothiazine radical cation consuming reaction. Meanwhile, the CT band also significantly decreases, this is further proves that the presence of radical cations is essential for the charge transfer.

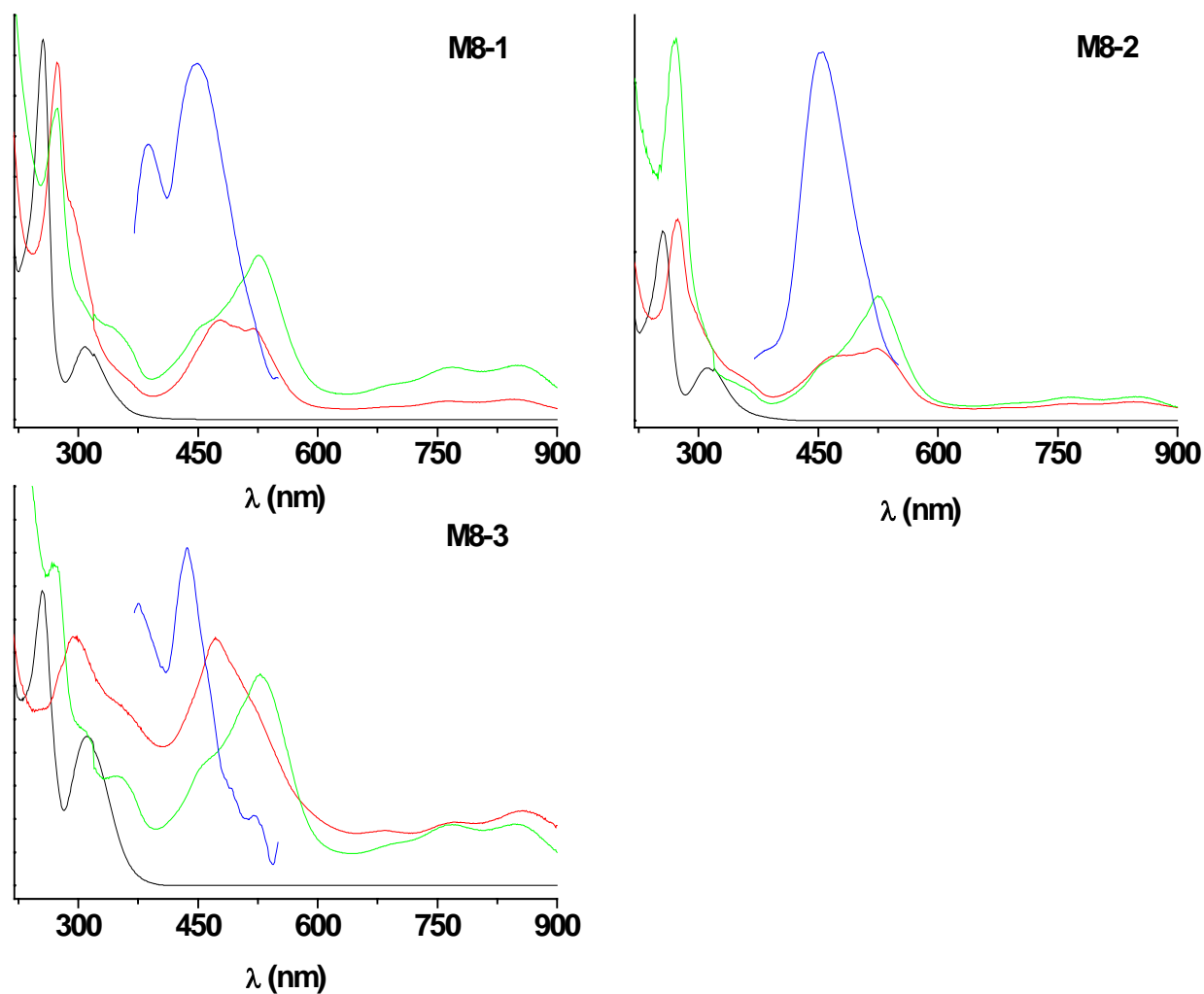


Figure 59. UV-Vis spectra of the hybrid mesoporous materials **M8-1**, **M8-2**, **M8-3** (black lines), the absorptions of the corresponding radical cationic samples **M8-1-BF<sub>4</sub>**, **M8-2-BF<sub>4</sub>**, **M8-3-BF<sub>4</sub>** (red lines), **M8-1-SbCl<sub>6</sub>**, **M8-2-SbCl<sub>6</sub>**, **M8-3-SbCl<sub>6</sub>** (green lines), and the emission spectra of the modified samples **M8-1**, **M8-2**, **M8-3** (blue lines).

The same experiments were carried out to investigate the properties of the hybrid material **M8** (Figure 59). The absorption of these hybrid materials are similar to precursor **8**, showing two bands with maxima at  $\sim 255$  nm and  $\sim 310$  nm. Similar to **M7**, the samples **M8** also present a slight blue shift compared to the corresponding organic compound **8**. From Figure 60, we can see that the intensity of the band at  $\sim 310$  nm is gradually increased by increasing the amount of phenothiazine in the materials. The inset graphic shows that the normalized

spectrum present no position shifting by change of the concentration of organic groups, but the peaks are slightly broadened, which is also similar to the data of **M7**.

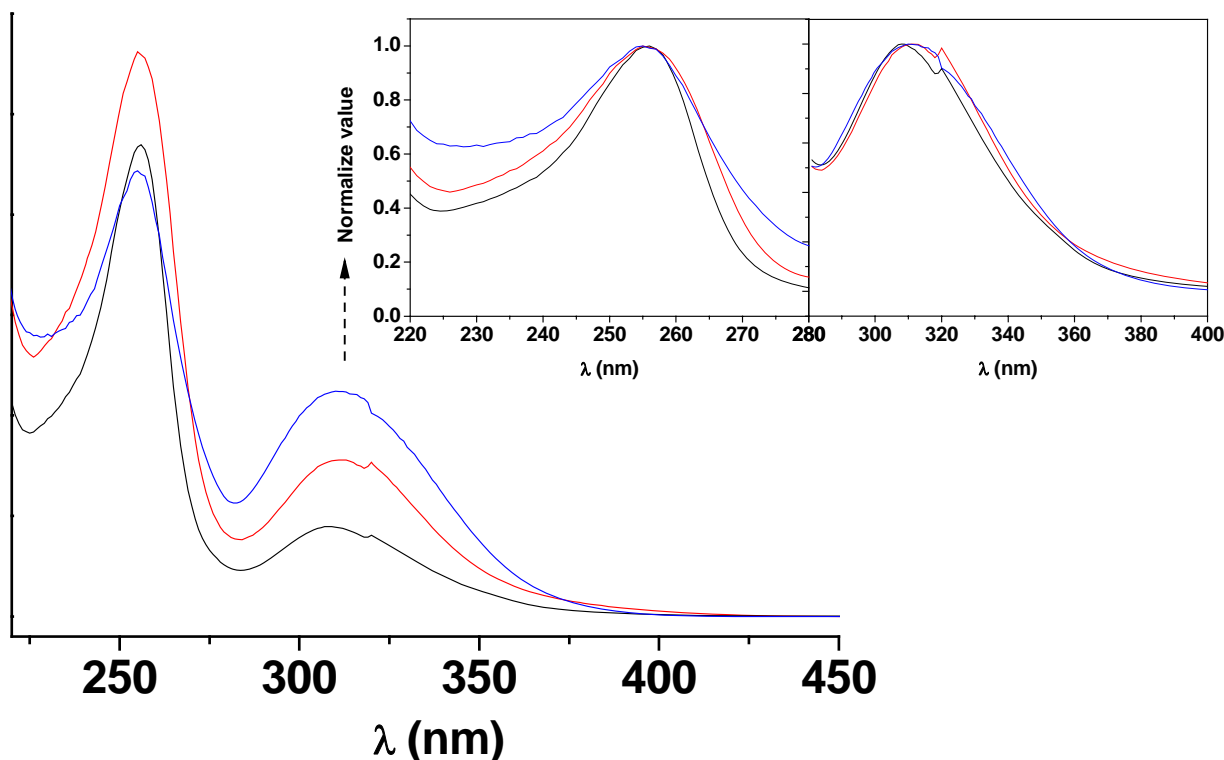


Figure 60. UV-Vis spectra of the hybrid mesoporous materials **M8-1** (black curve), **M8-2** (red curve), and **M8-3** (blue curve). The inset graphic shows the normalized absorptions of **M8** for comparison.

In the emission spectra of the hybrid materials **M8**, once again a blue shift of the peak maximum can be observed compared to the organic precursor. Especially, the sample **M8-3** with the highest loading of phenothiazine (0.54 mmol/g) shows a 23 nm shift to higher energy, with a Stokes-shift of  $9930\text{ cm}^{-1}$ . Detailed observation of these three samples in the normalized spectrum (Figure 61) show that **M8-2** (0.40 mmol/g) has the narrowest single emission band with the lowest emission energy and a Stokes-shift of  $10220\text{ cm}^{-1}$ , while, **M8-1** (0.26 mmol/g) has a dual emission spectrum with a quite remarkable Stokes-shift of  $10250\text{ cm}^{-1}$ , and **M8-3** has the shortest wavelength of emission. Compared to **M7**, **M8** show a larger variation of the emission by changing the concentration of phenothiazine in the materials.

This result must have some relation to the differences of the molecular structures. The molecular size as well as the hexyl chain should influence the emission, similar to their influence on the structure of the materials which also might feedback to the emission properties.

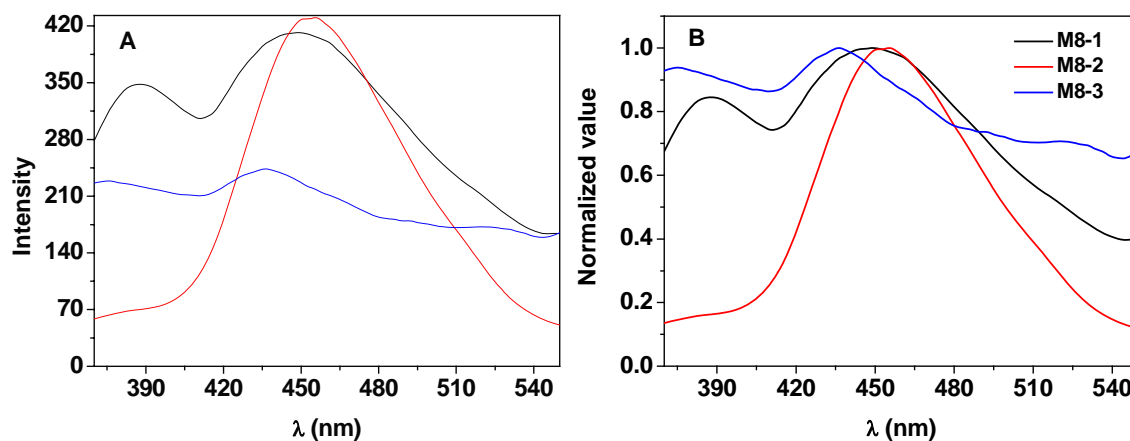


Figure 61. (A) The emission spectra of **M8**, and (B) normalized emission spectra of **M8**.

Again this group of materials was treated with one electron-accepter agents (Figure 59, for  $\text{NOBF}_4$  presenting the red lines, and for  $\text{SbCl}_6$  presenting the green lines). A color change to red can be observed as soon as the oxidizing agents are added, which is corroborated by the typical absorption band of the phenothiazine radical cation at around 520 nm. In the case of  $\text{NOBF}_4$  oxidized samples, the peak centers turn to shift to higher energies, especially, for the high loading sample **M8-3**. The charge transfer band in the near-IR can be observed for all the oxidized samples, and the intensity of this band increases by increasing the amount of phenothiazine.

The optical investigation of the biphenothiazine containing hybrid materials **M9** is illustrated in Figure 62. The absorption spectra of these two samples present two broad bands at ~268 and ~325 nm. Compared to the absorption of the mono-phenothiazine functionalized hybrid materials (**M7** and **M8**), both bands are red shifted, which is attributed to the conjugation of two phenothiazine cores. These two samples show quite similar spectra (see Figure 63). The normalized spectra are shown in the inset of Figure 63. No change of the peak

position can be observed, but a slight broadening of the bands is observed in the spectrum of the high loading sample.

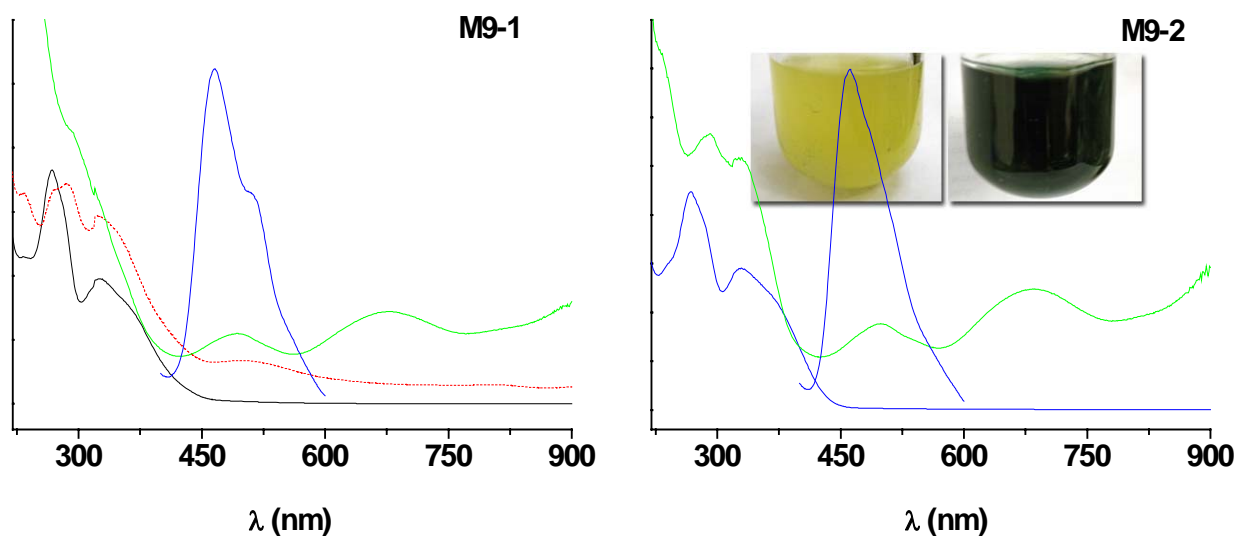


Figure 62. UV-Vis spectra of the hybrid mesoporous materials **M9-1**, and **M9-2** (black curves), **M9-1-SbCl<sub>6</sub>**, and **M9-2-SbCl<sub>6</sub>** (green curves), and the emission spectrum of the modified samples **M9-1**, and **M9-2** (blue curves). The inset picture demonstrates the color change caused by the oxidation of **M9-2** using **SbCl<sub>5</sub>**.

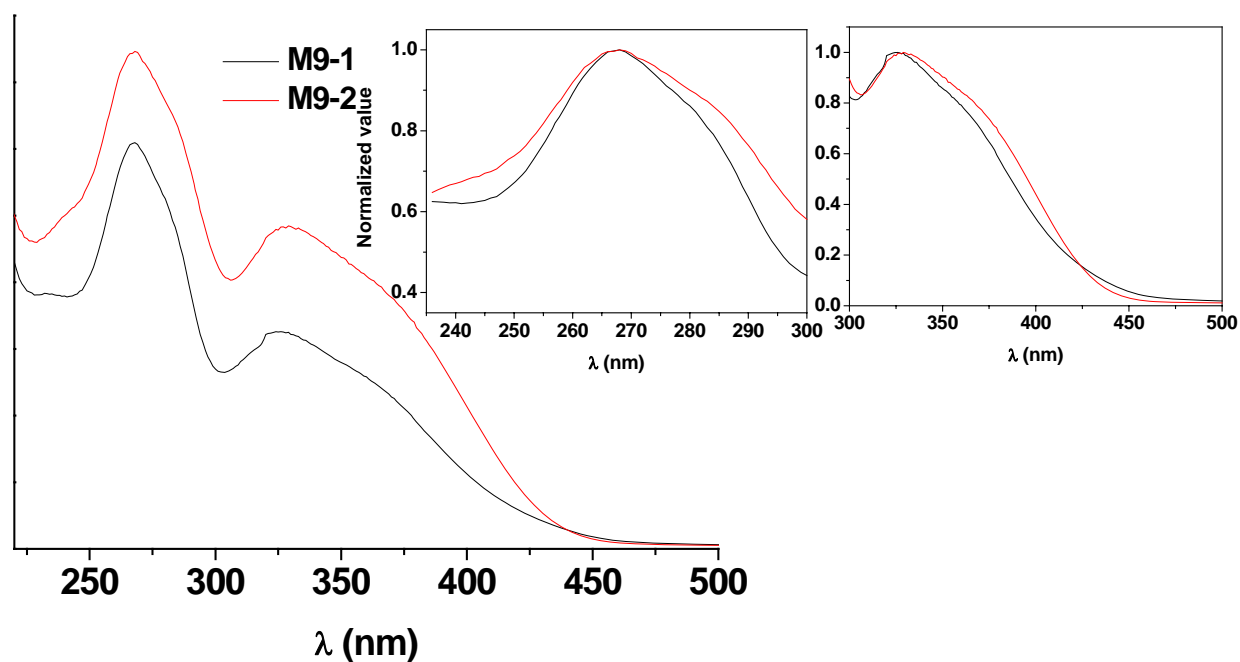


Figure 63. UV-Vis spectra of the hybrid mesoporous materials **M9-1** (black curve), and **M9-2** (red curve). The inset graphic shows the normalized absorptions of **M9** for better comparison.

The emission spectra of **M9-1** and **M9-2** are presented in Figure 62 as blue lines, a more detailed presentation is given in Figure 64. The peak maximum of **M9-2** (461 nm) is slightly blue shifted compared to the position of **M9-1** (467 nm). Additionally, **M9-1** has a more apparent shoulder at 512 nm.

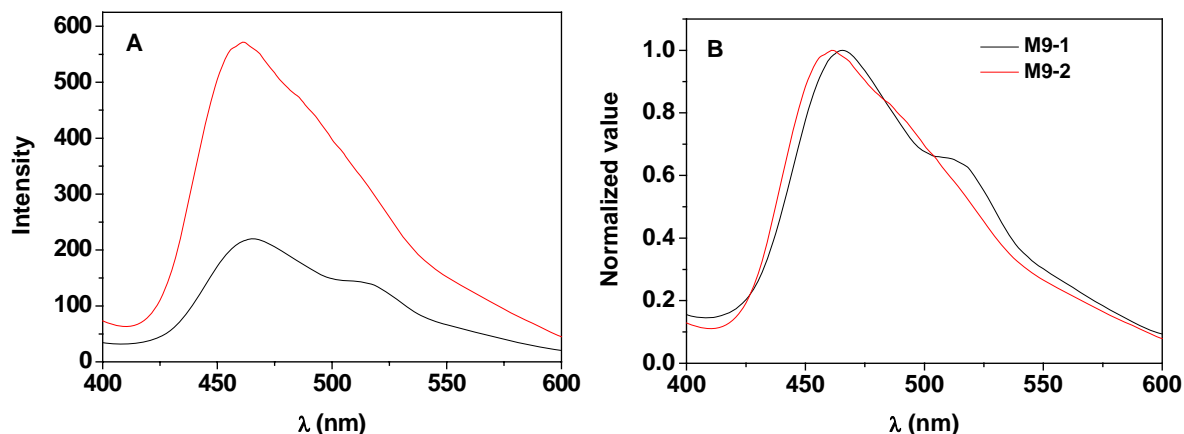


Figure 64. (A) The emission spectra of **M9**, and (B) normalized emission spectra of **M9**.

These two samples also underwent treatment with oxidizing agent. The absorption spectrum of the radical cation carrying materials, obtained by treatment with  $\text{SbCl}_5$ , are presented in Figure 62 as green lines. Oxidation of these two biphenothiazine functionalized materials with the strong oxidant  $\text{SbCl}_5$  furnished dark greenish products with absorption spectra, which are different to those of the mono-phenothiazine radical cations discussed before. This result indicates the presence of dicationic specimen as a consequence of the oxidation of biphenothiazines<sup>112, 176</sup>. Therefore, the broad absorption band in the visible-NIR region can be partially assigned to an intramolecular charge transfer band, and partly to an intermolecular charge transfer band. From the magnified spectrum of these two radical cation containing materials (Figure 65), the enhancement of charge transfer bands and the coincidence of a red shift of the absorption can be observed by an increase of phenothiazine loading.



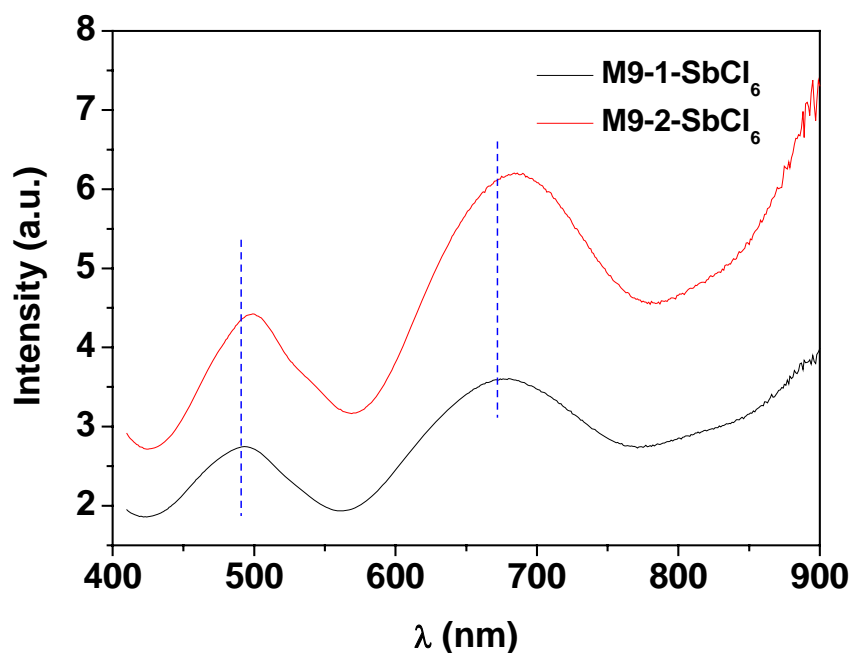


Figure 65. Magnified spectra of the radical cationic samples of **M9** (oxidized by  $\text{SbCl}_5$ ).

The radical cation of **M9** is stable too. The deep dark color is preserved for weeks if the material is stored under nitrogen. Exposing **M9-2-SbCl<sub>6</sub>** materials to the air at room temperature for 3 days, a color fade can be observed. Simultaneously, a strong absorption at 344 nm appears (Figure 66, green line). This is similar to the mono-phenothiazine samples. Compared to the spectrum of the fresh radical cation samples (Figure 66, red line), the bands located in the visible-NIR region is almost vanished, so as the absorption at  $\sim 500$  nm is significantly decreased.

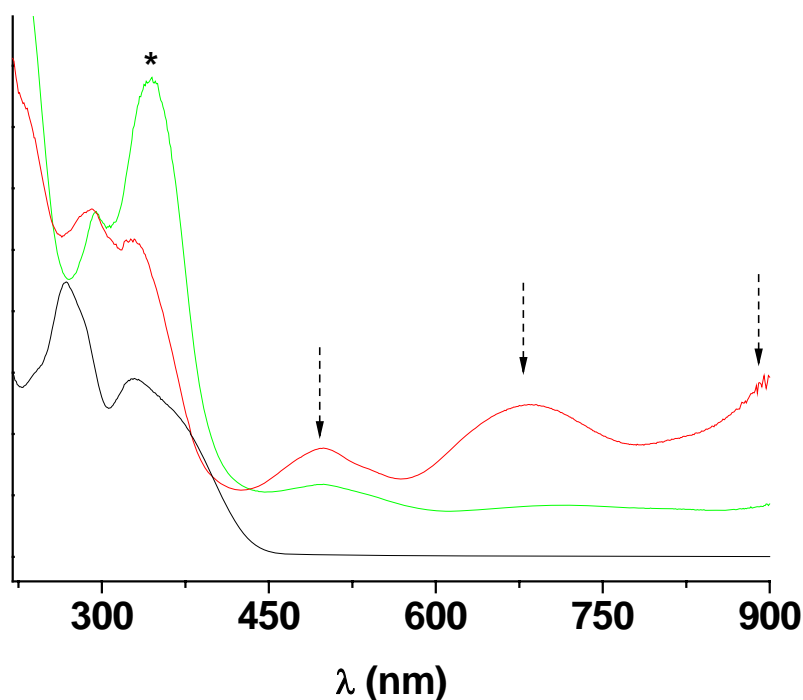


Figure 66. UV-Vis spectrum of hybrid mesoporous material **M9-2** (black line), the absorptions of the corresponding fresh radical cationic sample **M9-2-SbCl<sub>6</sub>** (red line), and of the radical cationic sample exposed to the air after three days (green line).

An interesting phenomenon occurs when **M9** is treated with the relatively weak oxidant  $\text{NOBF}_4$ . Addition of  $\text{NOBF}_4$  makes the suspension change its color from yellow to dark green. However, after removing the solvent, the greenish powder is not as dark as **M9-1-SbCl<sub>6</sub>** and shows a different adsorption spectrum (Figure 67, red line). A significant absorption band at 355 nm appears. Normally, the biphenothiazine radical cation should be more stable than the mono phenothiazine radical. But a reaction occurs, wherein the biphenothiazine radical cation is involved. We presumed that the reaction might have some relations to the silanol groups on the silica surface. Thus a capping silanol process was carried out for **M9-1** by using the hexamethyldisilazane as silylating agent. The silylated **M9-1-Si** presents a spectrum similar to the original **M9-1** (Figure 67, black line and blue line). This indicates that the further modification has no influence on the phenothiazine molecule. In the oxidation process of **M9-1-Si** by addition of  $\text{NOBF}_4$ , the suspension first changes its color to

slightly red, then light green, and finally a yellow greenish powder is obtained. By exposing this oxidized sample to the air, the color fades to yellow immediately (inset graph of Figure 67). The absorption spectrum of this sample is shown in Figure 67 (purple line). It presents a single band at 376 nm and a totally straight line in the region of visible-NIR. It seems that the capping of the silanol groups is not beneficial for the radical cation stabilization, but speeds up the radical cation consuming reaction. This proves that the surface silanol groups can stabilize the phenothiazine radical cation in some extent. This result is in agreement with the work of Kevan's group<sup>120,232</sup>, who suggested that the silica network might act as an electron acceptor for the formation of stable physisorbed phenothiazine radical cations in porous silica materials. Using  $\text{SbCl}_5$  as the oxidant for **M9-1-Si**, a dark green powder can be achieved (inset graph of Figure 67) with similar spectrum to the corresponding **M9-1-SbCl<sub>5</sub>** material. Combining these opposite results, it seems that the counter ion or the redox potential of the oxidizing agent also has a strong influence on the stability of phenothiazine radical cation in this biphenothiazine modified material.

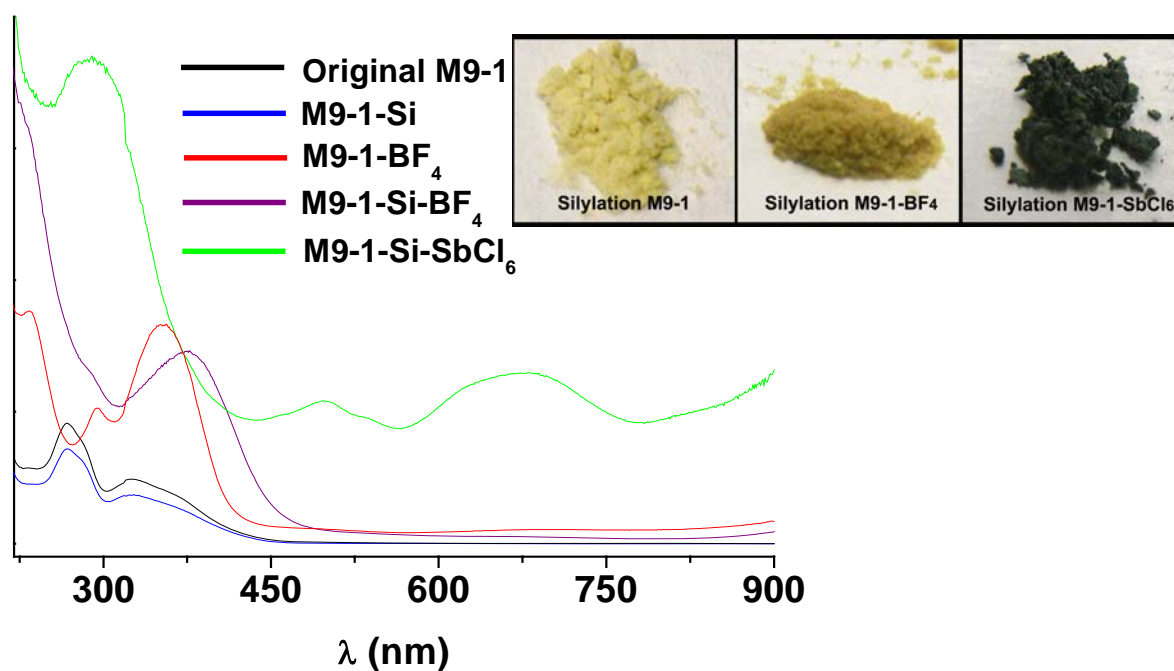


Figure 67. The absorption spectra of original **M9-1**, silylation **M9-1-Si** and their corresponding oxidized materials.

The substantial Stokes shifts in the phenothiazine system is attributed to significant geometrical changes occurring upon excitation from a highly nonplanar ground state to a largely planarized excited state. As a result, the Stokes shifts decrease with the extension of the conjugated systems<sup>228</sup>. Thus in Figure 68 a series of plots of the density of phenothiazine molecules versus the Stokes shifts are illustrated for the three groups of hybrid materials. The Stokes shifts decrease by increasing densities of phenothiazine in **M8** and **M9**. This indicates that with a higher loading of phenothiazine and thus a higher crowding of the pores, the excitation is facilitated. This is especially significant for **M9**. In the case of **M7**, a decrease of Stokes shifts is present from **M7-1** (0.33 mol/g) to **M7-2** (0.54 mmol/g), while, on the contrary, an increase can be observed for **M7-3** (0.77 mmol/g). As discussed in the section 2.2.4, the molecular structure has important influence on the structure of hybrid materials in the co-condensation synthesis system. The structure of precursor **7** is not as advantageous as **8** to cooperate with the template for the formation of regular micelles. Thus, the decrease of steric strain should be due to the relative high disorder of hybrid material **M7-3** with such a high loading of **7**.

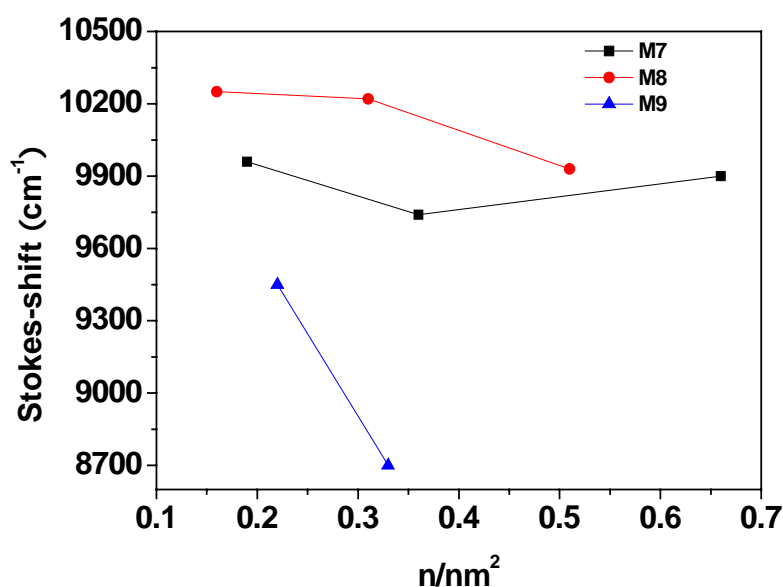


Figure 68. Correlation of the Stokes-shifts and the densities of phenothiazine molecules in the channels of the hybrid materials.

## EPR measurements

Electron paramagnetic resonance (EPR) was used to additionally confirm the existence of the stable phenothiazine radical cations in the hybrid materials. The EPR spectrum of **M9-3-SbCl<sub>5</sub>** is exemplarily shown in Figure 69. It reveals a g-value of 2.0053 as a characteristic property of a phenothiazine radical cation. Since the EPR signal is not well resolved, hyperfine coupling constants and anisotropic g-tensors cannot be determined. However, the high symmetry of the EPR spectrum indicates that the phenothiazine radicals are in a quit isotropic environment in the hybrid materials.

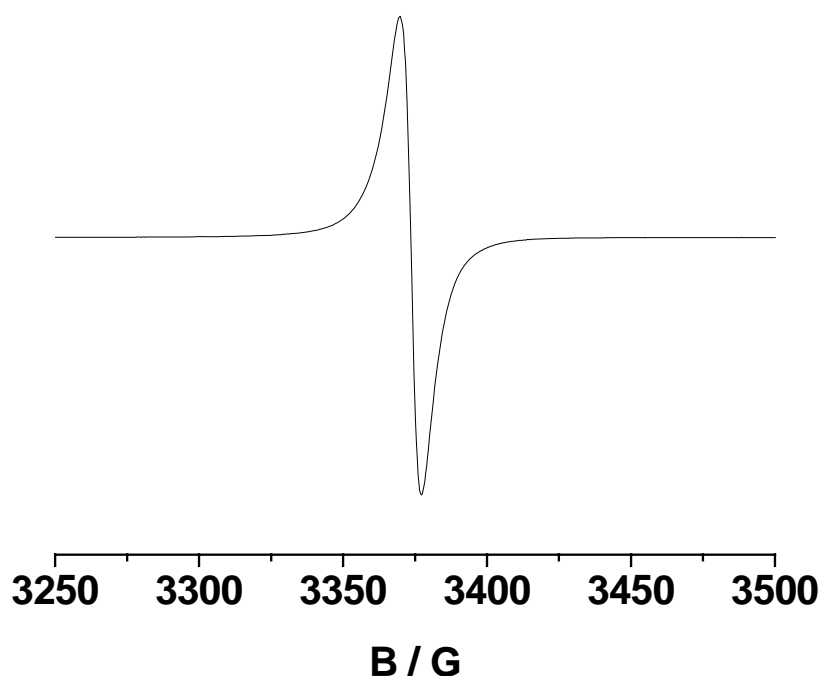


Figure 69. Q-band EPR spectrum of **M9-3-SbCl<sub>6</sub>** at 297 °C.

## **2.3 Synthesis and characterization of triazole-linked (oligo)phenothiazines in mesoporous silica materials obtained by an in-situ one pot method**

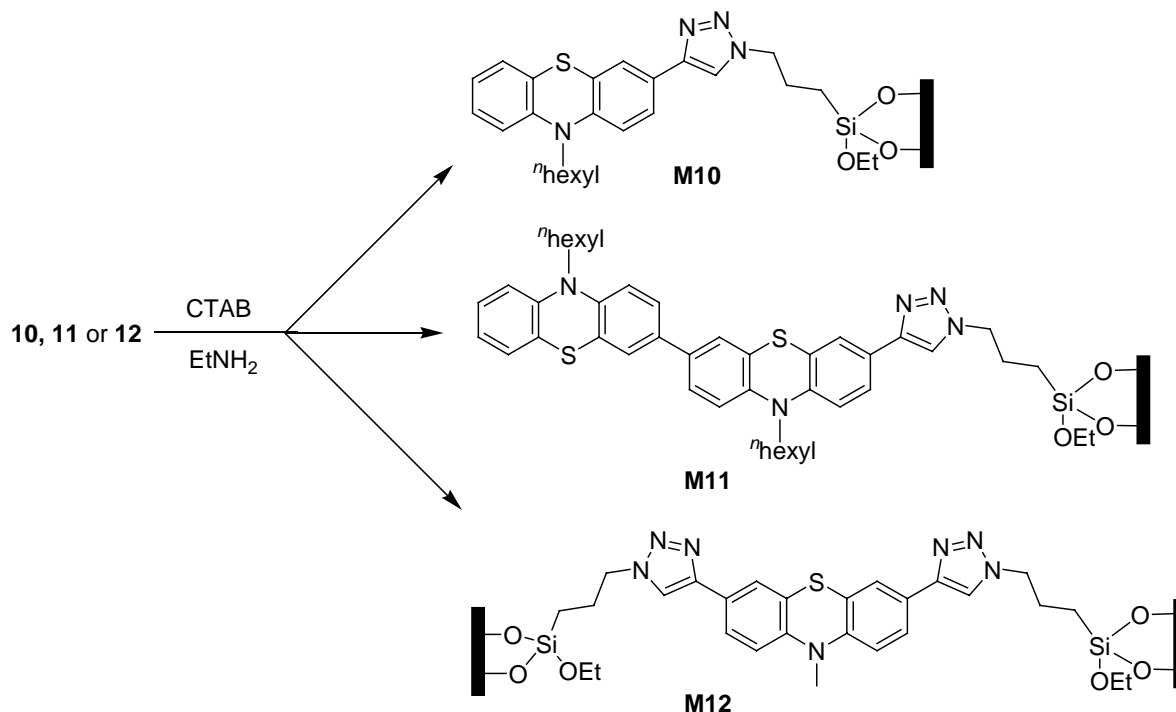
### **State of the art**

At the beginning of this section, a novel branch in the hybrid order mesoporous materials, which was developed in very recent years, has to be mentioned. It is periodic mesoporous organosilicas (PMOs) in which the organic fragments are located within the framework<sup>63, 233, 234</sup>. In general, such materials are formed by the hydrolysis and polycondensation of bis(trialkoxysilyl) organic precursors in the presence of a surfactant template. This results in a material containing the organic fragment, intergrated in the silica framework by means of two terminal silyl groups. An important feature of this framework modified ordered mesoporous materials is a regular distribution of the organic moieties within the framework. This effect is probably due to the limited thickness of wall of the materials combined with the interaction of guest molecules<sup>235</sup>. In some cases, a crystal type framework with periodically arranged organic fragments can be obtained<sup>65</sup>. Such syntheses are perfect models for us to array the phenothiazine molecules, similar to a 'crystal' hybrid material. Thus we introduced a phenothiazine bearing two triazole groups as linkers (precursor **12**) into MCM-41 type PMOs. The aim is to study the possibility of an ordered arrangement of this type of organic moiety supported by the confinement of a preordered mesoporous framework. Additionally, compared to a simple anchoring of the organic moiety, which mainly exists at the pore's surface, use of a bridging organosilane is an alternative. The main advantage is that the organic group resides in a confined geometry in the pore wall of a high surface area material, and hardly causes a steric hindrance to further introduction of other guest molecules<sup>236</sup>, such as electron acceptor molecule in our case.

### 2.3.1 Synthesis of hybrid mesoporous materials

The organic precursors of **10**, **11**, and **12** were synthesized by A. W. Franz, our partner from the group of Prof. T. J. J. Müller. The hybrid materials were prepared as outlined in Scheme 16. To continue the concept of introducing a large amount of uniformly distributed phenothiazines into the ordered mesoporous materials, as well as for comparison with the other materials reported in this thesis, a similar in-situ process as mentioned in the last section was performed for the synthesis of this series of hybrid materials. CTAB as the template defines the size of the pores, which is normally located in the range of 2 to 3 nm by the procedure of our synthesis. This size is the critical size of modified phenothiazine molecules. The aim of this limitation is to confine the molecules for the formation of oriented phenothiazines inside the channels. To achieve a uniform distribution of organic moieties, a proper organic solvent had to be chosen, which not only can dissolve the precursor very well, but also will not disturb the ordering of the micelles. As mentioned in the last section, methanol as a favorite cosolvent had been used to increase the degree of ordering of the mesostructure<sup>182</sup>. Thus we preserved it for the synthesis of the triazole linked phenothiazine hybrid mesoporous materials. However, another cosolvent had to be used to dissolve precursors **11** and **12**, due their poor solubility in methanol or in TEOS. It turned out that tetrahydrofuran was an appropriate choice, which excellently dissolved the precursors, and caused no phase separation when added to a mixture of methanol and TEOS. Additionally, a small amount of THF will not change the diameter of the micelles, due to the small hydrophobic part of the solvent. Additionally, THF is not sufficiently bipolar to fully enter the hydrophobic-hydrophilic bi-layer region, which would decrease the curvature of surface<sup>6</sup>. In some case it was reported that THF can be used as the major solvent for the formation of ordered mesoporous thin films by the EISA method<sup>237</sup>. Thus this new cosolvent provided us highly ordered mesoporous materials with homogeneous organic modification. The

introduction of (oligo)phenothiazine triazoles (**10**, **11**, and **12**) dyes the materials with a bright yellow color. The structure and the optical properties of these hybrid materials were systematically investigated.



Scheme 16. Synthesis of the mesoporous hybrid materials **M10**, **M11**, and **M12** by the in-situ synthesis method with CTAB as the template.

### 2.3.2 Structural properties of the mesoporous materials

#### Powder X-ray diffraction

Powder X-ray diffraction as a routine method to characterize the ordering of the mesostructure was carried out for all these hybrid materials. The pattern of **M10** is presented in Figure 70. The reflection of the 100 plane of hexagonal symmetry is located at  $2\theta = 2.1^\circ$ , which corresponds to a *d*-value of 4.20 nm. Additionally, an overlapping broad band can be observed in the  $2\theta$  range of  $3.4\text{--}4.8^\circ$ , which should be the diffraction of the 110 and 200 planes of the hexagonally symmetric lattice of the MCM-41 type materials<sup>7</sup>. This result demonstrates the presence of a periodic arrangement of pores in the materials, though the



sharpness of the diffraction peaks not very high. The broadened signals are due to the large amount of **10** that was incorporated inside the pores of this material (0.70 mmol/g, 30.4 wt%), which decreases the contrast density between the framework and the pore channels<sup>60, 163</sup>. Simultaneously, the flexibility of the large molecule **10** implies a strong strain on the cylindrical channels<sup>238</sup>. Therefore, the structure distortion is reflected by a decreased intensity and a broadening of the diffraction peaks. A decrease of the cell parameter  $a_0 = 4.85$  nm can be observed compared to the  $a_0 = 4.96$  nm of pure silica MCM-41 (section 2.2.3, Table 5). This phenomenon may also be explained by the large amount of **10** involved in the co-condensation synthesis, and the large size of the phenothiazine with the triazole head group, that will disturb the inorganic silica species to fully cover the surfactant micelles. Thus after hydrothermal hydrolysis and condensation of the silica species, a shrunken lattice value can be observed.

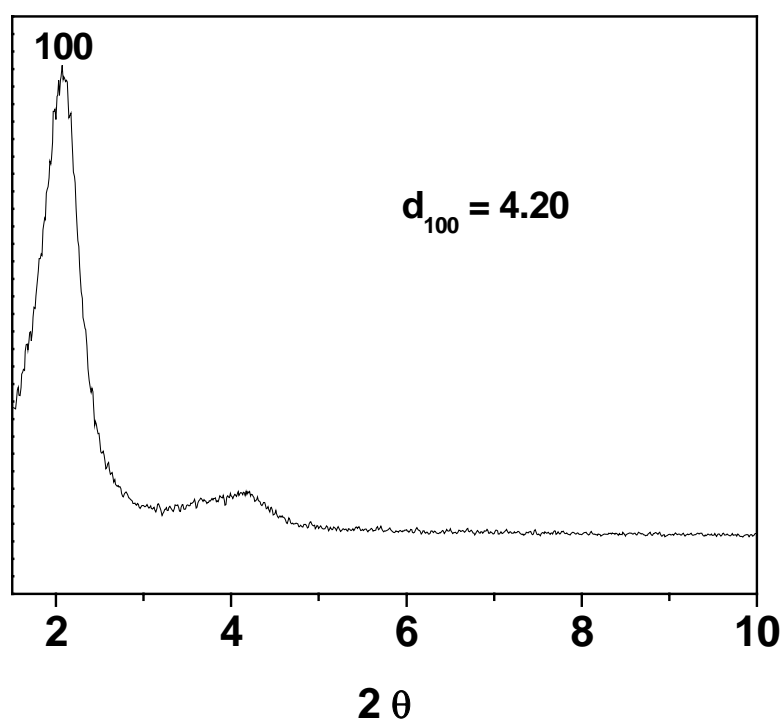
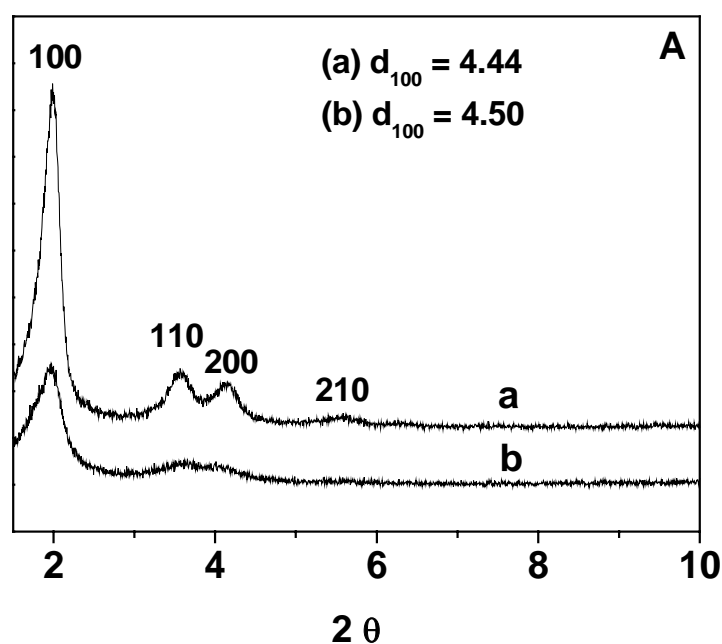


Figure 70. Powder XRD pattern of **M10**.

Figure 71 shows the powder XRD data of **M11-1** and **M11-2**, with different amounts of biphenothiazine **11** in the materials. The sample **M11-1** with a loading of 0.28 mmol/g of

biphenothiazine presents four typical distinguished Bragg diffraction peaks, which belong to the 100, 110, 200 and 210 planes. This series of peaks can be indexed to a two-dimensional hexagonal  $p6mm$  symmetry, which is similar to the pattern of ordered MCM-41, indicating a highly long-range ordered mesoporous structure. The  $d_{100}$  and  $a_0$  values of **M11-1** (4.44 nm and 5.13 nm) are larger than the  $d_{100}$  and  $a_0$  values of MCM-41 (4.30 nm and 4.96 nm). By increasing the loading of **11** to 0.43 mmol/g, hybrid material **M11-2** is obtained. The XRD pattern of this sample (Figure 71 b) shows a relatively broad diffraction peak of 100 plane with low intensity, and an overlapping band around  $2\theta = 4^\circ$  that can be assigned to the 110 and 200 plane. The apparent reduction in diffraction intensity and increase in peak width are often observed phenomena, which are due to the presence of a large amount of organic species inside the pore. These large size organic molecules either distort the pore structure, or decrease the contrast matching between framework and channel. Additionally, the peaks of **M11-2** are shifted to lower angle (diffraction of 100 phase) compared to **M11-1**, which corresponds to a larger  $d_{100}$  (4.50 nm) and a larger  $a_0$  (5.20 nm). This also might be due to the increased amount of the organic precursor **11** in the synthetic mixture. The extended size of the micelle attributes to a large unit cell value.



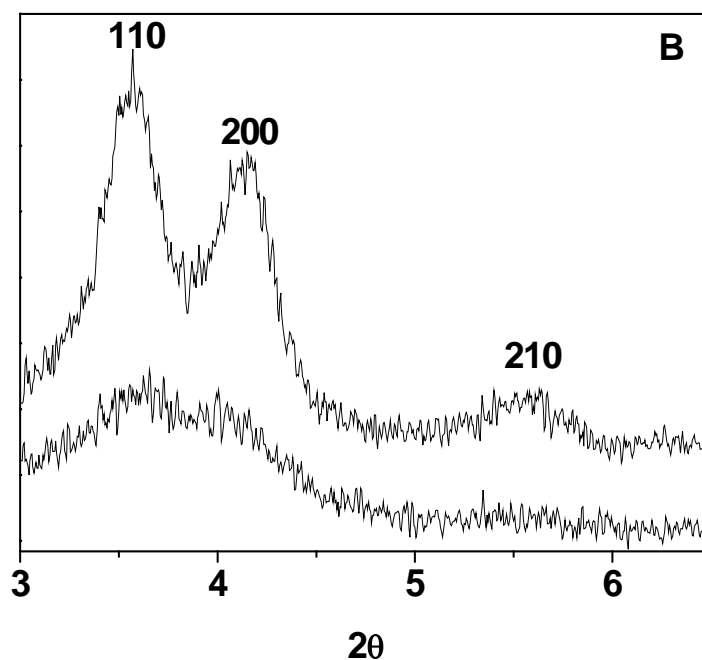


Figure 71. A: Powder XRD pattern of (a) **M11-1** and (b) **M11-2**; B: magnified signals at higher angle of these two samples.

The periodic structure of the template free mesoporous solid **M12**, obtained from a template supported co-condensation of the bridged organosilsesquioxane precursor **12** with TEOS, was determined by powder X-ray diffraction. The pattern is shown in Figure 72. It presents a Bragg reflection at about  $2\theta = 2^\circ$ , which confirms the formation of an ordered mesoporous structure with an interplanar  $d$  spacing of 4.48 nm and approximately uniform pore sizes. An overlapping and indistinct reflection in the low-angle region can be observed, indicating limited periodicity in the long-range order of the mesoporous system. This type of diffraction is similar to the mesostructure of the material with a wormhole-like pore system (or HMS silica phases)<sup>25</sup>. The decrease of periodicity in this solids was most likely due to the size and the geometry of the precursor **12**, which perturbs the micelles in the original sol. Hence, a disturbed crystallization process of the inorganic species is anticipated cycling with the less ordered micelles to obtain less ordered mesoporous material.

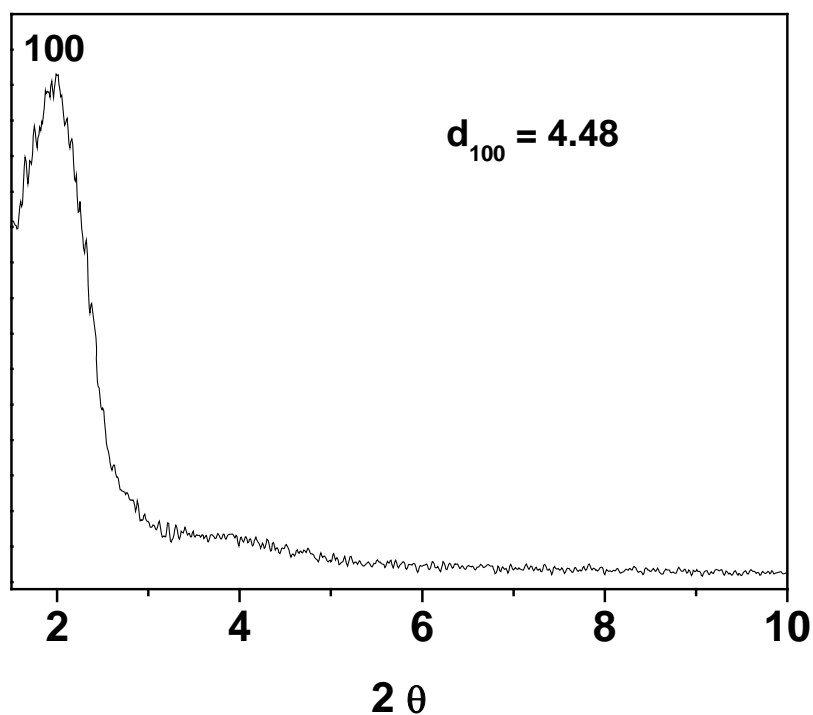


Figure 72. Powder XRD pattern of **M12**

#### N<sub>2</sub> adsorption and desorption

Nitrogen physisorption measurements were carried out for the determination of the pore structure and the surface parameters of these hybrid materials. The isotherms and the pore distribution curves are presented in the following figures and the corresponding textural parameters are collected in Table 8.

Figure 73 A shows the N<sub>2</sub> adsorption-desorption isotherm of **M10**, the profile of this isotherm corresponds to a type-IV isotherm, according to IUPAC nomenclature<sup>192</sup>, indicating the mesoporous property of this hybrid material. Furthermore, a sharp capillary condensation implies a quite uniform porous material, which is confirmed by the pore size distribution curve shown in Figure 73 B. From the desorption branch of the isotherm, a mean pore size of 2.36 nm was estimated by the BJH method combining with a specific surface area 536 m<sup>2</sup>/g, calculated by the BET method, this indicates the basic characteristics of the ordered mesoporous material. An apparent H4 type of hysteresis loop on the high pressure portion of isotherm can be indexed to uniform slit-shaped pores, which may be due to aggregates of

small particles or to connections between cylindrical channels<sup>166, 193</sup>. This hysteresis loop is corresponding to the small peak around 3.80 nm in the pore size distribution curve (Figure 73 B).

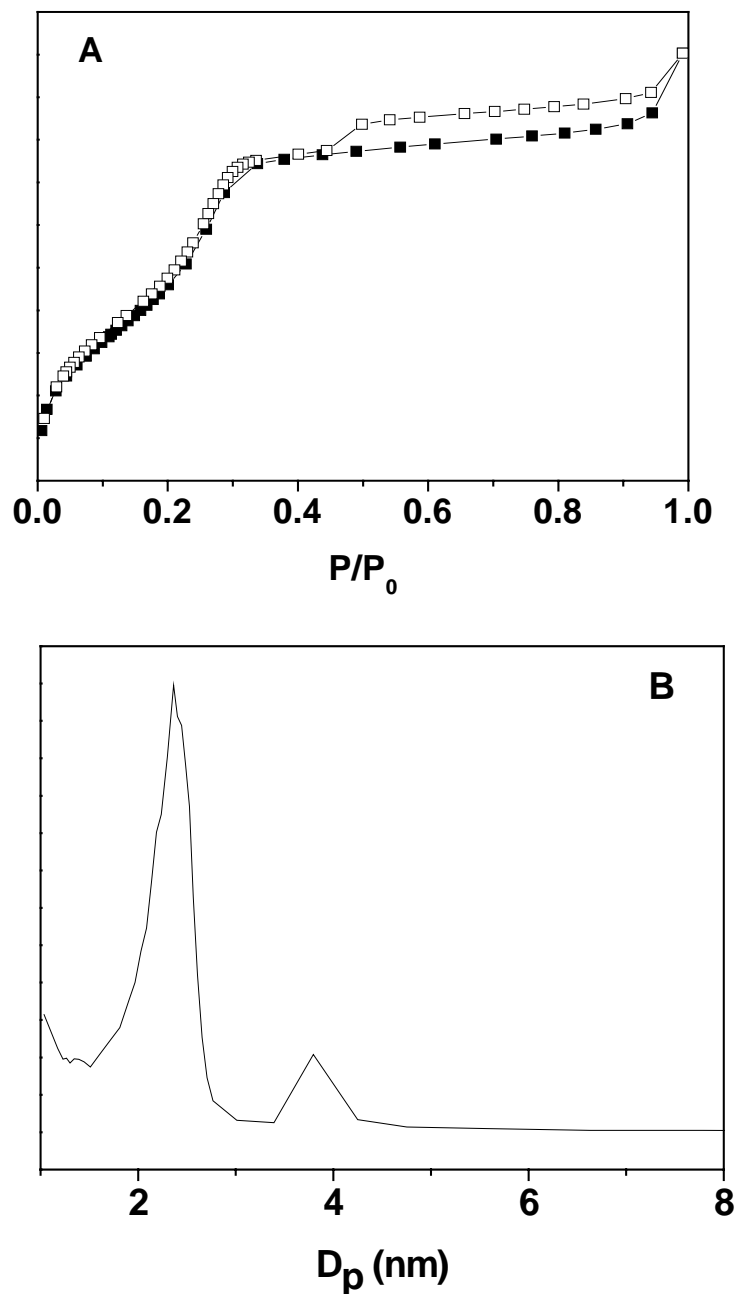
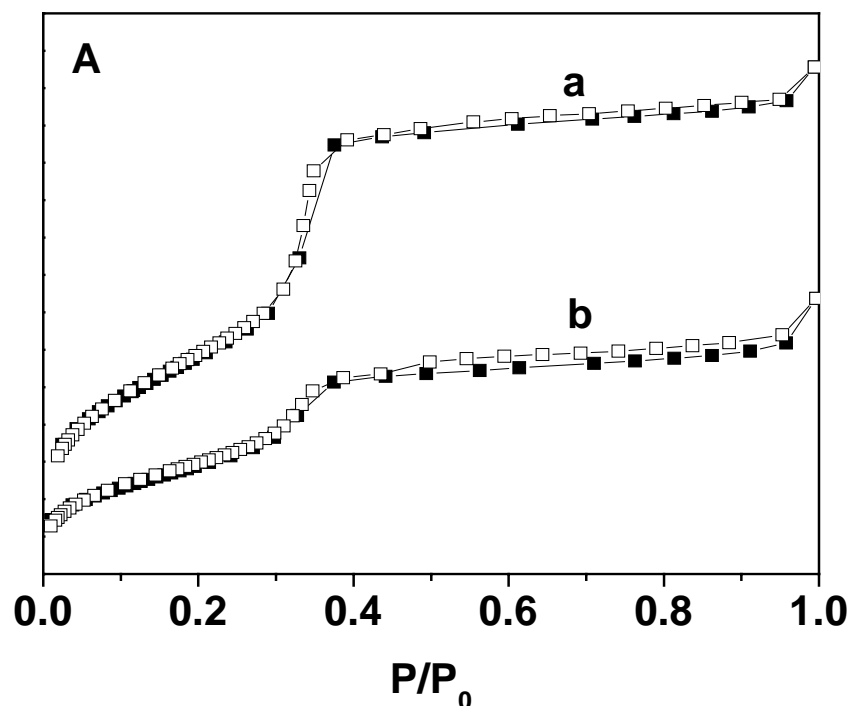


Figure 73. A) N<sub>2</sub> adsorption/desorption isotherms of **M10** (adsorption points are marked by solid squares and desorption points by empty squares); B) pore size distribution curves (deduced from the desorption data of the isotherms).

The isotherms of **M11** are presented in Figure 74. Both the samples which differ in the organic loading (**M11-1**: 0.28 mmol/g; **M11-2**: 0.43 mmol/g), show typical type-IV isotherms, which is a main feature of ordered mesoporous materials with a well-defined capillary condensation step at  $p/p_0$  0.28 and 0.24, respectively. The shift of the condensation point from **M11-1** to **M11-2** indicates a decrease of the pore size caused by increasing the percentage of the organic moiety in the material. Accordingly, a reduction to a lower nitrogen uptake demonstrates the decrease of surface area corresponding to an increase of material density with an increased loading of phenothiazine. Additionally, the curves of the pore size distribution (PSD), which are determined by the BJH method from the data of desorption branches of the isotherms, are presented in Figure 74 B. A slight decrease in the pore size by increasing of organic loading is committed by a significant deduction of the pore volume from 0.95 to 0.48 cm<sup>3</sup>/g (Table 8). However, both of the samples preserve a narrow pore size distribution, demonstrating the uniform pores of these materials.



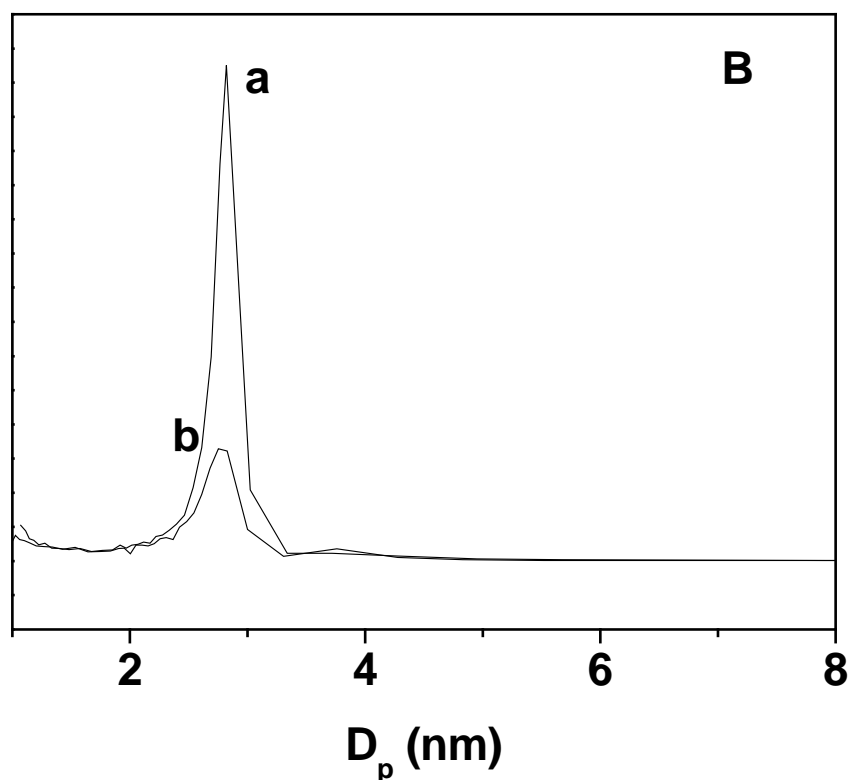


Figure 74. A) N<sub>2</sub> adsorption/desorption isotherms of (a) **M11-1**, and (b) **M11-2** (adsorption points are marked by solid squares and desorption points by empty squares). B) pore size distribution curves of (a) **M11-1**, and (b) **M11-2** (deduced from the desorption data of the isotherms).

The adsorption-desorption isotherm of **M12** is shown in Figure 75 A. Again a sharp capillary condensation step ( $p/p_0$  close to 0.2) indicates a uniform mesoporous material. Simultaneously, a type II uptake near the end section of the isotherm with a H4 type of hysteresis loop observed at higher partial pressures can be explained by interstitial cavities, which may be created by a textural porosity within the particles of the materials, or an intersecting disorder of the materials<sup>166, 193</sup>. A narrow pore-size distribution curve (Figure 75 B) with a mean pore size of 2.41 nm, calculated from the adsorption branch of the isotherm using the BJH algorithm, confirms the uniformity of the mesopores in the material. Another larger pore mainly located at 3.80 nm can also be observed, which is deduced from the uptake of the condensation step at  $p/p_0$  0.44. It might be due to the presence of intersecting pores

between the uniform particles. This material possesses a relatively high specific surface area of  $539 \text{ m}^2/\text{g}$ .

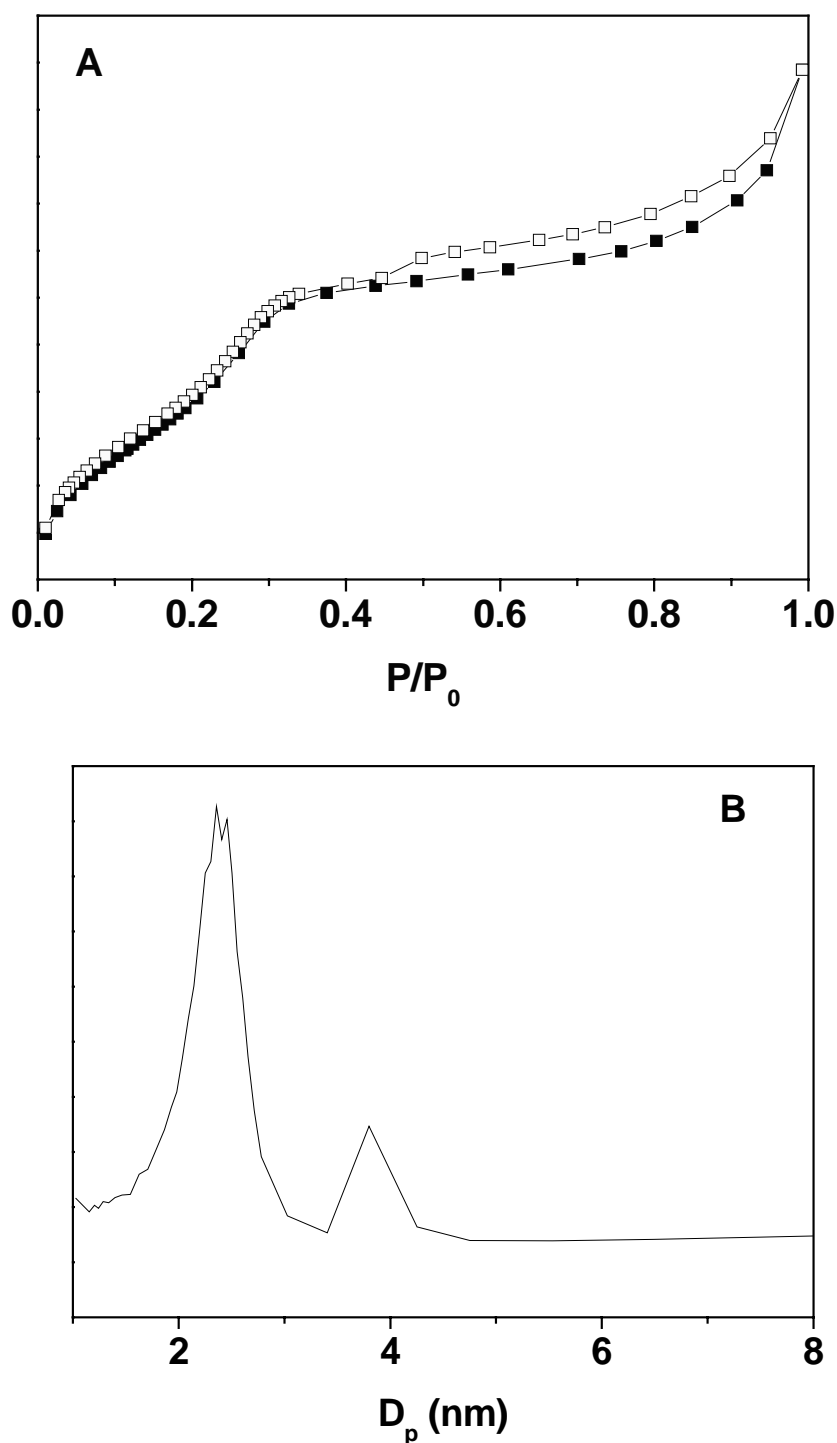


Figure 75. A)  $\text{N}_2$  adsorption/desorption isotherms of **M12** (adsorption points are marked by solid squares and desorption points by empty squares). B) pore size distribution curves of **M12** (deduced from the desorption data of the isotherms).



Table 8. Textural parameters of **M10**, **M11** and **M12** derived from the nitrogen adsorption-desorption analyses or powder X-ray diffraction and loading of phenothiazines in the hybrid materials

sample	$d_{100}^a$ (nm)	$a_0^b$ (nm)	$S_{BET}^c$ ( $m^2 g^{-1}$ )	$V_p^d$ ( $cm^3 g^{-1}$ )	$D_p^e$ (nm)	$w_t^f$ (nm)	content of phenothiazine <sup>g</sup>	
							( $mmol g^{-1}$ )	(wt %)
<b>M10</b>	4.20	4.85	536	0.36	2.36	2.49	0.70	30.4
<b>M11-1</b>	4.44	5.13	1086	0.96	2.82	2.31	0.28	18.3
<b>M11-2</b>	4.50	5.20	543	0.48	2.77	2.43	0.43	28.1
<b>M12</b>	4.48	5.17	539	0.41	2.41	2.76	0.28	14.9

<sup>a</sup>  $d_{100}$  is the d(100) spacing; <sup>b</sup>  $a_0$  is the cell parameter ( $a_0=2d_{100}/\sqrt{3}$ ); <sup>c</sup>  $S_{BET}$  is the BET surface area; <sup>d</sup>  $V_p$  is the pore volume; <sup>e</sup>  $D_p$  is the pore diameter; <sup>f</sup>  $w_t$  is the wall thickness  $a_0-D_p$ ; <sup>g</sup> calculated according to the content of nitrogen (CHN element analysis).

The estimated wall thickness of **M12** is 2.76 nm, which is rather thick compared to pure silica MCM-41 obtained under similar conditions, as well as to other hybrid materials, which contain anchored phenothiazines on the internal surface. This might be due to the relatively large molecule **12** (the molecule size is shown in Figure 76,  $L_1$  the length of the unflexible section and  $L_2$  is the maximum Si-Si distance) distributed inside the channel wall. The bond length of Si-O in an amorphous framework is normally about 1.6 Å. Considering the size of precursor molecule **12**, two speculative situations can be mentioned here. First, the molecules are embedded inside the walls of the material, or second, the molecules are outside of the wall and hang across the pore, with silicon atoms as two anchoring points.

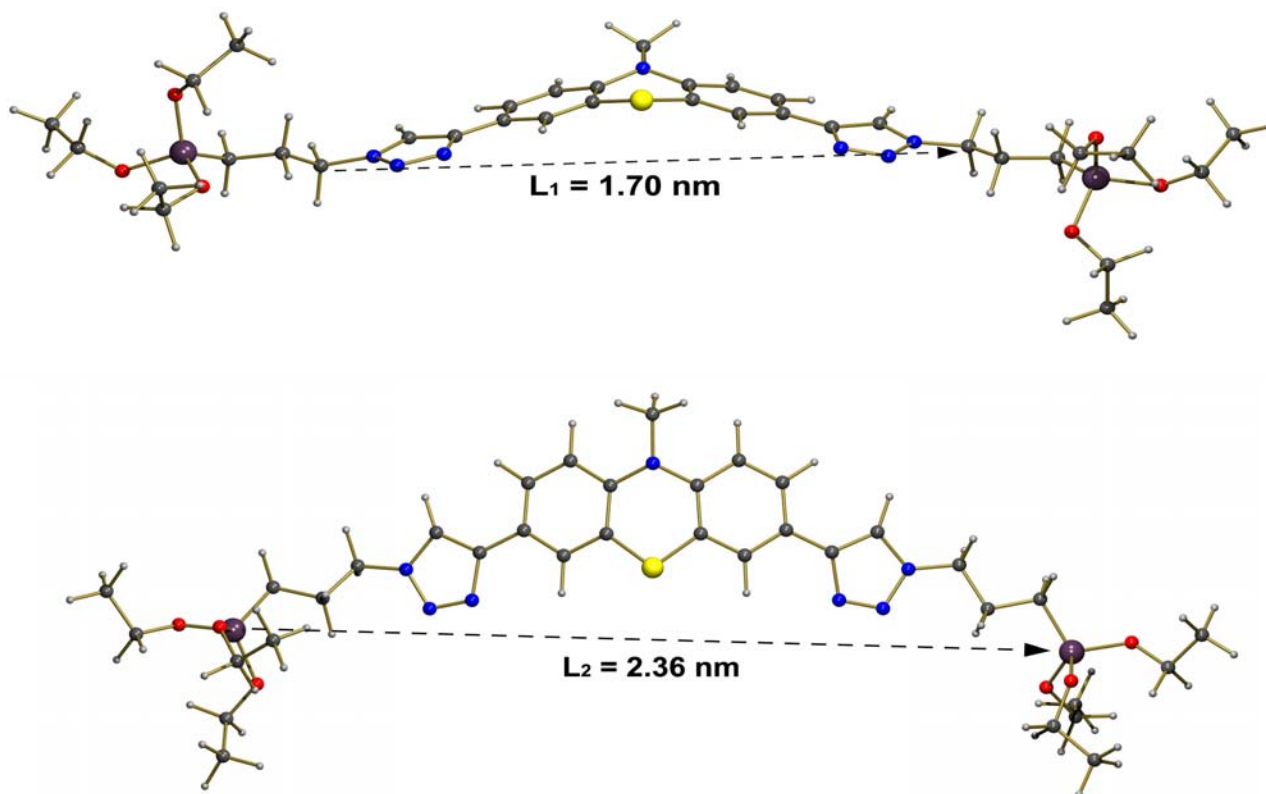


Figure 76. Molecular structure of precursor **12**.

### Electron microscopy

Transmission electron microscopy was used to investigate the mesoporous structure of these hybrid materials. The TEM image of **M10** is shown in Figure 77. The mesoscale pores can directly be observed in the large area of image A from the [10] direction, and the parallel channels can be seen in some area of image B from the [11] direction. However, instead of a hexagonal structure of highly ordered mesopores, the existence of relatively large areas of dislocations and disclinations<sup>239</sup> in the mesophase of this hybrid materials is obvious. It might be due to the presence of a large amount of the large-sized molecule hanging on the internal wall of the pores, which strains the wall to distort the pore shape. This structural defect involves a large strain field (the bend channels), and the large bend will break channels into many short sections in some area. Meanwhile, this TEM result is coherent to the pattern of

XRD, where a type of twisty arrangement of channels is present in this material, instead of the highly ordered hexagonal array.

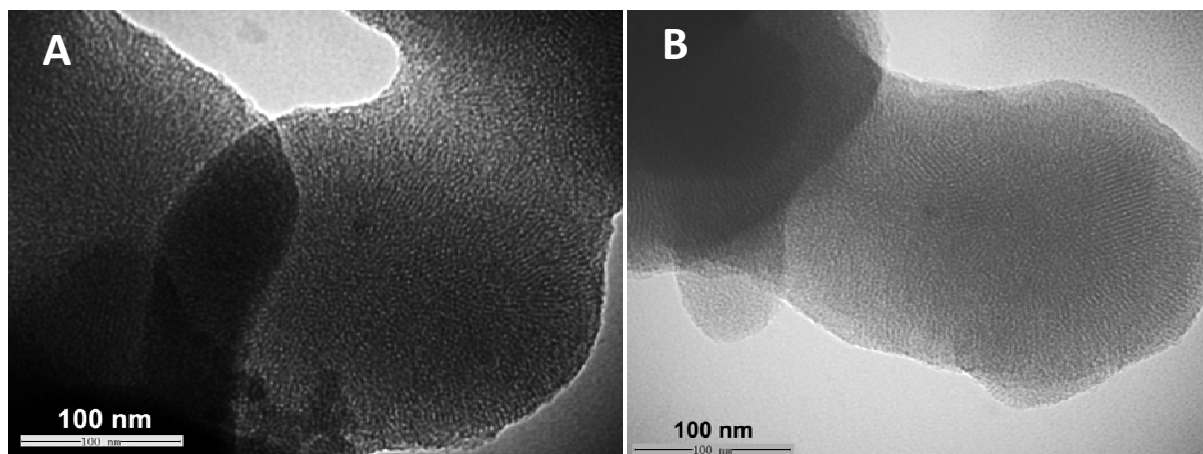


Figure 77. Transmission electron microscopy images **M10**.

A TEM analysis of **M11-1** revealed ordered arrays of cylindrical channels arranging along the [11] direction (Figure 78B) and demonstrates a highly ordered pore structure. This type of ordering can be observed even in the large area image Figure 78A, indicating the long-range order of this hybrid material as expected from the distinct diffraction pattern of the XRD. Two images of **M11-2** are presented in Figure 78C and D. From the image of the [10] direction (Figure 78C), a distorted pore structure can be observed, implying the reduced overall ordering of this material. However, a relatively ordered channel arrangement is preserved in the image D from area to area, proving the existence of a mesoporous structure with a slight decrease of ordering. It is according to the result of the XRD, and is often observed for hybrid materials with a highly organic loading.

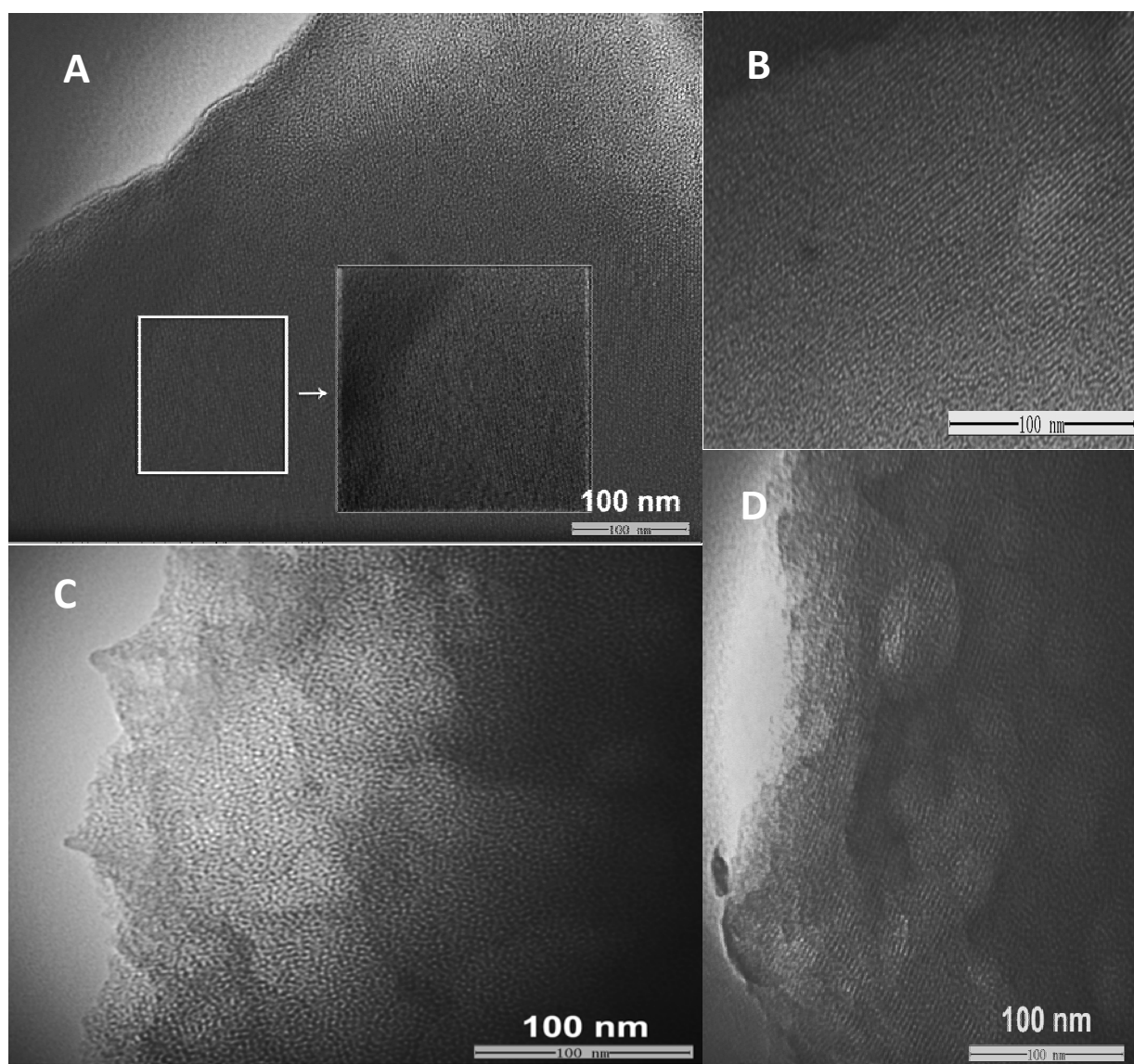


Figure 78. Transmission electron microscopy images, (A) **M11-1** large scale image, (B) **M11-1** perpendicular to the channel direction, (C) **M11-2** along the channel direction (D) **M11-2** perpendicular to the channel direction.

The transmission electron microscope (TEM) image of **M12** (Figure 79) shows the presence of wormhole-like structures rather than a 2D hexagonal mesostructure as expected from the XRD pattern. Thus, the mesostructural ordering of this material occurs in the range between unordered compounds and highly ordered periodic mesoporous organosilicas. This relative disordered structure might be due to the limitation of wall thickness of MCM-41 type of

materials, which are not sufficient for holding such large organic molecules. Thus it maybe an alternative way to embed this molecule into a material with thicker wall, such as SBA-15.

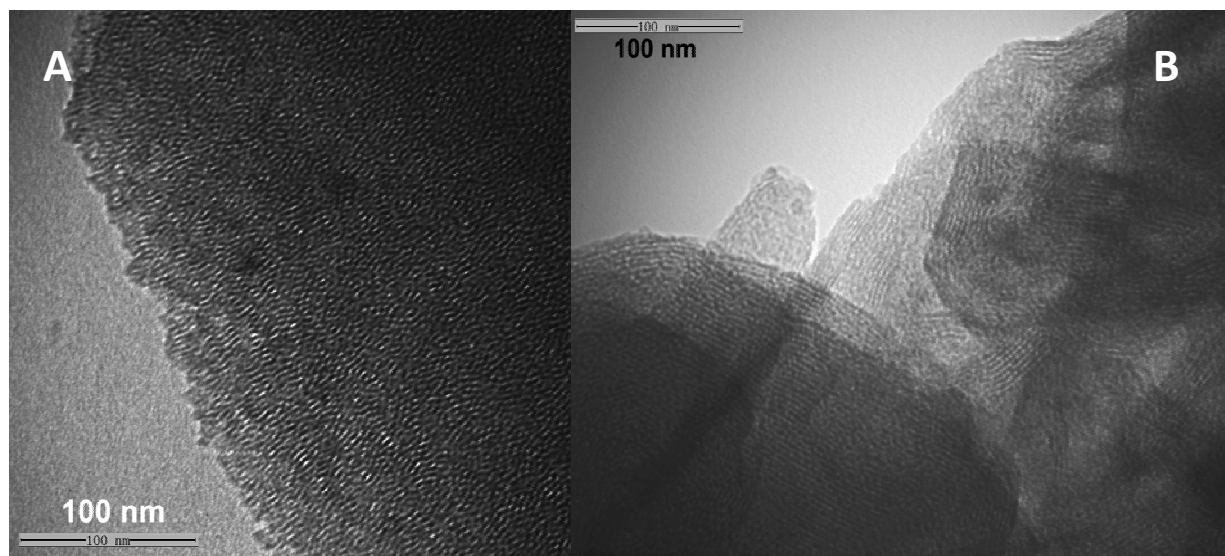


Figure 79. Transmission electron microscopy images, (A) **M12** along the channel direction, (B) **M12** perpendicular to the channel direction.

The morphology of the mesoporous materials can be influenced the synthetic conditions. Unpredictable effects in the synthesis of hybrid mesoporous materials by the co-condensation method occur from the amount of the organosilane precursor and the molecular structure of this precursor. As we had already shown in the last section, the urea linked phenothiazine precursors can change the morphology of final product by adjusting the concentration and the molecular structure. Accordingly the triazole linked precursor also can be responsible for a morphology change, as documented by the SEM image of **M10** (Figure 80). An aggregation of a large amount of small spherical particles can be observed. From the magnified picture in the left, the particles located inside this agglomerate have a smoother surface than the outside ones. Looking to it in detail, a lot of small particles are gathered on the outside particles, causing a rough surface. Anyhow, the assembling of small particles can be observed in this

material, which is supporting the analysis from the isotherm of N<sub>2</sub> adsorption/desorption experiment.

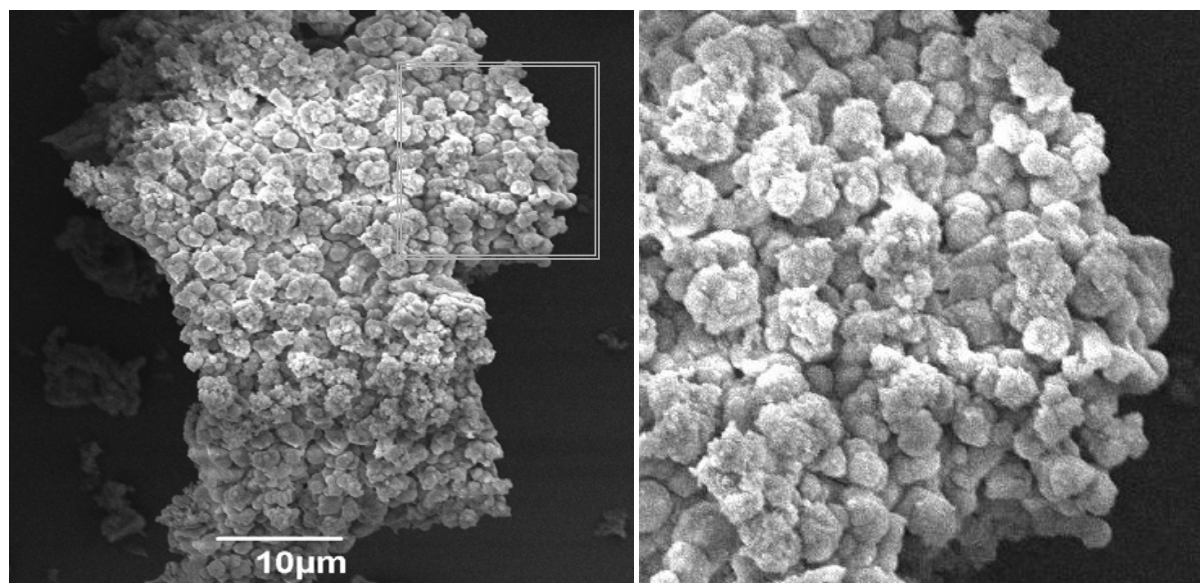


Figure 80. SEM image of hybrid mesoporous materials **M10** and a magnified picture of the partial area in the right.

### 2.3.3 Spectroscopic properties of the hybrid materials

#### FT-IR spectra

The presence of the triazole linked phenothiazine in **M10** is clearly revealed in the FT-IR spectrum of the solid (Figure 81). The C-H stretching vibration of methyl or methylene groups in the alkane chains causes the peaks around 2980-2820 cm<sup>-1</sup>. The strong peak at 1465 cm<sup>-1</sup> is attributed to the C-H deformation of the CH<sub>2</sub> group or the antisymmetric deformation of CH<sub>3</sub>. Additional to these significant characteristic signals of the organic moiety, the spectra of all hybrid materials also show some feature peaks of the silica framework. A broad band in the range of 3600-3200 cm<sup>-1</sup> can be assigned to the  $\nu_{\text{OH}}$  stretching vibration of the hydrogen bound internal silanol groups<sup>170</sup>. The broad bands at 1300 to 1100 cm<sup>-1</sup> are attributed to the asymmetric stretching vibration of various Si-O-Si bonds of the silica network. The band at

955  $\text{cm}^{-1}$  is attributed to the stretching vibration of surface  $\text{Si-O}^-$  groups, and the peak at 800  $\text{cm}^{-1}$  is attributed to the symmetric vibration of  $\text{Si-O-Si}$ . The strong peak at 460  $\text{cm}^{-1}$  can be assigned to the bending band of  $\text{Si-O-Si}$  <sup>210</sup>.

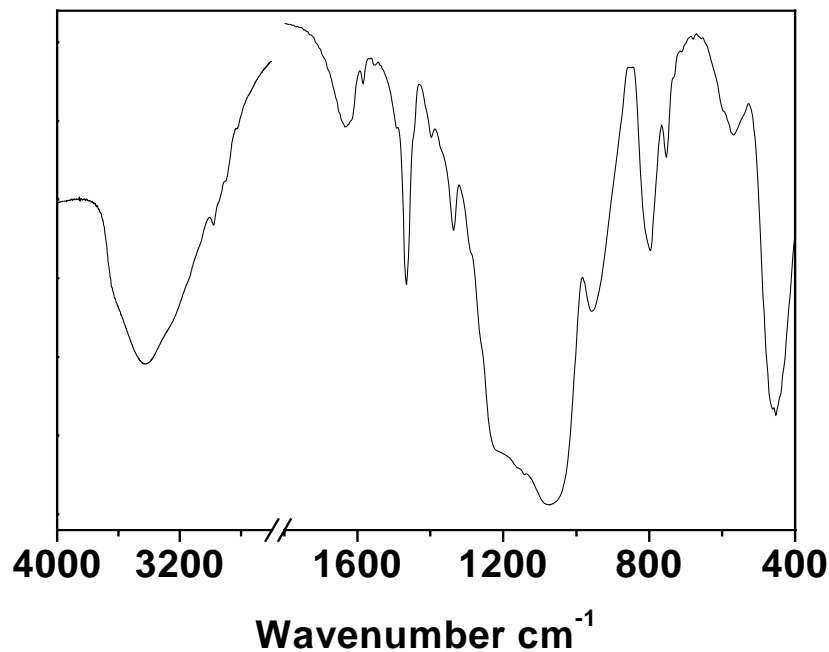


Figure 81. FT-IR spectrum of the hybrid material **M10**.

Figure 82 presents two spectra, which belong to **M11-1** and **M11-2**. Obviously the absorbance in the region of the C-H stretching vibrations (2980-2820  $\text{cm}^{-1}$ ) is more significant than for **M10**. In **M11** a biphenothiazine compound with two hexyl chains is used. Additionally, the relative intensity of the sharp signal of the C-H deformation vibration at 1460  $\text{cm}^{-1}$  is increased.

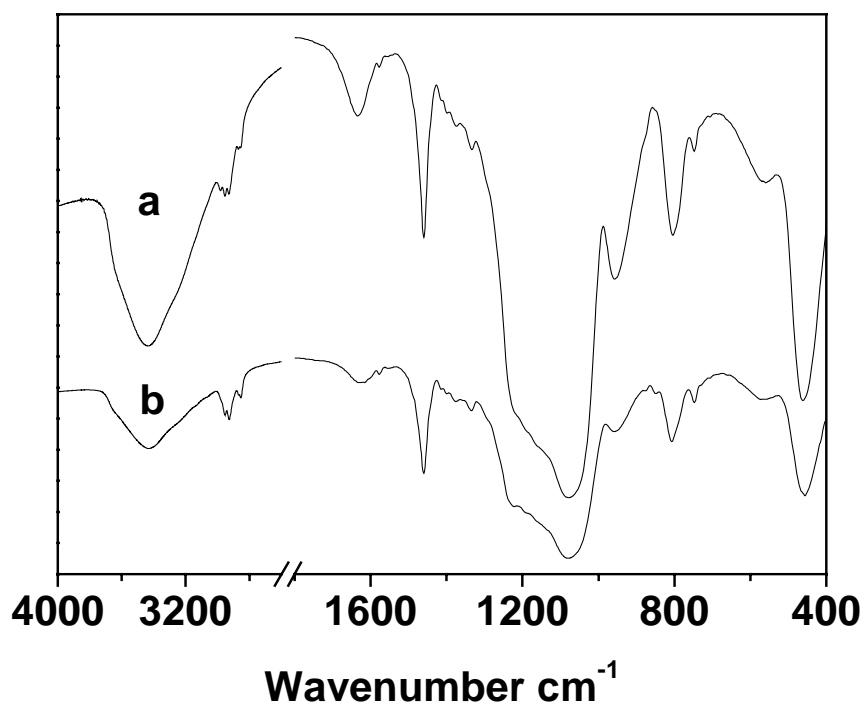


Figure 82. FT-IR spectrum of the hybrid materials **M11-1** and **M11-2**.

The FT-IR spectrum of **M12** is shown in Figure 83. The stretching vibration of C-H in the range of 2980-2820 cm<sup>-1</sup> is not as distinguished as in the spectrum of **M11**, which is due to a methyl substituted N position of the phenothiazine ring in molecule **12** instead of the hexyl chain in **11**. The same decrease of intensity can also be observed for the C-H deformation vibration at 1463 cm<sup>-1</sup>. However, the presence of these feature bands is the proof for the incorporation of the phenothiazine molecules in the material.



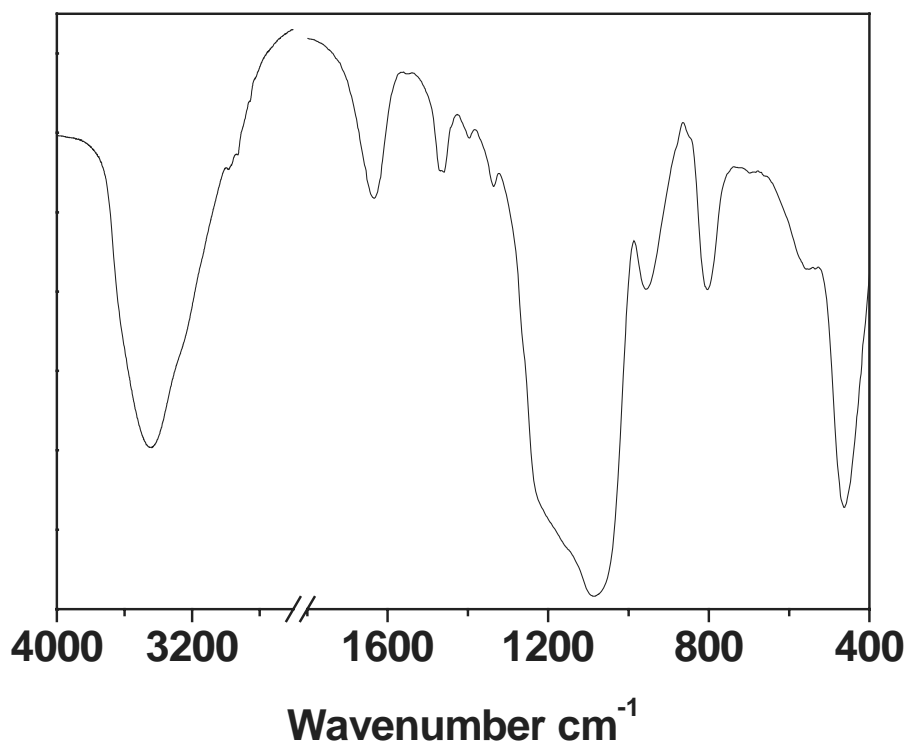


Figure 83. FT-IR spectrum of the hybrid material **M12**

#### <sup>13</sup>C CP MAS NMR spectra

The integrity of the phenothiazine molecules in the hybrid materials can be detected by solid state NMR spectroscopy. The <sup>13</sup>C CP-MAS NMR spectrum of **M10** exhibits signals (Figure 84), which match with the high resolution spectrum of precursor **10** in solution (Figure 84 red lines). This indicates that the organic moieties are not damaged during the hydrothermal synthesis and the acid extraction process. The resonances in the high field region can be mainly attributed to the carbon atoms of the hexyl chain, while there are still small amounts of Si-OCH<sub>2</sub>CH<sub>3</sub> groups or some ethanol from the template extracting process (singles at ~ 60 and ~ 16 ppm). An important resonance is appears at ~ 52 ppm, which is assigned to the -CH<sub>2</sub>-N group linked to the triazole. The signals in the range from 115 ppm to 132 ppm are assigned to the carbon atoms of the electronrich phenothiazine ring and the triazole ring.

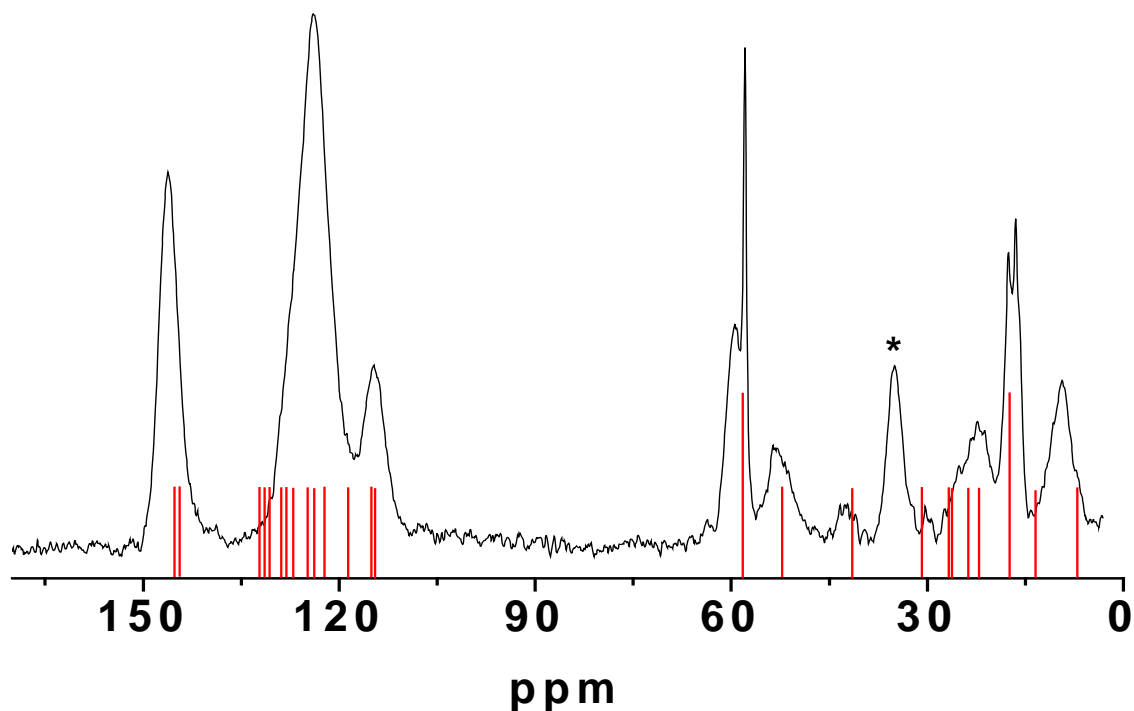


Figure 84.  $^{13}\text{C}$  CP-MAS NMR spectra of **M10**; the red lines give information on the position and the relative intensities in the solution NMR spectra of **10**.

Figure 85 shows the  $^{13}\text{C}$  CP MAS NMR spectrum of **M11-2**, the resonances of the supported material are consistent to the peaks of the organic precursor **11** (red lines), indicating the integrity of phenothiazine compound **11** in this material. The intense resonances in the low field region are mainly attributed to carbon atoms of the two phenothiazine cores. The preservation of a signal at  $\sim 52$  ppm corresponds to the carbon of the  $\text{CH}_2\text{-N}$  group, which indicates that no break happened between the propyl and triazole group. Other peaks in the high field region can be assigned to the carbon atoms of the hexyl side chain. This spectrum proves that phenothiazine has been linked inside the silica material by covalent bonds.

The solid state  $^{13}\text{C}$  NMR data of **M12** are presented in Figure 86. The matching between the signals of solid material and the liquid NMR spectrum of **12** in  $\text{CH}_2\text{Cl}_2$  proves the successful introduction of the precursor. Two signal marked with asterisk are assigned to a small amount of remnant template.

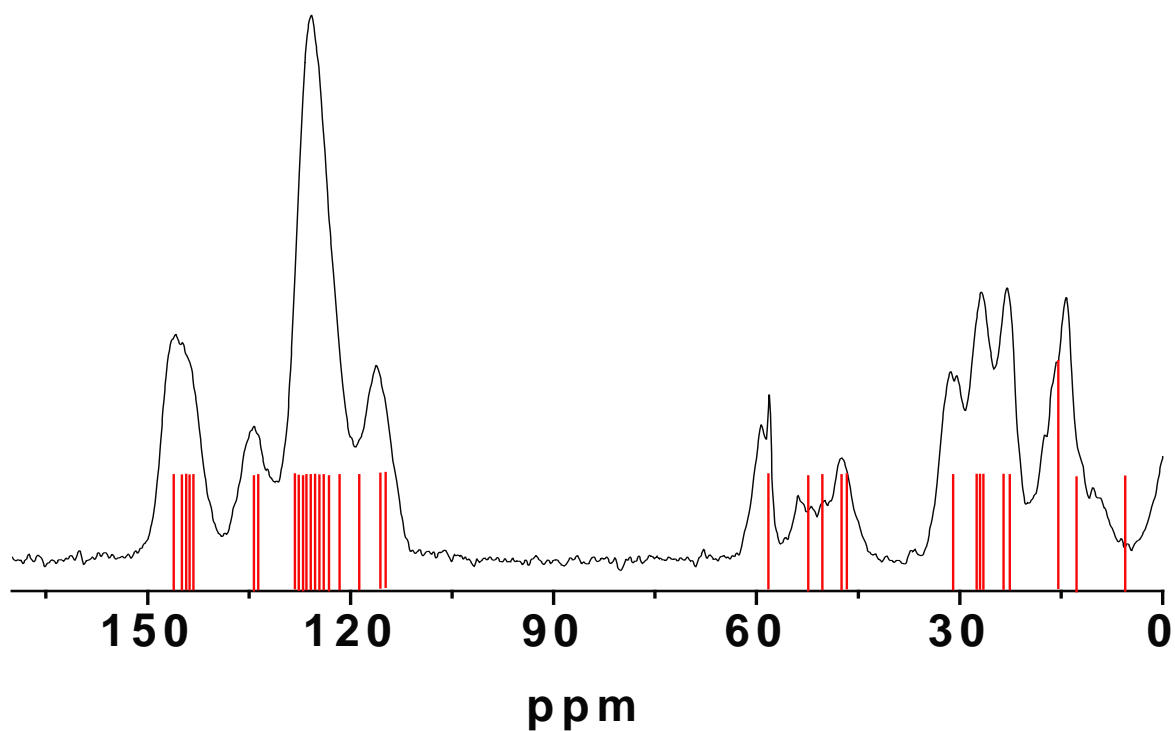


Figure 85.  $^{13}\text{C}$  CP-MAS NMR spectra of **M11-2**; the red lines give information on the position and the relative intensities in the solution NMR spectra of **11**.

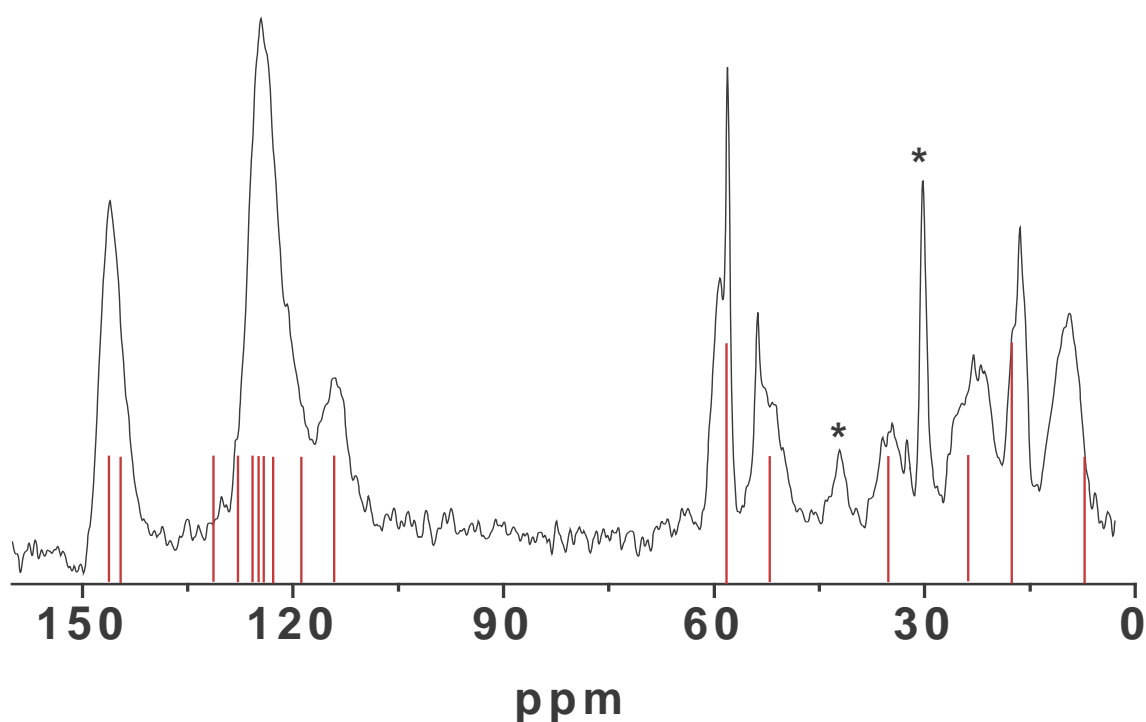


Figure 86.  $^{13}\text{C}$  CP-MAS NMR spectra of **M12**; the red lines give information on the position and the relative intensities in the solution NMR spectra of **12**.

$^{29}\text{Si}$  CP MAS NMR spectra

The  $^{29}\text{Si}$  CP-MAS NMR spectra confirm that the organic/inorganic moieties are the basic structure units of the hybrid mesoporous materials. Figure 87 presents the spectrum of **M10**, which displays two signals in the T region, indicating the presence of organosilica  $\text{T}^3$  species  $[\text{C-Si}(\text{OSi})_3]$  (-67 ppm) and  $\text{T}^2$  species  $[\text{C-Si}(\text{OSi})_2(\text{OH})]$  (-57 ppm)<sup>240</sup>. Due to the area of these two peaks,  $\text{T}^3$  presents the major substructure, indicating a sufficient hydrolysis/condensation of precursor **10** during the synthesis to achieve a strong linkage (three Si-O-Si covalent bonds) between the organic compound and the silica matrix. For the characteristics of the inorganic silica framework, the spectrum exhibits a small signal at -92 ppm, which can be assigned to the  $\text{Q}^2$   $[(\text{SiO})_2\text{Si}(\text{OR})_2]$  species, a sharp and high intense signal around -101 ppm, which is the region of  $\text{Q}^3$   $[(\text{SiO})_3\text{Si}(\text{OR})]$  (R = H, Me) as the majority, and another peak is present at -110 ppm corresponding to  $\text{Q}^4$   $[(\text{SiO})_4\text{Si}]$  species<sup>241</sup>.

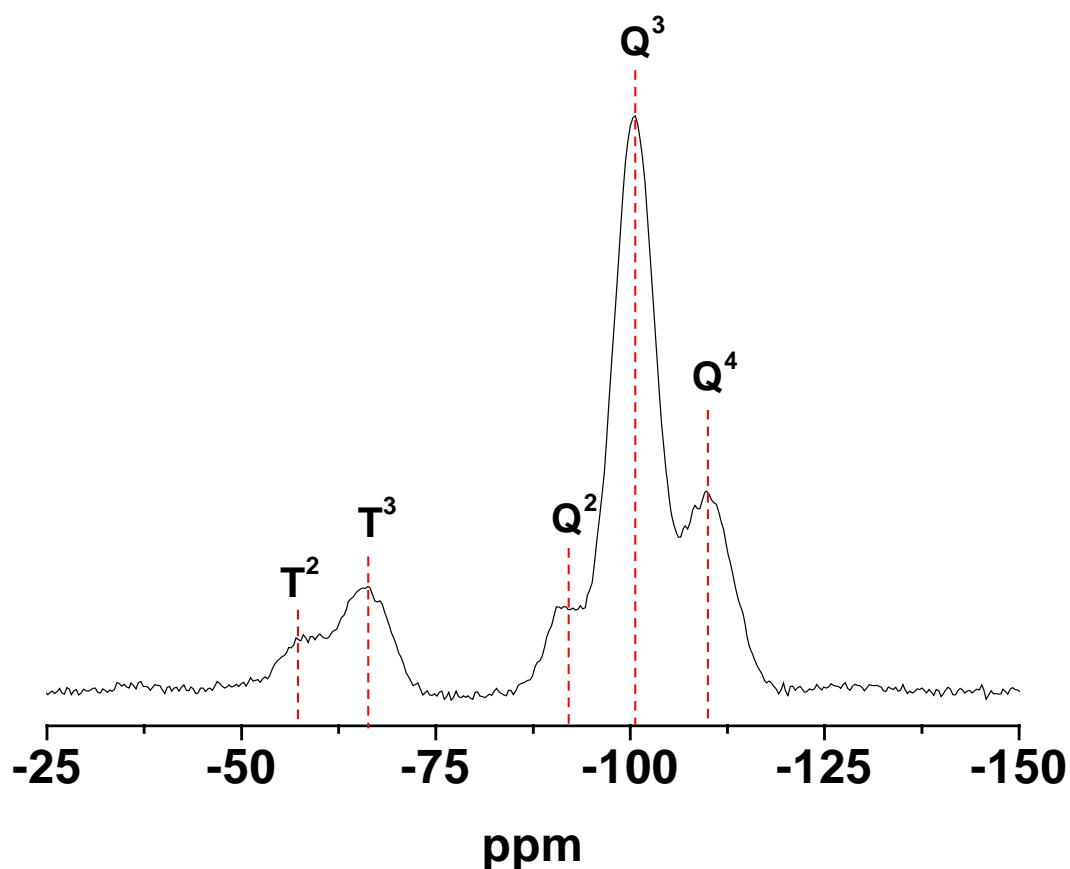


Figure 87.  $^{29}\text{Si}$  CP-MAS NMR spectra of **M10**.

An exemplified  $^{29}\text{Si}$  CP-MAS NMR spectrum of **M11-2** is shown in Figure 88. With a loading of 0.43 mmol/g of precursor **11**, a dominating  $\text{T}^3$  sites signal can be observed at -68 ppm, indicating that the organosilica is mainly present as  $\text{C-Si}(\text{OSi})_3$  species in this hybrid material. The maintaining of a large amount of isolated  $\text{Si-OH}$  groups is proved by the sharp peak at -100 ppm ( $\text{Q}^3$ ). Furthermore, the small resonance at -90 ppm, implies the residual geminal silanol sites. Both of them display the feasibility of further functionalization.

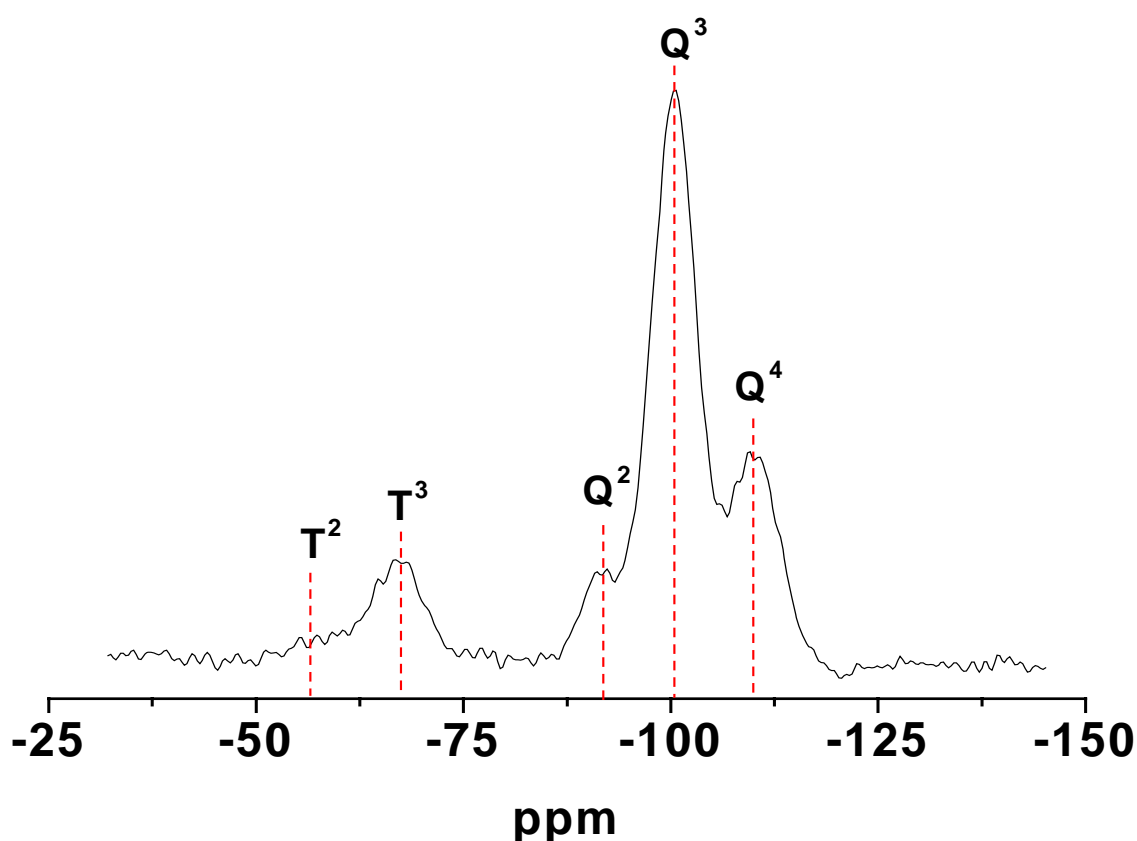


Figure 88.  $^{29}\text{Si}$  CP-MAS NMR spectra of **M11-2**.

The bridged organosilane **12** composing material **M12** exhibits the  $^{29}\text{Si}$  CP-MAS NMR spectrum shown in Figure 89. The  $\text{T}^n$  band signals are mainly centered around -68 ppm with a small shoulder around -57 ppm. This type of resonances discloses the relatively complete hydrolysis of the alkyoxysilanes of this precursor. Thus, it indicates that this molecule is embedded in the framework of the hybrid material with two bonded silicon atoms.

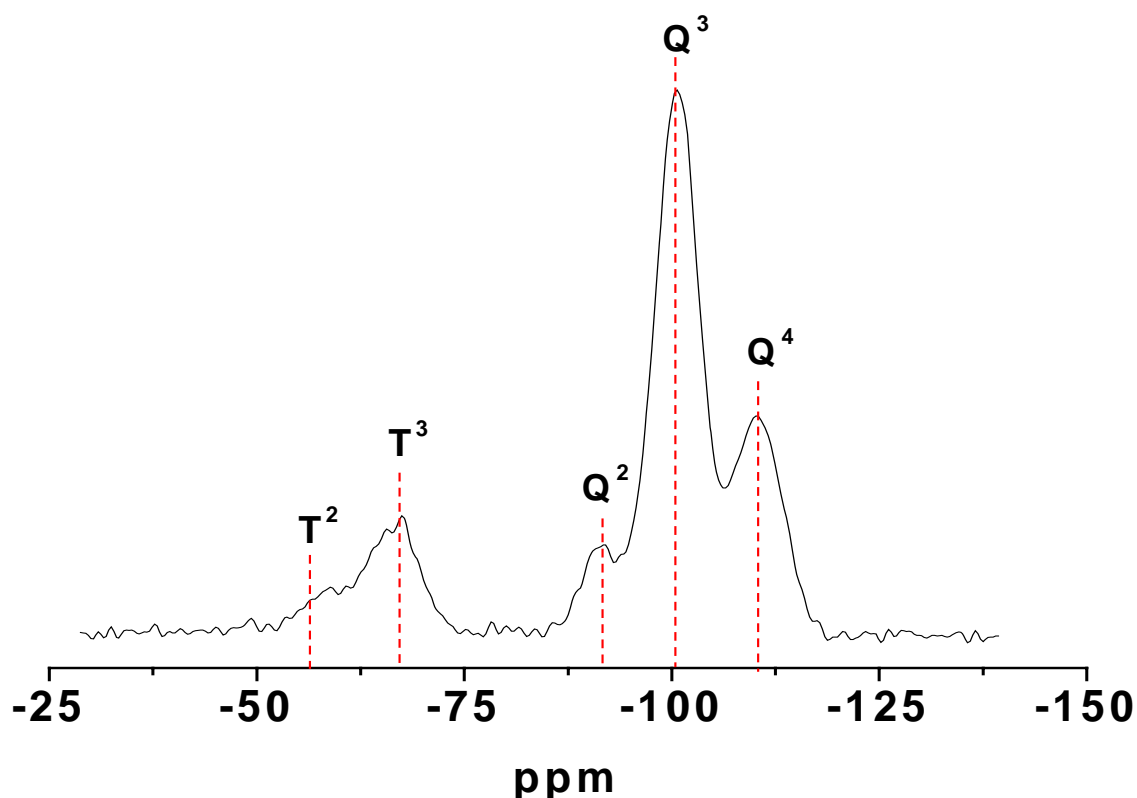


Figure 89.  $^{29}\text{Si}$  CP-MAS NMR spectra of **M12**.

### 2.3.4 Optical properties of the hybrid materials and the associated oxidized materials

Due to the presence of the directly linked triazolyl groups the electronic properties of the phenothiazine modified hybrid materials should differ from the systems discussed up to this point. Especially, **M12** where the bistriazole linked phenothiazine is immersed inside the silica framework should be interesting. We therefore investigated the adsorption and emission of these materials. The spectral data of the neat organic precursors and corresponding hybrid materials are shown in Table 9.

Table 9. Selected absorption and emission Spectra data

compound	$\lambda_{\max, \text{abs}}$ (nm) ( $\epsilon$ )	$\lambda_{\max, \text{em}}$ (nm)	Stokes-shift ( $\text{cm}^{-1}$ )
<b>10</b>	268, <b>318</b> <sup>a</sup>	<b>450</b> <sup>a</sup>	9200
<b>M10</b> <sup>b</sup>	260, <b>320</b>	<b>451</b>	9080
<b>11</b>	278, 328, <b>367</b> <sup>a</sup>	<b>470</b> , 505 (sh.) <sup>a</sup>	6000
<b>M11-1</b> <sup>b</sup>	276, 330, <b>370</b>	<b>484</b> , 509 (sh)	6360
<b>M11-2</b> <sup>b</sup>	275, 327, <b>376</b>	<b>500</b>	6670
<b>12</b>	276, <b>334</b> <sup>a</sup>	<b>459</b> <sup>a</sup>	8100
<b>M12</b> <sup>b</sup>	270, 327, <b>360</b>	390, <b>445</b>	5310

<sup>a</sup>  $\text{CH}_2\text{Cl}_2$  as solvent (the data were provided from our cooperating group). <sup>b</sup> UV-Vis diffuse reflectance result.

The hybrid material **M10** appears as a yellow colored powder. It exhibits two absorption bands at 260 and 320 nm (Figure 90 black curve) and an emission band at 451 nm (Figure 90 blue curve). Both the absorption and emission behavior is similar to the pure organic precursor **10**, which indicates the inclusion of molecule **10** in the hybrid mesoporous material. No strong interaction between the framework and the molecules can be detected. A quite remarkable Stokes shift ( $\sim 9000 \text{ cm}^{-1}$ ) is observed, which demonstrates a significant geometrical change upon the excitation from a highly non-planar ground-state to largely planarized excited state. This is often observed for phenothiazine derivatives<sup>108</sup>.

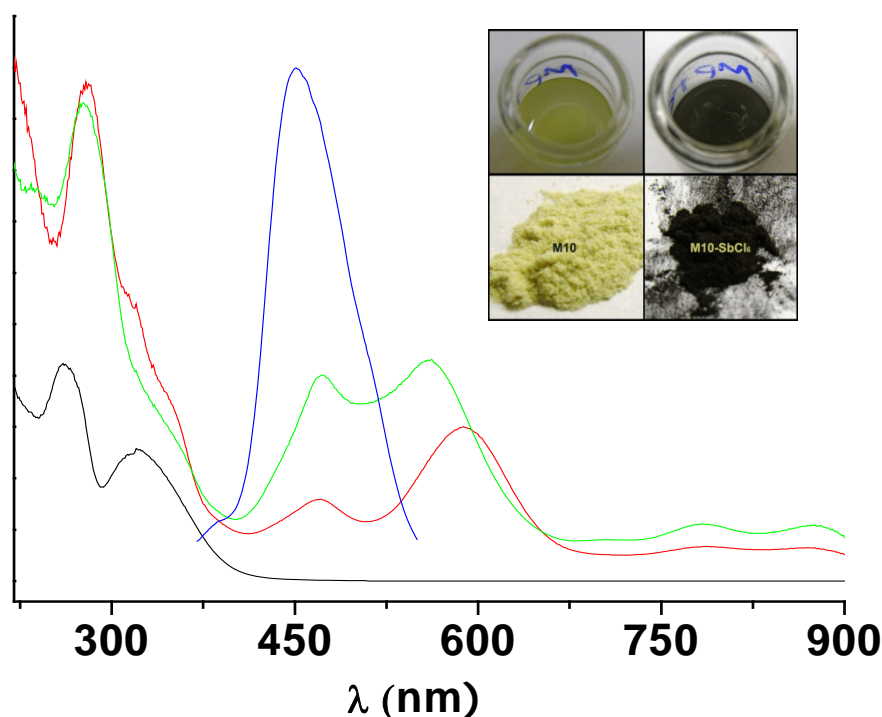
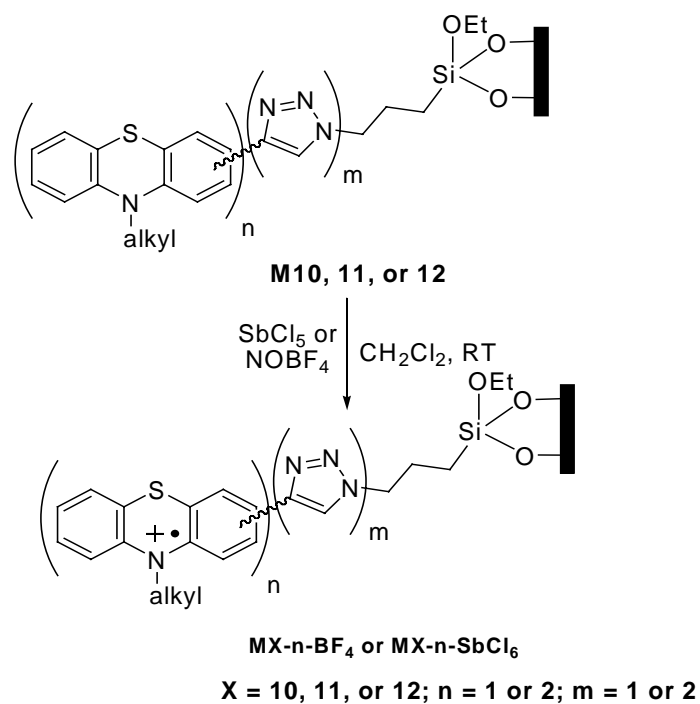


Figure 90. UV-Vis spectrum of the hybrid mesoporous material **M10** (black line), the absorptions of the corresponding radical cationic samples **M10-BF<sub>4</sub>** (red line), **M10-SbCl<sub>6</sub>** (green line), and the emission spectrum of **M10** (blue line). The inset picture demonstrates the color change caused by the oxidation of **M10** using  $\text{SbCl}_5$  in suspension and for the corresponding solid.

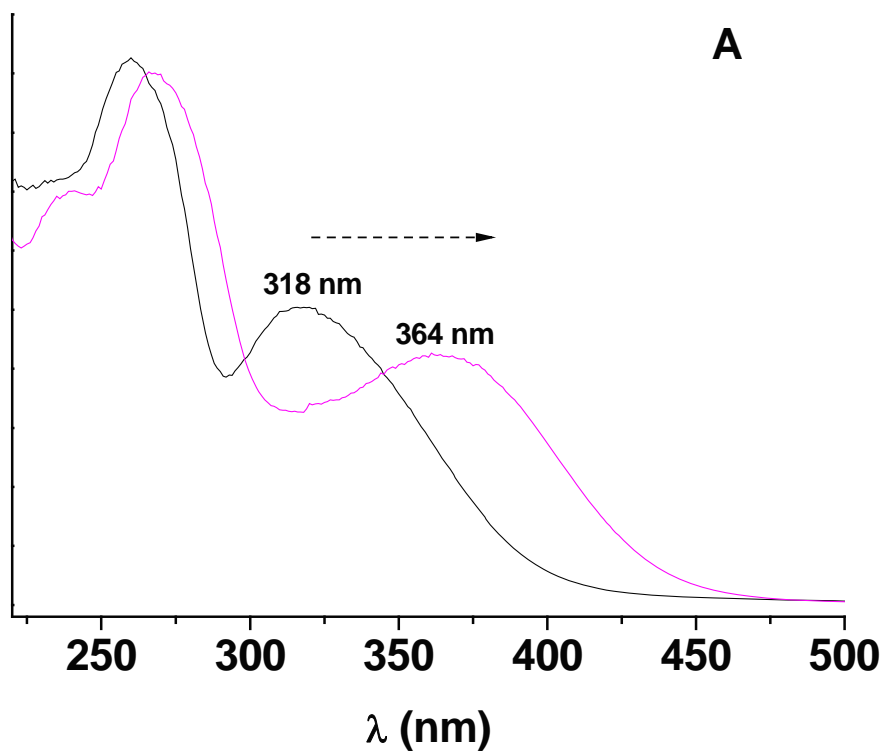
This material undergoes the formation of surface bound radical cations when treated with oxidizing agents (Scheme 17). The oxidation of the phenothiazine was carried out with the one-electron acceptors antimony pentachloride and  $\text{NOBF}_4$  in dichloromethane suspension, leaving  $\text{SbCl}_6^-$  and  $\text{BF}_4^-$  as the counter ion, respectively. The color changes from yellow to dark green-blue, immediately after addition of the oxidant to the suspension of **M10** in  $\text{CH}_2\text{Cl}_2$ . The dark colored radical cationic products' absorption spectra are presented in Figure 90 as red line for  $\text{PH}^{\bullet+}\text{BF}_4^-$  and as green line for  $\text{PH}^{\bullet+}\text{SbCl}_6^-$ . Some significant new absorption bands appear in low energy region. The mutual bands of these two radical cationic products are at 470, 780 and 880 nm. Additionally to these bands, a further strong absorption appears at 560 nm in **M10-SbCl<sub>6</sub>**, while shifts to 590 nm in **M10-BF<sub>4</sub>**. Additionally, all the



peaks are more intense when  $\text{SbCl}_5$  is used as the oxidant. This phenomenon is due to the strong oxidizing power of  $\text{SbCl}_5$  compared to  $\text{NOBF}_4$ .



Scheme 17. Oxidation of mesoporous phenothiazinyl hybrid materials.



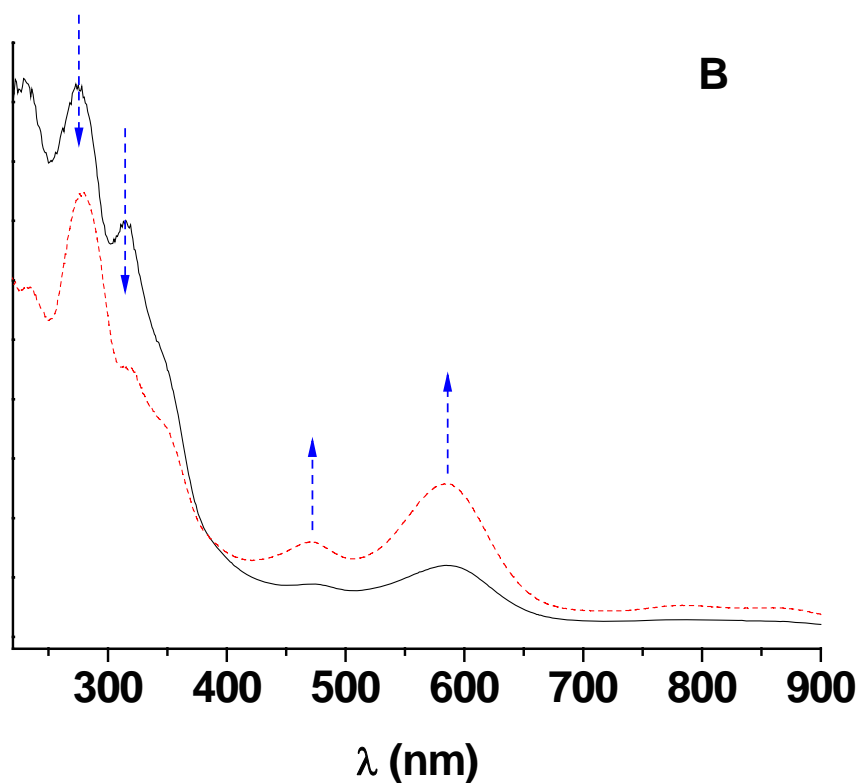


Figure 91. UV-Vis spectrum of (A) the hybrid mesoporous material **M10** (black line), and the absorptions of the corresponding protonated sample **M10-H**. (B) the radical cationic sample **M10-BF<sub>4</sub>** (black line), and the absorptions of the corresponding protonated sample **M10-BF<sub>4</sub>-H**.

Because of the presence of a triazole group in molecule **10**, which is directly bound to the phenothiazine ring, it is reasonable to expect that protonation will change the photochemical properties of this compound. Thus, a protonated hybrid material **M10-H** was synthesized by using TFA as the proton donor. A pronounced bathochromic shift of both absorption bands can clearly be observed after protonation (Figure 91 A). This result can be explained by the  $-I$  effect of the triazole ring. It will take electron density from the electron rich phenothiazine ring, and decrease the HOMO-LUMO gap. A secondary interaction between surface silanol groups and the protonated triazole can be assumed. The hydrophilic surface of the amorphous silica material might act like a polar solvent, and will therefore additionally influence the photochemical properties of the introduced organic moiety.

The same protonation experiment was carried out for the radical cationic material **M10-BF<sub>4</sub>**. The result is shown in Figure 91 B. Here a weak hypochromic effect can be observed for the absorption at 200 nm, while a weak hyperchromic effect can be observed for the peaks at 470 and 585 nm. The peaks, which are typical for the radical cation are intensified after protonation. In summary, a change in the adsorption spectra can be observed after protonation of the hybrid material, which may give a hint for a potential application of this hybrid material as a photochromic pH sensor.

**M11** is dark yellow colored compared to **M10**. The color of **M11** is more intense which can be explained with the large  $\pi$ -system in the biphenothiazine molecule. This fact is also reflected in the absorption and emission spectra, which are shown in Figure 92 and Table 9. Compared to the mono phenothiazine precursor **10**, **11** shows a red shift of the absorption bands resulting from a smaller HOMO-LUMO gap. In agreement with the data of the organic precursor, both hybrid materials have absorption bands at ~275, ~330, and a shoulder at ~370 nm. These absorptions are slightly red shifted compared to the data of the precursor (Table 9). This red shift is even more significant in the emission spectrum. The emission peak of **11** can be detected at 470 nm with a shoulder at 505 nm, while, in the case of **M11-1**, the emission is observed at 485 nm with a strong shoulder at 509 nm. The most apparent shift is found for the higher loading hybrid material **M11-2**, which has a strong blue emission at 500 nm. These results also indicate the enlargement of the  $\pi$ -system. Obviously the intermolecular interactions are stronger in **M11-2**. Another explanation of this result might be the following: the interaction of the triazole ring or the  $\pi$ -system with the framework walls of the silica material may cause an increase of parallel orientation of the triazole ring and the phenothiazine moiety and thus lead to a red shift of absorption and emission.

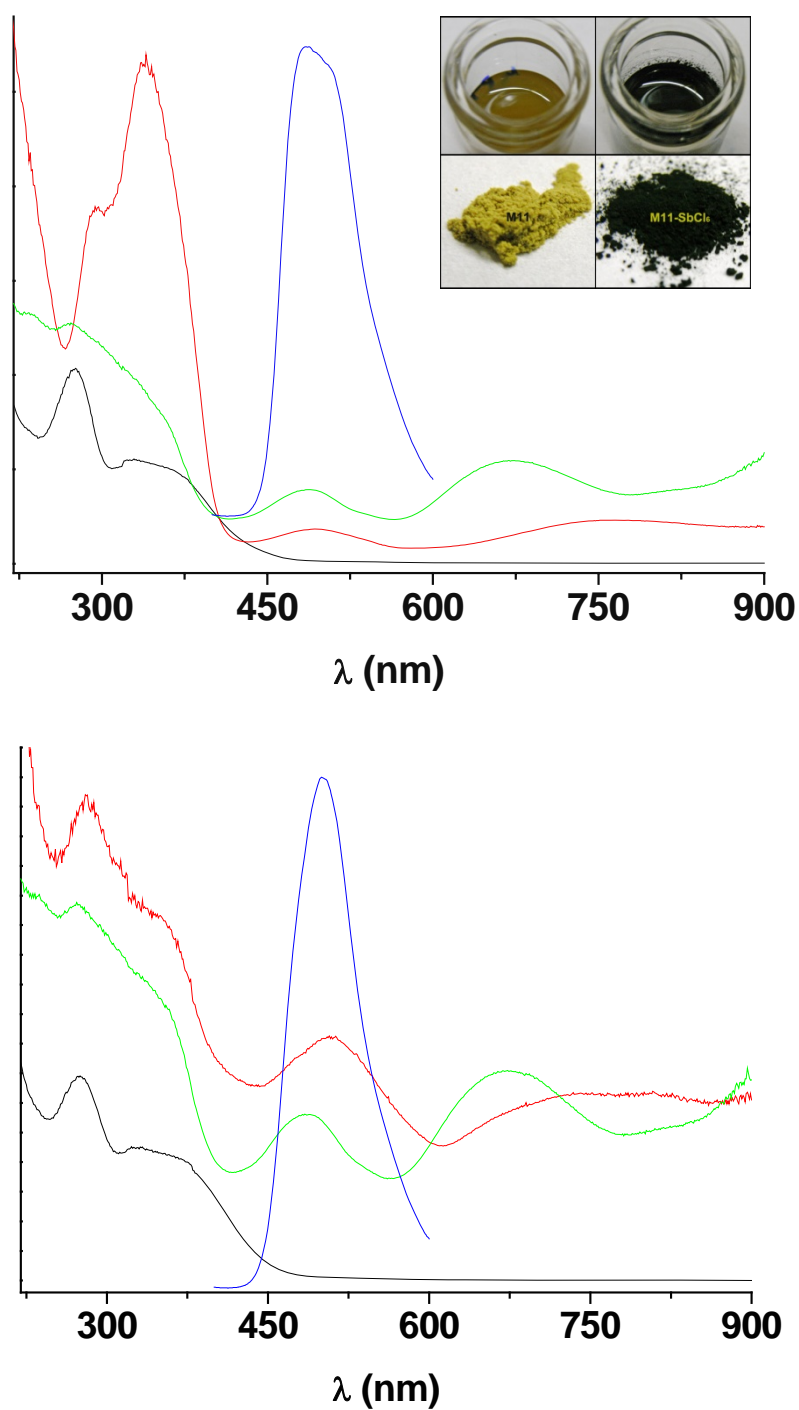


Figure 92. UV-Vis spectra of the hybrid mesoporous materials **M11-1**, and **M11-2** (black lines), the absorptions of the corresponding radical cationic samples **M11-1-BF<sub>4</sub>**, and **M11-2-BF<sub>4</sub>** (red lines), **M11-1-SbCl<sub>6</sub>**, and **M11-2-SbCl<sub>6</sub>** (green lines), and the emission spectra of the modified samples **M11-1**, and **M11-2** (blue lines). The inset picture demonstrates the color change caused by the oxidation of **M11-1** using  $\text{SbCl}_5$  in suspension and for the corresponding solid.

Addition of the one electron oxidants  $\text{SbCl}_5$  or  $\text{NOBF}_4$ , changes the color of material from yellow to dark green-blue. Several new absorption bands appear (Figure 92), such as an absorption at  $\sim 490$  nm and a broad band coming up in the NIR region. These absorptions are strongly intensified by increasing the phenothiazine loading. Compared to the data of **M10**, the biphenothiazine modified material present red shifted bands, especially, the bands in the NIR region. This phenomenon indicates that this bands should be assigned as charge transfer bands, which might be due to an inter- or intramolecular charge transfer.

The adsorption and emission spectra of **M12** are presented in Figure 93. Two absorption bands at 270 and 330 nm can clearly be observed, and a small shoulder appears at  $\sim 360$  nm. This sample displays a dual emission, with maxima around 445 and 390 nm, which are absent in the solution spectrum of precursor **12**. Considering that the molecules are uniformly distributed inside the silica framework, this dual emission is likely caused by conformational biases as a consequence of restricted restricted molecular rotation and relaxation.

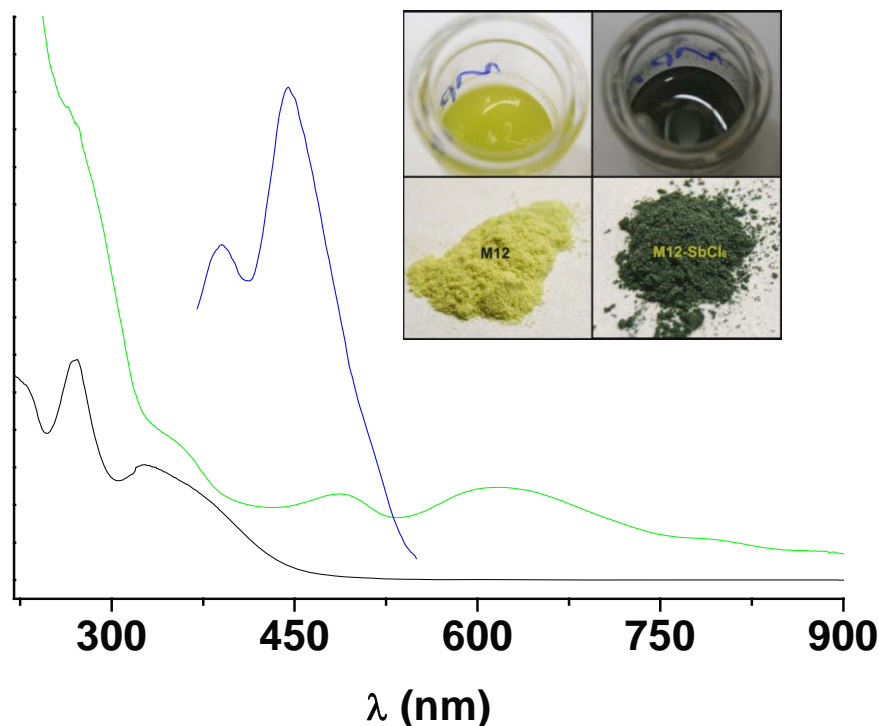


Figure 93. UV-Vis spectrum of the hybrid mesoporous material **M12** (black line), **M12-SbCl<sub>6</sub>** (green line), and the emission spectrum of the modified sample **M12** (blue line). The inset

picture demonstrates the color change caused by the oxidation of **M12** using  $\text{SbCl}_5$  in suspension and for the corresponding solid.

The oxidation of phenothiazine of **M12** was carried out with the one-electron acceptor antimony pentachloride in dichloroethan suspension. The treatment changes the material from a yellow to a greenish powder as illustrated in the inset picture of Figure 93. It also indicates that the phenothiazine molecules are reachable by  $\text{SbCl}_5$ . It is worth to note, that organic molecules are reachable even if they are located inside the wall. This has already been reported by others<sup>242</sup>. The absorption spectrum of the cationic material presents one band at 490 nm, another broad band at 620 nm. The absence of any significant absorption at long wavelengths ( $> 800$  nm) indicates that no intermolecular or intramolecular charge transfer occurs in this material. One reason for this might be the low concentration of the organic moiety in this material, another would be, that the phenothiazine molecules are mainly distributed inside the wall and are separated by silica species.

As we expected, the resulting deeply colored cationic materials preserve their color for weeks when stored under an atmosphere of nitrogen at ambient temperature. This discloses the high stability of phenothiazine radical cation in this type of hybrid materials.

#### EPR measurement

The electron paramagnetic resonance (EPR) spectrum can provide further evidence for the existence of stable phenothiazine radical cations in the hybrid materials. The EPR spectra of **M10-SbCl<sub>6</sub>** and **M12-SbCl<sub>6</sub>** are exemplarily shown in Figure 94. The g-values of these two samples are 2.0054 and 2.0050, respectively. The EPR signal is not well resolved, hyperfine coupling constants and anisotropic g-tensors cannot be determined. However, the high symmetry of the EPR spectrum indicates that the phenothiazine radicals are in a quite isotropic environment in the hybrid materials.

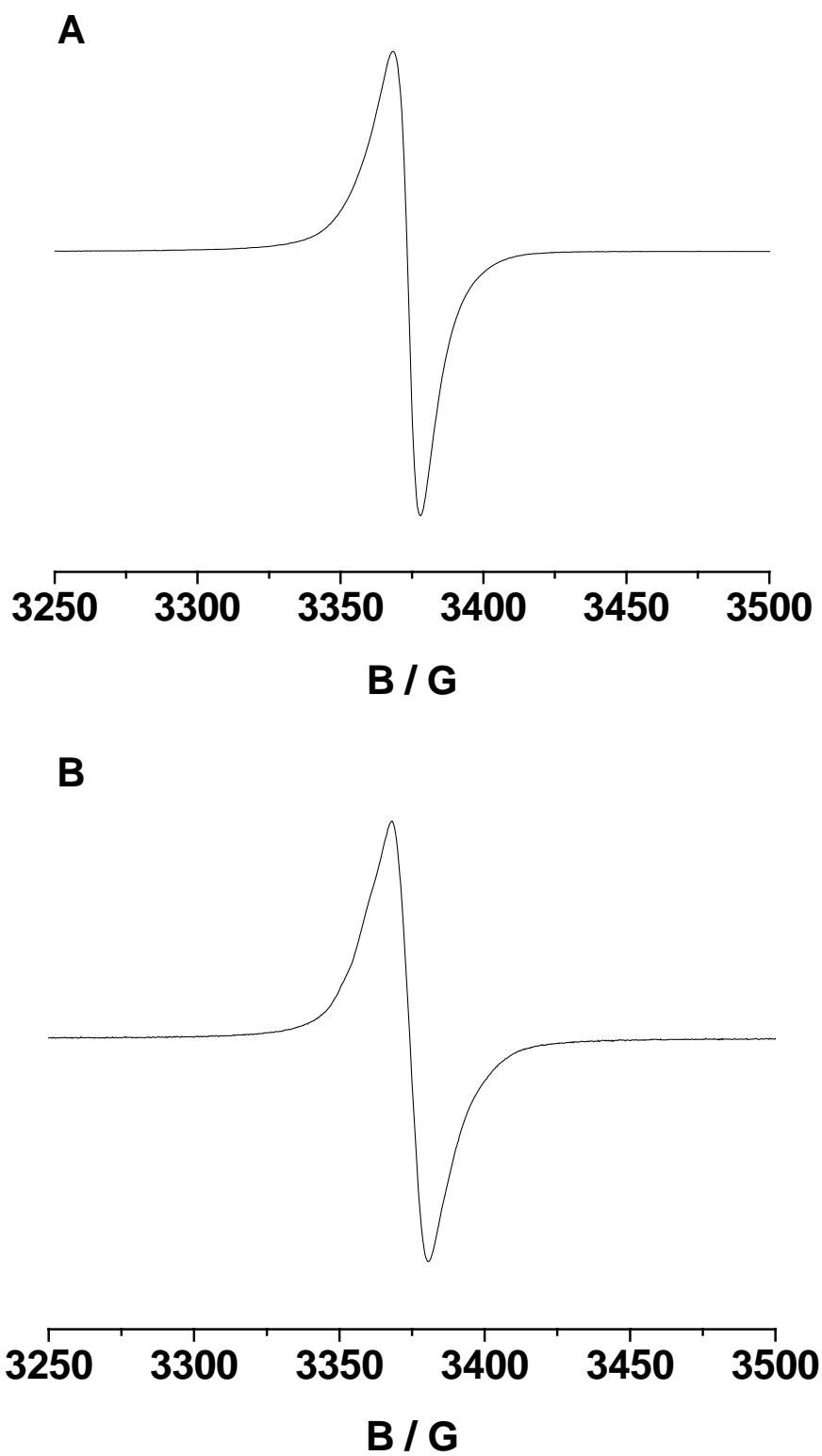


Figure 94. Q-band EPR spectra of (A) M10-SbCl<sub>6</sub> and (B) M12-SbCl<sub>6</sub> at 297 °C.

## **Chapter 3. Hybrid mesoporous materials containing covalently anchored *N*-phenylthiazolium salts as organo catalyst**

### **State of the art**

Since a couple of years organo catalysis has opened up new possibilities in organic synthesis and thus has found a remarkably increasing interest in chemical research <sup>243</sup>. A series of decisive breakthroughs could be realized especially for C–C coupling reactions using azole type catalyts. In a mechanistic sense, these reactions are often closely related to biological processes. Transferring some successful homogeneous organo catalysts into heterogeneous solid catalysts had been performed recently, exemplarily with proline <sup>244</sup>, and imidazolidine <sup>245</sup>.

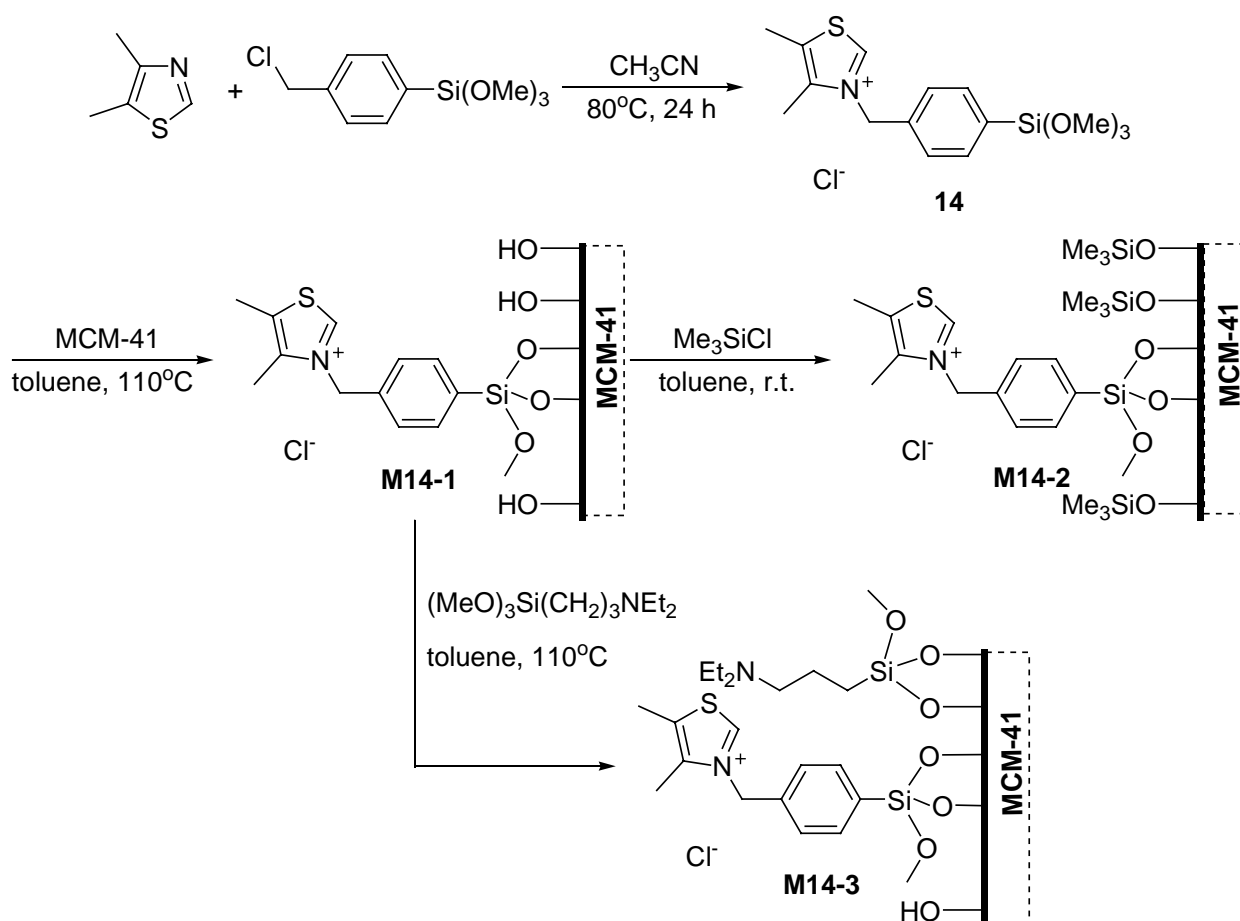
The thiazolium motif is found in thiamine (vitamine B<sub>1</sub>) in the nature, which is involved as the co-enzyme in a series of enzymatically catalyzed reactions such as C–C couplings in the fatty acid and carbohydrate metabolism. In organo catalysis, thiazolium salts have shown to be extremely useful catalysts for a number of nucleophilic acylation reactions, the most typical examples are benzoin condensation <sup>124</sup> and the Stetter reaction <sup>125</sup>. In theses process, the thiazolium fragment is used to generate an acyl anion equivalent starting from an aldehyde. The catalytically active species is a nucleophilic carbene. Based on this, thiazolium chemistry was extended to a series of further coupling reactions, like the Sila–Stetter reaction <sup>126</sup>,  $\alpha$ -amido ketones synthesis <sup>246</sup>, imidazole synthesis <sup>128</sup>, etc. The thiazolium motif even can be used as a catalyst for the living polymerization of lactones and lactides <sup>137</sup>.



## 3.1 Silica MCM-41 supported *N*-phenylthiazolium salts as organo catalyst for benzoin condensation and cross-coupling reactions

### 3.1.1 Synthetic procedures

The preparation of the hybrid heterogeneous catalysts **M14-1**, **M14-2**, and **M14-3** was processed as outlined in Scheme 18. Nucleophilic substitution of the chloro ligand of (*p*-chloromethyl)phenyltrimethoxysilane with 4,5-dimethylthiazole gave the ionic precursor **14**, which afforded the heterogenized catalyst **M14-1** when grafted onto mesoporous MCM-41. We have used a sub-stoichiometric amount of precursor **14** compared to the number of surface Si–OH groups which are available to allow further surface modification steps. It is known that the concentrations of surface silanol groups can dramatically influence the adsorption properties of MCM-41<sup>158</sup> and thus can considerably effect catalytic reactions<sup>240</sup>. Therefore, postsynthetic silylation using Me<sub>3</sub>SiCl was carried out to remove residual free Si–OH groups on the surface of **M14-1**, which achieved **M14-2**. Thiazolium catalyzed organic reactions require the presence of an external base, often a tertiary amine like NEt<sub>3</sub>, for the deprotonation of the carbon atom in the C2 position of the thiazolium ring. To include this base into the solid system, further post-synthetic treatment of **M14-1** with (*N,N*-diethylpropylamino)trimethoxysilane gave the double functionalized catalyst **M14-3** possessing basic co-catalytic sites on the surface in addition to the catalytically active thiazolium groups.

Scheme 18. Synthesis of thiazolium salt **14** and the derived heterogeneous catalysts

### 3.1.2 Structural characterization of the functionalized materials

In all stages of the preparation, the persistence of the mesostructure of the materials was monitored by powder X-ray diffraction (Figure 1). Corresponding to the hexagonal  $p6mm$  symmetry of the material, the XRD patterns of the parent MCM-41 show the (100), (110), (200) and (210) four Bragg reflections at  $2\theta$  angles of  $2\text{--}6^\circ$ , which indicate the highly ordered structure. After modified, the persistence of the first-order (100) and the second-order (110) and (200) reflections can be observed for all hybrid samples, which suggests the well preserved structure of the ordered materials<sup>247</sup>. A shift of the peak maximum can be observed after modification. This is probably because of anchoring of the thiazolium leads to a slight shrinkage of porous system, or the further shrinkage of silica wall during the heated

post-grafting process. The relative intensities of the XRD reflections of the catalysts also slightly decrease compared to neat MCM-41, which originates from the less diminished mesostructural order and/or reduced scattering contrast between the silica wall and the porous system<sup>248</sup>. It indicates the immobilization of the thiazolium salt and the subsequent surface modifications in the MCM-41 channels<sup>249</sup>.

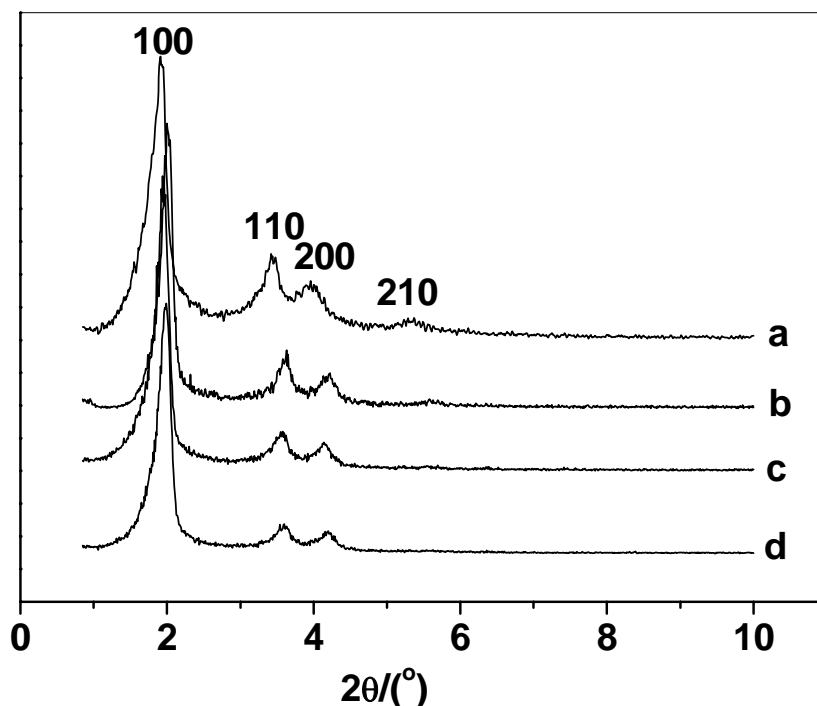


Figure 95. Powder XRD patterns of (a) neat MCM-41, (b) **M14-1**, (c) **M14-2** and (d) **M14-3**.

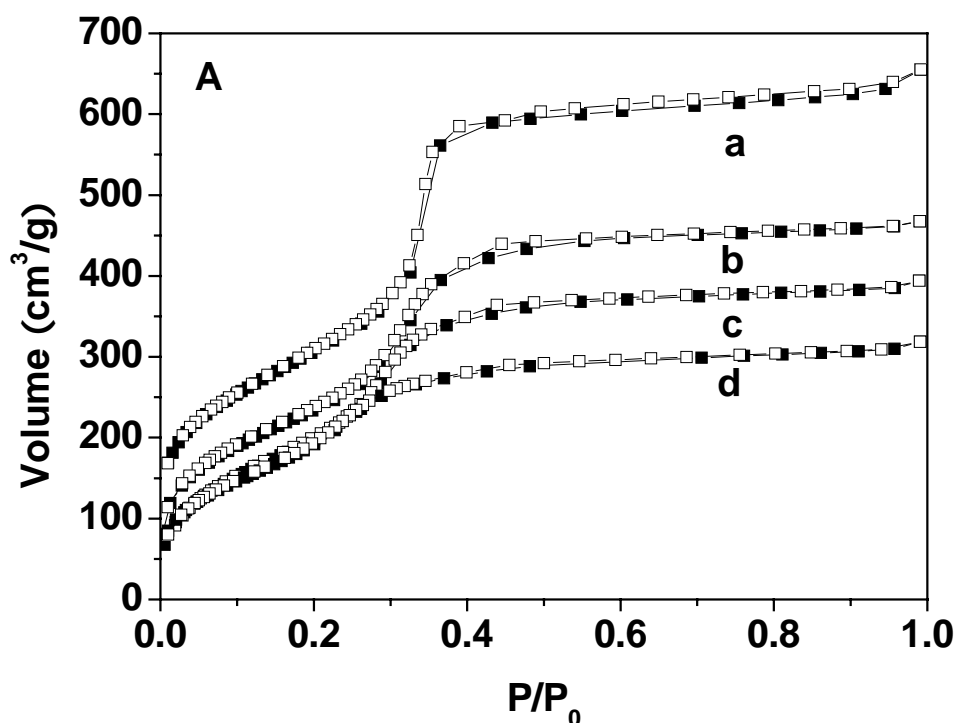
Surface areas, pore volumina and pore size distributions were determined by  $N_2$  adsorption–desorption measurements, the results are listed in Table 10. All samples displayed typical type IV isotherms (definition by IUPAC)<sup>250</sup>, the absence of hysteresis in the  $N_2$  isotherm of all the samples indicates the uniform pore sizes and ordered arranged cylindrical channels without any intersecting disordered channels. Sharp capillary condensation steps in the range of low  $p/p_0$  values (Figure 96 A), which are present in the isotherms of all the materials, are characteristic for mesoporous materials with narrow pore size distributions<sup>166</sup>. The pore size distribution curves, deduced from the desorption plot of the isotherm (Figure 96 B), suggest a step decreasing of the pore sizes, in order of **M14-3** < **M14-2** < **M14-1** <

**MCM-41**, due to the subsequent modification with different organo silanes. In addition, compared to the parent mesoporous MCM-41, the modified samples also exhibit a decrease of pore volume and surface areas, due to the presence of bulky organic molecules. This is a further indication for the functionalization of the internal surface of the mesoporous materials by covalent grafting<sup>70</sup>.

Table 10. Pore parameters and compositional information of parent MCM-41 and the modified MCM-41 based catalysts

sample	BET surface area (m <sup>2</sup> /g)	pore volume (cm <sup>3</sup> /g)	pore diameter (nm) <sup>a</sup>	loading of organic groups			
				element analysis			thermogravimetry weight loss (%) <sup>b</sup>
				C (%)	H (%)	N (%)	
<b>MCM-41</b>	1123	0.98	2.83				
<b>M14-1</b>	897	0.71	2.69	9.35	1.86	0.48	9.4
<b>M14-2</b>	766	0.64	2.52	12.41	2.37	0.34	10.7
<b>M14-3</b>	733	0.48	2.28	18.17	3.42	2.31	16.3

<sup>a</sup> pore diameter was calculated from adsorption branch b weight loss in the range of 300-600 °C.



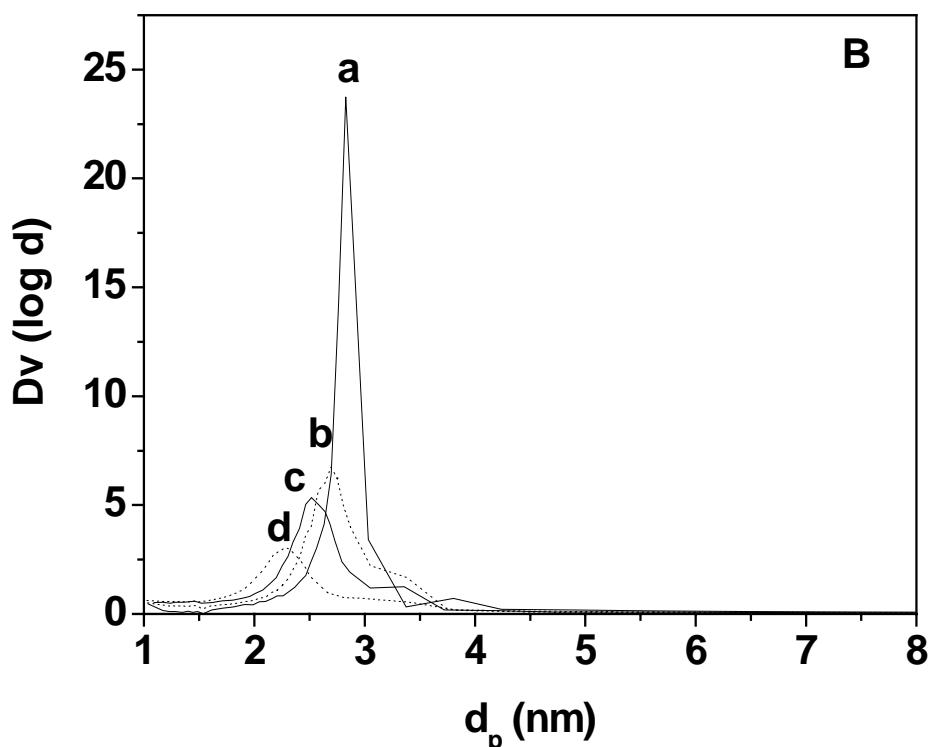


Figure 96. **A**) N<sub>2</sub> adsorption-desorption isotherms of (a) parent **MCM-41**, (b) **M14-1**, (c) **M14-2**, (d) **M14-3**; adsorption points are marked by solid circles and desorption points by empty circles. **B**) Pore size distributions of (a) parent **MCM-41**, (b) **M14-1**, (c) **M14-2**, (d) **M14-3**.

All three samples were analyzed by elemental analysis (CHN) and thermogravimetry (TG) to confirm the stepwise functionalization of the hybrid materials (Table 10). The loading of the thiazolium salt on sample **M14-1** is 0.34 mmol/g, which can be calculated from its nitrogen content (element analysis). This is also comparable to the result of the TG analysis. The amount of thiazolium salt in sample **M14-2** is 0.24 mmol/g, the amount of Me<sub>3</sub>Si can be roughly calculated as 1.10 mmol/g. For the *N,N*-dimethylaminopropyl modified sample **M14-3**, it is impossible to calculate the amount of the thiazolium groups and of the amine base separately, because of both of them contain nitrogen in the molecule. However the significant increase of the nitrogen amount and of the value of weight loss during TG indicate the introduction of the *N,N*-diethylpropylamino groups in the materials.

### 3.1.3 Characterization of the functionalized materials by solid-state NMR and IR spectroscopy

$^{27}\text{Si}$  CP-MAS NMR spectra provide direct evidence for the covalent incorporation organo catalyst system (Figure 97). The spectra of neat MCM-41 exhibits three resonance at -90.0, -102.5, -112.4 ppm corresponding to  $(\text{HO})_2\text{Si}(\text{OSi})_2$  ( $\text{Q}^2$ ),  $\text{HOSi}(\text{OSi})_3$  ( $\text{Q}^3$ ) and  $\text{Si}(\text{OSi})_4$  ( $\text{Q}^4$ ) species of the silica framework<sup>251</sup>. The  $\text{Q}^3$  sites are associated with isolated Si-OH groups, and the  $\text{Q}^2$  sites correspond to geminal silandiols. Grafting the thiazolium salt **14** onto the surface results makes the  $\text{Q}^2$  signal disappear, decreases the  $\text{Q}^3$  intensity and concomitant increases the  $\text{Q}^4$  intensity. For the organic/inorganic hybrid materials **M14-1**, **M14-2** and **M14-3** there are additional resonances for the organo silicon species  $\text{R-Si}(\text{HO})_2(\text{OSi})$  ( $\text{T}^1$ ),  $\text{R-Si}(\text{HO})(\text{OSi})_2$  ( $\text{T}^2$ ) and  $\text{RSi}-(\text{OSi})_3$  ( $\text{T}^3$ ). In general these resonances are expected to appear at -49, -59, -69 ppm<sup>252</sup>, which is the case for the amino functionalized system **M14-3**. For compounds **M14-1** and **M14-2**, these resonances are found at -65 ( $\text{T}^2$ ) and -74 ppm ( $\text{T}^3$ ), the resonance of  $\text{T}^1$  is too low in intensity to be observed. This means, that depending on the local chemical situation, the incoming organo silicon derivative finds at the anchoring point, it mainly will bind to two or three surface Si-OH groups. Since the  $^{29}\text{Si}$  resonance of the  $\text{SiMe}_3$  moiety in compound **M14-2** is observed with the expected chemical shift of around 12.0 ppm<sup>51</sup>, the differences of the  $\text{T}^2$  and  $\text{T}^3$  values should be due to the fact that an ionic species is grafted onto the surface. For the catalysts **M14-2** and **M14-3**, modified by  $\text{Me}_3\text{Si}$  and  $\text{Et}_2\text{N}(\text{CH}_2)_3\text{Si}$  groups respectively, a further decrease of the  $\text{Q}^3$  and  $\text{Q}^2$  intensities is observed parallel to an increase of the  $\text{Q}^4$  intensity. The changes in the relative intensities of the signals can be explained by the redistribution of the silicon sites during the surface modification<sup>253</sup>.

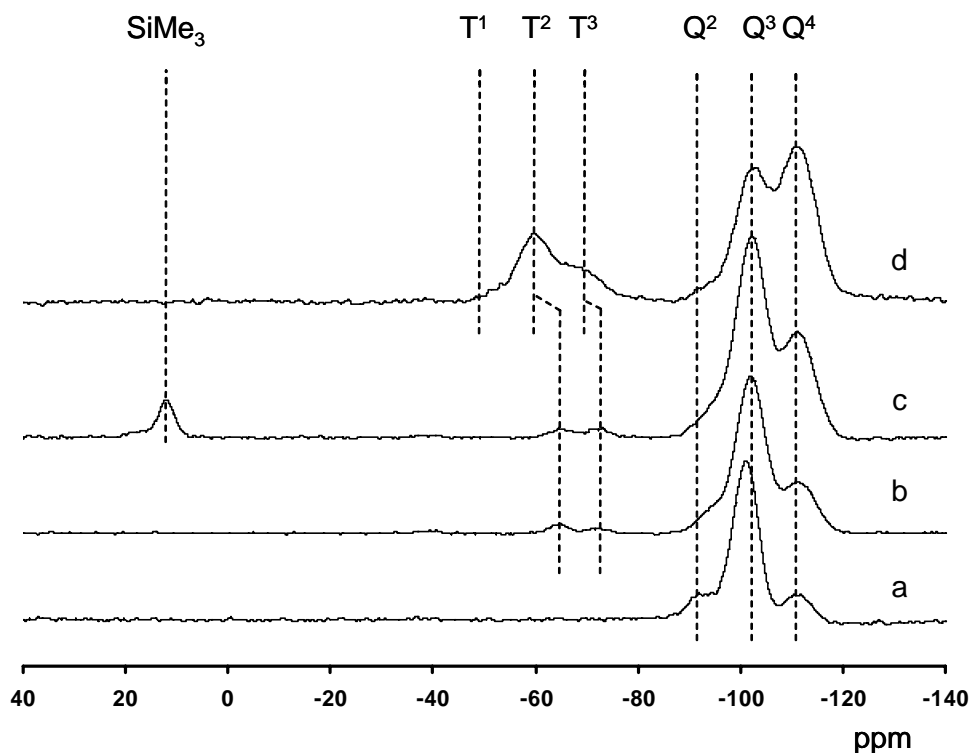


Figure 97. Solid state  $^{29}\text{Si}$  CP-MAS NMR spectra of (a) neat **MCM-41**, (b) **M14-1**, (c) **M14-2**, and (d) **M14-3**.

The successful grafting of the organic components was additionally verified by solid-state  $^{13}\text{C}$  CP-MAS NMR spectroscopy (Figure 98). **M4-1** presents a spectrum similar to that of the free thiazolium salt **14**, the resonances of which are assigned by the dashed lines. **M14-2** shows an almost similar spectrum, suggesting that the structure of the organic moiety is not affected by reaction of residual Si-OH groups with  $\text{Me}_3\text{SiCl}$ . The  $\text{Me}_3\text{SiO}$  moieties on the surface of **3** give a very strong resonance at  $-0.56$  ppm<sup>51</sup>. Sharp resonances in the spectra of **M14-1**, **M14-2**, and **M14-3** arising at about 16 ppm can be assigned to one of carbon atoms of ethanol incorporated in the materials during the Soxhlet extraction process.

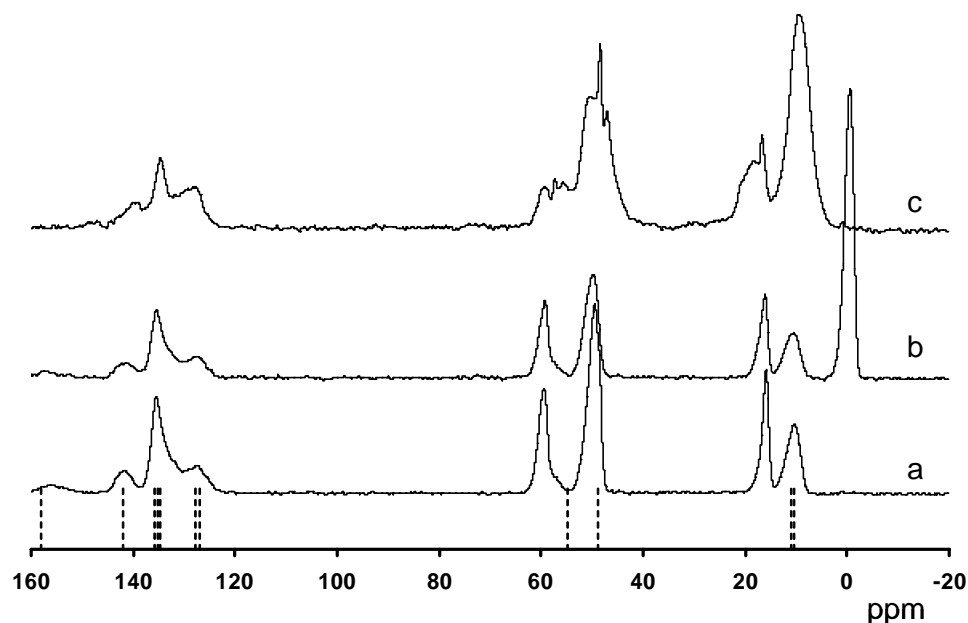


Figure 98. Solid state  $^{13}\text{C}$  CP-MAS NMR spectra of (a) **M14-1**, (b) **M14-2**, and (c) **M14-3**; the dashed lines are indicating the high resolution  $^{13}\text{C}$  NMR resonances of the precursor compound **14**.

In parallel, FT-IR spectroscopy was used to provide more information about the surface modification of the materials **2**, **3** and **4** (Figure 99). The spectra of all modified materials show an absorption in the range of  $3600\text{--}3200\text{ cm}^{-1}$  which can be assigned to the OH stretching vibration of silanol groups, the bands at  $1200$ ,  $1100$  and  $800\text{ cm}^{-1}$  can be attributed to the Si–O stretching vibration, and the peak at  $460\text{ cm}^{-1}$  is assigned to the bending vibrations of Si–O<sup>210</sup>. Additionally to these signals, which are the characteristic bands of SiO<sub>2</sub>, the spectra of the samples **M14-1**, **M14-2** and **M14-3** also present some further peaks, which origin from the modification with the organic component. An absorption at  $2980\text{--}2850\text{ cm}^{-1}$ , can be attributed to the CH stretching vibrations of alkyl groups as well as a band at  $1450\text{ cm}^{-1}$  is due to CH<sub>2</sub> and CH<sub>3</sub> deformations<sup>168</sup>. Subsequent to the modification with Me<sub>3</sub>Si or Et<sub>2</sub>N(CH<sub>2</sub>)<sub>3</sub>Si, an increasing intensity of these bands can be observed, especially in



the case of aminopropyl modification. These results indicate the anchoring of organic molecules on the surface of the silica material.

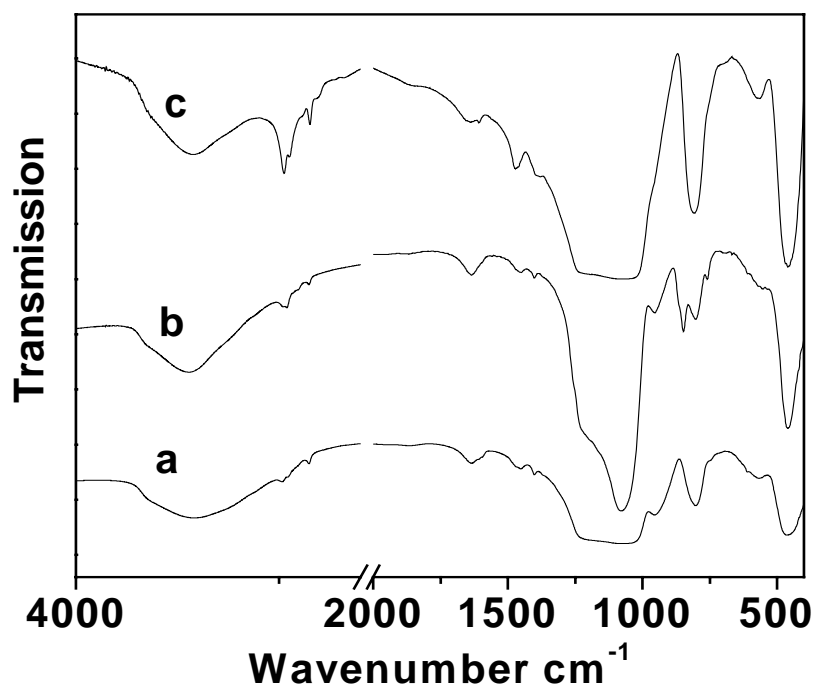
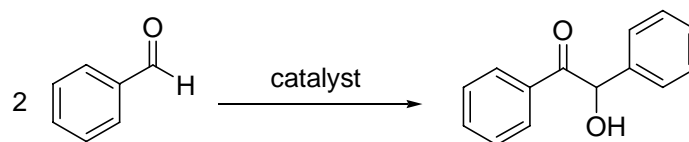


Figure 99. FT-IR spectra of sample (a) **M14-1**, (b) **M14-2**, and (c) **M14-3**.

### 3.1.4 Catalytic properties of the heterogenized thiazolium salts

The performance of the synthesized catalysts was first investigated for the benzoin condensation with benzaldehyde, which is a typical test reaction for thiazolium based organo catalysts (Scheme 19)<sup>254</sup>. An initial survey over a series of solvents and the amount of external base demonstrated that methanol would be the solvent of choice and Et<sub>3</sub>N concentrations of about 0.22 mol/l should give optimum results. An influence of the surface structure of the support on the activity of the hybrid catalyst was observed, since the application of the silylated system **M14-2** instead of **M14-1** slightly increases the yield of benzoin from 62 % up to 66%. The yields can further be improved up to 81% by doubling the reaction time to 48 h (Table 2).



Scheme 19

Table 11. Activity of the heterogenized catalysts in the benzoin condensation of benzaldehyde <sup>a</sup>

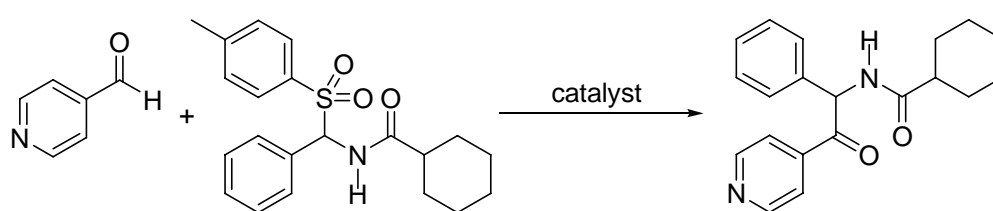
entry	sample	[Et <sub>3</sub> N](mol/l)	solvent	[BA]:[Et <sub>3</sub> N] <sup>b</sup>	yield(%) <sup>c</sup>
1	<b>M14-1</b>	0.22	CH <sub>2</sub> Cl <sub>2</sub>	3:1	31
2	<b>M14-1</b>	0.22	MeOH	3:1	62/74 <sup>d</sup>
3	<b>M14-2</b>	0.22	MeOH	3:1	66/81 <sup>d</sup>
4	<b>M14-1</b> <sup>e</sup>	0.22	MeOH	3:1	18/25 <sup>d</sup>
5	<b>M14-2</b> <sup>e</sup>	0.22	MeOH	3:1	42 <sup>d</sup>
6	<b>M14-3</b>	-	MeOH	3:1	11/20 <sup>d</sup>
7	<b>M14-1</b>	-	MeOH	3:1	-

<sup>a</sup> all reactions were performed in refluxing solvents, with 0.67 mol/l of benzaldehyde [BA] and 0.22 mol/l of Et<sub>3</sub>N, and 1.5 mol % catalyst with respect to benzaldehyde. <sup>b</sup> molar ratio. <sup>c</sup> determined by GC-MS analysis using biphenyl as internal standard. <sup>d</sup> yields of benzoin after 24h/48h. <sup>e</sup> the catalyst **2** was used in a second run.

It's worth to point out, that the catalyst **M14-3** containing a tertiary amine covalently grafted on the surface, gives benzoin with 20% yield in a 48 h run in the absence of any external base. Although the yield of benzoin is significantly lower than for the combination of **M14-1**/triethylamine (62% after 24 h) we successfully could proof our principle, that organic basic sites grafted on the surface of such materials can substitute the external base Et<sub>3</sub>N (catalysts **M14-1** and **M14-2** do not give any conversion in the absence of the amine). We assign the reduced activity to the fact that only a part of the basic sites will be in sufficient close proximity to the thiazolium centres and thus will be able to activate the catalyst by deprotonation. Therefore, a longer alkyl chain between the nitrogen and the silicon atom should be beneficial in this context.

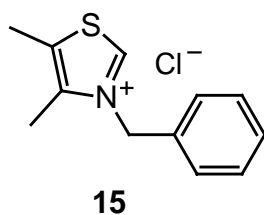
Unfortunately, the reactivity of catalyst **M14-2** dropped dramatically after recycling. In the second run a yield of only 25% could be obtained after a 48 h reaction. This result may be due to the use of protic methanol as the solvent in combination with basic Et<sub>3</sub>N, which might degrade the support and result in leaching of the active sites or in a restructuring of the mesoporous material. Moreover, the relatively less dropped recycle in result of the silylated and thus more hydrophobic catalyst **M14-2** from 81% (entry 3) to 42 % (entry 5), indirectly proves the significant influence of the protic solvent to hydrophilic surface. On the basis of these observations, we were convinced that these phenomena could be avoided by performing a catalytic reaction in an aprotic and less polar solvent.

We thus switched to the thiazolium catalyzed cross-coupling of aldehydes with acyl imines to  $\alpha$ -amido ketones<sup>246</sup>, a reaction which can be carried out in a broad variety of aprotic solvents. This reaction not only can effectively produce biologically important  $\alpha$ -amido ketones but also demonstrates the versatility of the Stetter protocol<sup>255</sup>. As expected, 4-pyridinecarbaldehyde and an  $\alpha$ -tosylated amide can be transferred into the desired  $\alpha$ -amido ketone in the presence of the heterogenized organo catalysts with good to excellent yields (Scheme 20).



Scheme 20.

In the first step of the optimization of the reaction conditions, the influence of the solvent on the catalytic performance of **M14-1** was tested (Table 12). It turned out, that non-protic CH<sub>2</sub>Cl<sub>2</sub> gave the best results (entry 1), which was also found for the appropriate homogenous catalyst **15** (entry 5, Scheme 21).



Scheme 21

Table 12. Solvent effects on the addition of 4-pyridinecarbaldehyde to *N*-[(4-methylphenylsulfonyl)(phenyl)methyl]cyclohexanecarboxamide catalyzed by **M14-1** and **15**<sup>a</sup>.

entry	catalyst	solvent	Et <sub>3</sub> N	time (h)	yield <sup>e</sup> (%)
1	<b>M14-1</b> <sup>b</sup>	CH <sub>2</sub> Cl <sub>2</sub>	5	2	82
2	<b>M14-1</b> <sup>c</sup>	CH <sub>3</sub> CN	5	2	71
3	<b>M14-1</b> <sup>c</sup>	THF	5	2	49
4	<b>M14-1</b> <sup>c</sup>	toluene	5	2	30
5	<b>15</b> <sup>b,d</sup>	CH <sub>2</sub> Cl <sub>2</sub>	5	2	97
6	<b>15</b> <sup>c,d</sup>	CH <sub>3</sub> CN	5	2	85
7	<b>15</b> <sup>c,d</sup>	THF	5	2	59
8	<b>15</b> <sup>c,d</sup>	toluene	5	2	41

<sup>a</sup> the reaction was performed with 1.0 equiv of *N*-[(4-methylphenylsulfonyl)-(phenyl)methyl]cyclohexanecarboxamide, 1.1 equiv of 4-pyridinecarbaldehyde, 5 equiv Et<sub>3</sub>N, and 7 mol % of catalyst with respect to tosylated amide in 15 mL of solvent. <sup>b</sup> reaction temperature: 35°C; <sup>c</sup> reaction temperature: 60°C. <sup>d</sup> homogeneous catalysis with soluble ligand. <sup>e</sup> isolated yield by chromatography (EtOAc/Hexane).

Next, the amount of Et<sub>3</sub>N was optimized with CH<sub>2</sub>Cl<sub>2</sub> as the solvent. With two equivalents of Et<sub>3</sub>N, **M14-1** gave 62% yield after 2 h (Table 13, entry 1). The decrease of the yield may be assigned to an interference of Et<sub>3</sub>N with acidic surface sites, since the silylated catalyst **3** gave the product in 70% under the same reaction conditions (entry 3). Increasing the amount of Et<sub>3</sub>N to five equivalents increased the yield up to 82% for **M14-1** (entry 4) and

to more than 90% for the silylated congener **M14-2** (entry 5). We assign this also to a facilitated diffusion of the substrates, the base and product in the trimethylsilylated pores.

Table 13. Activity of the catalysts in the addition of 4-pyridinecarbaldehyde to *N*-[(4-methylphenylsulfonyl) (phenyl)methyl] cyclohexanecarboxamide <sup>a</sup>.

entry	catalyst	Et <sub>3</sub> N	time (h)	yield <sup>d</sup> (%)
1	<b>M14-1</b>	2	2	62
2	<b>M14-1</b> <sup>b</sup>	2	24	50
3	<b>M14-2</b>	2	2	70
4	<b>M14-1</b>	5	2	82
5	<b>M14-1</b> <sup>b</sup>	5	24	71
6	<b>M14-2</b>	5	2	91
7	<b>M14-2</b> <sup>b</sup>	5	24	79
8	<b>M14-2</b> <sup>c</sup>	5	24	67
9	<b>M14-3</b>	0	2	-
10	neat-MCM 41	5	2	-

<sup>a</sup> the reaction was performed with 1.0 equiv of *N*-[(4-methylphenylsulfonyl)-(phenyl)methyl]cyclohexanecarboxamide, 1.1 equiv of 4-pyridinecarbaldehyde, and 7 mol % of catalyst with respect to tosylated amide in 15 mL of CH<sub>2</sub>Cl<sub>2</sub> at 35°C. <sup>b</sup> the catalyst was reused for a second run, <sup>c</sup> the catalyst was reused for a third run. <sup>d</sup> isolated yield by chromatography (EtOAc/Hexane).

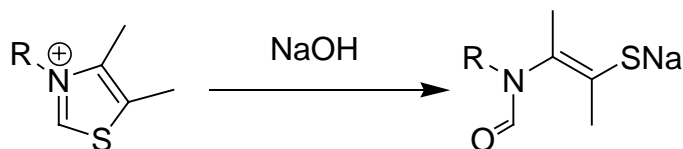
The catalysts **M14-1** and **M14-2** present promising stability and recyclability, with only a low decrease of activity after recycling (entries 2, 5, 7, and 8). With the amino functionalized system **M14-3** no product formation could be detected (entry 9). In this reaction, the base is required for the conversion of the tosylamide to the acylimine as well as for the deprotonation of the thiazolium moiety <sup>246</sup>. We assume that the first step requires a free base, since amino functionalization of the surface worked in benzoin condensation, where deprotonation of the thiazolium catalyst is required too. In this case, the amount of anchored base could be

increased by introducing a lot of a long chain amino compound or by combining **M14** with polymer amin compounds as the co-catalyst.

### 3.2 One step co-condensation synthesis of *N*-phenylthiazolium salt functionalized silica SBA-15

#### State of the art

We attempted to attach this thiazolium salt on MCM-41 by using one-pot co-condensation of **14** with TEOS in the presence of CTBA and NaOH. However, the product has no activity for both of the testified reactions. The reason is, that thiazole ring will open in NaOH/H<sub>2</sub>O solution, as illustrated in Scheme 22. An alternative synthesis way would be performed in an acid condition. Additionally, a larger pore substrate like SBA-15 is also attractive for the fast delivery of reagents to the catalyst point. Thus, two thiazolium salts modified organo catalysts prepared by co-condensation method with SBA-15 structural substrate.

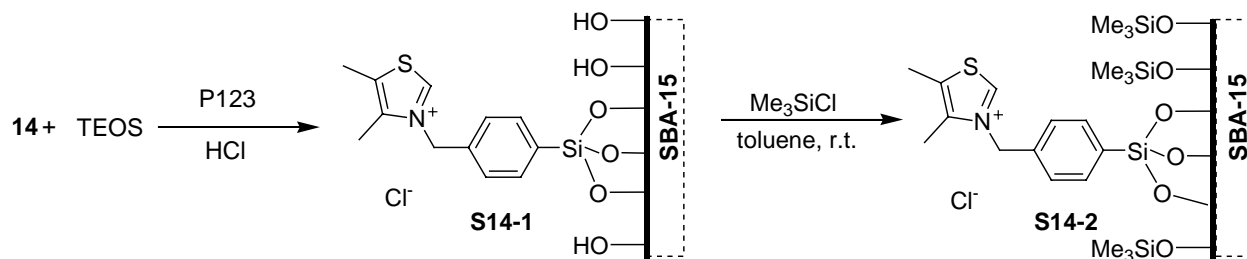


Scheme 22.

#### 3.2.1 Synthetic procedures

The preparation of the hybrid heterogeneous catalysts **S14-1** and **S14-2** was processed as outlined in Scheme 23. The ionic precursor **14** was mixed with TEOS. A one pot co-condensation process using P123 as the template under acidic conditions, afforded the heterogenized catalyst **S14-1**. Following extraction by EtOH eliminates the organic template and releases the pores. This hybrid catalyst has the SBA-15 type of mesostructure with an amorphous silica framework, which also provides sufficient unoccupied silanol groups for further modification. From the former result, it discloses that the concentrations of surface

silanol groups have an important influence on the catalytic reactions in this system. Therefore, postsynthetic silylation using  $\text{Me}_3\text{SiCl}$  was carried out to remove residual free Si-OH groups on the surface of **S14-1**, which achieved **S14-2**.



Scheme 23. Synthesis of a heterogenous organo catalyst by a one step co-condensation method.

### 3.2.2 Structural characterization of the functionalized materials

The mesostructures of the hybrid catalysts **S14-1** and **S14-2** were determined by a X-ray diffraction (XRD) measurement. The XRD patterns of these two samples are presented in Figure 100. Three (hkl) reflections of (100), (110) and (200) in the  $2\theta$  range of  $0.8\text{--}2^\circ$  were observed, which can be indexed to the two-dimensional (2D) hexagonal  $p6mm$  symmetry. However, a less intense diffraction of the (100) plane indicates slightly distorted hexagonally symmetric channels, due to the strain generated from the covalently bound organic groups, or the ionic nature of the organic precursor **14**, which might disturb the surfactant-silicate assembly, leading to a less ordered mesophase in the co-condensation synthesis process. After further silylation with  $\text{Me}_3\text{SiCl}$ , the relative intensities of (100) reflection of **S14-2** slightly decreases compared to **S14-1**, which indicates that the further modifying organic groups are introduced, with reducing scattering contrast between the silica wall and the porous system<sup>248</sup>.

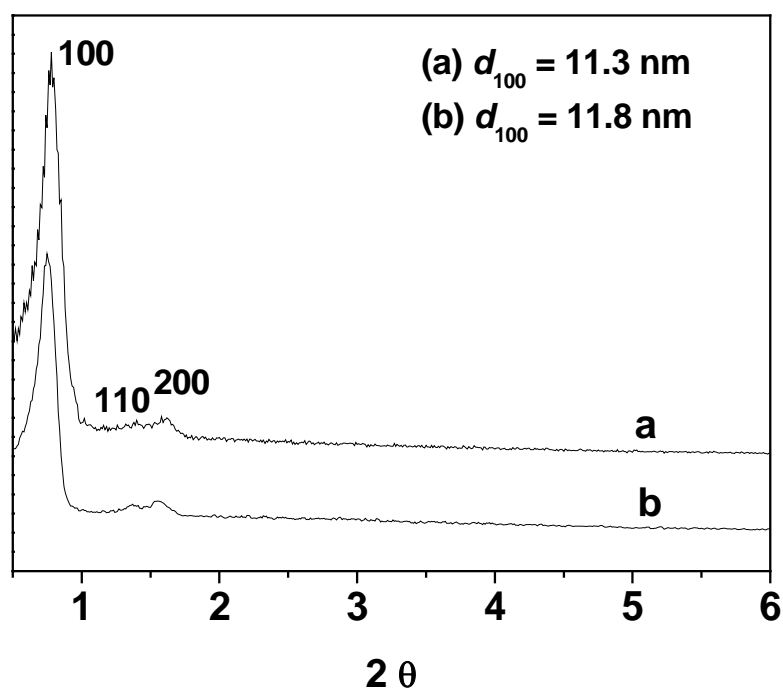


Figure 100. Powder XRD patterns of (a) S14-1, (b) S14-2

The  $N_2$  isotherm of **S14-1** displays a well-defined hysteresis loop of type H1 according to the IUPAC classification<sup>192</sup> (Figure 101 A). This type of hysteresis loop is related with capillary condensation and desorption in opened cylindrical and large mesopores. The sharp adsorption and desorption branch of this isotherm is indicative for a narrow pore size distribution, which is confirmed by the calculated pore size distribution (PSD) curve deduced from desorption branch using the BJH method (Figure 101 B). The Brunauer–Emmett–Teller (BET) surface area of **S14-1** calculated from the adsorption data at relative pressures of 0.05–0.20 in the isotherms, was  $634 \text{ m}^2\text{g}^{-1}$ , with a pore size centering at 5.67 nm. Similarly adsorption desorption behavior is preserved by the silylated material **S14-2**, which implies that the further modification has no severe influence on the structure of substrate material. The position of the condensation point obtained a slight shift to lower relative pressure, which presents a small decrease in pore size. A narrow pore size distribution curve of **S14-2** is similar to the parent substrate **S14-1** (Figure 101 B). The main pore size, pore volume and specific surface areas (BET) of these two samples are listed in Table 14. A slightly decrease



in some parameters can be seen after further hydrophobic modification, due to the introduction of more organic compounds into the channel.

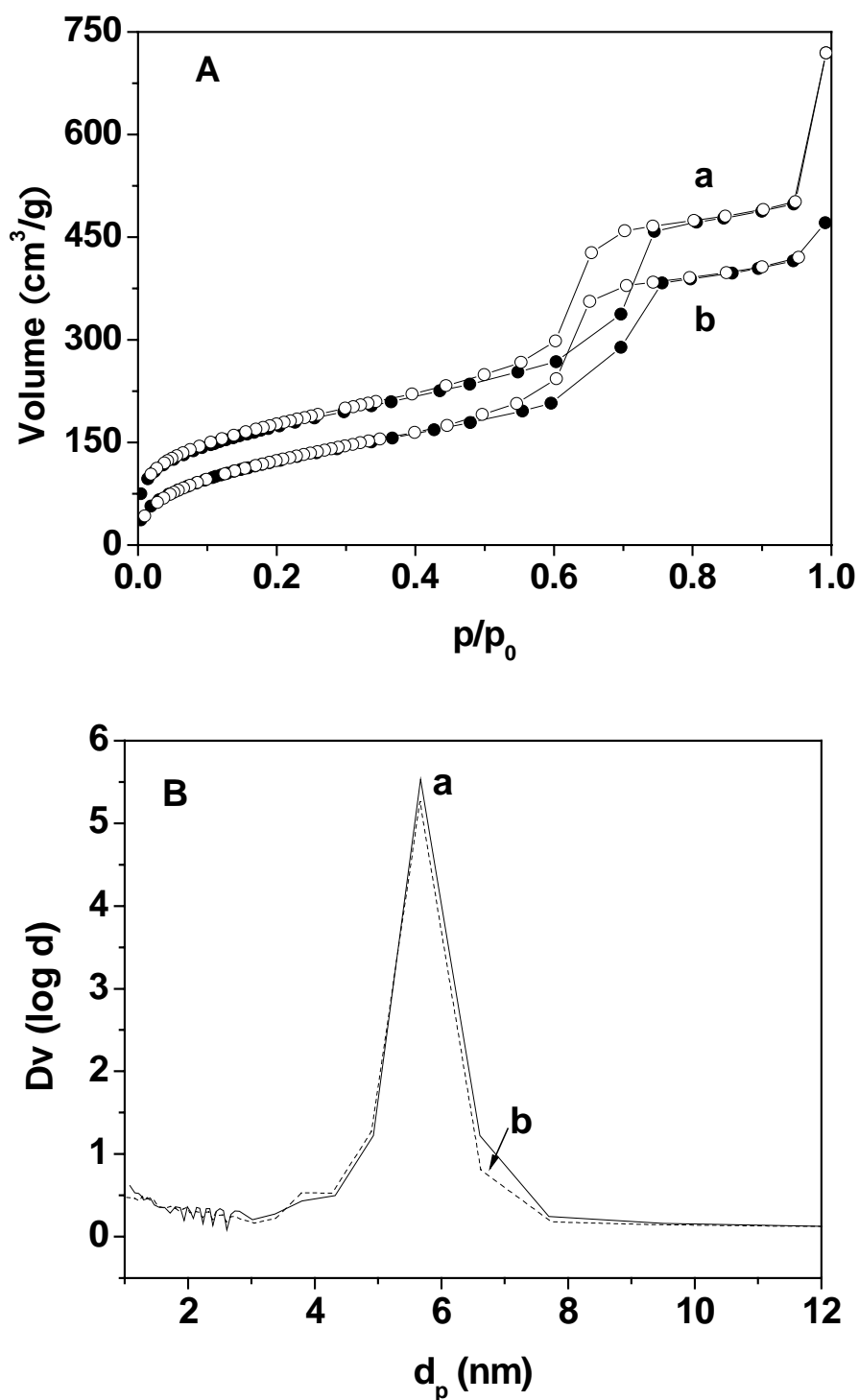


Figure 101. **A**)  $N_2$  adsorption-desorption isotherms of (a) **S14-1**, and (b) **S14-2**; adsorption points are marked by solid circles and desorption points by empty circles. **B**) pore size distributions of (a) **S14-1**, and (b) **S14-2**.

Table 14. Pore parameters and compositional information of the hybrid catalysts **S14-1** and **S14-2**.

Sample	$d_{100}^a$ (nm)	$a_0^b$ (nm)	$S_{BET}^c$ ( $m^2 g^{-1}$ )	$V_p^d$ ( $cm^3 g^{-1}$ )	$D_p^e$ (nm)	$w_t^f$ (nm)	content of organo catalyst loading <sup>g</sup>			
							C	H	N	amount
<b>S14-1</b>	11.3	13.0	634	0.77	5.67	7.33	15.47	3.15	0.62	0.44
<b>S14-2</b>	11.8	13.6	476	0.64	5.65	7.95	18.46	3.99	0.48	0.34

<sup>a</sup>  $d_{100}$  is the (100) spacing; <sup>b</sup>  $a_0$  the cell parameter ( $a_0 = 2d_{100}/\sqrt{3}$ ); <sup>c</sup>  $S_{BET}$  is the BET surface area; <sup>d</sup>  $V_p$  = pore volume; <sup>e</sup>  $D_p$  = pore diameter; <sup>f</sup>  $w_t$  is the wall thickness  $a_0 - D_p$ ; <sup>g</sup> calculated according to the content of nitrogen (CHN element analysis).

### 3.2.3 Characterization of the heterogenized catalyst by thermogravimetry, solid-state NMR and IR spectroscopy

Elemental (CHN) and thermogravimetric analysis were carried out to investigate the loading of thiazolium salts on the hybrid materials. The elemental analysis results are listed in Table 14. A quantificational calculation of the amount of the introduced thiazolium salt based on the N content, reveals 0.44 mmol/g of the thiazolium salt on the sample **S14-1**, and 0.34 mmol/g on the sample **S14-2**. Figure 102 presents the TG and DTG curves of these two samples. The weight loss below 150 °C with an endothermic peak can be attributed to the desorption of physisorbed water. It is apparent that **S14-1** absorbs more water than **S14-2**. This result provides a direct evidence for the hydrophobic surface of the Me<sub>3</sub>Si modified heterogenized catalyst. The decomposition of the organic compound begins at 200 °C and the weight loss is lasting up to 650 °C. In the case of **S14-1** a large weight loss (7.8 %) combined with a double peak in the DTG curve (a broad peak at ~ 260 °C and a sharp peak at ~ 300 °C) can be observed, which implies a two steps decomposition of the thiazolium salt. There is no significant peak centered at ~ 170 °C, which is the well known decompositions temperature of P123<sup>256</sup>, indicating that the remnant amount of template is small. A sharp exothermic peak

appears at  $\sim 300$  °C concomitant with a fast weight loss, due to the combustion of the thiazolium salt. This is most probably attributed to the thiazole ring. The sustaining weight loss from 330 °C to 650 °C combined with a stable exothermic curve, might be due to the decomposition of the phenyl group of the thiazolium salt, the residual carbonaceous, and the dehydroxylation of the silica framework<sup>257</sup>. The total weight loss from 150 °C to 650 °C is 16.2 %, which is 5.7 % higher than the prediction from the elemental analysis data (ca. 10.5 %). This discrepancy is likely to arise from a combination of (i) residual small amounts of template; (ii) unhydrolyzed –OMe groups of the organic silane (see the <sup>13</sup>C CP-MAS NMR result); (iii) removing of water due to the condensation of silanol groups of the silica framework.

The TG–DTG behaviors of these two samples are rather similar, which is indicating that the further silylation reaction has no influence on the modified thiazolium salt. However, different weight loss can be calculated based on three temperature ranges (see Table 15). It is worth to point out that a small shoulder peak can be observed in the DTG curve of **S14-2** at ca. 180 °C concomitant with an endothermic peak in the heat flow curve (marked by a star in Figure 102), which should be assigned to the evaporation of silane (TMCS) monomer and dimers absorbed at the material surface<sup>258</sup>. For easier comparison, a weight loss ratio of different temperature range ( $W_{RT} = W_T/W_{150-650}$ , which  $W_T$  is the weight loss in different temperature range, T present the temperature range, and  $W_{150-650}$  is the total weight loss from 150 to 650 °C) is given. The  $W_{R150-330}$  of **S14-2** is less than of **S14-1**, due to the further modification decreases the weight ratio of the thiazolium salt. This result is consistent with the result of the elemental analysis, and further proves that the decomposition at this temperature is mainly attributed to the thiazole ring. The  $W_{R330-650}$  of **S14-2** is higher than of **S14-1**, which results from the introduced Me<sub>3</sub>Si groups. The covalently bound trimethylsilane is stable and normally burns off at high temperatures<sup>258</sup>. Meanwhile, the presence of the

micropore in SBA-15<sup>36</sup> can provide a protection for this small group and shift the decomposition to even higher temperatures. The total weight loss from 150 to 600 °C of **S14-2** is 16.9 %. We suppose that the essential weight loss attributed to the condensation of silanol groups of the framework and the remaining organic surfactant is similar in these two samples. Then the information of the elemental analysis gives the accurate amount of thiazolium salt in **S14-2** (8.1 wt%). The essential weight loss of **S14-1** is 5.7 % corresponding to 5.9 % of **S14-2**. Thus, the amount of modifying Me<sub>3</sub>Si groups can be estimated to ca. 0.64 mmol/g.

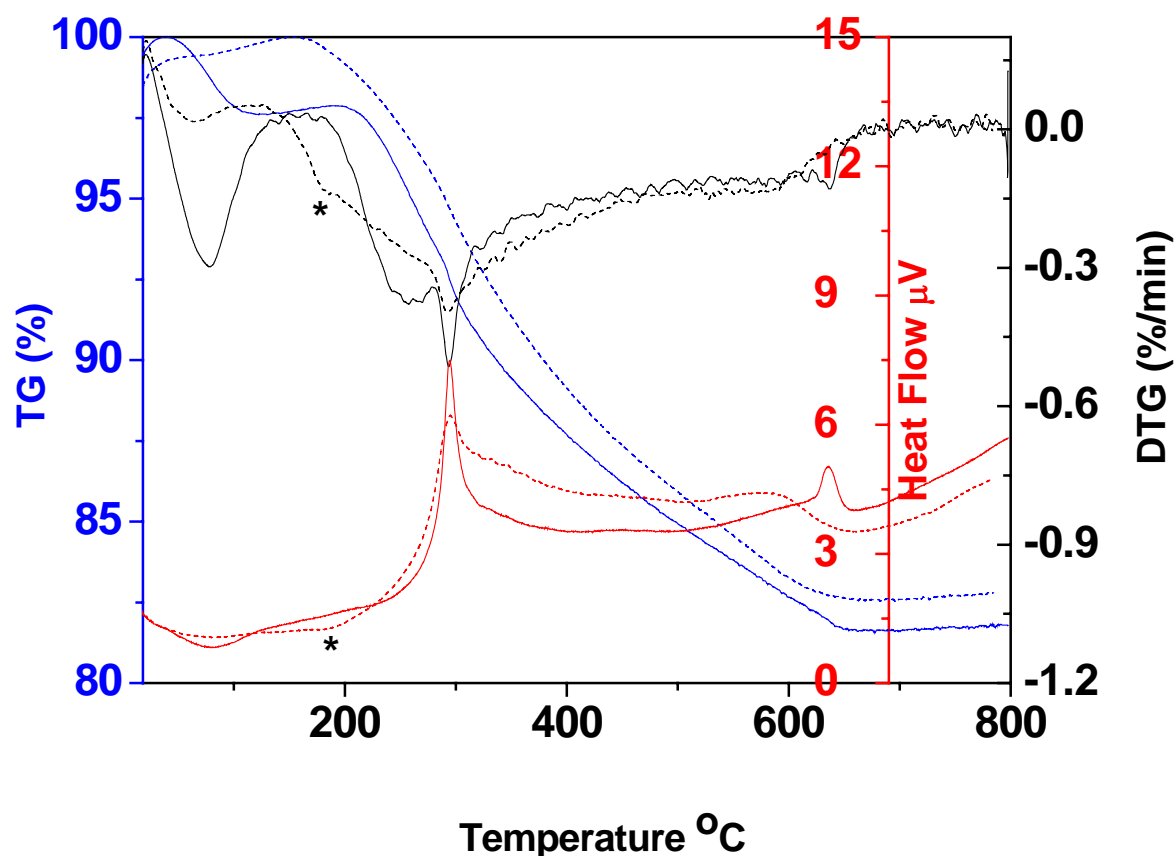


Figure 102. Thermogravimetric and differential thermogravimetric (TG–DTG) analyses of **S14-1** (solid lines) and **S14-2** (dash lines).

Table 15. The information of organic loading derived from the TG–DTG analysis

sample	temperature	$W_T^a$	$W_{RT}^b$	corresponding decomposition	calculation of the content
<b>S14-1</b>	<150	2.2	-	physisorbed water	
	150-330	7.8	48.2	combustion of the organic compound; dehydroxylation of the silica framework	
	330-650	8.4	51.8		
<b>S14-2</b>	<150	0.5	-	physisorbed water	
	150-330	7.2	42.6	combustion of the organic compound; dehydroxylation of the silica framework	0.64 mmol/g of (Me <sub>3</sub> Si-)
	330-650	9.7	57.4		

<sup>a</sup> weight loss at different temperature ranges calculated from TG data; <sup>b</sup> weight loss ratio at different temperature ranges.

Furthermore, FT–IR spectroscopy was performed to provide more information on the organic moieties in these two samples (Figure 103). The most significant signals of the materials can be assigned to the silica framework, such as the bands at 1200, 1100 and 800  $\text{cm}^{-1}$  attributed to the Si–O stretching vibration, and the peak at 460  $\text{cm}^{-1}$  due to the bending vibration of Si–O<sup>170</sup>. One broad band locates in the region of 3600-3200  $\text{cm}^{-1}$ , which can be assigned to the  $\nu_{\text{OH}}$  stretching vibration of the hydrogen bound internal silanol groups. Except to these characteristic bands of the silica material, the presence of some additional peaks features the organic-inorganic hybrid materials. In this case, the signal at 2980-2850  $\text{cm}^{-1}$  is the resulting from the CH stretching vibrations of methylene or methyl groups, and the band at 1450  $\text{cm}^{-1}$  is due to CH<sub>2</sub> or CH<sub>3</sub> deformation vibrations<sup>167</sup>. The further modification by binding of Me<sub>3</sub>Si groups, deduces an increased intensity of these bands<sup>259</sup>. These results prove the hybrid nature of these two samples.

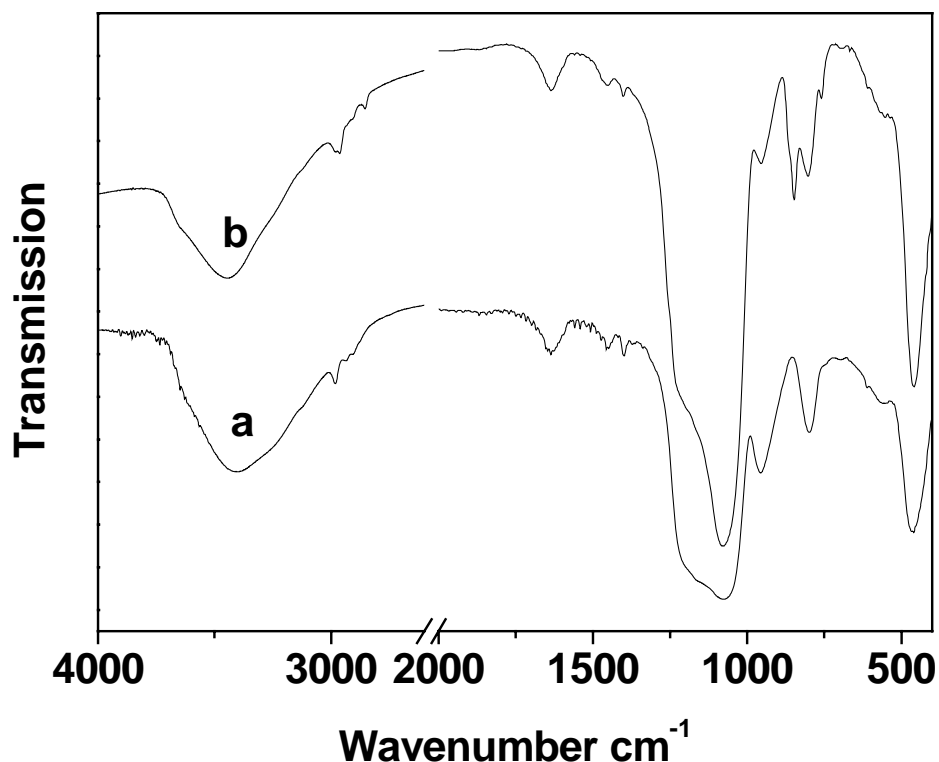


Figure 103. FT-IR spectra of sample (a) **S14-1**, and (b) **S14-2**.

Simultaneously, solid state  $^{27}\text{Si}$  CP-MAS NMR was carried out to further investigate the incorporation of the organic compounds and give direct information to confirm the covalent attachment. The data of **S14-1** is presented in Figure 104. Similar to the usual amorphous silica materials, the exhibition of three resonances at  $-91$ ,  $-101$ , and  $-110$  ppm indicates the three types of silica species in the framework, which are  $(\text{HO})_2\text{Si}(\text{OSi})_2$  ( $\text{Q}^2$ ),  $\text{HOSi}(\text{OSi})_3$  ( $\text{Q}^3$ ) and  $\text{Si}(\text{OSi})_4$  ( $\text{Q}^4$ )<sup>251</sup>, respectively. The  $\text{Q}^3$  sites are associated with isolated Si-OH groups, and the  $\text{Q}^2$  sites correspond to geminal silandiols, both implying the possibility of a further modification. The important resonances for the organo silicon species  $\text{R-Si}(\text{HO})(\text{OSi})_2$  ( $\text{T}^2$ ) and  $\text{RS}-(\text{OSi})_3$  ( $\text{T}^3$ ) are shown at  $-70$  and  $-78$  ppm, which is different to the usual  $\text{T}^n$  resonances expected to appear at  $-59$  and  $-69$  ppm<sup>252</sup>. The shift of the T value should be due to the fact that an ionic species are covalently bound onto the silica surface. Additionally, the absence of  $\text{R-Si}(\text{HO})_2(\text{OSi})$  ( $\text{T}^1$ ) silicon species indicates a relatively stable bonding is achieved by the method of co-condensation.

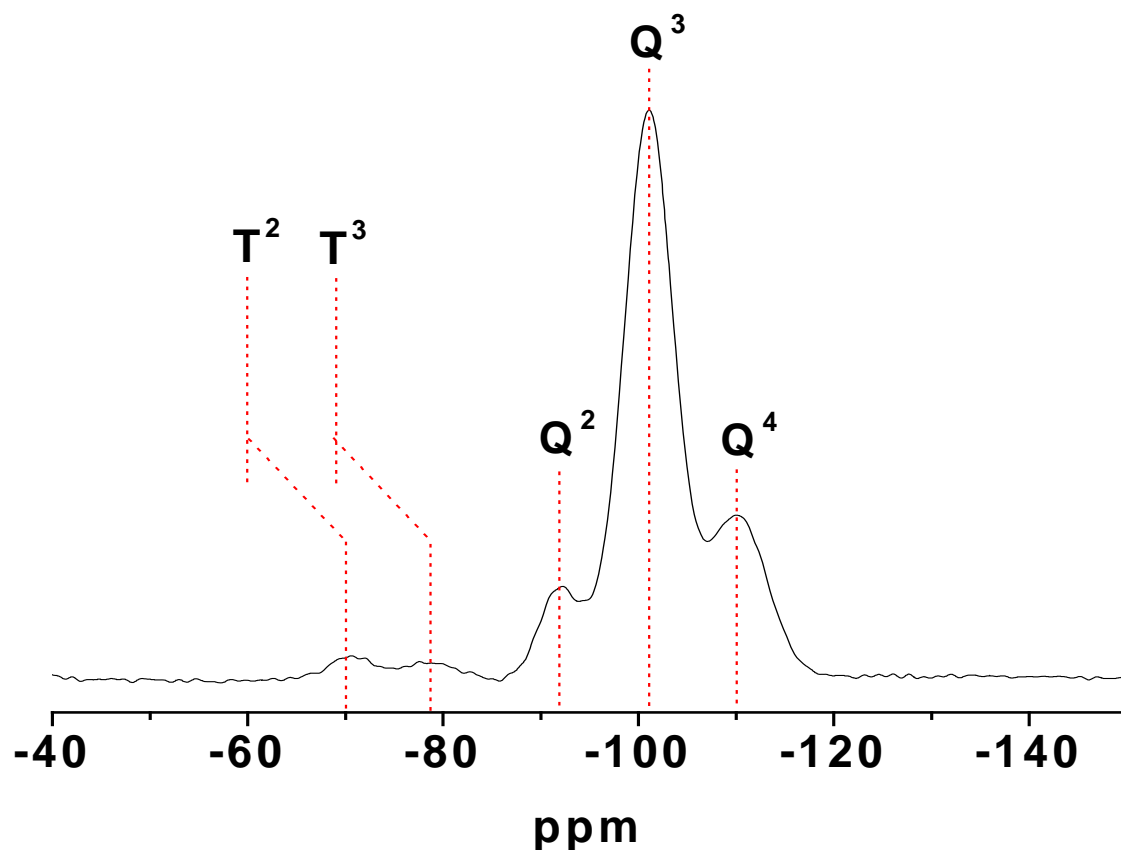


Figure 104. Solid state  $^{29}\text{Si}$  CP-MAS NMR spectrum of (a) **S14-1**.

The introduction and the integrality of the thiazolium salts was additionally verified by solid-state  $^{13}\text{C}$  CP-MAS NMR spectroscopy (Figure 105). The solid spectrum appears similar to the result of the precursor thiazolium salt in  $\text{CDCl}_3$ . The overlapping peaks at low field can be separately assigned to the carbon atom of the benzene and the thiazole ring. The peak at 158 ppm can be assigned to the resonance of C2 on the thiazole ring. The carbon atoms of the methyl groups appear at ca. 11 ppm. Two sharp singles at  $\delta$  60 and 16 ppm are the result of remnant ethanol from the template extracting process, or the side product of the hydrolysis reaction of TEOS.

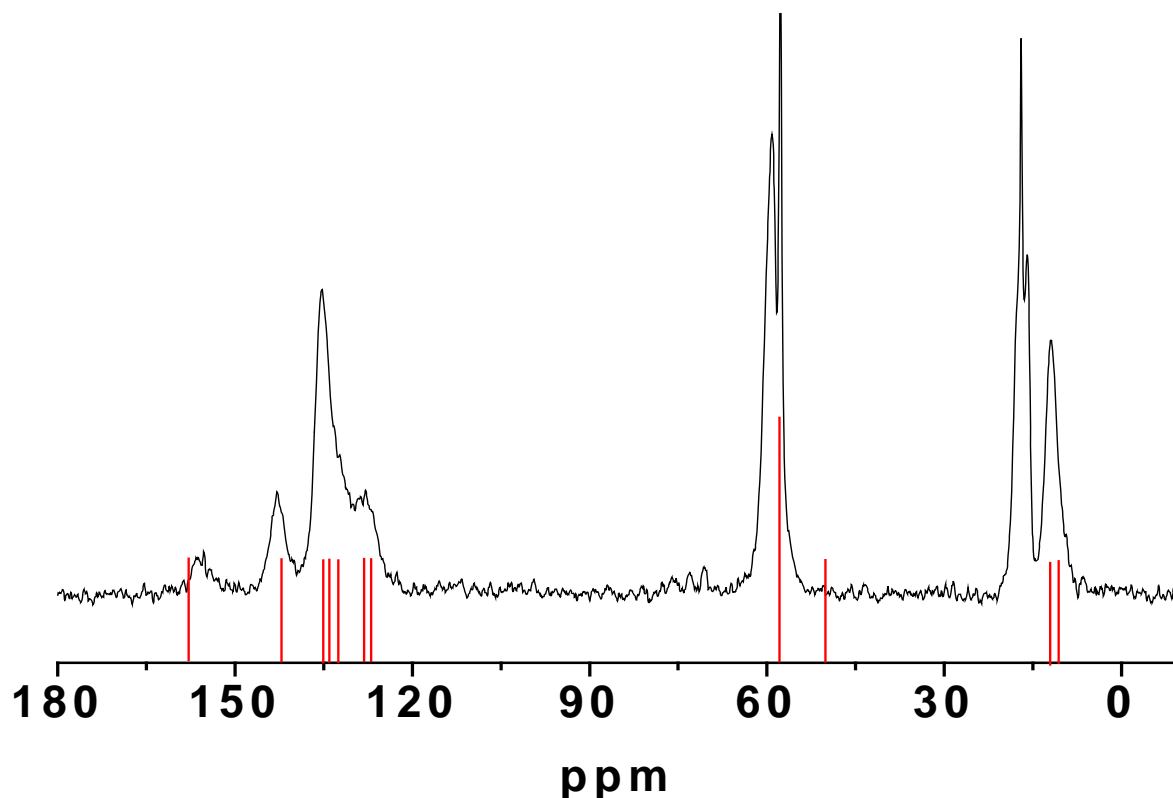


Figure 105. Solid state  $^{13}\text{C}$  CP-MAS-NMR spectrum of (a) **S14-1**; the solid lines are indicating the high resolution  $^{13}\text{C}$  NMR resonances of the precursor compound **14**.

### 3.2.4 Catalytic properties of the heterogenized thiazolium salts

The catalytic properties of these two groups of organo hybrid catalysts were investigated in the catalyzed cross-coupling of aldehydes with acyl imines to  $\alpha$ -amido ketones. The optimized condition had been selected from our former work. As expected 4-pyridinecarbaldehyde and an  $\alpha$ -tosylated amide can be transferred into the desired  $\alpha$ -amido ketone in the presence of **S14-1** or **S14-2** with the yields of 83% and 90%, respectively (see Table 16). This result is comparable to the result of **M14-1** and **M14-2** and indicates a similar activity of these two groups of heterogenous catalysts. Considering that the pore size of the **S14** samples is ca. 3 nm larger than of the **M14** samples, it implies that the size effect of channel has no significant influence on this reaction, as far as the pore size is above 2 nm. Additionally, the similar reaction activity demonstrates that the thiazolium salt is not



embedded in the framework or even in the micropores of SBA-15 after the co-condensation synthesis. As before, the polarity of the surface still acts as a key issue to increase the reaction yield. It seems that the diffusion of the substrates is strongly influenced by the amount of silanol groups on the surface. Probably the formation of hydrogen bonds to the surface hampers the diffusion of the substrates or the product. Furthermore, the catalyst **S14-1** and **S14-2** present promising stability and recyclability with only a low decrease of activity after recycling (entries 2, 4 and 5).

Table 16. Activity of the catalysts in the addition of 4-pyridinecarbaldehyde to *N*-[(4-methylphenylsulfonyl)(phenyl)methyl]cyclohexanecarboxamide <sup>a</sup>.

entry	catalyst	Et <sub>3</sub> N	time (h)	yield <sup>d</sup> (%)
1	<b>S14-1</b>	5	2	83
2	<b>S14-1</b> <sup>b</sup>	5	2	76
3	<b>S14-2</b>	5	2	90
4	<b>S14-2</b> <sup>b</sup>	5	2	84
5	<b>S14-2</b> <sup>c</sup>	5	2	75

<sup>a</sup> the reaction was performed with 1.0 equiv of *N*-[(4-methylphenylsulfonyl)(phenyl)methyl]cyclohexanecarboxamide, 1.1 equiv of 4-pyridinecarbaldehyde, and 7 mol % of catalyst with respect to tosylated amide in 15 mL of CH<sub>2</sub>Cl<sub>2</sub> at 35 °C. <sup>b</sup> the catalyst was reused for a second run, <sup>c</sup> the catalyst was reused for a third run. <sup>d</sup> isolated yield by chromatography (EtOAc/Hexane).

### **3.3 Covalent anchoring of organic thiazolium salts on periodic mesoporous organosilicas as organo catalysts for cross-coupling of aldehydes with acylimines reaction**

#### **State of art**

Since 1999, a new series of inorganic–organic hybrid materials denoted periodic mesoporous organosilicas (PMOs) have been synthesized by using bridge-bounded silsesquioxane molecules  $(R'O)_3\text{-Si-R-Si}(OR')$  in the presence of supramolecular structure directing agents<sup>63, 233, 251</sup>. So far, silylated precursors containing methylene, ethylene, phenylene rings, thiophene and many other organic groups have been used to form the walls of PMOs<sup>54, 260</sup>. In this way, the materials can reach a high degree of organic modification. In some cases, the nature of the organic bridges can deduce a molecular-scale periodicity inside the channel walls, e.g. by using rigid unsaturated or aromatic compounds as organosilica precursors<sup>65, 261-264</sup>. In comparison with the pure inorganic silica mesoporous materials, PMOs not only maintain a highly order structure, high surface areas and pore volumina, but also combine this with high hydrothermal and mechanical stability due to the hydrophobicity imparted by the organic components in the framework<sup>265, 266</sup>. Thus, these materials attracted much attention and are considered to have a high application potential.

In very recent years, functionalized PMOs were also developed by introduction of various organic moieties into periodical mesoporous materials for different application, such as chromatography, adsorption, photonics, electrochemiluminescenc and gas storage<sup>267-270</sup>. In the field of heterogenized catalysts, a vast of effort have been devoted to synthesise of sulfonic acid functionalised ethane-, benzene- or biphenyl-bridged mesoporous materials by co-condensation or grafting, which show high catalytic activity in various acid catalyzed reactions<sup>271-273</sup>. At the same time, several groups also successfully introduced different chiral

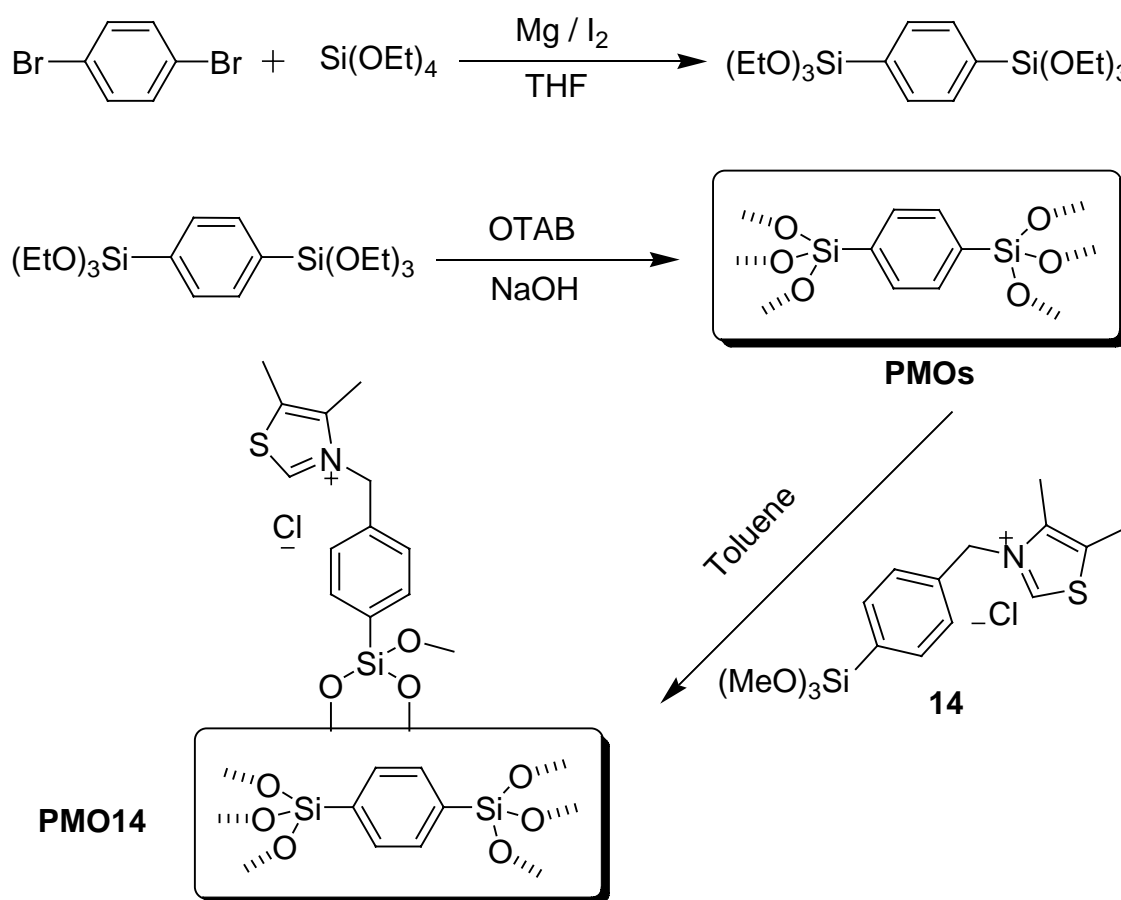
moieties or heteroatoms into PMOs as the catalytically active centre<sup>274-278</sup>. More interestingly, in some cases the hydrophobic surface of PMOs can also enhance the catalytic activity<sup>279</sup>.

In last part, we introduced immobilized thiazolium salts **14** into pure silica MCM-41 or SBA-15 materials with the aim to facilitate the catalyst recovery and recycling. The catalytic reaction results exhibited that a hydrophobic surface modification is beneficial for this reaction. Here we introduce this active catalyst into the phenylene-bridged periodic mesoporous organosilicas. The reason of choosing phenylene-bridged hybrid mesoporous organosilicas as the substrate is that the benzene rings are aligned in a circle around the pores between two silicate side chains in the wall of this material. This property provides hydrophobic benzene layers and hydrophilic silicate layers with an interval of 7.6 Å along the channel direction. As usual, the silicate chains are terminated by Si–OH at the surface. Thus it is a highly suitable catalyst support, which can be further functionalized by a simple grafting process, as well as provide hydrophobic surface to enhance the dispersion of organic reactant during the catalysis reaction.

### 3.3.1 Synthetic procedures

The preparation of the hybrid heterogeneous catalyst was processed as outlined in Scheme 24. The first step was the preparation of the precursor 1,4-bis(triethoxysilyl)benzene, which was synthesized by a one step Grignard reaction and distillation in vacuo as established in the literature<sup>280</sup>. A clear liquid was obtained as the final product and certified by NMR, elemental analysis and FT-IR. Mesoporous benzene-silica hybrid materials (**PMOs**) were obtained via a surfactant-mediated synthesis using octadecyltrimethyl ammonium bromide (OTAB) under hydrothermal conditions with NaOH as the hydrolyzing catalyst. The elimination of the template was performed by HCl/EtOH extraction, and anchoring of the thiazolium salt was done via reacting 1 mmol of 4,5-dimethyl-3-(4-trimethoxysilylphenyl)-

methyl)thiazoliumchloride (**14**) and the Si–OH groups on the surface of 1.0 g of **PMO**. This post-grafting process produced the organo hybrid catalyst **PMO14**, with 0.34 mmol/g catalytically active sites, corresponding to 9.9 wt % of organic compounds on the materials (calculated from the elemental analysis result). The yield of the grafting is 43.6 %, while in the case of pure silica MCM-41 as substrate the grafting yield is 66.7 %. This result indicates that the surface of pure silica MCM-41 is richer of reactive silanols than the surface of **PMOs**.



Scheme 24. Synthesis process for the **PMO** and for the supported heterogenous catalyst **PMO14**.

### 3.3.2 Structural characterization of the functionalized materials

The powder X-ray diffractions (PXRD) of the benzene-bridged hybrid mesoporous organosilica (**PMO**) shows three Bragg reflexes for the (100), (110) and (200) planes in the

range of lower-angles  $2\theta < 10^\circ$  (Figure 106), which can be assigned to the typical two-dimensional hexagonal ( $P6mm$ ) symmetry of the mesoporous structure<sup>281</sup>. In addition to these lower angle diffractions, the patterns at  $10 < 2\theta < 40^\circ$  display three additional sharp diffraction peaks at  $2\theta$  values of 12, 23 and  $35^\circ$  (with  $d$  spacings of 7.6, 3.8, and 2.5 Å), which can be assigned to a molecular scale periodicity in the walls along the channel directions. This periodic wall has a spacing of 7.6 Å, due to the  $\pi$ - $\pi$  stacking of benzene bridging groups<sup>65</sup>. The above XRD results demonstrate that besides a well formed hexagonal array of mesostructural pores, this materials also contains crystal-like pore walls. After functionalized with the thiazolium salt under grafting conditions, there is no apparent position change for the diffraction in lower angle region or the medium angle region compared to the parent substrate **PMO**, which indicates the preservation of the  $P6mm$  symmetry with similar cell parameters. The intensity of all the peaks were decreased, as it was observed for the other materials before<sup>273</sup>.

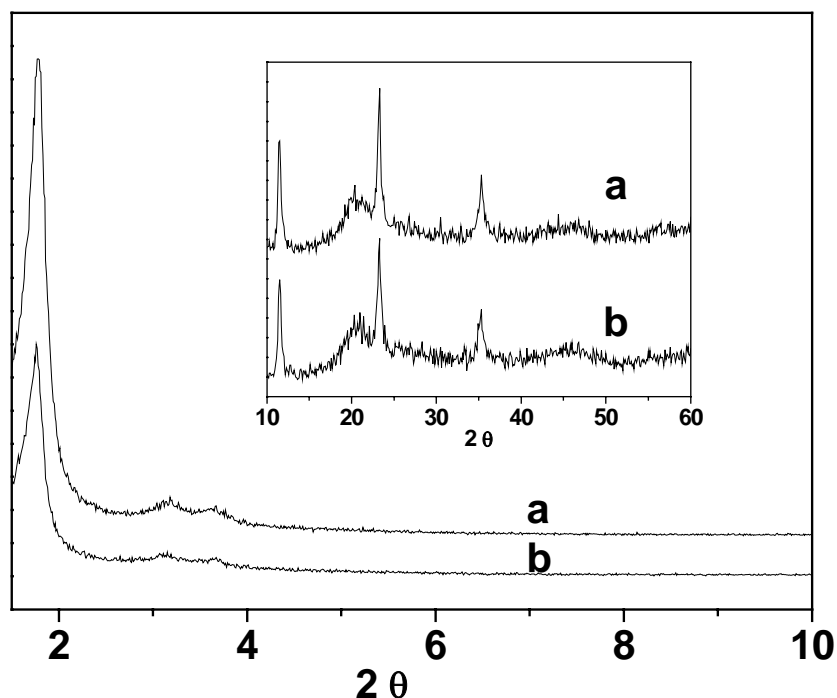
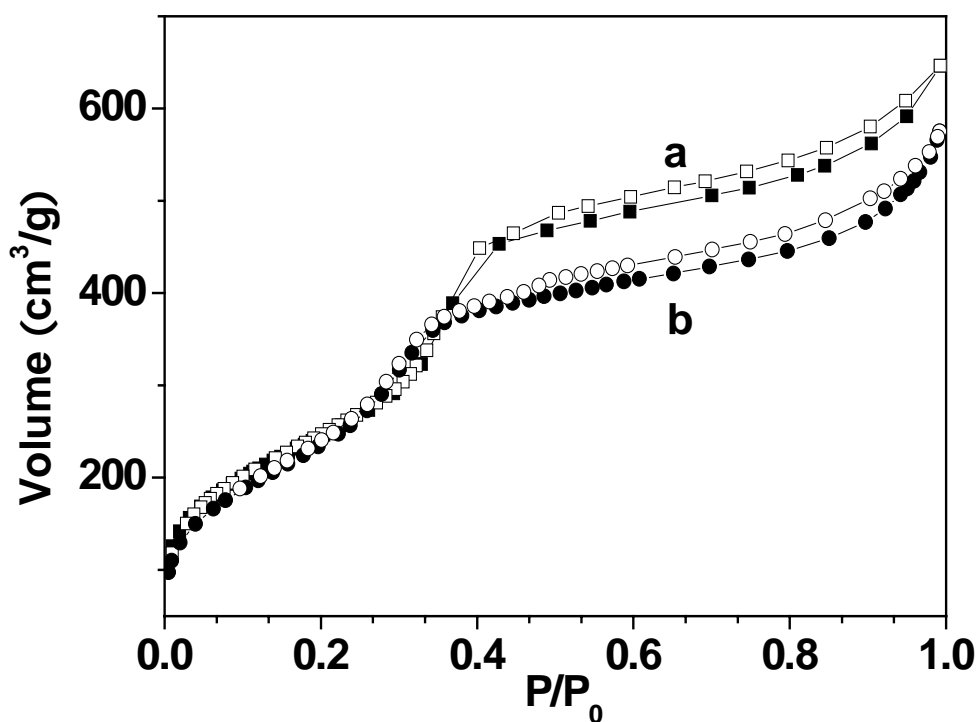


Figure 106. XRD patterns of (a) **PMO** and (b) **PMO14**, and the inset graphic shows the medium-angle diffraction of samples.

The nitrogen adsorption isotherms of **PMO** and the functionalized material **PMO14** exhibited type IV isotherms with a typical capillary condensation step in the relative pressure ( $P/P_0$ ) range of 0.2–0.4<sup>166</sup> (Figure 107). The  $N_2$  adsorption desorption behavior is similar to the original reports of PMO obtained with ODTA as the surfactant<sup>146,282</sup>. This indicates that both samples consisted with well-defined mesoporous structures and combine relatively narrow pore size distributions. The Brunauer–Emmett–Teller (BET) surface area of **PMO** calculated from the experimental data at relative pressures of 0.05 – 0.20 in the isotherms, was  $976 \text{ m}^2\text{g}^{-1}$ . After functionalization with the thiazolium salt, the surface area decreased to  $882 \text{ m}^2\text{g}^{-1}$ . This reduction can also be observed from the data of pore size and pore volume (Table 17) and is due to the incorporation of organic moieties on the surface of the pore channels.



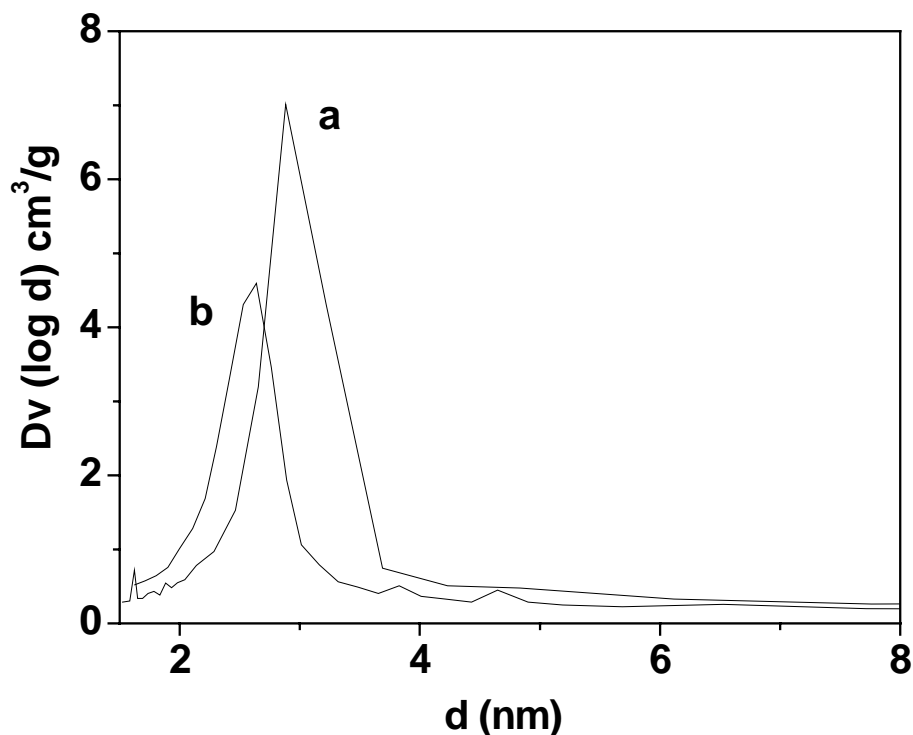


Figure 107. Nitrogen adsorption-desorption isotherms of (a) **PMO** and (b) **PMO14**; adsorption points are marked by filled circles/squares and desorption points by empty circles/squares; **B)** pore size distributions of (a) **PMO**, and (b) **PMO14**.

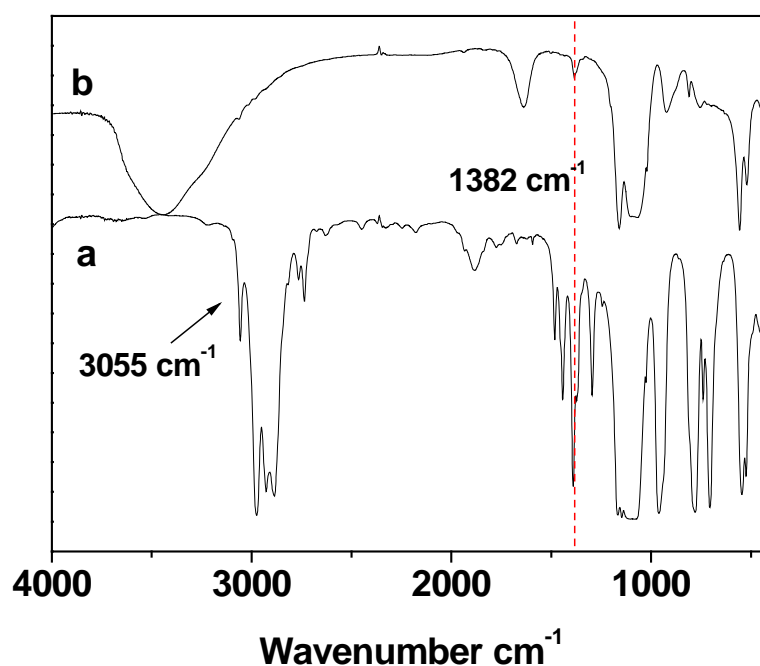
Table 17. Pore parameters and compositional information of parent **PMO** and the modified **PMO14** organo catalyst.

sample	$d_{100}^a$ / nm	$a^b$ / nm	$S_{\text{BET}}^c$ / $\text{m}^2\text{g}^{-1}$	$V$ / $\text{cm}^3\text{g}^{-1}$	$D_p$ nm	pore wall <sup>d</sup> nm	content of thiazolium <sup>e</sup>	
							$\text{mmolg}^{-1}$	wt %
<b>PMOs</b>	4.96	5.73	976	0.94	2.89	1.42	-	-
<b>PMOTZ</b>	4.97	5.74	882	0.87	2.57	1.58	0.34	9.9

<sup>a</sup>  $d_{100} = 1.5418/(2\sin\theta)$  for a hexagonal symmetry. <sup>b</sup> unit cell parameter  $a = 2d_{100}/\sqrt{3}$ . <sup>c</sup> specific BET surface area. <sup>d</sup> pore wall thickness calculated as the difference between  $a$  and  $d_p$ . <sup>e</sup> according to the nitrogen content of elemental analysis.

### 3.3.3 Characterization of the functionalized materials by solid-state NMR, FT-IR spectroscopy and thermogravimetric properties

FT-IR spectroscopy was carried out to investigate the nature of the materials as well as to give some evidence for the incorporation of thiazolium salts. For comparison, the spectrum of 1,4-bis(triethoxysilyl)benzene is shown in Figure 108, labeled as a. The strong peaks below  $3000\text{ cm}^{-1}$  can be assigned to the C–H stretching vibration of ethyl groups, while the relatively weak single peak around  $3050\text{ cm}^{-1}$  is due to the C–H stretching vibration of the benzene ring. The absorptions around  $1500$  to  $1400\text{ cm}^{-1}$  attributes to the C=C stretching vibrations in aromatics and the C–H bending vibrations. Additionally, a broad signal at  $1100\text{ cm}^{-1}$  can be pointed to the symmetric Si–O–Si vibration. After hydrothermal synthesis, the material **PMO** presents broad overlapping bands around  $3400\text{ cm}^{-1}$ , which are due to the OH stretching vibrations of the Si–OH groups (Figure 108 b). The strong peak at  $1382\text{ cm}^{-1}$  is preserved in spectra of the solid materials **PMO**. After modifying with thiazolium salts, a new peak at  $1444\text{ cm}^{-1}$  can be observed in the spectrum of **PMO14** (Figure 108 c), which is a C–H deformation vibration of the thiazolium unit. It is relatively weak due to the limited amount of grafting, but it still demonstrates the introduction of thiazolium salts.





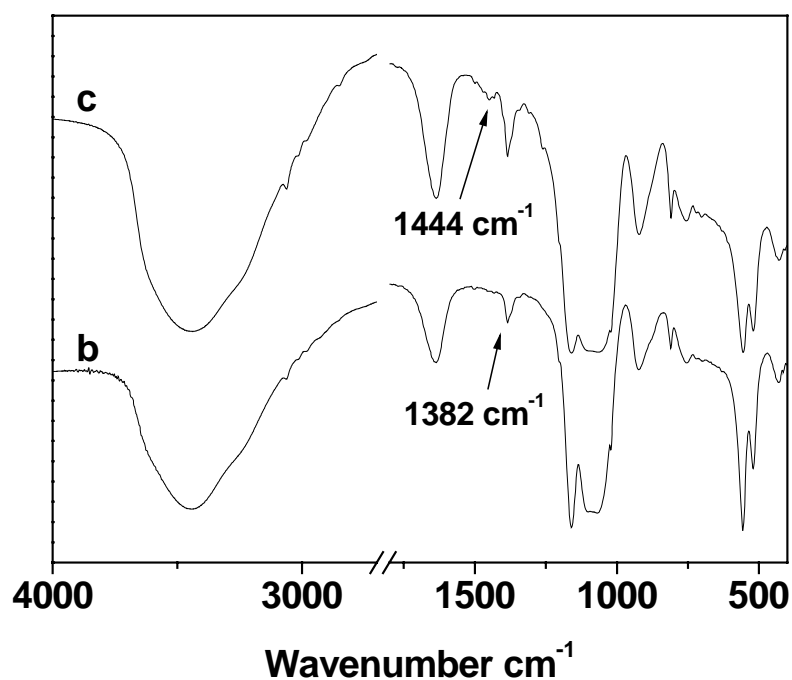


Figure 108. FT-IR spectra of (a) precursor compound 1,4-bis(triethoxysilyl)benzene and (b) PMOs, (c) PMO14.

The thermogravimetric curves recorded in the air for the surfactant free **PMO** and the modified material **PMO14** are presented in Figure 109. The TG–DTG curve of **PMO** exhibited a small portion of weight loss below 100 °C with an endothermic peak, corresponding to the desorption of physisorbed water. This low amount of absorbed water demonstrates the hydrophobic property of **PMO**. No weight loss can be assigned to the decomposition of any surfactant. It usually should appear between 100 and 300 °C. This result confirms the complete surfactant removal by solvent extraction. A main weight loss occurs from 500 to 650 °C with a strong exothermic peak, which corresponds to the combustion and release of the organic fragments from the pore wall. For **PMO14**, a much larger weight loss can be observed at the temperature of water desorption than for **PMO**. It is attributed to the thiazolium salt modification, which makes the surface of the material more hydrophilic. The thiazolium salt extremely absorbs water from surrounding atmosphere. An additional weight loss with an exothermic peak can be observed from 200 to 350 °C, which

can be assigned to the partial decomposition of the thiazolium salt, since this feature is absent in the thermal curve of **PMO**. This result again implies the introduction of thiazolium salts into the periodic organic mesoporous materials.

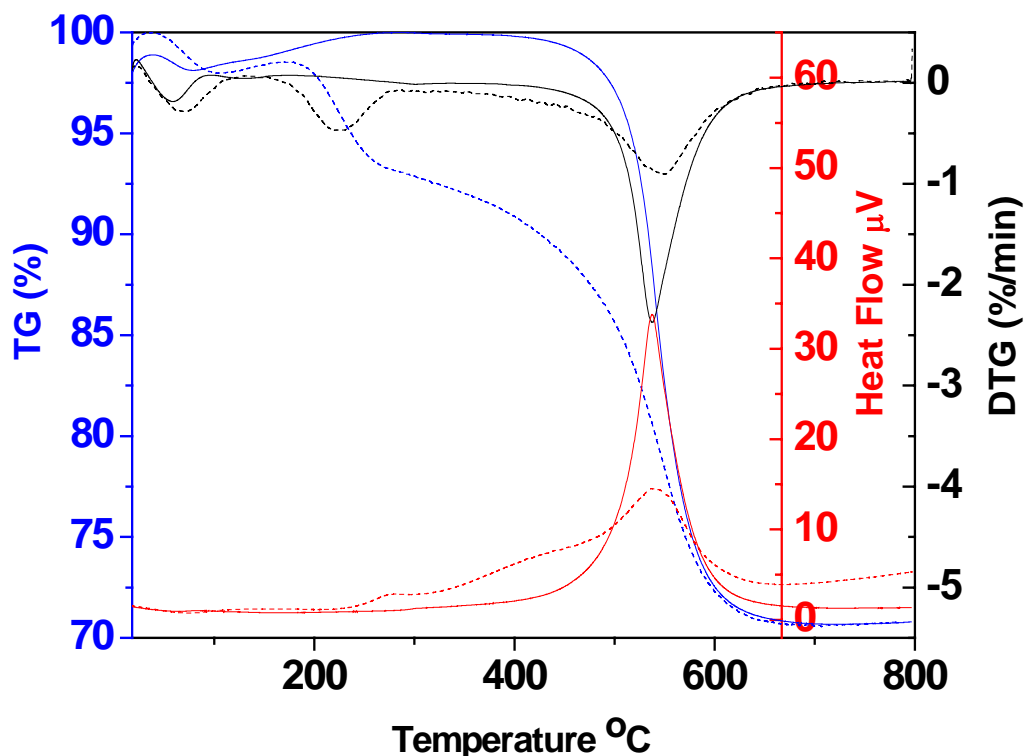


Figure 109. Thermogravimetric and differential thermogravimetric (TG–DTG) analyses of **PMO** (solid lines), and **PMO14** (dash lines).

Solid-state  $^{29}\text{Si}$  CP–MAS NMR was used to detect the covalent binding situation of the silica species in **PMO14**. The spectrum is shown in Figure 110. The exhibiting peaks at ca.  $\delta$  –62, –71, –80 ppm can be attributed to  $\text{R–Si}(\text{HO})_2(\text{OSi})$  ( $\text{T}^1$ ),  $\text{R–Si}(\text{HO})(\text{OSi})_2$  ( $\text{T}^2$ ) and  $\text{R–Si}(\text{OSi})_3$  ( $\text{T}^3$ ) organosiliceous species, respectively. No peak for  $\text{Q}^n$  [ $\text{Q}^n = \text{Si}(\text{OSi})_n(\text{OH})_{4-n}$ ] species can be observed, which indicates that no carbon-silicon bond cleavage of the organo silica precursor occurred during the synthesis of **PMO** or the grafting process.

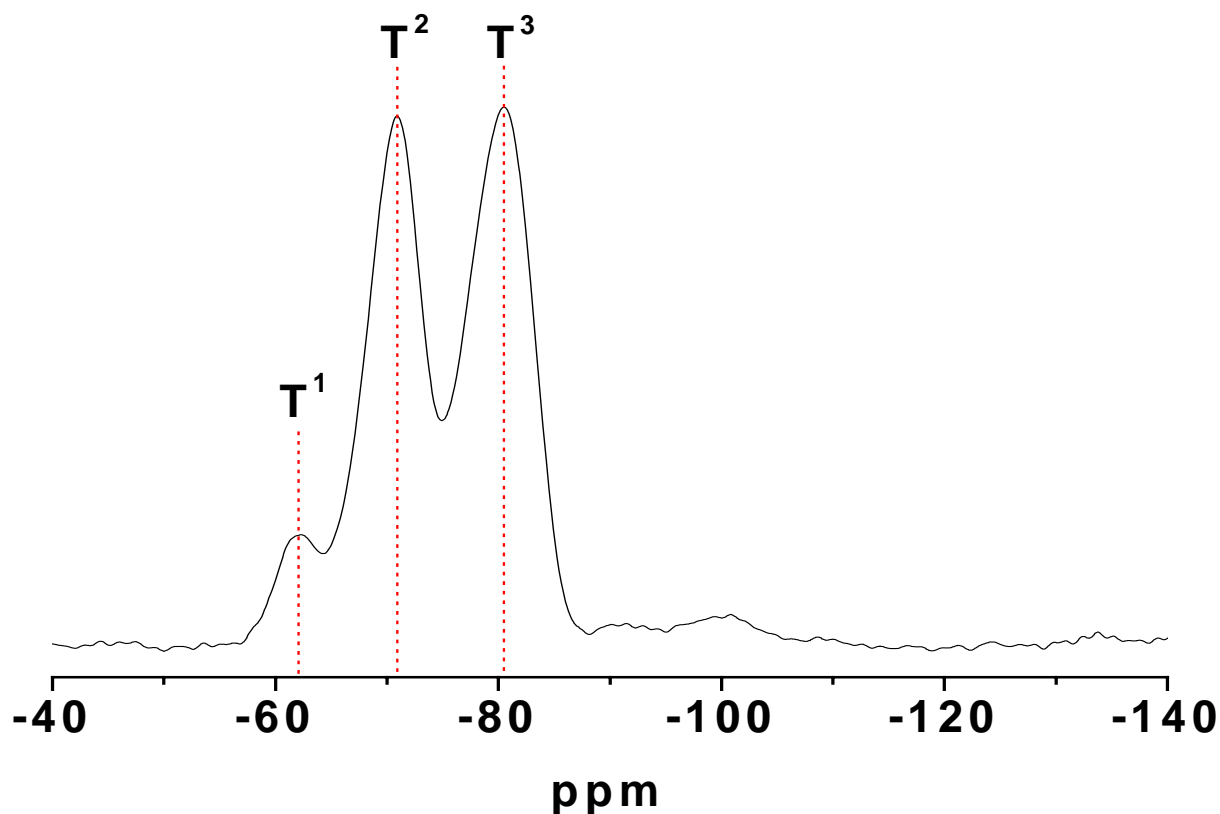


Figure 110. Solid state  $^{29}\text{Si}$  CP-MAS NMR spectrum of **PMO14**.

The integrity of the organic fragment can be proved by the solid-state  $^{13}\text{C}$  CP-MAS NMR spectrum of **PMO14**, which is presented in Figure 111. The extremely sharp peak at ca. 133 ppm is attributed to the carbon atoms of the benzene ring of the framework building block (1,4-bis(triethoxysilyl)benzene). It should overlap with the resonances of the thiazole ring. The small shoulder peak centering at ca.  $\delta$  127 ppm can be assigned to the carbon atoms of the phenyl group of the thiazolium salt, demonstrating the successful modification. The further resonances at ca. 58, 49, and 12 ppm (an amplified spectra is given in Figure 111) give a further evidence of covalently bound thiazolium salt **14** on this hybrid material. The remnant ethanol from the extracting process or the free ethanol formed as a side product of grafting reaction gives the resonances at ca.  $\delta$  60 and 16 ppm.

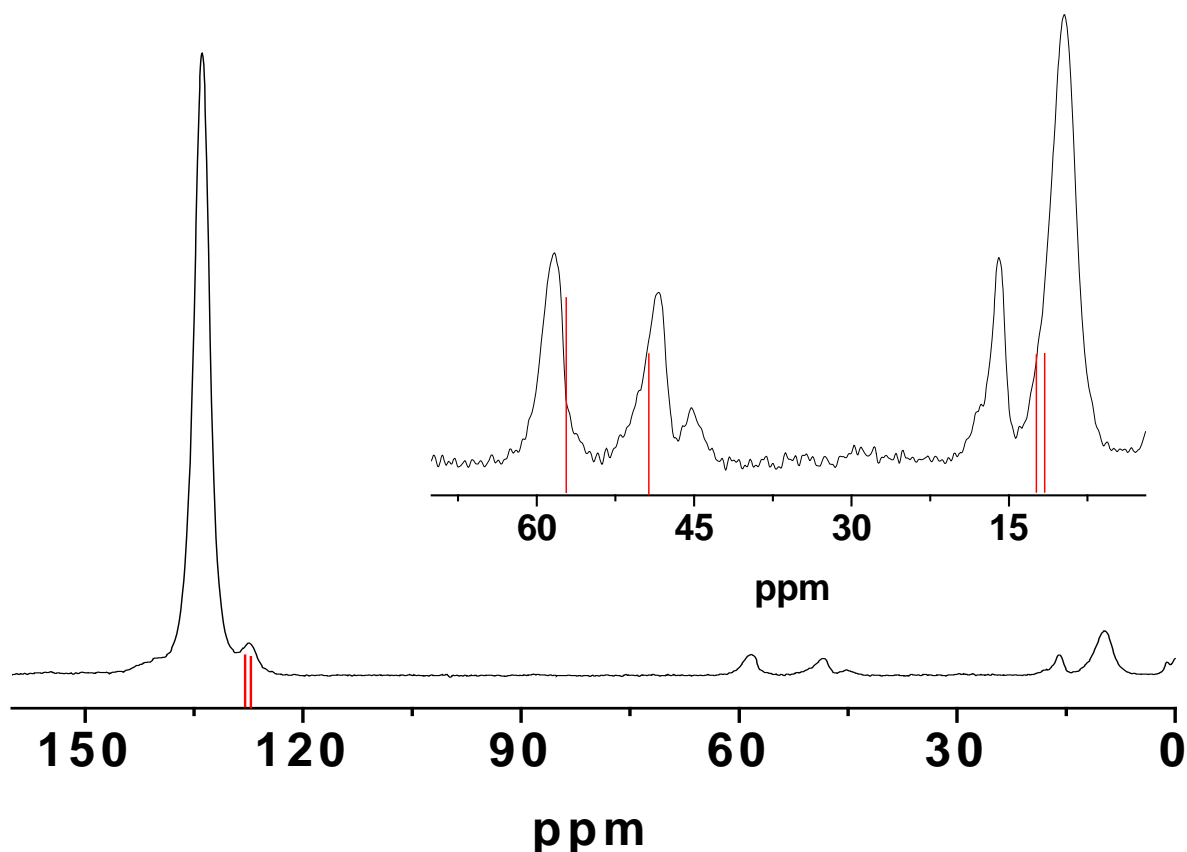


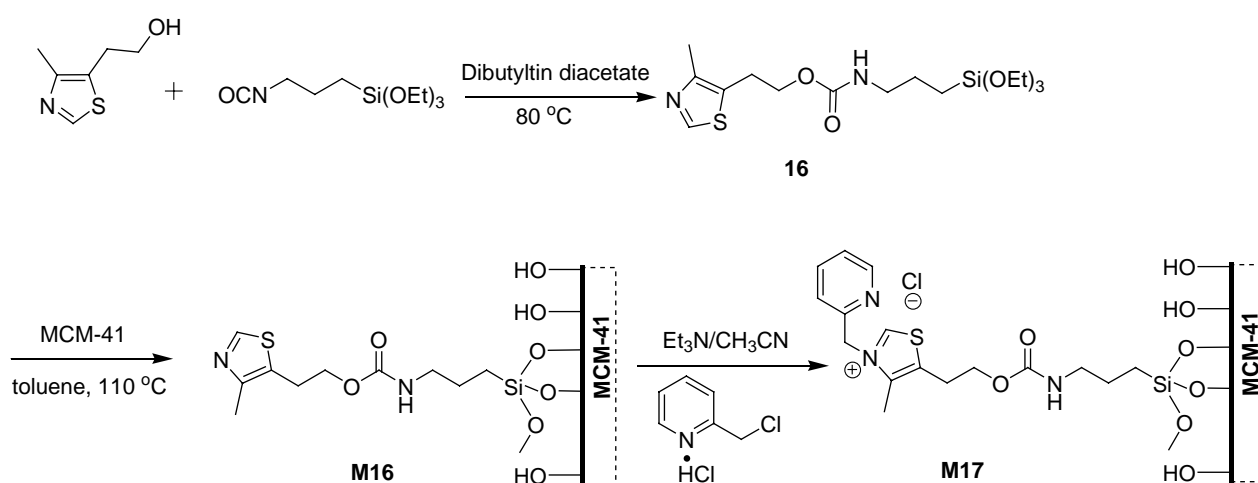
Figure 111. Solid state  $^{13}\text{C}$  CP-MAS NMR spectrum of **PMO14**; the solid lines are indicating the high resolution  $^{13}\text{C}$  NMR resonances of the precursor compound **14**.

### 3.4 Synthesis of a carbamate-linked thiazolium salt with a basic site in the same molecule covalently bonded on silica MCM-41

#### 3.4.1 Synthetic process

The alcohol 5-(2-hydroxyethyl)-4-methylthiazole can be quantitatively transformed by addition of 1-isocyanato-3-triethoxysilyl propane prepared at 80 °C under a nitrogen atmosphere in the presence of dibutyltin diacetate as catalyst to give the desired triethoxysilyl functionalized carbamate **16** as shown in Scheme 25. Directly connecting a picolyl group to the thiazole ring by nucleophilic substitution of the chloro ligand of 2-picolyl chloride

hydrochloride with **16** worked, but the attempts to purify the product failed due to a rapid hydrolysis of the product. The separation of the two ionic compound ( $\text{Et}_3\text{N}\cdot\text{HCl}$  and desired ionic product) was impossible. An alternative way was performed by directly grafting **16** onto silica MCM-41 and offered product **M16** as a colorless powder. Subsequently, a nucleophilic substitution reaction was carried out between an excess of 2-picolyyl chloride and the thiazole ring of the anchored molecules, which afforded product **M17** as a yellow powder.



Scheme 25.

### 3.4.2 Information of the organic composition and the catalytic properties of the heterogenized catalyst.

The element analysis (CHN) was carried out for calculating the organic loading. The results are listed in Table 18. Using 1.0 mmol of **16** with 1.0 g of pure silica MCM-41 provided a loading of 0.31 mmol/g, corresponding to a grafting yield of 40 %g (supposing the hydrolysis of the organosilane is 100 %). Subsequently the nucleophilic substitution reaction deduces a higher amount of N in the material **M17**, corresponding to a 0.34 mmol/g loading of thiazolium salt (supposing all the nitrogen atoms are from the thiazolium salts). This result indicates that some of the N is attributed to the adsorption of 2-picolyyl chloride and this strong adsorption might be due to an interaction of nitrogen with the silanol groups of

material surface. Thus, an efficient washing process should be carried out for the purification of this catalyst.

Table 18. Compositional information of the hybrid materials and the activity of catalyst in cross coupling reaction

sample	content of organic group loading				reaction data <sup>b</sup>		
	C	H	N	mmol/g <sup>a</sup>	Et <sub>3</sub> N	time (h)	yield (%) <sup>c</sup>
<b>M16</b>	8.99	2.36	0.88	0.31	-	-	-
<b>M17</b>	9.85	1.85	1.43	0.34	5	4	53
					-	24	-

<sup>a</sup> calculated from the nitrogen content; <sup>b</sup> the reaction was performed with 1.0 equiv of *N*-[(4-methylphenylsulfonyl)(phenyl)methyl]cyclohexanecarboxamide, 1.1 equiv of 4-pyridine carbaldehyde, 5 equiv of Et<sub>3</sub>N, 300 mg of catalyst and 15 mL of CH<sub>2</sub>Cl<sub>2</sub> at 35 °C. <sup>c</sup> isolated yield by chromatography (EtOAc/Hexane).

The catalytic property of this organo hybrid catalyst (**M17**) was investigated in the catalyzed cross-coupling of aldehydes with acyl imines to  $\alpha$ -amido ketones, in which the former thiazoliums salt **14** can gave quite good reactivity. Thus, it is used as a model reaction to testify the formation of the picolyl substituted thiazolium salt to be present in the hybrid material **M17**. It turned out that under the optimized reaction condition, **M17** can give the product in 53% (Table 18), which demonstrates the successful introduction of the picolyl moiety to the nitrogen atom of the thiazole ring.

The bonding of picolyl offers the opportunity to introduce basic sites in close proximity to the thiazolium ring, as it is found in thiamine (vitamin B1). This base may deprotonate the carbon atom in the C2 position, which provides a mimic catalyst for thiamine. Thus a reaction without external base (Et<sub>3</sub>N) was carried out to determine the possibility of this ‘intramolecular deprotonation’ in **M17**. However, after 24 h reaction, there is no product

formed (Table 18), considering that this result should be attributed to the fact that the cross coupling reaction is not a suitable reaction for the investigation of the deprotonation of this catalyst. As we mentioned before, this cross coupling reaction needs more base for the conversion of the tosylamide to the acylimine. Thus, a suitable reaction should be chosen for the further investigation of this catalyst.

## **Chapter 4. Sulfonic acid functionalized mesoporous materials**

### **State of art**

The invention of ordered mesoporous silica materials brought a new round of developing acid solid catalysts. The acidification concept was first transferred from the zeolites, where the incorporation of Al atoms within the framework of the silica materials creates acidic sites. However, only low acid strengths can be achieved due to the amorphous nature of this material. An alternative way to improve the acidity of such Al containing mesoporous materials is due to 'zeolite seeds' as framework precursors. Simultaneously, the introduction of some other inorganic species into the pores of the mesoporous silica materials, such as phosphotungstic acid, heteropoly acids and sulfated metal oxides etc. can also provide active centers for acid-catalyzed reactions. However these pure inorganic materials designed by a simple supporting technique can not overcome the leaching problem. Thus, a different concept based on organic sulfonic acid functionalized silica materials was developed. The pioneering works dealing with the preparation of sulfonic-acid-functionalized solid silica materials, which can be traced back to 1989<sup>283</sup>. An organic sulfonic acid was for the first time introduced into mesoporous materials in 1998<sup>284</sup>. In this work, the preparation starts by covalently attaching propane-thiol groups on pure silica mesoporous materials, followed by the oxidation of the thiol groups to sulfonic acids. The amount of acidic sites can be adjusted by the grafting technique<sup>285</sup>, by the number of reactive silanol groups on the surface of different mesoporous substrates<sup>286</sup>, as well as by a co-condensation method to for a direct preparation for a high loading of S-H in the mesoporous materials<sup>287</sup>. An interesting development is the in-situ oxidation of mercaptopropyl groups by a direction co-condensation



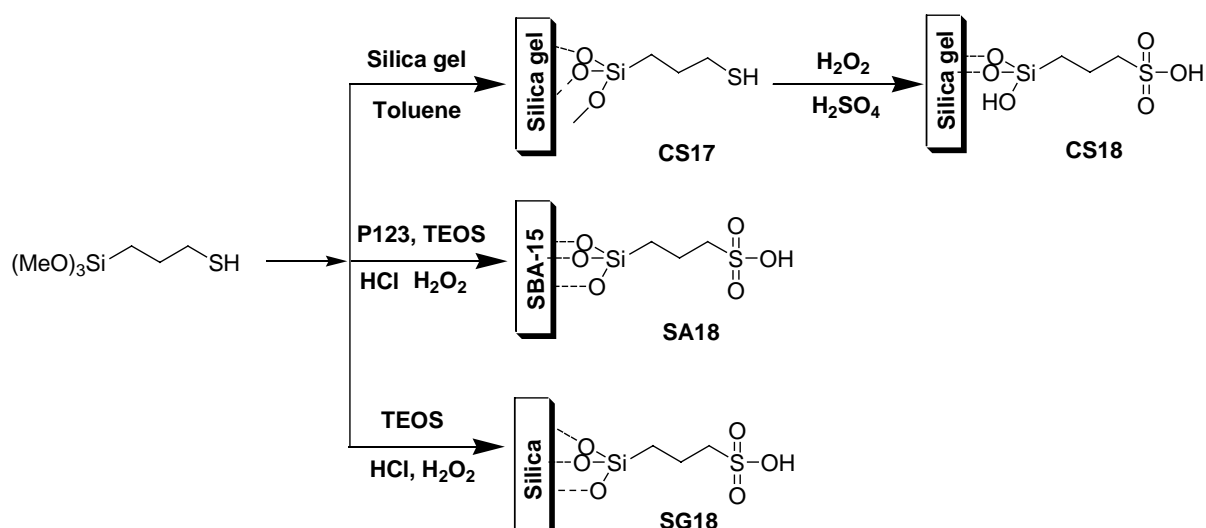
synthesis procedure<sup>288</sup>. Thereby the sulfonic group can be obtained without a postoxidation treatment. Thus, it can overcome the drawbacks of the postoxidation process, such as the losing of structural order, the leaching of sulfur species, as well as the insufficient oxidation. A investigation of the acid strength shows that such alkylsulfonic acid functionlized materials have stronger acid strengths than Al-MCM-41. However, it is still lower than a commercial sulfonic acid resin like Amberlyst-15, due to the poor electron withdrawing effect of the alkyl chain compared to an aromatic ring. Thus, a series of arenesulfonic acid functionalized hybrid mesoporous materials were investigated as acid solid catalysts<sup>147</sup>, which have similar acid strengths as the commercial resins and combine higher surface area as well as high stability. As a result, the reaction activity is improved by this strong acid functionalization<sup>151</sup>.

From the point of hybrid mesoporous material synthesis it is apparent that a high amount of organic loading combined with an ordered structure is the most expected result. By comparison of different ways to achieve organo sulfonic acid functionalized mesoporous materials, the favorable route would be the co-condensation synthesis in a one pot reaction as proposed by Stucky's group<sup>288</sup>. This method was also extended to the synthesis of an arenesulfonic acid functionalized mesoporous material by using the commercial available 2-(4-chlorosulfonylphenyl)ethyltrimethoxysilane<sup>147</sup>. Thus this method became our choice to produce the solid acid materials. However, considering the costs, a commercial silica gel with a relatively high surface area and uniform pores was also used as substrate. In this case, the post grafting route is the only choice to obtain the covalently anchored organic modification. As mentioned, the limitation of the grafting process is the main drawback of this material. An alternative way to reduce the price as well as to keep the high loading and high surface area of the final hybrid material, can be performed by an optimized sol-gel synthesis, which can provide a porous silica material with a large amount of accessible sulfonic acid sites. Based

on this, three different preparation methods and two different organosilane precursors were used to synthesize the solid sulfonic acid as heterogenized catalysts.

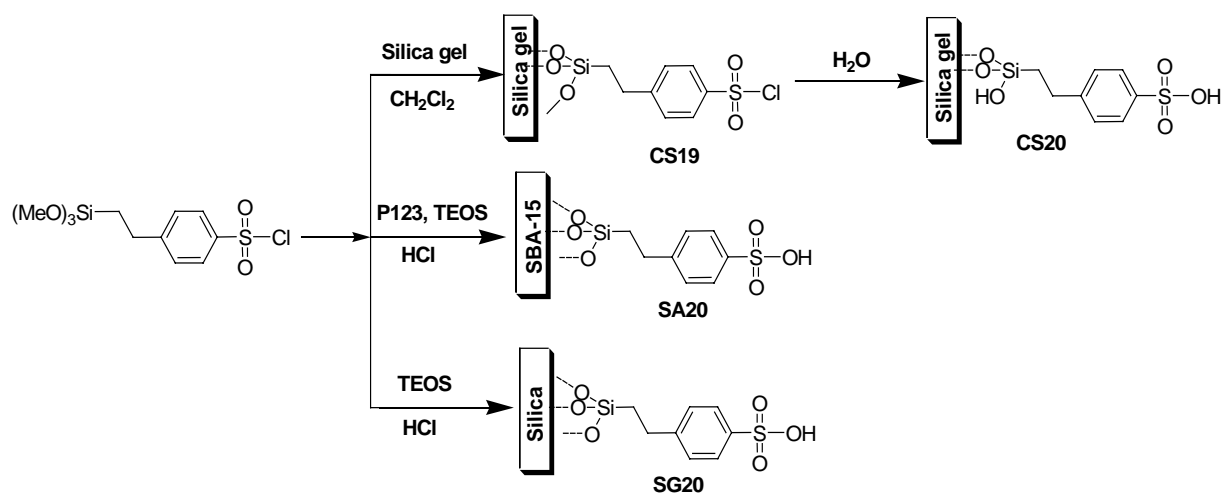
#### 4.1 Synthetic procedure

A series of alkylsulfonic acid functionalized silica materials were prepared by three different ways as illustrated in Scheme 26: (1) 3-mercaptopropyltrimethoxysilane (MPTMS) was covalently bound on commercial silica gel by a silylation reaction in toluene under reflux, which afforded **CS17**. Postsynthetically, the thiol groups were treated to yield sulfonic groups by sequential oxidation with  $\text{H}_2\text{O}_2$ , acidification, and washing to provide **CS18**. (2) A one-step synthetic strategy was performed to produce **SA18**<sup>288</sup>, which is based on the co-condensation of tetraethoxysilane (TEOS) and MPTMS, in the presence of the surfactant P123 and  $\text{H}_2\text{O}_2$  in HCl aqueous solutions. This synthetic way can in situ oxidize thiol groups to sulfonic groups, as well as fashion an ordered mesoporous structure. (3) A one-pot sol-gel method was tried to produce a hybrid acid/amorphous silica material with a high accessible capacity of acid and a reasonable surface area (**SG18**). Here TEOS was used as the major silica source and co-condensed with an adjustable amount of MPTMS under acidic conditions through an in-situ oxidizing process without using other templating agents. This way can reduce the costs and avoid using an organic solvent. Here an alternative and even cheaper silica source could be the sodium metasilicate, due to the fact that a similar siliceous oligomer like TEOS can be achieved under highly acidic conditions.



Scheme 26. Procedure for the synthesis of propylsulfonic acid-functionalized silica materials.

Compared to aliphatic sulfonic acid groups, aromatic sulfonic acid groups with a phenyl group adhered to the sulfonic group usually show higher acid strengths and catalytic activities in acid-catalyzed reactions. Thus, three similar methods as described above were performed to produce arenesulfonic acid functionalized hybrid porous materials (Scheme 27). First, 2-(4-chlorosulfonylphenyl)ethyltrimethoxy silane (CSPTMS) was introduced on commercial silica gel by a post grafting method using  $\text{CH}_2\text{Cl}_2$  as the solvent at room temperature (**CS19**). Further hydrolysis of the chlorosulfonyl groups to the corresponding sulfonic acid functionalized material (**CS20**) is achieved under acidic conditions. The grafting process was also performed in toluene under reflux condition, but a condensation polymer appeared, and the resultant materials showed an extremely low acid capacity. A one-step co-condensation method allowed the efficient anchoring of arenesulfonic groups on the pore surface of SBA-15 mesostructured materials using P123 as templating agent (Scheme 27, sample **SA18**). The template free sol-gel process was also applied for the introduction of arenesulfonic groups to achieve an amorphous silica hybrid material **SG20**.



Scheme 27. Procedure for the synthesis of arenesulfonic acid-functionalized silica materials

## 4.2 Structural properties of the organic-acid functionalized silica materials

### Powder X-ray diffraction

All of the alkylsulfonic acid and arenesulfonic acid functionalized commercial silica gels and the materials prepared by the sol-gel method (**CS18**, **SG18**, **CS20** and **SG20**) exhibit the typical XRD pattern of amorphous silica. No additional diffraction peaks in the  $2\theta$  range of  $0.5^\circ$  to  $10^\circ$  indicate the absence of a long-range ordered mesoporous structure in these materials. On the contrary, the samples **SA18** and **SA20** present a series of peaks in the  $2\theta$  range of  $0.5\text{--}3^\circ$  (see Figure 112), which are corresponding to (100), (110) and (200) diffractions. This type of diffraction pattern can be indexed to the hexagonal  $p6mm$  symmetry, which is the characteristic pattern of SBA-15 type mesoporous materials.

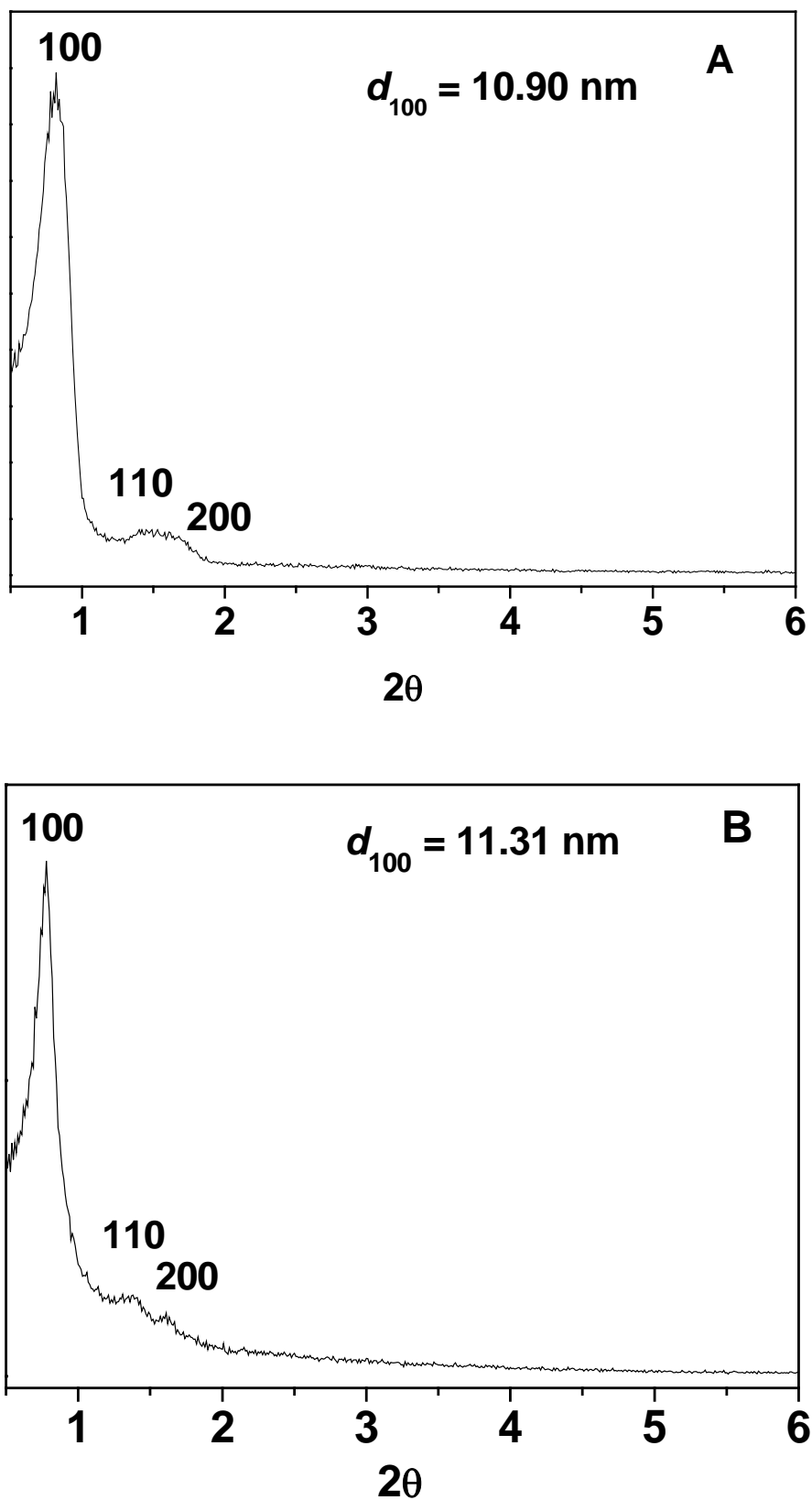
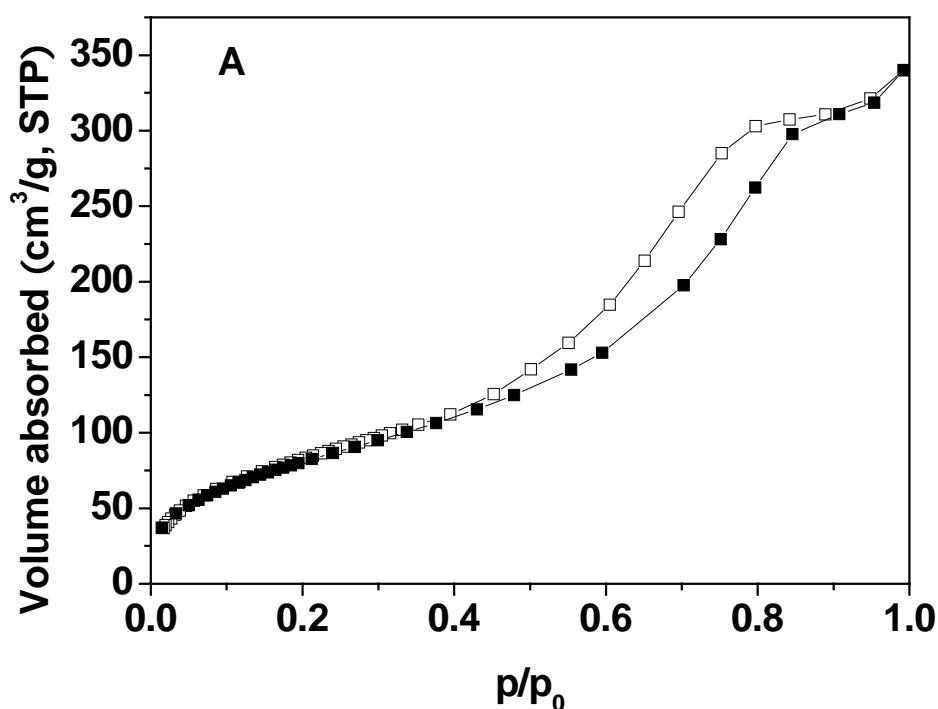


Figure 112. Powder XRD patterns of (A) SA18 and (B) SA20

N<sub>2</sub> adsorption-desorption measurements

N<sub>2</sub> adsorption-desorption measurements were carried out to determine the textural properties of these hybrid materials. The summarized data are listed in Table 1. The adsorption-desorption isotherm of the arenesulfonic acid modified commercial silica gel (**CS18**) is shown in Figure 113A. A type IV isotherm is presented with a hysteresis loop at a relatively high pressure, which demonstrates a material with meso-scaled pore size normally larger than 4 nm<sup>192</sup>. The pore size distribution curve derived from the data of desorption branch is shown in Figure 113B. The half width of this distribution is about 5.1 nm. These results imply that this material preserves the mesoporous properties after modification. Before grafting, the commercial silica gel had a surface area of 500 m<sup>2</sup>g<sup>-1</sup> and average pore size of 6.0 nm. However, after incorporation the surface area decreases to 192 m<sup>2</sup>g<sup>-1</sup>. This indicates the loading of the organic groups on the support occupying the internal pore, thus decreasing the surface area and increasing the density of the final hybrid materials. At the same time, the post-oxidized sulfonic acid always induces the surface area, and the pore volume, which has been widely reported in different substrates<sup>287-289</sup> (MCM-41, SBA-15, microsilica, etc.).



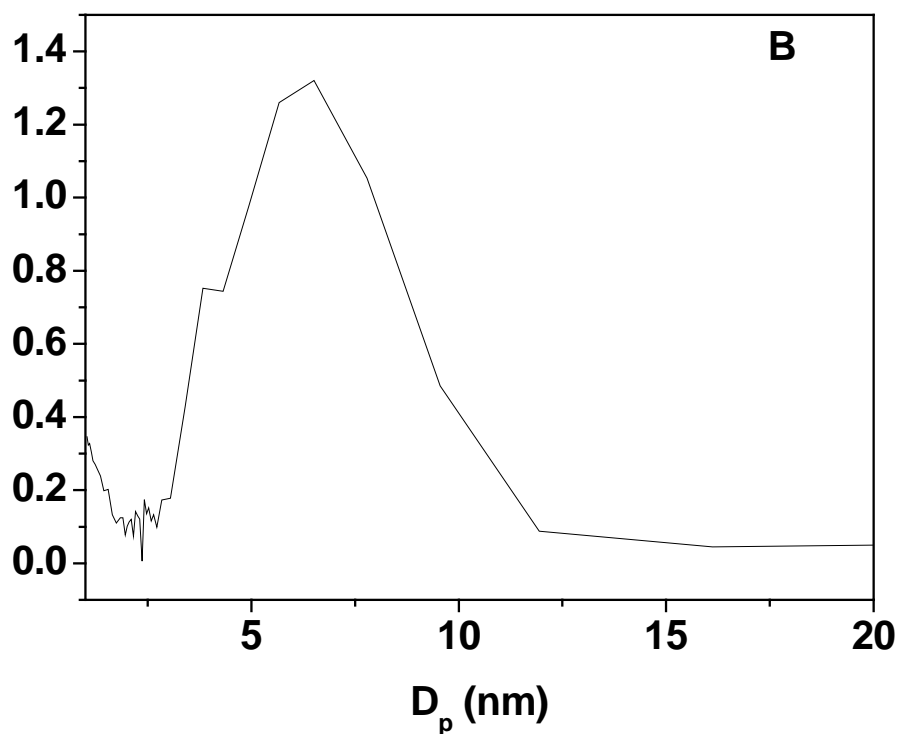


Figure 113. (A)  $N_2$  adsorption-desorption isotherm of **CS18**, adsorption points are marked by solid squares and desorption points by empty squares. (B) Pore size distribution of **CS18**.

Figure 114A shows the isotherm of **SA20**, which presents a featured type of the isotherm of SBA-15 materials with a sharp capillary condensation step beginning at  $p/p_0 \sim 0.65$ . This characteristic indicates the presence of cylindrical channels with a uniform distribution and a relative large size of the pores in this material. Figure 114A illustrates the pore size distribution curve of **SA20** combined a 1.62 nm half width of distribution peak, indicates the narrow distribution.

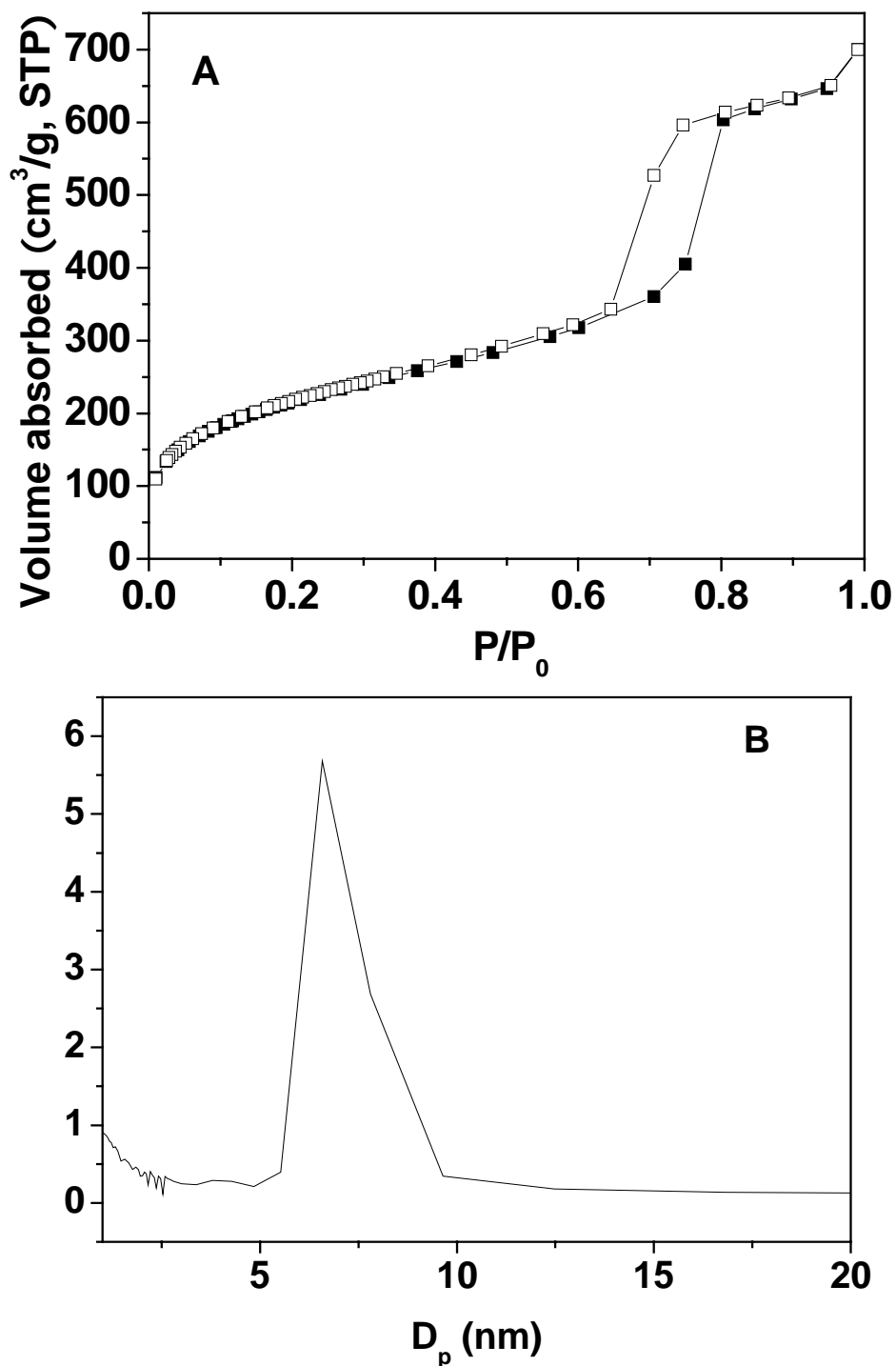


Figure 114. (A) N<sub>2</sub> adsorption-desorption isotherm of **SA20**, adsorption points are marked by solid squares and desorption points by empty squares. (B) Pore size distribution of **SA20**.

The isotherm of the hybrid arenesulfonic acid material **SG20** prepared by sol-gel method, exhibits a reversible Type I isotherm which indicates a microporous solids having a relatively small external surfaces (Figure 115A). A small hysteresis loop can be observed in the range of



$p/p_0$  0.38~0.70, disclosing that a capillary condensation takes place in mesopores. Additionally, the hysteresis loop can be assigned to the type H2, which implies a not well-defined distribution of the pore size. It can be further proved by the PSD curve calculated by the BJH method from desorption branch in Figure 115B. This type of hysteresis loop is normally attributed to a type of ink-bottle pore.

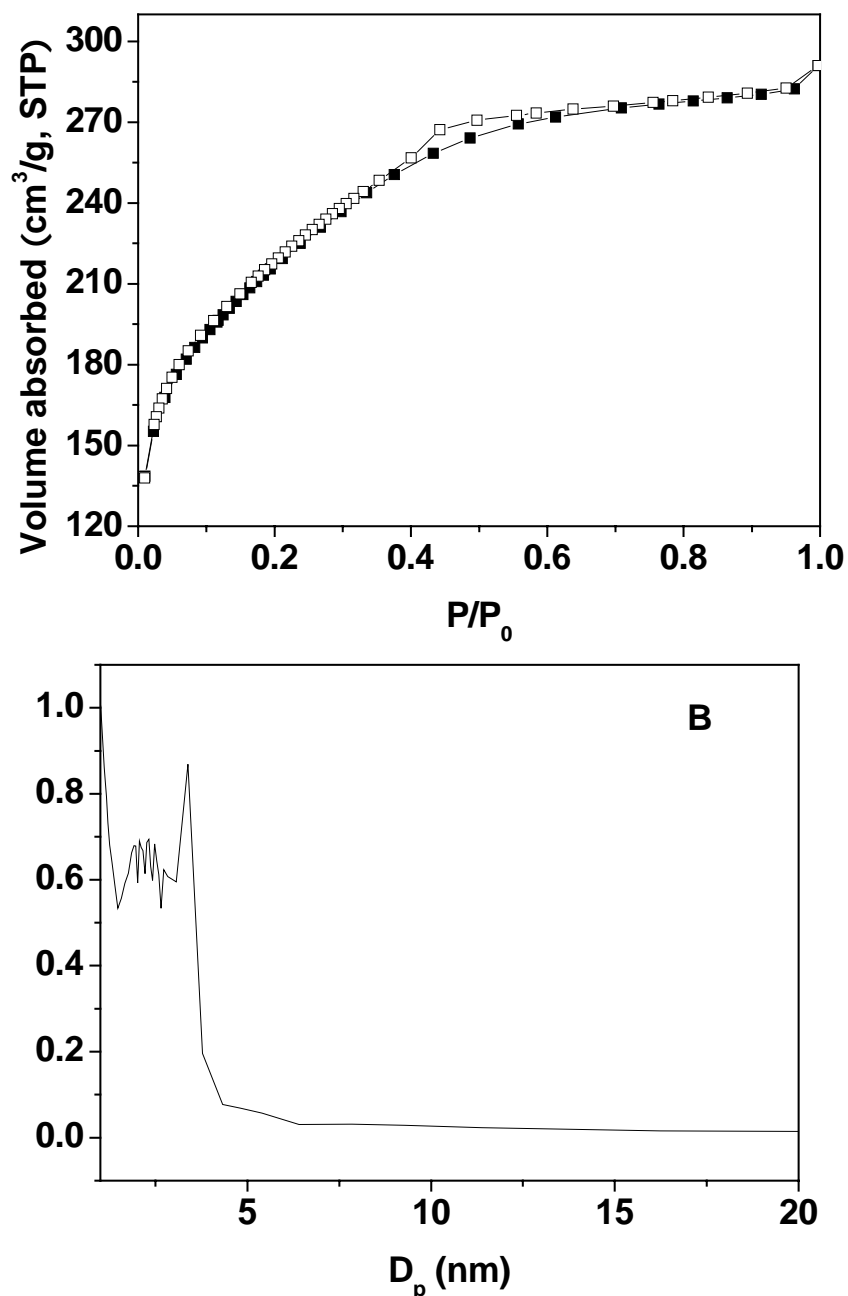


Figure 115. (A) N<sub>2</sub> adsorption-desorption isotherm of **SG20**, adsorption points are marked by solid squares and desorption points by empty squares. (B) Pore size distribution of **SG20**.

Table 19. Structural and textural properties and composition information of organic-acid functionalized silica materials

sample	type	$D_p^a$ (nm)	$S_{BET}$ ( $m^2g^{-1}$ )	$V_p$ ( $cm^3g^{-1}$ )	theory amount <sup>b</sup>	acid <sup>c</sup> ( $mmolg^{-1}$ )	incorpora tion (%)
<b>CS</b>	-	6.0	~500	0.75	-	-	-
<b>CS18</b>	Alk-SO <sub>3</sub> H	6.5	308	0.49	1.62	0.35	22
<b>SA18</b>	Alk-SO <sub>3</sub> H	-	-	-	1.40	1.10	79
<b>SG18</b>	Alk-SO <sub>3</sub> H	-	-	-	1.40	1.18	84
<b>CS20</b>	Ar-SO <sub>3</sub> H	-	-	-	0.81	0.38	47
<b>SA20</b>	Ar-SO <sub>3</sub> H	6.6	789	1.00	1.28	0.88	69
<b>SG20</b>	Ar-SO <sub>3</sub> H	-	765	0.44	1.28	1.15	90

<sup>a</sup> The peak position of the distribution curves by BJH. <sup>b</sup> Expected acid capacity at 100 % of incorporation and 100 % of conversion to sulfonic acid. <sup>c</sup> mmol of H<sup>+</sup> per g SiO<sub>2</sub>, obtained by NaOH titration.

### 4.3 Characterization of the organic component in the hybrid materials

#### Acid-base titration

The accessibility of acidic centers in the materials was determined by acid-base titration. The H<sup>+</sup> was exchanged by sodium chloride (NaCl, 2M), and the resulting acidic solution was titrated by dropwise addition of 0.01 M NaOH (aq). The acid capacity of the hybrid materials is summarized in Table 19. All of them are less than the theoretically expected acid capacity and the corresponding incorporation ratio are calculated. The post grafting synthetic method gave the lowest output, due to the limitation by the silanol groups in the support. Especially, the sample **CS18**, which undergoes a postsynthesis oxidation treatment presents the most lowest incorporation. The co-condensation (including template and without template) provides a high degree of organotrialkoxysilane incorporation and a high conversion to sulfonic acid.

## FT-IR spectroscopy

The exemplified IR spectra of **CS17** and **CS18** are shown in Figure 116. Evidence for the presence of thiol groups on the commercial silica gel is clearly observed in the IR spectrum of **CS17**. The strong vibration at ca.  $2900\text{ cm}^{-1}$  is assigned to C–H stretching vibrations of the propyl chains. Additionally, a weak vibration corresponding to the –SH group at  $2570\text{ cm}^{-1}$  can be observed. The absence of this signal in the spectrum of **CS18** proves the total conversion of thiol to sulfonic group. However, a decrease in the C–H vibration can be clearly seen, indicating a loss of sulfur species during the postsynthetic oxidation process.

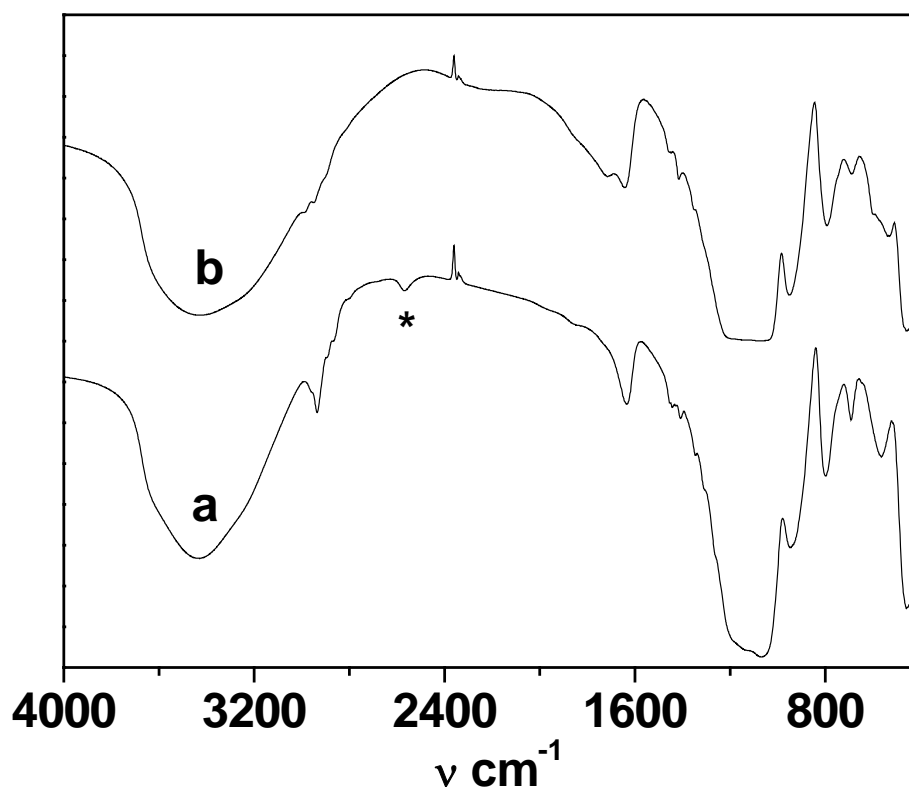
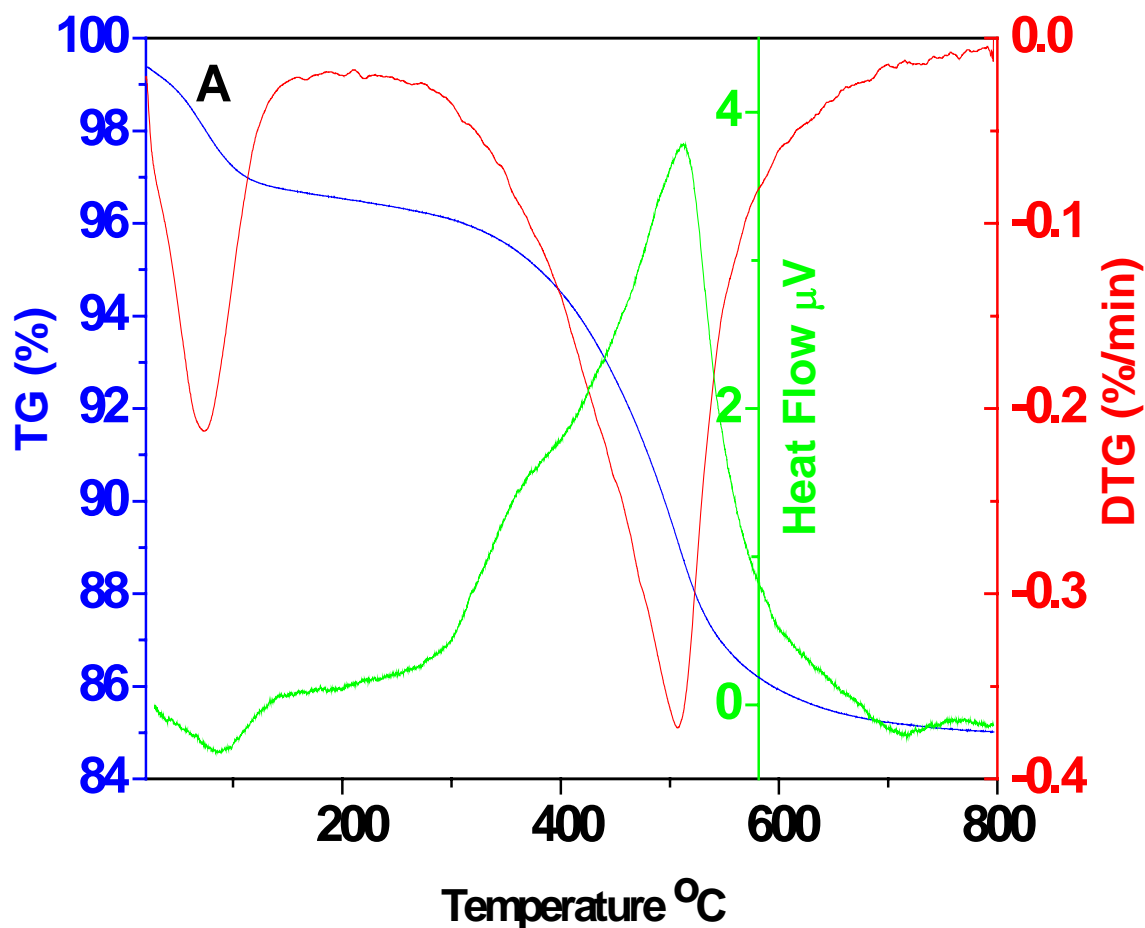


Figure 116. FT-IR spectra of samples (a) **CS17**, and (b) **CS18**.

## Thermogravimetry

The thermogravimetric analysis was performed to determine the arenesulfonic group in **CS20** and **SA20**. The TG–DTG analysis **CS20** is presented in Figure 117A. A strong desorption peak centers at  $510\text{ °C}$  arises from the arenesulfonic organic group. The weight

loss from 320 °C to 670 °C is ca. 11.0 %, corresponding to 0.59 mmol/g arenesulfonic groups in the material. It is higher than the result of acid-base titration, which might be due to the condensation of silica framework and the unreachable organic groups, which is buried during the postsynthetic oxidation process. The TG–DTG analysis of SA20 show two peaks at ca. 250 °C and 540 °C, which can be assigned to the decomposition of remnant template (P123) and the organic sulfonic groups, separately. The weight loss from 320 °C to 670 °C is 18.0%. It presents 0.97 mmol/g of organic sulfonic loading. It is just slightly higher than the data from titration, proving the high accessibility of sulfonic groups in this material.



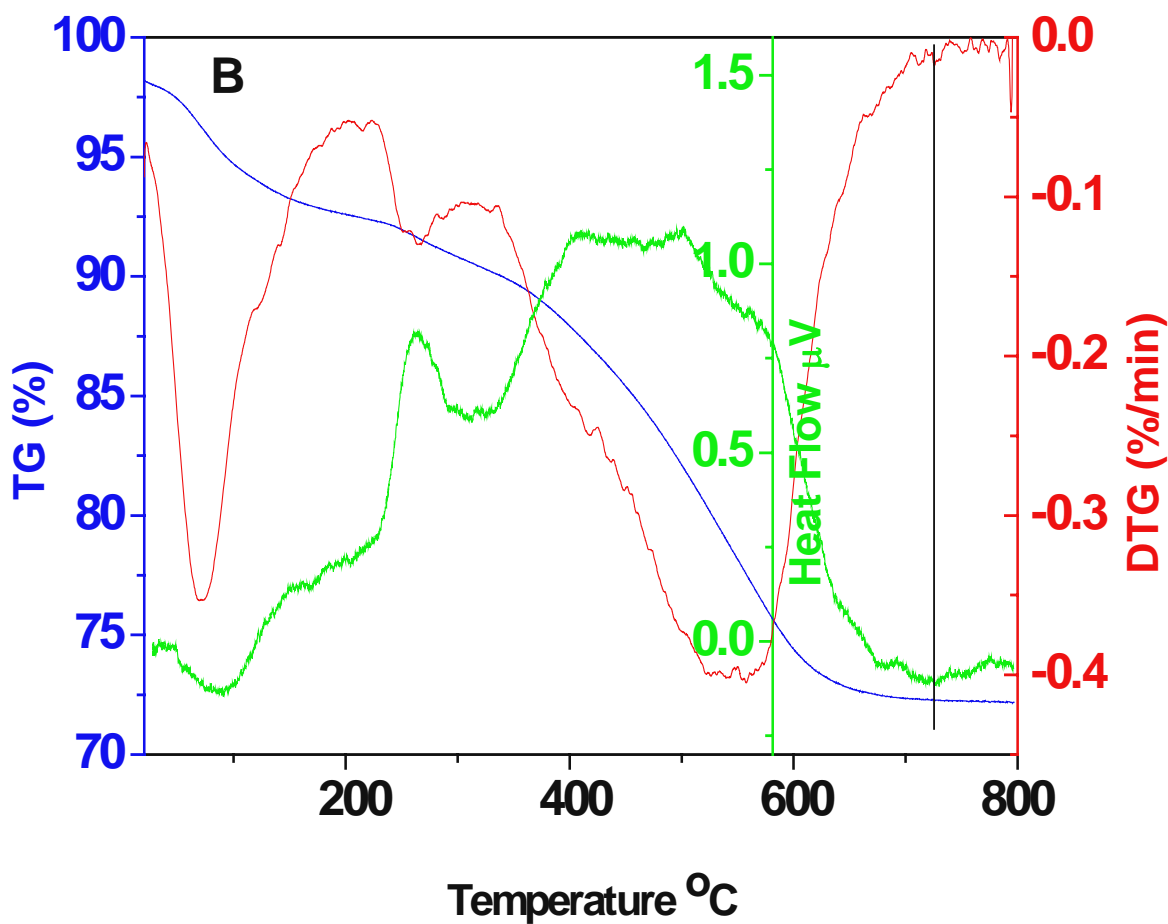


Figure 117. Thermogravimetric and differential thermogravimetric (TG–DTG) analyses of (A) CS20 and (B) SA20

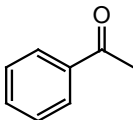
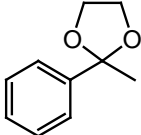
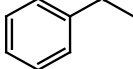
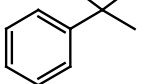
#### 4.4 Application as catalysts

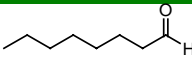
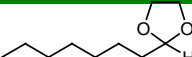
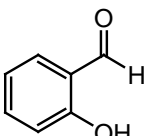
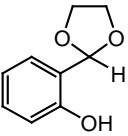
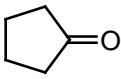
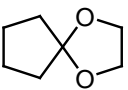
##### Acetalization reaction

The catalytic properties of these solid acids were evaluated in the acetalization of ketones and aldehydes. It had been reported that a propylsulfonic acid functionalized FSM mesoporous material is an efficient catalyst for this reaction<sup>144, 152, 290</sup>. First an exemplified acetalization of acetophenone with ethylene glycol was performed with the same weight of catalysts (Table 20 entries 1-6). Among the alkylsulfonic acid functionalized samples (Table 20 entries 1-3), the maximum yield was obtained on the SA18 and the yield follows the order

**SA18** > **SG18** > **CS18**. As expected, the yield after 10 h reaction increases with an increasing amount of sulfonic acid groups. Thus **CS18** with 0.35 mmol of acidic sites gives the lowest yield. However, it is worth to notice that **SG18** (1.18 mmol/g) has a similar amount of acid as **SA18** (1.10 mmol/g), but presents a slightly lower final yield, which indicates that the structure might also have influence on the reaction. **SG18** contains a large amount of micro-size pores, thus some of the sulfonic acid sites are not accessible for the diffusing reactant molecules or the release of product molecules is not possible in the small pores. Similar phenomena can be observed for the arenesulfonic functionalized catalysts. The yield follows the order of **SA20** > **SG20** > **CS20**. However, the arenesulfonic functionalized catalysts give higher yields than the alkylsulfonic containing catalysts, probably due to the high acid strength. It can further be proved by exemplified kinetic plots of **CS18** and **CS20** (Figure 118) that **CS20** has a sharper initial slope than **CS18**. Since these two catalysts have very similar acid site loading, this result should be attributed to the high acid strength of the aromatic substituted sulfonic acid. As well, the more hydrophobic surface of phenyl containing catalyst may have some positive attributions to this result<sup>152</sup>.

Table 20. Organic sulfonic acid functionalized solid materials catalyzing the acetalization of carbonyl compounds with ethylene glycol.

entry	catalyst	substrate	time	product	yield (%)
1	<b>CS18</b> <sup>a</sup>		10		60
2	<b>SA18</b> <sup>a</sup>		10		88
3	<b>SG18</b> <sup>a</sup>		10		84
4	<b>CS20</b> <sup>a</sup>		10		72
5	<b>SA20</b> <sup>a</sup>		10		95
6	<b>SG20</b> <sup>a</sup>		10		90

7	CS20 <sup>b</sup>		1		97, 94 <sup>c</sup> , 91 <sup>d</sup> , 88 <sup>e</sup>
8	SA20 <sup>b</sup>		1		98, 96 <sup>c</sup> , 94 <sup>d</sup> , 92 <sup>e</sup>
9	SG20 <sup>b</sup>		1		97, 95 <sup>c</sup> , 93 <sup>d</sup> , 90 <sup>e</sup>
10	CS20 <sup>b</sup>		12		84
11	SA20 <sup>b</sup>		12		80
12	SG20 <sup>b</sup>		12		75
13	CS20 <sup>b</sup>		3		90
14	SA20 <sup>b</sup>		3		86
15	SG20 <sup>b</sup>		3		80

<sup>a</sup> The reaction was carried out by refluxing the mixture carbonyl compound (5.0 mmol) and ethylene glycol (6.0 mmol) in toluene with a catalyst (10 mg). <sup>b</sup> The reaction was performed under same condition except using a catalyst (0.1 mol% respect to the carbonyl compound). <sup>c</sup> second cycle. <sup>d</sup> third cycle. <sup>e</sup> fourth cycle.

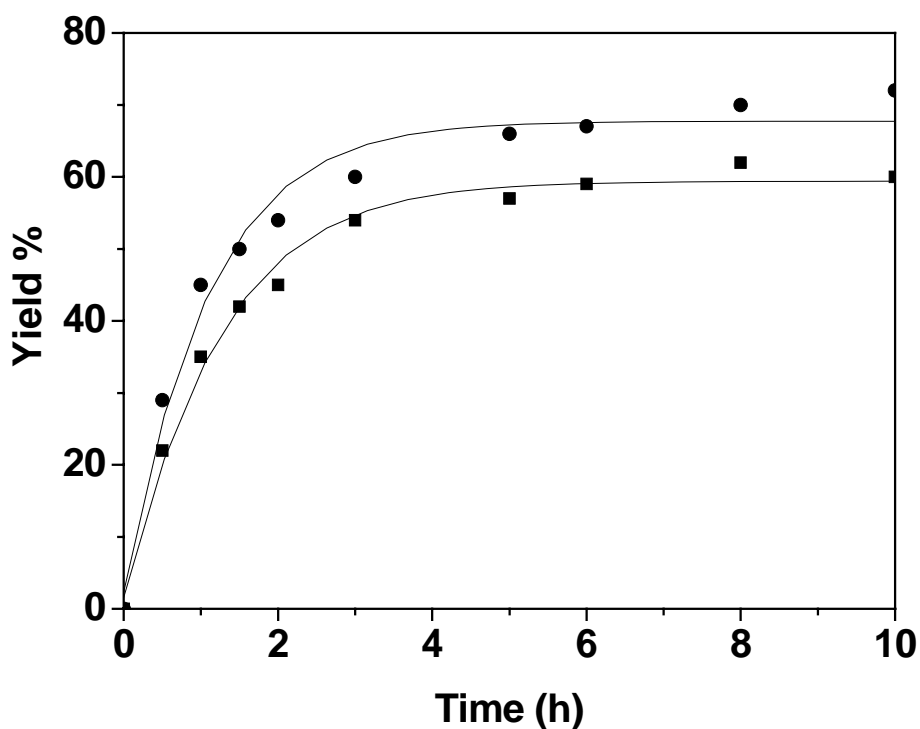


Figure 118. Plot of GC yield versus time for the acetalization of acetophenone by (■) CS18, and (●) CS20. The catalyst amount was 10 mg.

With the same amount of acid on different catalysts (0.1 mol%) was carried out in the acetalization of various carbonyl compounds with ethylene glycol (Table 20 entries 7-15). As

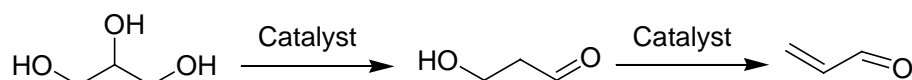
expected *n*-octanal always provides a high yield of the dioxolane compound in a short time, since the nature of this aldehyde is beneficial for the nucleophilic addition. As well, the easy diffusion of flexible alkyl-chain compound in the solid catalyst, may also enhance the overall reaction rate. Salicylaldehyde needs a longer reaction time gives lower yield, due to the steric resistance of the phenyl group. Cyclopentanone as a ketone also provides rather good yields up to 90% after 3h. Comparing the same reaction for different catalyst, the yields follow the order **CS20** > **SA20** > **SG20**. This result should be attributed to a structural effect, since these reactions are now performed with the same amounts of sulfonic acid. The low yield of **SG20** is due to the microporous property rising high diffusional limitations as well as less accessibility of active sites for the reactant molecules. The same reason can be used to explain the result of **SA20**: it is well known that the SBA-15 structural material is containing a portion of micro-pores in the wall<sup>36</sup>. On the contrary, the commercial silica gel has exposed pores in the meso-scale, which are easily accessible for the reactant molecules. The reusability of the arenesulfonic acid anchored catalysts was investigated three times for the acetalization of *n*-octanal in order to see the stability of heterogenized catalysts (entries 7-9). It was found that the high activity of catalysts is preserved well.

#### Glycerol to acrolein reaction

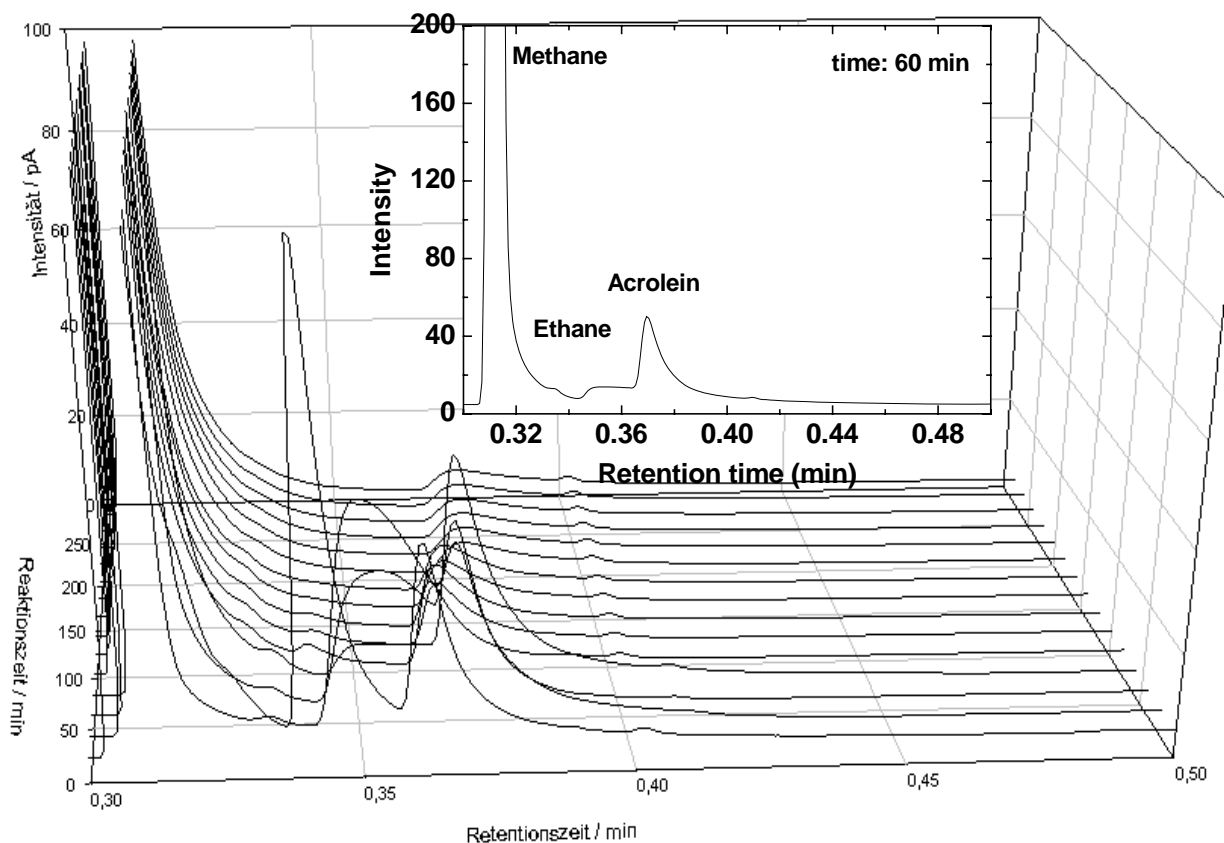
Recently, the catalytic conversion of biomass derived feedstocks for the synthesis of value-added fuels, chemicals and materials has been attracting much attention, since the shortage of petroleum is an emergency issue<sup>291</sup>. Thus, large surplus of glycerol as a byproduct (10 % in weight) in manufacturing biodiesel fuel by transesterification of seed oils with methanol bring a new opportunity to converse it into value-added chemicals. Acrolein as one of the commercially valued products can be synthesized by the double dehydration of glycerol by acid catalysts<sup>292</sup>. Hence, it is a suitable reaction to testify our hybrid organic acid functionalized materials.



The arenesulfonic functionalized commercial silica gel and SAB-15 material (**CS20** and **SB20**) were tested in fixed bed gas phase reactor for a glycerol to acrolein reaction at 200 °C (Scheme 28). The choice of arenesulfonic containing solids was decided by the high thermo stability of this organic group (high decomposition temperature beginning at 350 °C in atmosphere by the TG–DTG result).



Scheme 28.

Figure 119. Gas-phase on line GC data of the **CS20** catalyzed glycerol to acrolein reaction.

Two reactions were performed and the on-line GC data are shown in Figure 119 for catalyst **CS20** and in Figure 120 for catalyst **SA20**. The production of acrolein is proved in both reactions, and the product can be detected with a short induction period. **SA20** gives higher reaction rate than **CS20**, which is due to the inclusion of more acid sites in this catalyst. With

this catalyst the reaction can be finished within 40 min and the highest amount of acrolein appeared at 20 min.

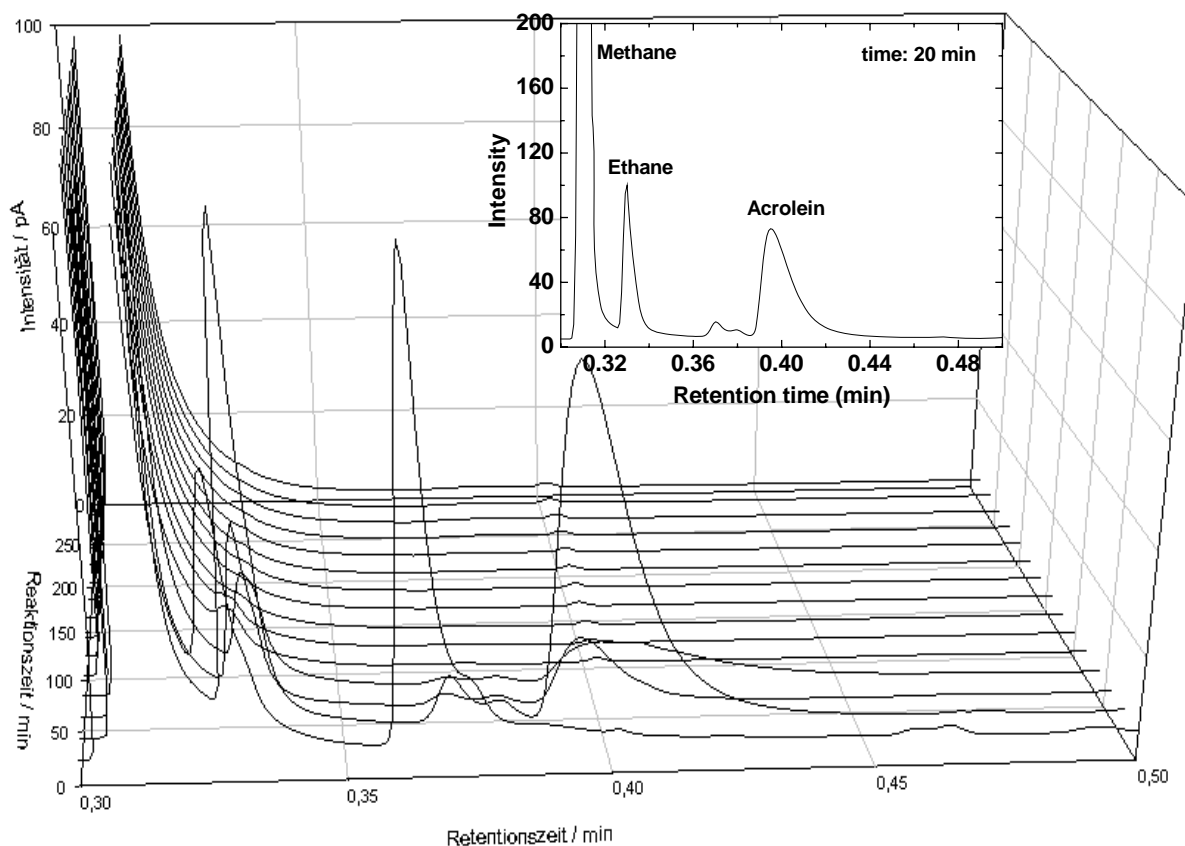


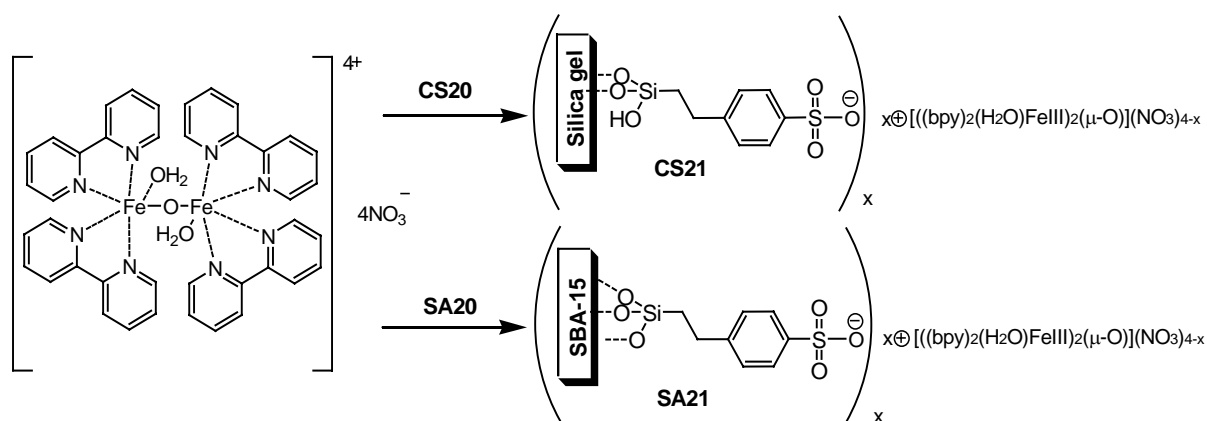
Figure 120. Gas-phase on line GC data of the SA20 catalyzed glycerol to acrolein reaction.

#### 4.5 Arenesulfonic acid functionalized material as an ion exchanging support for application in catalysis

The sulfonic acid containing hybrid materials not only serve as Brønsted acid catalyst, but also play a role as supporting materials to incorporate metal salts<sup>293</sup>, metal complexes<sup>80</sup>, and ionic liquids<sup>294</sup>. These further functionalized hybrid materials have been successfully investigated and applied in the field of catalysis<sup>295</sup>, electronics<sup>296</sup>, and optics<sup>81</sup>. Here we present a  $\mu$ -oxo-bridged diferric complex incorporated into the organic sulfonic hybrid materials and its application in alkene oxidation.

## Synthetic process

The arenesulfonic acid functionalized material **CS20** and **SA20** with a monovalent cation-exchange capacity of 0.38 and 0.80 mmol/g were used as substrates. The synthetic route is illustrated in Scheme 29. The incorporation of  $[\text{((bpy)}_2(\text{H}_2\text{O})\text{Fe}^{\text{III}})_2(\mu\text{-O})](\text{NO}_3)_4$  into the hybrid silica materials was conducted by suspending the support in the fresh complex acetonitrile solution under stirring for 1 day and subsequent washing with acetonitrile. The samples were characterized after drying under reduced pressure. A color change of the solution can be observed after addition of **SA20** powder from dark red (with slightly green) to greenish yellow, while a color fade is happens after the addition of **CS20**. The final product **SA21** is a yellow powder and **CS21** is slightly brown.



Scheme 29. Synthesis process of the Fe(III) containing hybrid materials **CS21** and **SA21**.

## Characterization

To determine the amount of the Fe(III) complex loading, elemental analysis was performed for the solid samples, and the results are listed in Table 21. The interaction of the Fe(III) complex and the sulfonic groups should occur through electrostatic interactions and might be cooperative with the interaction between the phenyl rings on the surface and the bipyridine rings of the complex. Supposing all the Fe(III) complexes (considering the complex as a four fold cation) are anchored by interacting with four sulfonic groups, the amount of the

incorporation can be calculated from the nitrogen data of the elemental analysis: it is 0.27 and 0.38 mmol/g for **CS21** and **SA21**, respectively. However, the monovalent cation-exchange capacity of the substrates is not sufficient for containing such high amounts of complexes. Hence the major involving sulfonic sites would be two or one (see the calculated results in Table 21). These results are also reasonable to consider the geometric influence. The elemental analysis can give a rough estimated content of complex loading of 0.24~0.20 mmol/g for **CS21** and 0.34~0.28 mmol/g for **SA21**. Further investigations were carried out by UV-vis spectroscopy to provide the accurate amount of incorporation by detecting the concentration change of the exchanged solution, as well as the quantitative analysis of Fe<sup>3+</sup> by ICP. Here as a first hint, the estimated contents of 0.21 mmol/g for **CS21** and 0.31 mmol/g for **SA21** were used in the later catalytic experiments.

Table 21. Organic content information of the exchanged samples

sample	substrate	acidic capacity (mmol/g)	elemental analysis			possible content (mmol/g) <sup>a</sup>			
			C	H	N	1 <sup>b</sup>	2 <sup>b</sup>	3 <sup>b</sup>	4 <sup>b</sup>
<b>CS21</b>	<b>CS20</b>	0.38	14.10	1.50	3.03	0.27	0.24	0.21	0.20
<b>SA21</b>	<b>SA20</b>	0.80	21.57	2.28	4.32	0.38	0.34	0.31	0.28

<sup>a</sup> The calculation is based on the nitrogen data of the element analysis. <sup>b</sup> The supposing number of interacting sulfonic acid sites.

The absorption spectra of hybrid samples **CS21** and **SA21** are displayed in Figure 121. Both spectra present two strong absorptions in the UV region. The band at 360 nm for **CS21** and 355 nm for **SA21** can be assigned to allowed oxo-to-iron charge transfers<sup>297</sup>. A broad and weak band observed apparently in **CS21** at ~530 nm, while not so obviously observed in **SA21**, is attributed to a forbidden oxo-to-iron charge transfer and suggested to be correlated to the Fe-O-Fe angle<sup>298</sup>. This results indicate the incorporation of the Fe(III) complex in the materials.

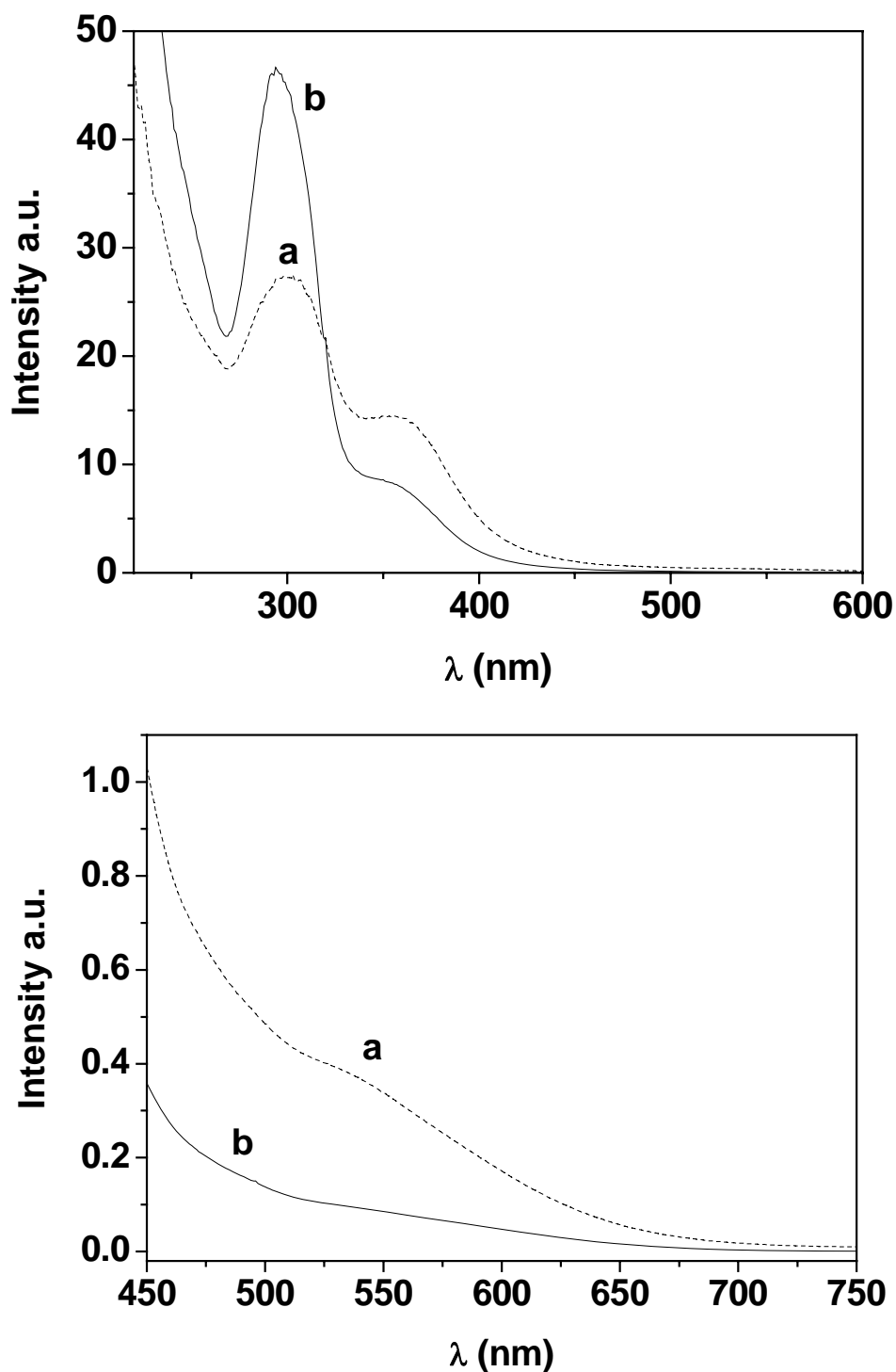
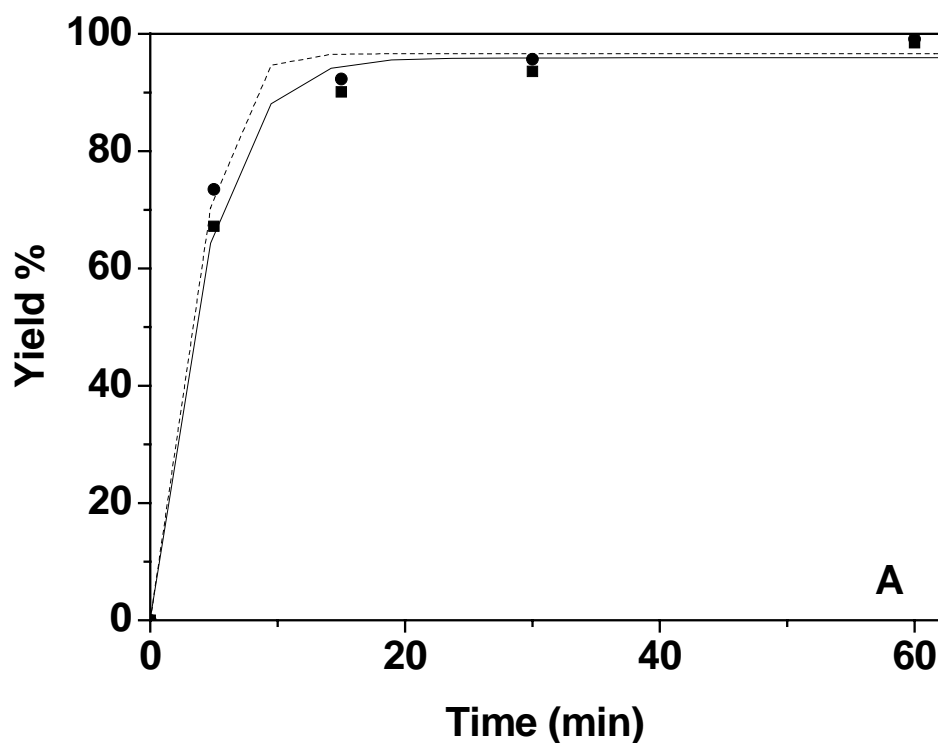


Figure 121. Uv-vis spectra of (a) CS21 and (b) SA21

#### Catalytic results

The catalytic activity of these two solid samples modified by an Fe(III) complex are first testified by the epoxidation of cis-cyclootene with commercial peracetic acid. The kinetic

plots of **SB21** and **CS21** are exhibited in Figure 122A. Both catalysts display a prominent initial conversion, the initial rate per catalytic site can be estimated as  $269 \text{ h}^{-1}$  for **SB21** and  $294 \text{ h}^{-1}$  for **CS21**, respectively. The fact that the value of **CS21** is slightly higher than **SB21** might arise from the different diffusion properties of the samples. After one hour, both processes have almost reached the total conversion of cis-cyclooctene with nearly 100% selectivity (see the entries 1 and 5 in Table 22). The recyclability of the modified catalysts was examined by reusing them after filtration at the reaction temperature with sufficiently washing. The nearly total conversion was kept at least up to three times of recycling (entries 2, 3, 4, and 6 in Table 22). However, in the blank reaction test, using pure substrate **SA20**,  $\text{Na}^+$  exchanged substrate **SA20-Na**, and no other solid at all, the high conversions are preserved after one hour reaction. This is due to the fact that peracetic acid itself is capable of epoxidizing the cis-cyclooctene. The catalyst **SA21** was also tested for the epoxidation with  $t\text{BuOOH}$  and the plot of conversion vs. time is presented in Figure 122B. After 3h of reaction, the conversion can reach to 45% with 85% epoxidation selectivity.



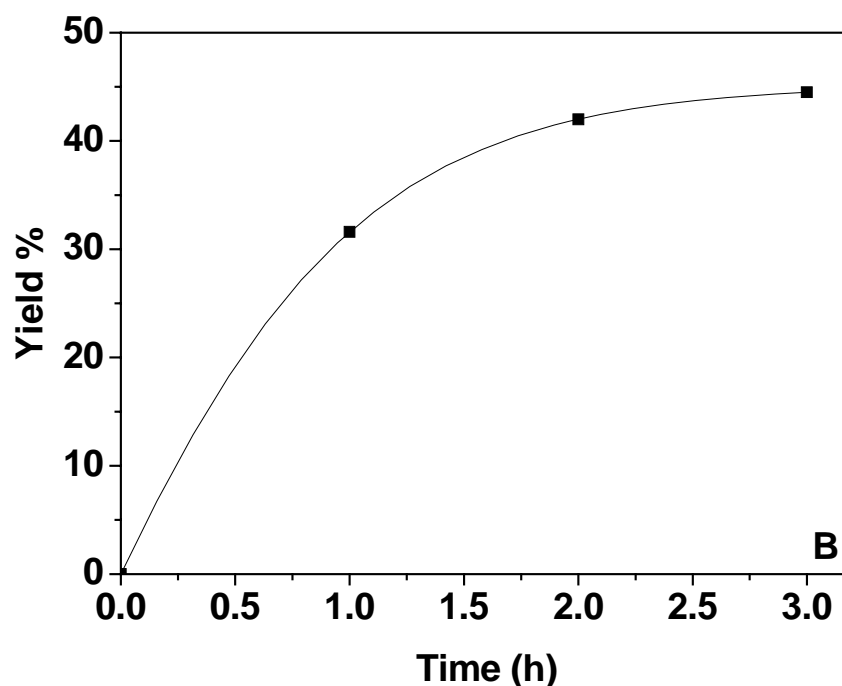


Figure 122. Plot of GC conversion versus time for the epoxidation of cis-cyclooctene (A) catalyzed by (■) SA21, and (●) CS21 using peracetic acid. (B) catalyzed by SA21 using tBuOOH as oxide.

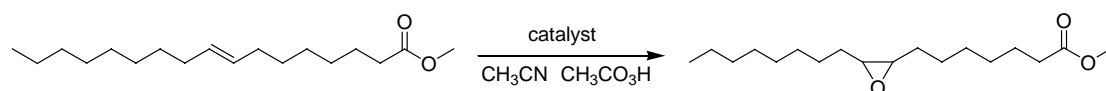
Table 22. Epoxidation of cis-cyclooctene with Fe(III) complex modified solid catalyst

entry	catalyst	oxide	time (min)	conversion <sup>g</sup> %	yield <sup>g0</sup> %
1	SA21 <sup>a</sup>	CH <sub>3</sub> CO <sub>3</sub> H	60	99	98
2	SA21 <sup>a,b</sup>	CH <sub>3</sub> CO <sub>3</sub> H	60	96	94
3	SA21 <sup>a,c</sup>	CH <sub>3</sub> CO <sub>3</sub> H	60	98	97
4	SA21 <sup>a,d</sup>	CH <sub>3</sub> CO <sub>3</sub> H	60	96	96
5	CS21 <sup>a</sup>	CH <sub>3</sub> CO <sub>3</sub> H	60	99	98
6	CS21 <sup>a</sup>	CH <sub>3</sub> CO <sub>3</sub> H	60	96	95
7	SA20 <sup>a</sup>	CH <sub>3</sub> CO <sub>3</sub> H	60	99	97
8	SA20-Na <sup>a,e</sup>	CH <sub>3</sub> CO <sub>3</sub> H	60	93	91
9	- <sup>a</sup>	CH <sub>3</sub> CO <sub>3</sub> H	60	98	96
10	SA21 <sup>f</sup>	tBuOOH	180	45	38

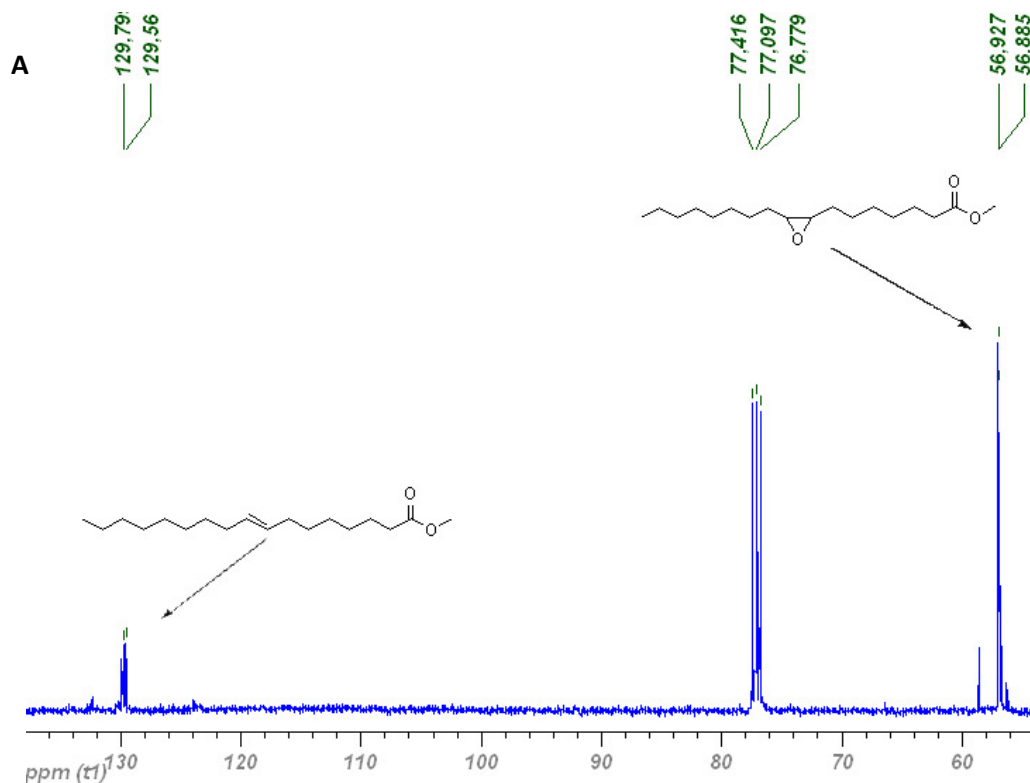
<sup>a</sup> The reaction was carried out at 0 °C, with a mixture of cis-cyclooctene (5.0 mmol) and 2 equivalents of peracetic acid in MeCN with a catalyst (0.25 mol% resp. to cis-

cyclooctene). <sup>b</sup> second cycle. <sup>c</sup> third cycle. <sup>d</sup> fourth cycle. <sup>e</sup> Na<sup>+</sup> exchanged **SA20** as catalyst. <sup>f</sup> the reaction was performed under reflux, with a mixture of cis-cyclooctene (1.0 mmol) and 1.1 equivalent of tBuOOH in CHCl<sub>3</sub> with catalyst **SA21** (0.5 mol% resp. to cis-cyclooctene). <sup>g</sup> detected by GC using decane as the internal standard.

Epoxidation of methyl oleate with peracetic acid in the presence of **SA21** (see Scheme 30) was also performed to test the catalytic property of this Fe(III) complex modified hybrid material. After one hour of reaction, the substrate and product were extracted by pentane. In the <sup>13</sup>C NMR (Figure 123A) spectrum appear two peaks at ca. δ 59 ppm, which can be assigned to the carbon atoms of the epoxy ring indicating the presence of the desired product. Quantitative analysis can be achieved by the <sup>1</sup>H NMR spectra (Figure 123B), and the conversion of methyl oleate can be calculated as 88% and the yield of epoxy product is 50%.



Scheme 30





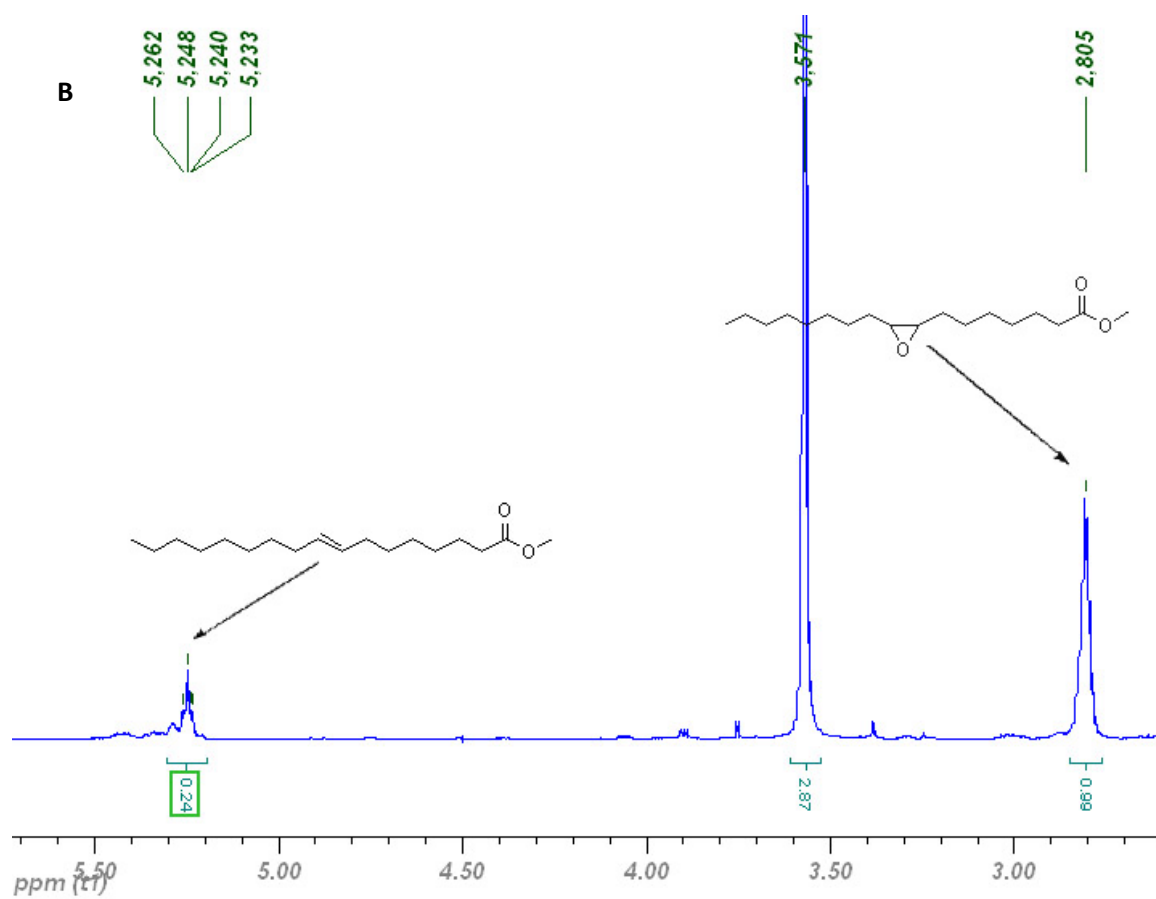


Figure 123. The NMR analysis of epoxidation of methyl oleate (A)  $^{13}\text{C}$  NMR and (B)  $^1\text{H}$  NMR

## Conclusion

A series elaborately well designed (oligo)phenothiazines are covalently bonded into order mesoporous material by post grafting or in-situ co-condensation process. The well ordered mesostructures were verified by XRD and N<sub>2</sub> adsorption measurement. Especially, the influence of various molecular structures to the final structures of materials was discussed in detail, which might provide a scope for the further molecular design. The introduction of (oligo)phenothiazine molecules in the hybrid materials was proved by the means of FT-IR, UV-Vis and solid state MAS NMR spectroscopy. Two types of one electron acceptors antimony pentachloride and NOBF<sub>4</sub>, were used to generate the (oligo)phenothiazine radical cations. The existence and distinguished stability of these radical cations in the hybrid materials was confirmed by UV-Vis and EPR spectroscopy. Additionally, a broad absorption and in the visible-NIR region can be observed in the in-situ synthesized materials, which can be associated with a charge resonance transition of cofacially oriented (oligo)phenothiazines and their corresponding radical cations. A further solid state electrochemical characterization of these hybrid materials gave evidence for the presence of a long-range electron transfer route via electron exchange between the adjacent phenothiazines (electron hoping). Thus, in this hybrid system, the mesoporous structure of the materials act as the proper substance. It can not only provide the mechanical stability, easy accessible pathway, but also can arrange the (oligo)phenothiazines by a nanoscale size effect, which is important for the intermolecular orientation, so as to the formation of  $\pi$ -conjugated hybrid materials with utility electrochemical properties. Additionally, the transparency of silica framework and the interesting photo luminescence features of (oligo)phenothiazines present a potential application of these hybrid materials in the area of optical sensors. A hint for this work comes from the triazole linked (oligo)phenothiazine material.

Thiazolium salts functionalized ordered mesoporous materials were first synthesized by covalently anchoring a thiazolyl silane onto mesoporous silica MCM-41, silica SBA-15 and PMO materials by different methods. The results of powder X-ray diffraction and N<sub>2</sub> adsorption show the presence of the long range ordered two-dimensional hexagonal mesostructure of all the materials. The loading of organo catalyst was detected by elemental and thermal gravimetric analysis. The integrity and covalently anchoring of the organic groups in the modified mesoporous materials is confirmed by the characterization of solid-state <sup>13</sup>C and <sup>29</sup>Si CP–MAS NMR spectroscopy, TG-DTG, and FT-IR spectroscopy. The thiazolium salt functionalized solids are active catalysts for the reaction of benzoin condensation and the cross-coupling of aldehydes with acylimines to yield  $\alpha$ -amido ketones. Moreover, the catalytic activity of the heterogenized organo catalyst can further be enhanced by silylation of the residual Si-OH groups using Me<sub>3</sub>SiCl, due to an increased hydrophobicity of the support's surface. The recyclability of the catalysts depends on the solvent used for the reaction: here aprotic and solvents of low polarity turned out to be beneficial.

Two types of sulfonic acids were introduced into three types of silica materials by grafting, co-condensation (with template), and sol-gel (without template), respectively. The structural and textural properties were determined by XRD and N<sub>2</sub> adsorption measurement. The organic loadings were assisted by FT-IR and thermogravimetric analysis. The acid capacities of these materials were detected by acid-base titration. The catalytic properties of these solid acids were evaluated by acetalization and glycerol to acrolein reaction. Additionally, the application of these acids as ion exchanged supporters was carried out by the incorporation of  $[(\text{bpy})_2(\text{H}_2\text{O})\text{Fe}^{\text{III}}]_2(\mu\text{-O})(\text{NO}_3)_4$  on the materials. The epoxidation reaction was used to testify these complex exchanged materials.

## Outlook

- (1) The electrical conductivity may be further proved by the examination of electrorheological (ER) properties of the in-situ synthetic materials or the contactless microwave absorption technique<sup>299</sup>.
- (2) The in-situ synthetic method can be adjusted by change the ratio of the template vs. the phenothiazine precursor, which should bring different morphologies to these hybrid materials.
- (3) The bis-thiazole linked phenothiazine might be further installed in the framework of SBA-15. Some transition metal may be introduced by one-pot synthetic process or by the postsynthesis using the nitrogen donor of thiazole ring. The introduced transition metal atom may be play as an electron acceptor.
- (4) The urea group linked phenothiazinely silane might be performed in a self-assemble polymer material. The intermolecular H-bond and an extending long alkyl chain (C3 to C16 etc.) could be benefit for the ordering of final product. A lamellar or sandwich structure would be expected<sup>178</sup>.
- (5) The planar structure of phenothiazine radical cation would be facility for achieving the material with molecular-scale order, such as by an in-situ hydrolysis of crystal or precipitated solid precursor method.
- (6) The phenothiazine radical cation might be supported on some cation exchanged materials. The amount of loading and the mobility of phenothiazine may be advantaged for the intermolecular communication and electron transfer. The same way may also perform for the incorporation of thiazolium salts.
- (7) The thiazolium salts functionalised PMO can achieved by grafting or co-condensation method in the material with MCM-41 or SBA-15 structure. These materials may be

not severe leaching during the benzoin condensation reaction or the reaction can be well performed in an aprotic solvent.

## Experimental section

### 4.1 General considerations

All the reactions related with organosilanes have to be performed under an inert atmosphere of nitrogen, except the synthesis of the neat silica materials. The solvents were dried and distilled according to standard procedures<sup>300</sup>. Reagents were purchased from ACROS, Aldrich, Fluka, ABCR and Merck and used without further purification unless otherwise noted. The products were purified by flash column chromatography on silica gel 60 (mesh 70-230). The reaction progresses were monitored by thin-layer chromatography performed on silica gel plates. For the detection UV light of wavelength 254 and 366 nm was used.

### 4.2 Characterization

Powder X-ray diffraction is a useful tool to confirm the structure of solid materials. The peak positions in a certain pattern are related to the geometry of the unit cell. The  $2\theta$  value is related to the  $d$ -spacing of the corresponding reflection (spacing of the diffracting planes) by the Bragg Equation ( $\lambda = 2d_{hkl}\sin\theta_{hkl}$ ). Where  $\lambda$  is the wavelength of the X-ray,  $d$  is the spacing between the planes in the atomic lattice and  $hkl$  are the Miller indices of the planes. Unit cell parameter ( $a_0$ ) of a hexagonal lattice can be calculated from,  $a_0 = 2d_{100}/\sqrt{3}$ . The unit cell dimension determined by XRD is also used to calculate the frame wall thickness of the channels of the mesoporous materials. The powder X-ray patterns were recorded on a Siemens D5005 X-ray diffractometer operating at 40 kV and 30 mA using monochromatic  $\text{CuK}\alpha$ -radiation ( $\lambda_{\text{CuK}\alpha} = 0.15405$  nm). The diffraction experiments were conducted at  $2\theta$  values from  $0.5^\circ$  to  $8.0^\circ$  for SBA-15 structural materials,  $1.5^\circ$  to  $10^\circ$  for MCM-41 structural materials, and  $1.5^\circ$  to  $60^\circ$  for PMO materials.

N<sub>2</sub>-adsorption/desorption isotherms were measured at 77 K on a Quantachrome Autosorb 1 sorption analyzer after evacuation of the samples at 120 °C overnight. The specific surface areas were calculated by the Brunauer-Emmett-Teller (BET) equation using adsorption data in the low relative pressure range from 0.05 to 0.2 and the pore size distribution curves were obtained from the desorption branch by the Barret-Joyner-Halenda (BJH) method. Pore volumes were estimated at a relative pressure ( $p/p_0$ ) of  $\sim 0.94$ , assuming full surface saturation with nitrogen.

Scanning electron micrographs (SEM) were recorded using an analytical scanning electron microscope of the type JEOL JSM-6490LA equipped with a tungsten cathode. Prior to taking the micrographs, the samples were sputtered with gold using a JEOL JFC-1200 fine coater. Gold sputtering increases the conductivity of the samples and therefore gives a better resolution. Transmission electron micrographs (TEM) were obtained on a JEOL JEM 1200 EX instrument at an acceleration voltage of 120 kV. Samples for TEM analysis were prepared by sonicating the powdered samples for 30 min in ethanol, followed by depositing on a holey carbon film supported by a copper grid.

The thermogravimetric and differential thermogravimetric (TG-DTG) analyses were carried out on a SETARAM Setsys 16/MS instrument using an alumina pan in the flow of air (80 mL/min) atmosphere from room temperature to 800 °C with a heating rate of 5 °C/min. Elemental analyses were carried out on a Carlo Erba (model EA 1108) Elemental Analyzer. The diffuse reflectance UV-Vis spectroscopy of the solid samples were measured on a Perkin-Elmer Lambda 18 spectrometer equipped with an accessory (RSA-PE-19M) in the range of 200–900 nm. Neat MCM-41 or SBA-15 was used as the reference. The Fourier transform infrared spectra (FT-IR) of the solid or the liquid samples were recorded in the range of 4000 to 400 cm<sup>-1</sup> on a JASCO FT/IR-6100 spectrometer. The solid samples were supported in a KBr pellet and prior to analysis the samples were set under vacuum for 10 min to reduce the

physically adsorbed water.  $^1\text{H}$  and  $^{13}\text{C}$  NMR spectra were recorded with a Bruker Avance 400 spectrometer. Proto-decoupled solid-state  $^{13}\text{C}$  and  $^{29}\text{Si}$  CP-MAS NMR measurements were carried out on a Bruker DSX Avance spectrometer at resonance frequencies of 100.6 and 79.5 MHz, respectively. Q-band CW EPR experiments were performed at 297 K on a Bruker EMX 10-40 spectrometer. Cyclic voltammetry experiments (EG & G potentiostatic instrumentation) were performed under argon in dry and degassed  $\text{CH}_2\text{Cl}_2$  at room temperature and at scan rates of 100, 250, 500, and 1000  $\text{mVs}^{-1}$ . The electrolyte was tetrabutylammoniumhexafluorophosphate ( $\text{Bu}_4\text{NPF}_6$ , 0.025 M). The working electrode was a 1 mm platinum disk, the counter-electrode was a platinum wire and the reference electrode was an Ag/AgCl electrode. The potentials were corrected to the internal standard of  $\text{Fc}/\text{Fc}^+$  in  $\text{CH}_2\text{Cl}_2$  ( $E_0^{0/+1} = 450 \text{ mV}$ )<sup>301</sup>. The solid state cyclic voltammetry experiments were carried out with abrasive samples on a glassy carbon electrode. The modified electrode was used in a standard three-electrode setup with a platinum counter electrode and a silver wire covered with AgCl as reference electrode. Potentials were calibrated with ferrocene against the standard potential of a saturated Ag/AgCl electrode. The measurements were made in acetonitrile with  $\text{Bu}_4\text{NPF}_6$  as supporting electrolyte in a concentration of 0.1 mol/l. The electrochemical measuring system was an EcoChemie Autolab PGSTAT30 potentiostat/galvanostat.

## 4.3 Synthetic process

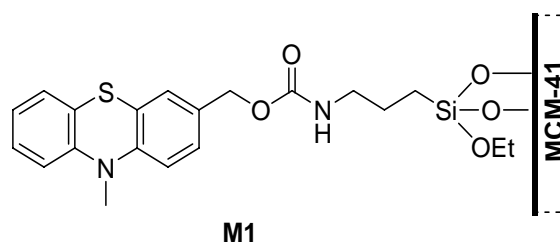
### 4.3.1 Synthesis of pure silica MCM-41

Siliceous MCM-41 materials were synthesized as described in the literature<sup>302</sup>. A typical procedure was the following: 15.46 g of an aqueous solution of ethylamine (70%, 240 mmol ethylamine) were added to a stirred solution of distilled water (175 ml). 5.10 g (14 mmol) of cetyltrimethylammonium bromide (CTAB) and 20.80 g (100 mmol) of tetraethylorthosilicate



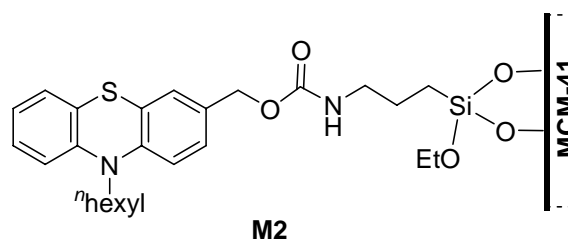
(TEOS) were added dropwise. The reaction mixture was stirred for further 4h at room temperature before being heated to 100 °C for 1 day. The product was recovered by filtration and washed thoroughly with distilled water, and dried at 80 °C overnight. The elimination of the template was performed by extraction with HCl/EtOH under reflux.

4.3.2 Synthesis of (10-methyl-10H-phenothiazin-3-yl)methyl-3-(triethoxysilyl)propyl-carbamate (**1**) modified mesoporous MCM-41 material (**M1**).



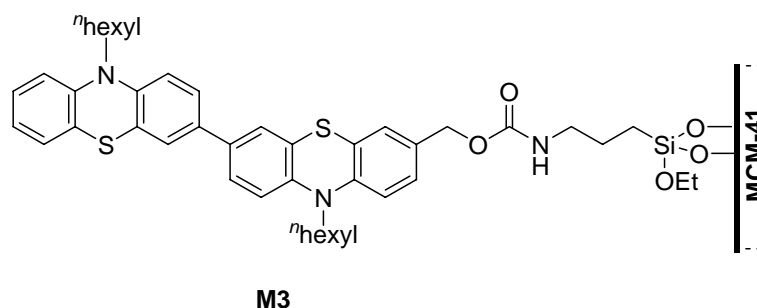
1.50 g of pure siliceous MCM-41, which was previously degassed at 150 °C for 4 h, were suspended in 60 ml of dry toluene. 0.71 g (1.44 mmol) of precursor **1**, dissolved in 5 ml of dry dichloromethane, were added. The mixture was heated to reflux for 24 h under a nitrogen atmosphere. The solids were filtered off, washed with dichloromethane and subsequently transferred to a Soxhlet extraction equipment to be extracted with CH<sub>2</sub>Cl<sub>2</sub> for 24 h under nitrogen protection. After being dried under a vacuum at 50 °C, the product **M1** was obtained as a colorless powder. Elemental analysis for **M1**: found C, 12.10; H, 2.17; N, 1.14, which corresponds to a loading of 0.41 mmol/g.

4.3.3 Synthesis of (10-hexyl-10H-phenothiazin-3-yl)methyl-3-(triethoxysilyl)propyl-carbamate (**2**) modified mesoporous MCM-41 material (**M2**).



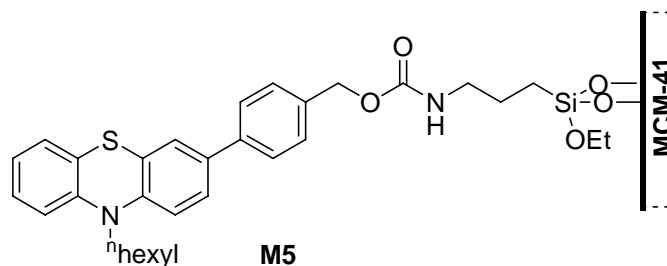
A similar procedure was used as in the synthesis of **M1**, except that 1.00 g of pure siliceous MCM-41 and 0.54 g (0.96 mmol) of precursor **2** were used. The product **M2** was obtained as a colorless powder. Elemental analysis for **M2**: found C, 11.01; H, 2.53; N, 0.95, which corresponds to a loading of 0.34 mmol/g.

4.3.4 Synthesis of (10,10'-dihexyl-10H,10'H-3,3'-biphenothiazin-7-yl)methyl-3-(triethoxysilyl)propylcarbamate (**3**) modified mesoporous MCM-41 material (**M3**).



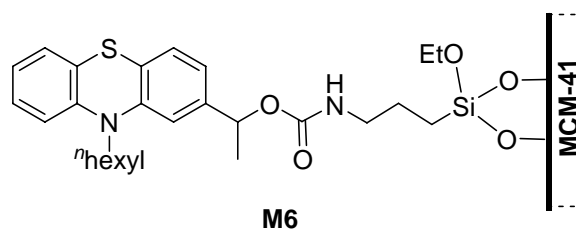
A similar grafting procedure was used. 0.50 g of pure siliceous MCM-41 with 0.40 g (0.47 mmol) of **3** were used to obtain **M3** as a colorless powder. Elemental analysis for **M3**: found C, 5.34; H, 1.48; N, --.

4.3.5 Synthesis of 4-(10-hexyl-10H-phenothiazin-3-yl)benzyl-3-(triethoxysilyl)propylcarbamate (**5**) modified mesoporous MCM-41 material (**M5**).



The grafting procedure was performed as before, typically, a total of 0.50 g of pure siliceous MCM-41 and 0.30 g (0.48 mmol) of **5** were mixed to produce **M5** as a yellow powder. Elemental analysis for **M5**: found C, 10.07; H, 2.71; N, 0.67, which corresponds to a loading of 0.24 mmol/g.

#### 4.3.6 Synthesis of 1-(10-hexyl-10*H*-phenothiazin-2-yl)ethyl-3-(triethoxysilyl)propylcarbamate (**6**) modified mesoporous MCM-41 material (**M6**).

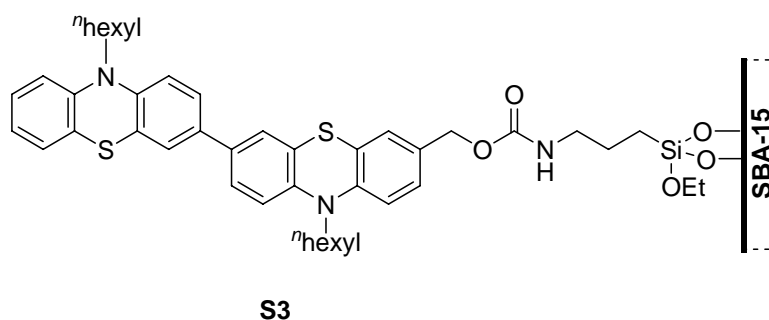


1.50 g of pure siliceous MCM-41 and 0.83 g (1.44 mmol) of **6** were applied to achieve **M6** by the post grafting method. The product **M6** is a colorless powder. Elemental analysis for **M6**: found C, 13.10; H, 2.66; N, 0.85, which corresponds to a loading of 0.30 mmol/g.

#### 4.3.7 Synthesis of pure silica SBA-15

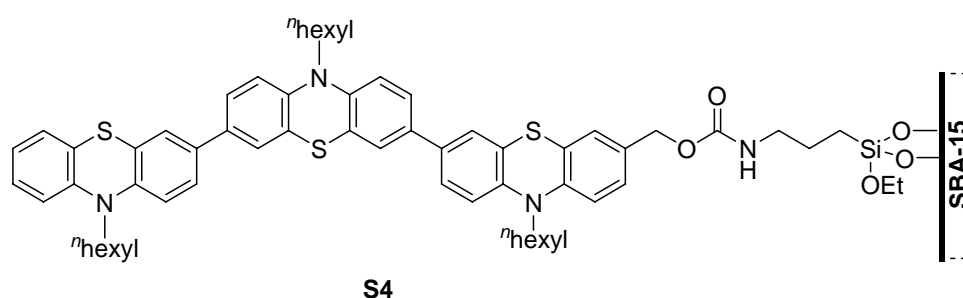
SBA-15 was synthesized according to the procedure reported by Zhao et al.<sup>7, 32</sup>. In a typical preparation, 4 g of Pluronic 123 were dissolved under stirring in 125 g of 1.9 M HCl at room temperature. The solution was heated to 40 °C before adding tetraethylorthosilicate. The resultant mixture was stirred for 20 h at 40 °C, followed by aging at 100 °C for 24 h under static conditions. The solid product was recovered by filtration and dried at 80 °C overnight. The template was removed from the as-synthesized material by extraction with ethanol under reflux condition.

#### 4.3.8 Synthesis of (10,10'-dihexyl-10*H*,10'*H*-3,3'-biphenothiazin-7-yl)methyl-3-(triethoxysilyl)propylcarbamate (**3**) modified mesoporous SBA-15 material (**S3**).



A similar grafting process was also performed for the modification of SBA-15 materials. 0.40 g of pure siliceous SBA-15 mixed with 0.17 g (0.2 mmol) of **3** in toluene under reflux was applied. The **S3** was obtained as a yellow powder. Elemental analysis for **S3**: found C, 16.39; H, 3.32; N, 1.33, which corresponds to a loading of 0.32 mmol/g.

4.3.9 Synthesis of (10,10'-dihexyl-7'-(10-hexyl-10*H*-phenothiazin-3-yl)-10*H*,10'*H*-3,3'-biphenothiazin-7-yl)methyl-3-(triethoxysilyl)propylcarbamate (**4**) modified mesoporous SBA-15 material (**S4**).

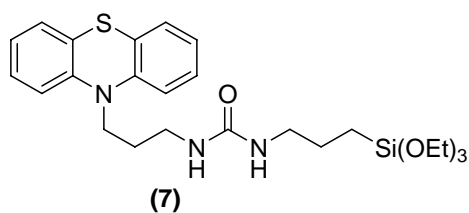


0.30 g of pure siliceous SBA-15 combining 0.152 g (0.135 mmol) of **4** went through a post grafting procedure to get the **S4** as a yellow powder. Elemental analysis for **S4**: found C, 13.47; H, 3.15; N, 0.95, which corresponds to a loading of 0.17 mmol/g.

4.3.10 Generation of the radical cations containing materials

(1) By  $\text{NOBF}_4$ : 0.10-0.30 g of the hybrid materials were previously degassed at 50 °C for 3h and suspended in 5 ml of dry dichloromethane. The solution was stirred at room temperature and a molar excess of  $(\text{NO})\text{BF}_4$  was added. The color of the samples immediately changed. The solids were filtered off, extracted with dichloromethane and dried under vacuum. (2) By  $\text{SbCl}_5$ : The process is same as mentioned above. A molar excess of  $\text{SbCl}_5$  was added as oxidizing agent. The color of the samples immediately changed. The solid was collected by filtration, then extracted with dichloromethane and dried under vacuum.

4.3.11 Synthesis of (10*H*-phenothiazine-10-yl)propyl-3-(triethoxysilyl)propylurea (**7**)



0.70 g (2.39 mmol) of 10-propanamine-10*H*-phenothiazine hydrochloride were mixed with 0.48 g (4.8 mmol) of triethylamine in 30 ml of degassed dry CH<sub>2</sub>Cl<sub>2</sub> and stirred for 30 min under nitrogen atmosphere. Then 0.66 g (2.7 mmol) of 3-(triethoxysilyl)propylisocyanate were added dropwise at room temperature. The reaction was monitored by TLC (silica gel plates). The solvent was removed in vacuum. The residue was purified by chromatography on silica gel (hexane/ethyl acetate 1:5) to give 1.05 g (87 %) of a colorless waxy solid. Anal. calc. for C<sub>25</sub>H<sub>37</sub>N<sub>3</sub>O<sub>4</sub>SSi (503.73): C 59.61, H 7.40, N 8.34; found: C 59.10, H 7.51, N 8.20. <sup>1</sup>H NMR (CDCl<sub>3</sub>, 600 MHz): δ = 0.58 (t, *J* = 8.4 Hz, 2 H), 1.24 (t, *J* = 7 Hz, 9.0 H), 1.52 (m, 2 H), 2.00 (m, 2H), 3.02 (q, *J* = 6 Hz, 2H), 3.30 (q, *J* = 6 Hz, 2H), 3.82 (q, *J* = 7.2 Hz, 6H), 3.99 (t, *J* = 6 Hz, 2H), 4.46 (br, 1H), 4.90 (br, 1H), 6.93-6.99 (m, 4H), 7.19 (m, 4H). <sup>13</sup>C NMR (CDCl<sub>3</sub>, 150.92 MHz): δ = 7.6 (CH<sub>2</sub>), 18.3 (CH<sub>3</sub>), 23.6 (CH<sub>2</sub>), 26.7 (CH<sub>2</sub>), 39.0 (CH<sub>2</sub>), 42.8 (CH<sub>2</sub>), 45.4 (CH<sub>2</sub>), 58.4 (CH<sub>2</sub>), 116.0 (CH), 122.9 (C), 125.4 (CH), 127.6 (CH), 127.8 (CH), 145.3 (C), 158.2 (C=O).

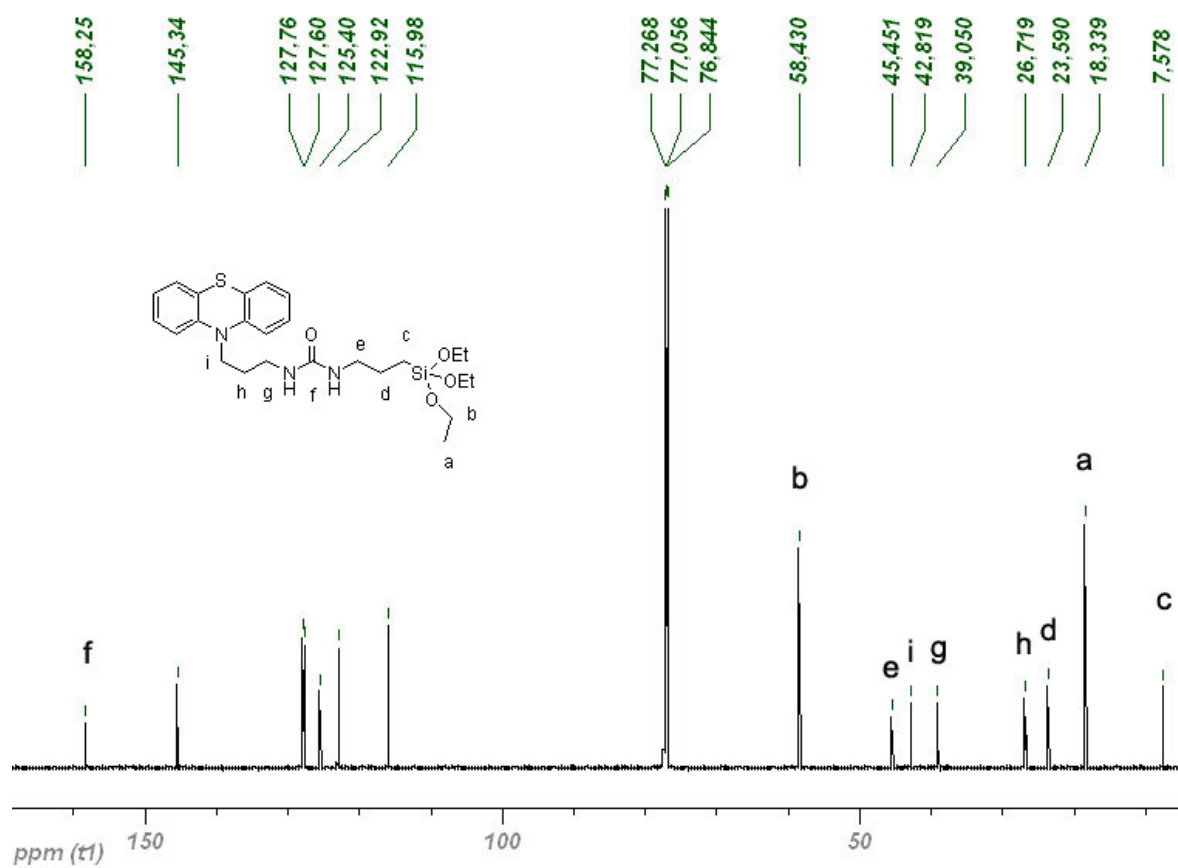


Figure 124.  $^{13}\text{C-NMR}$  spectrum of 7.

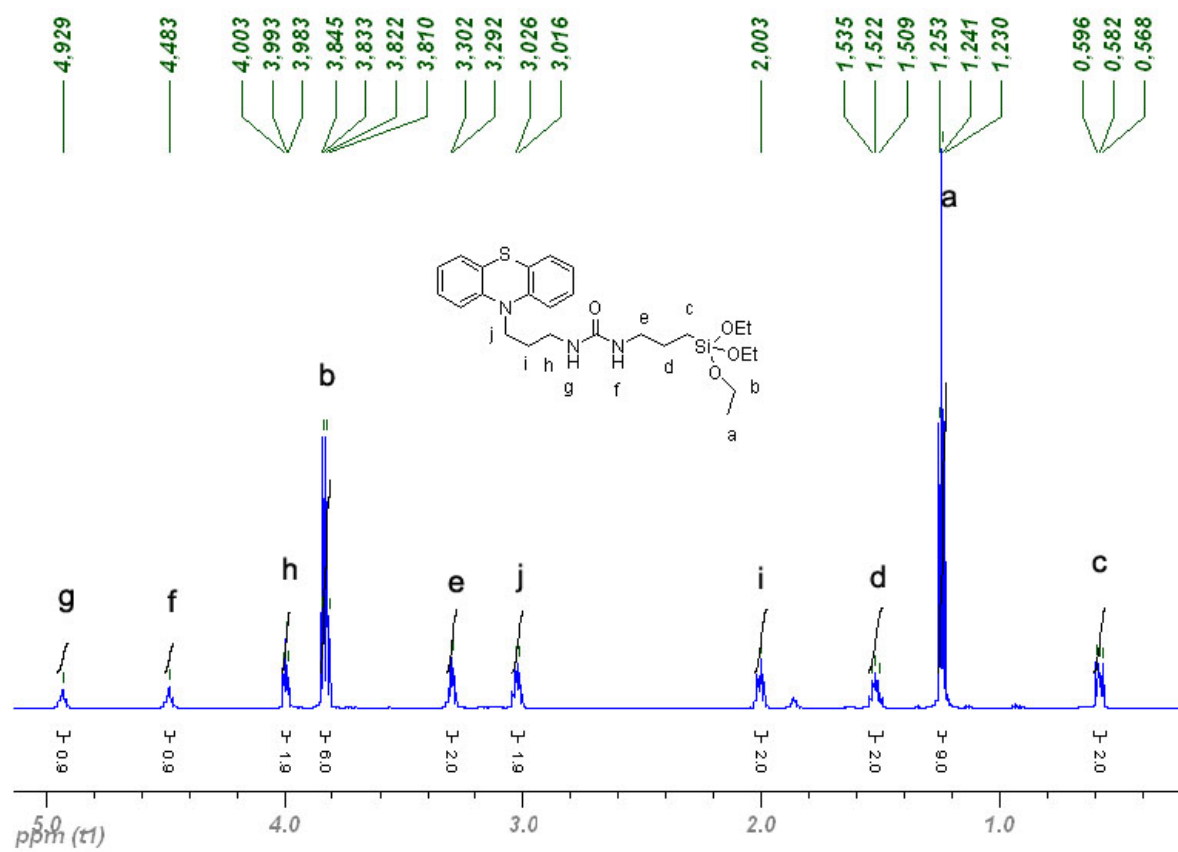
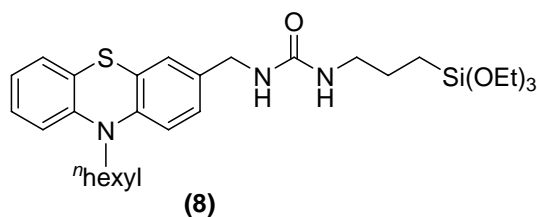


Figure 125.  $^1\text{H-NMR}$  spectrum of 7.

4.3.12 Synthesis of (10-hexyl-10*H*-phenothiazine-3-yl)methyl-3-(triethoxysilyl)propylurea (**8**)

1.00 g (2.9 mmol) of 3-methanamine-10-hexyl-10*H*-phenothiazine hydrochloride were mixed with 0.59 g (5.8 mmol) dry of triethylamine in 30 ml of degassed dry CH<sub>2</sub>Cl<sub>2</sub> and were stirred for 30 min under nitrogen atmosphere. Then 0.83 g (3.2 mmol) of 3-(triethoxysilyl)propylisocyanate was added dropwise at room temperature. The reaction was monitored by TLC (silica gel plate). The solvent was removed in vacuo. The residue was purified by chromatography on silica gel (hexane/ethyl acetate 2:5) to give 1.17 g (72 %) as a colorless solid. Anal. calc. for C<sub>29</sub>H<sub>45</sub>N<sub>3</sub>O<sub>4</sub>SSi (559.84): C 62.22, H 8.10, N 7.51; found: C 61.60, H 7.98, N 7.20. <sup>1</sup>H NMR (CDCl<sub>3</sub>, 400 MHz): δ = 0.60 (t, *J* = 8.2 Hz, 2 H), 0.86 (t, *J* = 6.8 Hz, 3H), 1.21 (t, *J* = 7 Hz, 9.0 H), 1.27-1.31 (m, 4H), 1.41 (m, 2H), 1.60 (m, 2H), 1.77(m, 2H), 3.14 (m, 2H), 3.70-3.87 (m, 8H), 4.15 (m, 2H), 4.80 (br, 1H), 4.92 (br, 1H), 6.7-6.9(m, 3H), 7.0-7.2 (m, 4H). <sup>13</sup>C NMR (CDCl<sub>3</sub>, 150.92 MHz): δ = 7.9 (CH<sub>2</sub>), 14.3 (CH<sub>3</sub>), 18.7 (CH<sub>3</sub>), 22.9 (CH<sub>2</sub>), 24.0 (CH<sub>2</sub>), 27.0 (CH<sub>2</sub>), 31.8 (CH<sub>2</sub>), 43.3 (CH<sub>2</sub>), 44.1 (CH<sub>2</sub>), 47.8 (CH<sub>2</sub>), 58.8 (CH<sub>2</sub>), 115.7 (CH), 115.9(CH), 122.6 (CH), 125.0 (C), 126.9 (C), 127.6 (CH), 127.8 (CH), 133.9 (CH), 144.8 (C), 145.6 (C), 158.6 (C=O).

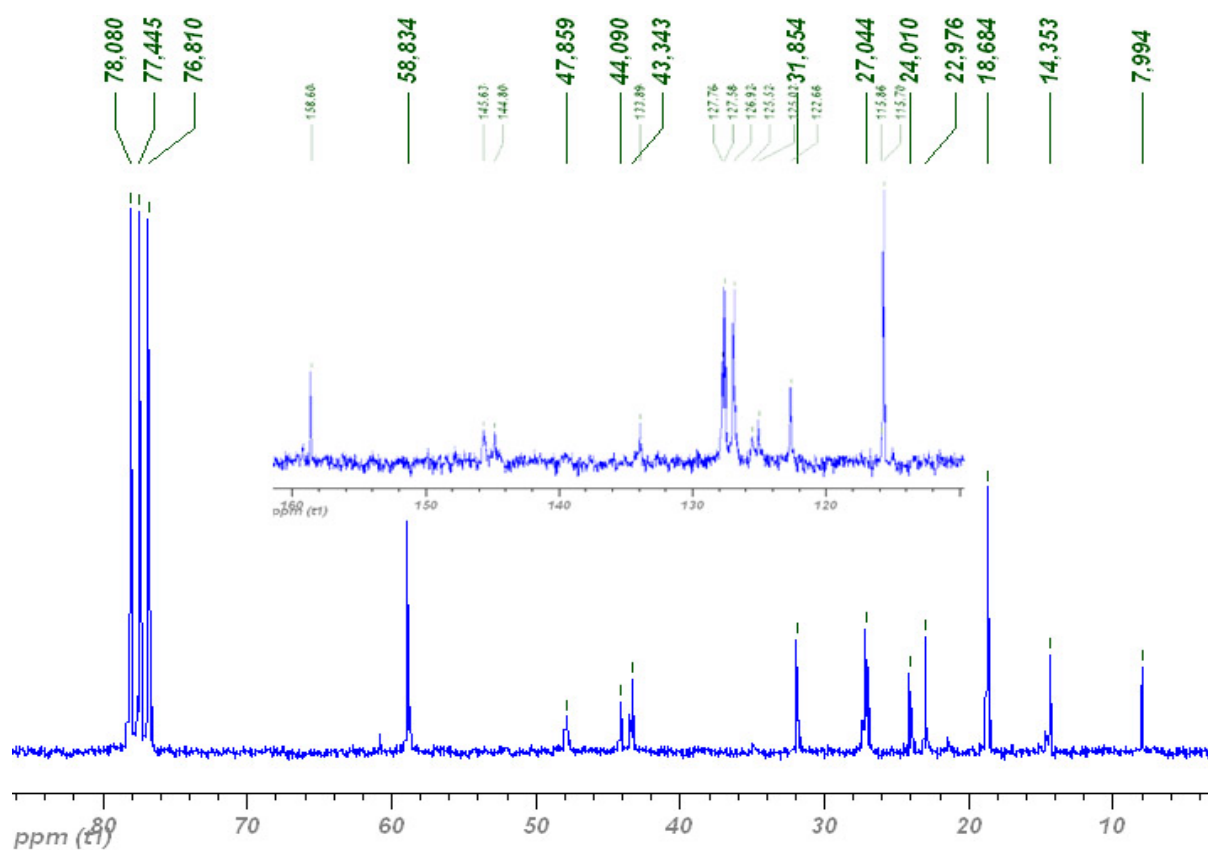


Figure 126.  $^{13}\text{C}$ -NMR spectrum of **8**.

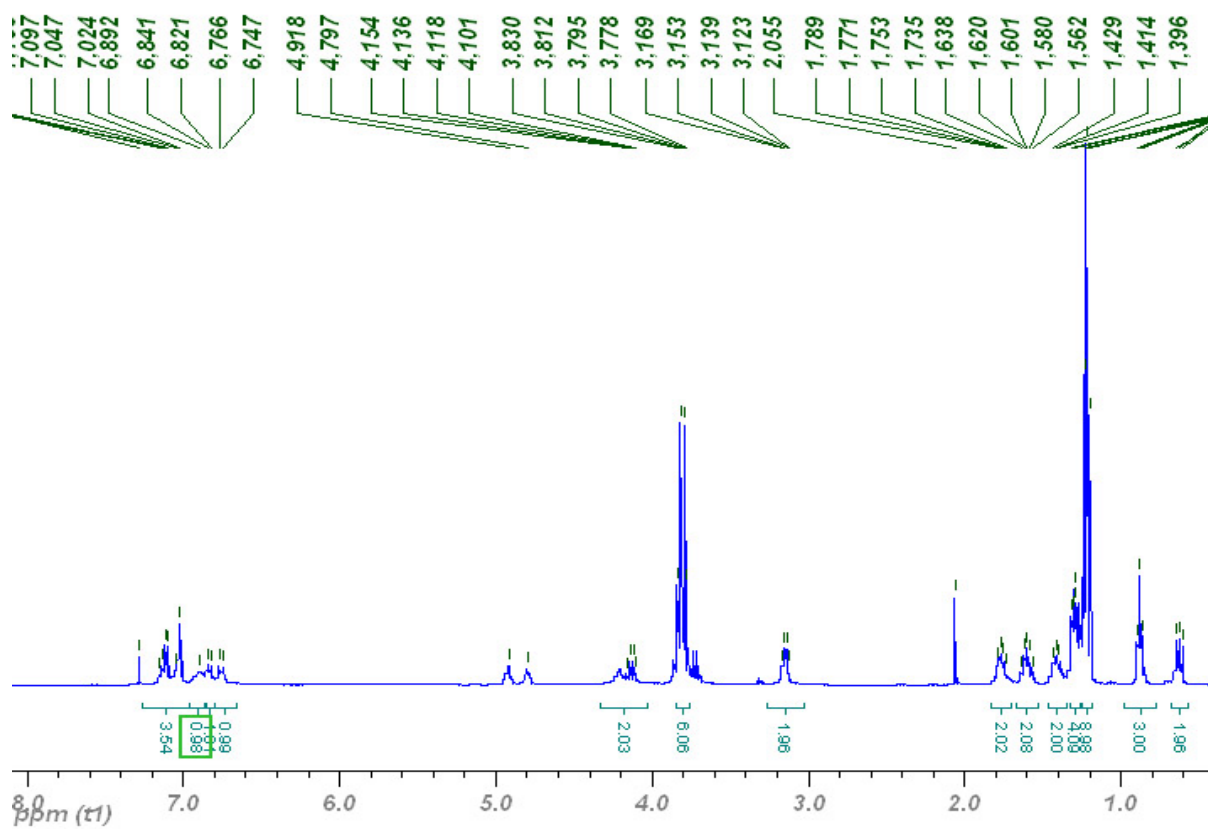
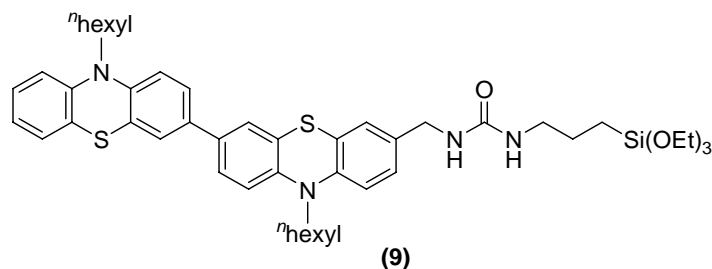


Figure 127.  $^1\text{H}$ -NMR spectrum of **8**.



4.3.13 Synthesis of (10,10'-dihexyl-10*H*,10*H*'-3,3'-biphenothiazine-7-yl)methyl-3-(triethoxysilyl)propylurea (**9**)

0.81 g (1.27 mmol) of 7-methanamine-10,10'-dihexyl-10*H*,10*H*'-3,3'-biphenothiazine hydrochloride mixed with 0.26 g (2.54 mmol) of triethylamine (mmol) in 30 ml of degassed dry CH<sub>2</sub>Cl<sub>2</sub> were stirred for 30 min under a nitrogen atmosphere. Then 0.35 g (1.40 mmol) of 3-(triethoxysilyl)propylisocyanate were added dropwise at room temperature. The reaction was monitored by TLC (silica gel plates). The solvent was removed in vacuo. The residue was purified by chromatography on silica gel (hexane/ethyl acetate 1:3) to give 0.64 g (65 %) as a yellow oily product. Anal. calc. for C<sub>47</sub>H<sub>64</sub>N<sub>4</sub>O<sub>4</sub>S<sub>2</sub>Si (841.25): C 67.10, H 7.67, N 6.66; found: C 66.60, H 7.98, N 6.40. <sup>1</sup>H NMR (CDCl<sub>3</sub>, 400 MHz): δ = 0.62 (t, *J* = 8.0 Hz, 2 H), 0.86 (t, *J* = 7.0 Hz, 6H), 1.21 (t, *J* = 7 Hz, 9H), 1.27-1.31 (m, 8H), 1.40 (m, 4H), 1.61 (m, 2H), 1.75 (m, 4H), 3.14 (m, 2H), 3.71-3.90 (m, 10H), 4.14 (m, 2H), 5.41 (br, 1H), 5.25 (br, 1H), 6.65 (d, *J* = 6, 1H), 6.71 (d, *J* = 6, 1H), 6.81 (m, 4H), 7.01 (m, 2H), 7.12 (m, 1H), 7.19-7.27 (m, 4H). <sup>13</sup>C NMR (CDCl<sub>3</sub>, 150.92 MHz): δ = 7.6 (CH<sub>2</sub>), 14.0 (CH<sub>3</sub>), 18.3 (CH<sub>3</sub>), 22.6 (CH<sub>2</sub>), 23.6 (CH<sub>2</sub>), 26.6 (CH<sub>2</sub>), 26.7 (CH<sub>2</sub>), 31.5 (CH<sub>2</sub>), 42.9 (CH<sub>2</sub>), 43.5 (CH<sub>2</sub>), 47.5 (CH<sub>2</sub>), 58.4 (CH<sub>2</sub>), 114.3 (CH), 115.2 (CH), 115.3 (CH), 115.6 (CH), 116.4 (CH), 122.3 (CH), 124.4 (C), 125.0 (CH), 125.1 (CH), 126.5 (CH), 126.6 (CH), 127.2 (CH), 127.4 (CH), 129.5 (CH), 129.9 (C), 133.7 (C), 133.8 (C), 134.5 (C), 143.7 (C), 144.2 (C), 158.7 (C=O).

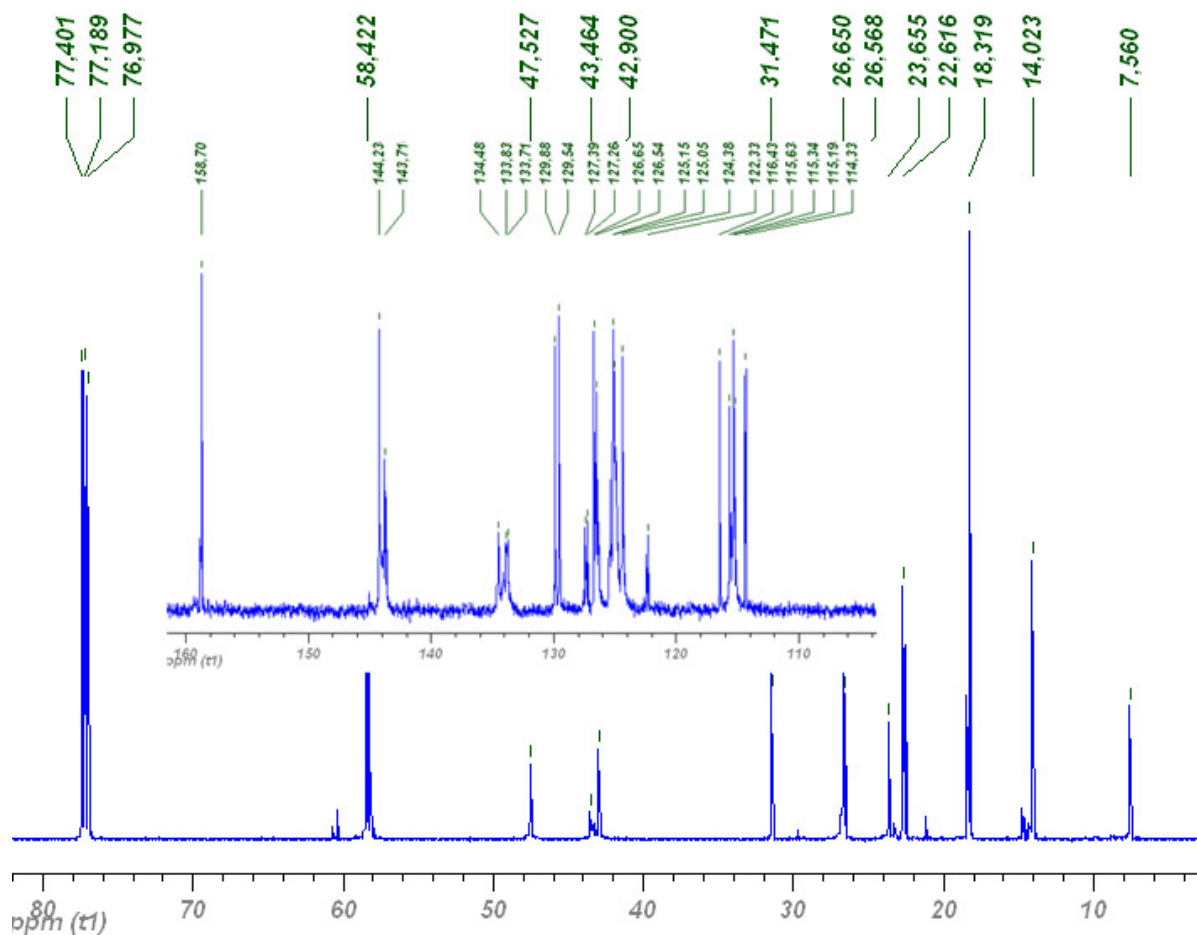
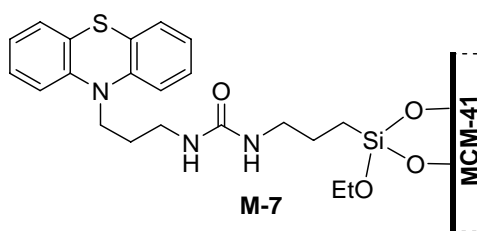


Figure 128. <sup>13</sup>C-NMR spectrum of **9**.

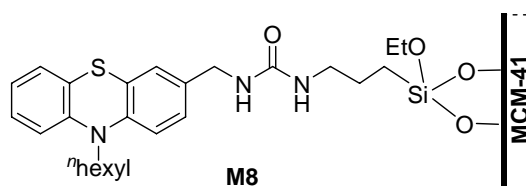
#### 4.3.14 Synthesis of (10-*H*-phenothiazine-10-yl)propyl-3-(triethoxysilyl)propylurea (**7**) functionalized mesoporous materials (**M7**).



In a typical synthetic procedure an aqueous solution of CTAB was mixed with ethylamine under stirring. Then a solution of precursor **7** in methanol and a proper amount of TEOS were added dropwise. The composition of mixture in molar ratio was 1.0 : x : 0.14 : 2.4 : 2.0 : 100 SiO<sub>2</sub>/7/CTAB/EtNH<sub>2</sub>/methanol/H<sub>2</sub>O (x = 0.025 for **M7-1**, 0.049 for **M7-2**, and 0.075 for **M7-**

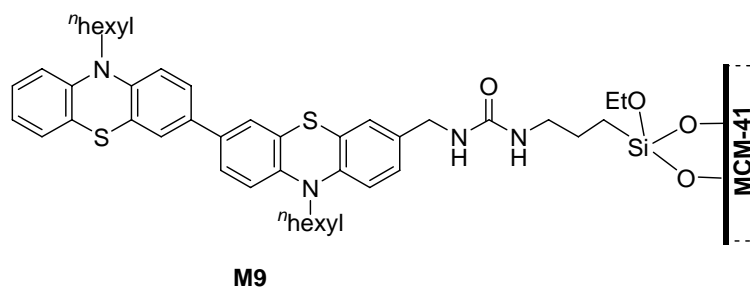
3). The reaction mixture was stirred for further 24 h to achieve a homogenous mixture of the organosilane with TEOS at room temperature before being heated to 100 °C for 24 h. The product was recovered by filtration, washed thoroughly with distilled water until neutral. The white powderous material was obtained by vacuum drying at 50 °C. The surfactant (CTAB) was extracted by twofold stirring 1.0 g of the as-synthesized hybrid material in 80 ml of ethanol and 1.0 ml of an aqueous solution of HCl (36 %) under reflux for 8h. The resulting solid was then filtered, washed with ethanol and CH<sub>2</sub>Cl<sub>2</sub> and vacuum dried at 50 °C. Elemental analysis for **M7-1**: C, 11.68; H, 2.05; N, 1.37; which corresponds to a loading of 0.33 mmol/g. **M7-2**: C, 16.53; H, 2.83; N, 2.26; which corresponds to a loading of 0.54 mmol/g. **M7-3**: C, 20.33; H, 2.81; N, 3.25; which corresponds to a loading of 0.77 mmol/g.

4.3.15 Synthesis of (10-hexyl-10*H*-phenothiazine-3-yl)methyl-3-(triethoxysilyl)propylurea (**8**) functionalized mesoporous materials (**M8**).



The synthesis of **M8** is similar to the procedure of **M7**. The composition of the mixture in molar ratio was 1.0 : x : 0.14 : 2.4 : 2.0 :100 SiO<sub>2</sub>/**8**/CTAB/EtNH<sub>2</sub>/methanol/H<sub>2</sub>O (x = 0.022 for **M8-1**, 0.037 for **M8-2**, and 0.052 for **M8-3**) The final products were colorless powders. Elemental analysis for **M8-1**: C, 10.16; H, 2.60; N, 1.10; which corresponds to a loading of 0.26 mmol/g. **M8-2**: C, 17.79; H, 3.23; N, 1.68; which corresponds to a loading of 0.40 mmol/g. **M8-3**: C, 19.81; H, 3.59; N, 2.25; which corresponds to a loading of 0.54 mmol/g.

4.3.16 Synthesis of (10,10'-dihexyl-10*H*,10*H*'-3,3'-biphenothiazine-7-yl)methyl-3-(triethoxysilyl)propylurea (**9**) functionalized mesoporous materials (**M9**).

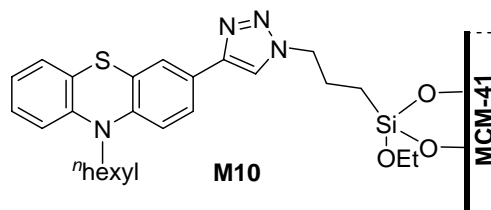


The synthesis of **M9** is similar to **M7**. The composition of the mixture in molar ratio was 1.0 : x : 0.14 : 2.4 : 2.0 : 100 SiO<sub>2</sub>/9/CTAB/EtNH<sub>2</sub>/methanol/H<sub>2</sub>O (x = 0.026 for **M9-1**, and 0.036 for **M9-2**). The final products were yellow powders. Elemental analysis for **M9-1**: C, 15.24; H, 2.40; N, 1.54; which corresponds to 0.28 mmol/g. **M9-2**: C, 19.79; H, 2.97; N, 1.93; which corresponds to 0.34 mmol/g.

#### 4.3.17 Silylation of **M9-1** (**M9-1-Si**)

The silylation reaction was carried out by adding hexamethyldisilazane (5 mmol) diluted in 5 ml of *n*-hexane to 0.50 g of dehydrated **M9-1** material suspended in 20 ml of dry toluene. After stirring the reaction mixture for 24 h at room temperature, the sample was collected by filtration and sufficiently washed with *n*-hexane. The silylated material was dried under vacuum for 4 h at 30 °C.

#### 4.3.18 Synthesis of 10-methyl-3-(1-(3-(triethoxysilyl)propyl)-1*H*-1,2,3-triazol-4-yl)-10*H*-phenothiazin (**10**) functionalized mesoporous materials (**M10**).



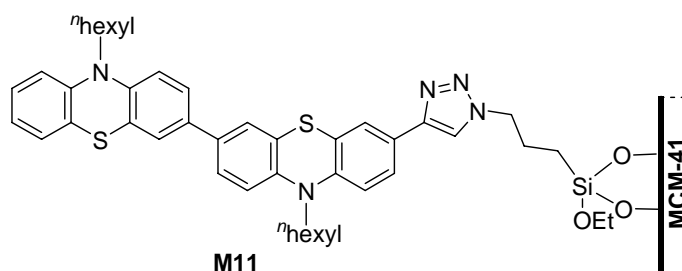
**M10** was synthesized by a one-pot synthetic method, which is similar to **M7**. The composition of the mixture in molar ratio was 1.0 : x : 0.14 : 2.4 : 2.0 : 100 SiO<sub>2</sub>/10/CTAB/EtNH<sub>2</sub>/methanol/H<sub>2</sub>O (x = 0.085 for **M10**). The final product was a yellow

powder. Elemental analysis for **M10**: C, 20.63; H, 3.34; N, 3.94; which corresponds to a loading of 0.70 mmol/g.

#### 4.3.19 Protonation of **M10** (**M10-H**) and the corresponding radical cation containing sample (**M10-BF<sub>4</sub>-H**).

The protonation experiment was performed in a Schlenk tube charged with 50 mg of **M10** or **M10-BF<sub>4</sub>**. The sample was previously dried under vacuum at 50 °C for 3h and a drop of trifluoroacetic acid (TFA) was added to the flask with gentle stirring for 30 min and subsequent vacuum drying.

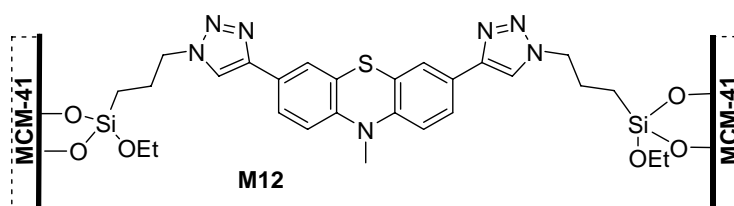
#### 4.3.20 Synthesis of 10,10'-dihexyl-7-(1-(3-(triethoxysilyl)propyl)-1*H*-1,2,3-triazole-4-yl)-10*H*,10'*H*-3,3'-biphenothiazin (**11**) functionalized mesoporous material (**M11**).



**M11** was obtained by an adjusted method, for which THF as a co-solvent was chosen for a homogenous mixture of TEOS and the precursor **11**. An aqueous solution of CTAB mixed with ethylamine was stirred. Then a solution of precursor **11** in methanol/THF and a proper amount of TEOS was added dropwise. The composition of the mixture in molar ratio was 1.0 : x : 0.14 : 2.4 : 2.0 : 2.0 : 100 SiO<sub>2</sub>/**11**/CTAB/EtNH<sub>2</sub>/methanol/ THF/H<sub>2</sub>O/ (x = 0.03 for **M11-1**, and 0.055 for **M11-2**) The reaction mixture was stirred for further 24 h at room temperature before being heated to 100 °C for 24 h. The product was filtered off, washed thoroughly with distilled water until neutral and with a small amount of ethanol. The white powderous material was obtained by vacuum drying at 50 °C. The surfactant (CTAB) was extracted by twofold stirring of 1.0 g of the as-synthesized hybrid material in 80 mL of

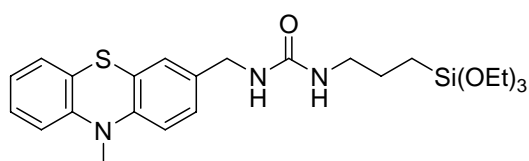
ethanol and 1.0 ml of an aqueous solution of HCl (36 %) under reflux for 8h. The resulting solid was then filtered, washed with ethanol and CH<sub>2</sub>Cl<sub>2</sub> and vacuum dried at 50 °C. Elemental analysis for **M11-1**: C, 19.92; H, 2.92; N, 1.93 which corresponds to 0.28 mmol/g. **M11-2**: C, 27.79; H, 2.97; N, 3.04; which corresponds to 0.43 mmol/g.

4.3.21 Synthesis of 10-methyl-3,7-bis(1-(3-(triethoxysilyl)propyl)-1H-1,2,3-triazole-4-yl)-10H-phenothiazin (**M12**) functionalized mesoporous materials (**M12**).



**M12** was prepared by a similar procedure like **M11**. The composition of the mixture in molar ratio was 1.0 : x : 0.14 : 2.4 : 2.0 : 2.0 : 100 SiO<sub>2</sub>/**M12**/CTAB/EtNH<sub>2</sub>/methanol/THF/H<sub>2</sub>O (x =0.04 for **M12**). A yellow product was obtained. Elemental analysis for **M12**: C, 12.67; H, 2.82; N, 2.78; which corresponds to a loading of 0.28 mmol/g.

4.3.22 Synthesis of (10-methyl-10H-phenothiazine-3-yl)methyl-3-(triethoxysilyl)propylurea (**13**)



1.12 g (4.02 mmol) of 10-methyl-10H-phenothiazine-3-yl-methylamine hydrochloride mixed with 1.12 ml (8.0 mmol) triethylamine (8.0 mmol) of in degassed dry CH<sub>2</sub>Cl<sub>2</sub> (100 ml) were stirred for 30 min under nitrogen atmosphere. Then 1.0 g (4.0 mmol) of 3-(triethoxysilyl)propylisocyanate were added dropwise at room temperature. The reaction was monitored by TLC (silica gel plates). The solvent was removed in vacuo. The residue was

purified by chromatography on silica gel (hexane/ethyl acetate 2:5) to give 1.67 g (85 %) as a yellow powder. Anal. calc. for  $C_{24}H_{35}N_3O_4SSi$  (489.70): C 58.86, H 7.20, N 8.58; found: C 59.21, H 7.50, N 8.41.  $^1H$  NMR ( $CDCl_3$ , 400 MHz):  $\delta$  = 0.62 (t,  $J$  = 7.2 Hz, 2 H), 1.22 (t,  $J$  = 7 Hz, 9.0 H), 1.61 (m, 2H), 3.15 (t,  $J$  = 7.2 Hz, 2H), 3.34 (s, 3H), 3.80 (m, 9H), 4.23 (d,  $J$  = 4.2 Hz, 2H), 4.74 (br, NH), 4.87 (br, NH), 6.7-6.9(m, 3H), 7.0-7.2 (m, 4H).  $^{13}C$  NMR ( $CDCl_3$ , 150.92 MHz):  $\delta$  = 7.5 ( $CH_2$ ), 18.3 ( $CH_3$ ), 23.6 ( $CH_2$ ), 35.3 ( $CH_3$ ), 42.9 ( $CH_2$ ), 43.7 ( $CH_2$ ), 58.4 ( $CH_2$ ), 114.0 (CH), 122.4(CH), 123.1 (CH), 123.6 (C), 126.2 (C), 126.7 (CH), 127.5 (CH), 133.6 (CH), 144.9 (C), 145.7 (C), 158.2 (C=O).

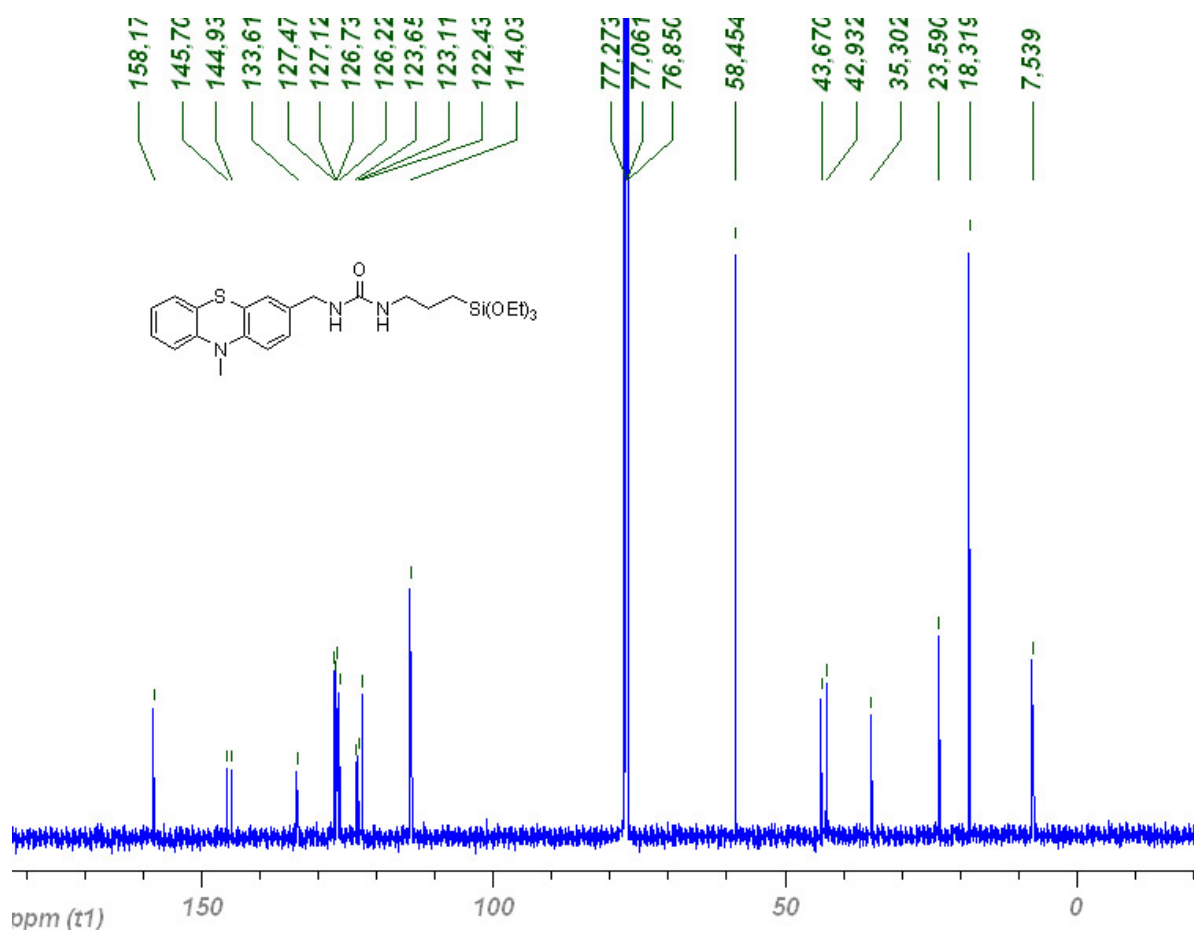


Figure 129.  $^{13}C$  NMR spectrum of **13**.

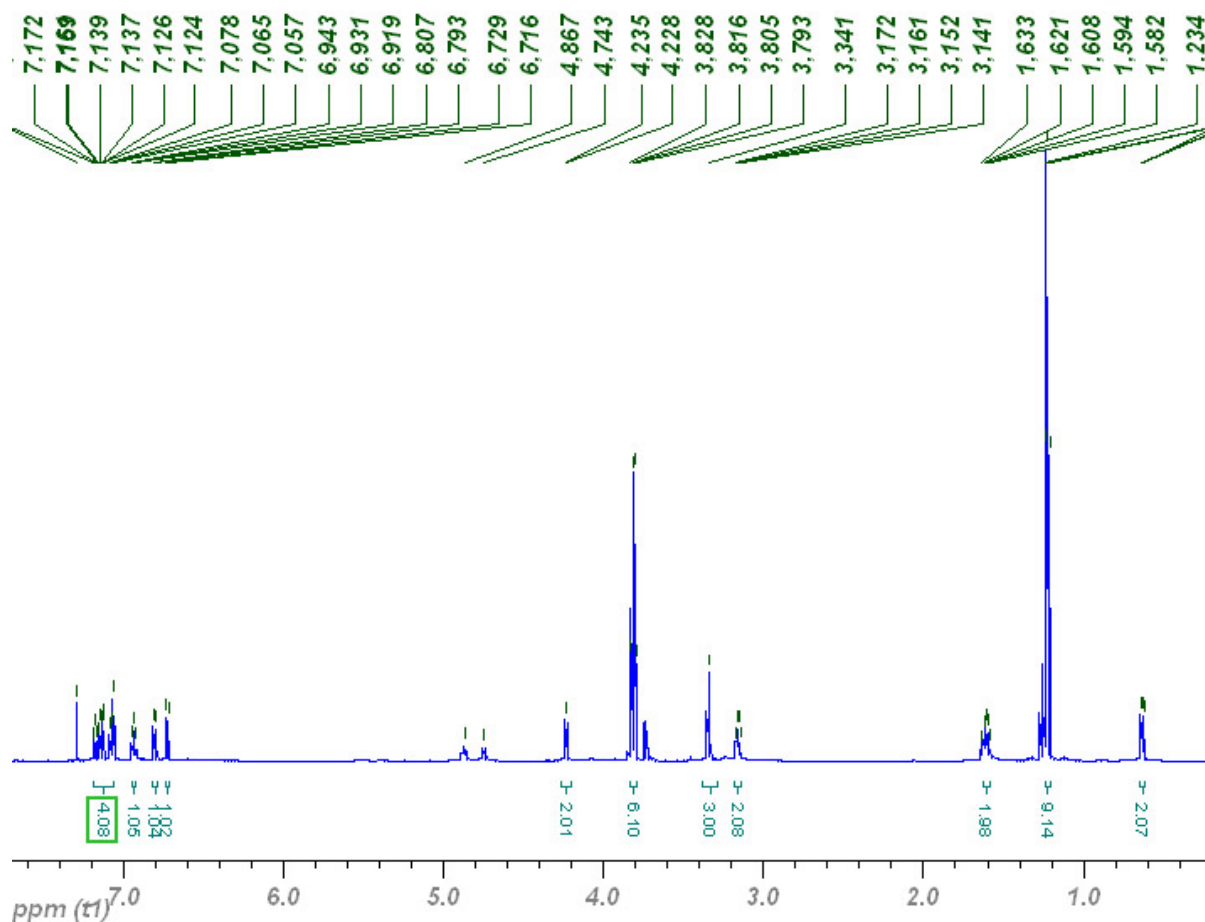
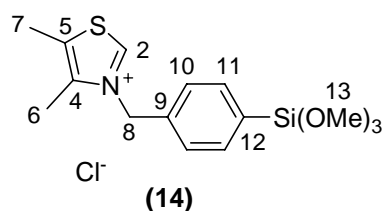


Figure 130.  $^1\text{H}$  NMR spectrum of **13**.

#### 4.3.23 Synthesis of 4,5-dimethyl-3-(4-trimethoxysilylphenylmethyl)thiazoliumchloride (**14**)



1.13 g (10 mmol) of 4,5-dimethylthiazole and 2.47 g (10 mmol) of (*p*-chloromethyl)phenyltrimethoxysilane were dissolved in 5 mL of dry acetonitrile and heated under an atmosphere of  $\text{N}_2$  to reflux for 24 h. All volatiles were removed in vacuum. Washing the solid residue with dry diethylether and filtering under  $\text{N}_2$  protection, resulted in **1** as a yellow powder (yield 81%). Elemental analysis: calcd. C 49.92, H 6.10, N 3.88; found: C 49.34, H 5.98, N 3.77. The numbering for the assignment of the NMR spectra is given in the



scheme above:  $^1\text{H}$  NMR (600 MHz,  $\text{CDCl}_3$ )  $\delta$  = 11.9 (s,  $\text{H}^2$ ), 7.63 (d,  $^3J_{\text{HH}} = 7.8$  Hz,  $\text{H}^{11}$ ), 7.36 (d,  $^3J_{\text{HH}} = 7.8$  Hz,  $\text{H}^{10}$ ), 6.19 (s,  $\text{H}^8$ ), 3.58 (s,  $\text{H}^{13}$ ), 2.47 (s,  $\text{H}^6$ ), 2.36 (s,  $\text{H}^7$ ).  $^{13}\text{C}$  NMR (600 MHz,  $\text{CDCl}_3$ )  $\delta$  = 158.1 ( $\text{C}^2$ ), 142.0 ( $\text{C}^4$ ), 135.7 ( $\text{C}^{12}$ ), 134.4 ( $\text{C}^9$ ), 133.0 ( $\text{C}^5$ ), 131.1 ( $\text{C}^{11}$ ), 127.5 ( $\text{C}^{10}$ ), 57.1 ( $\text{C}^{13}$ ), 50.9 ( $\text{C}^8$ ), 12.6 ( $\text{C}^6$ ), 12.1 ( $\text{C}^7$ ).

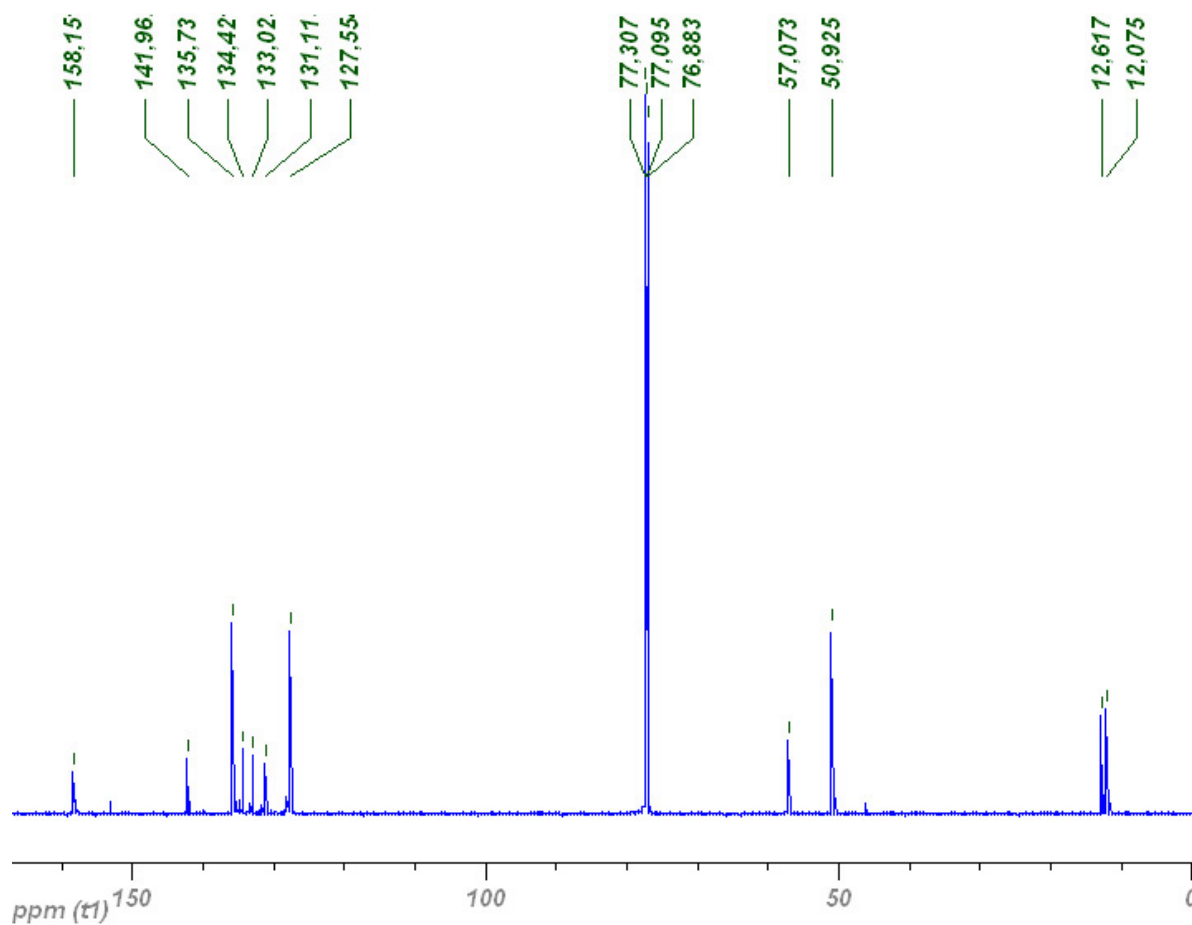


Figure 131.  $^{13}\text{C}$  NMR spectrum of **14**.

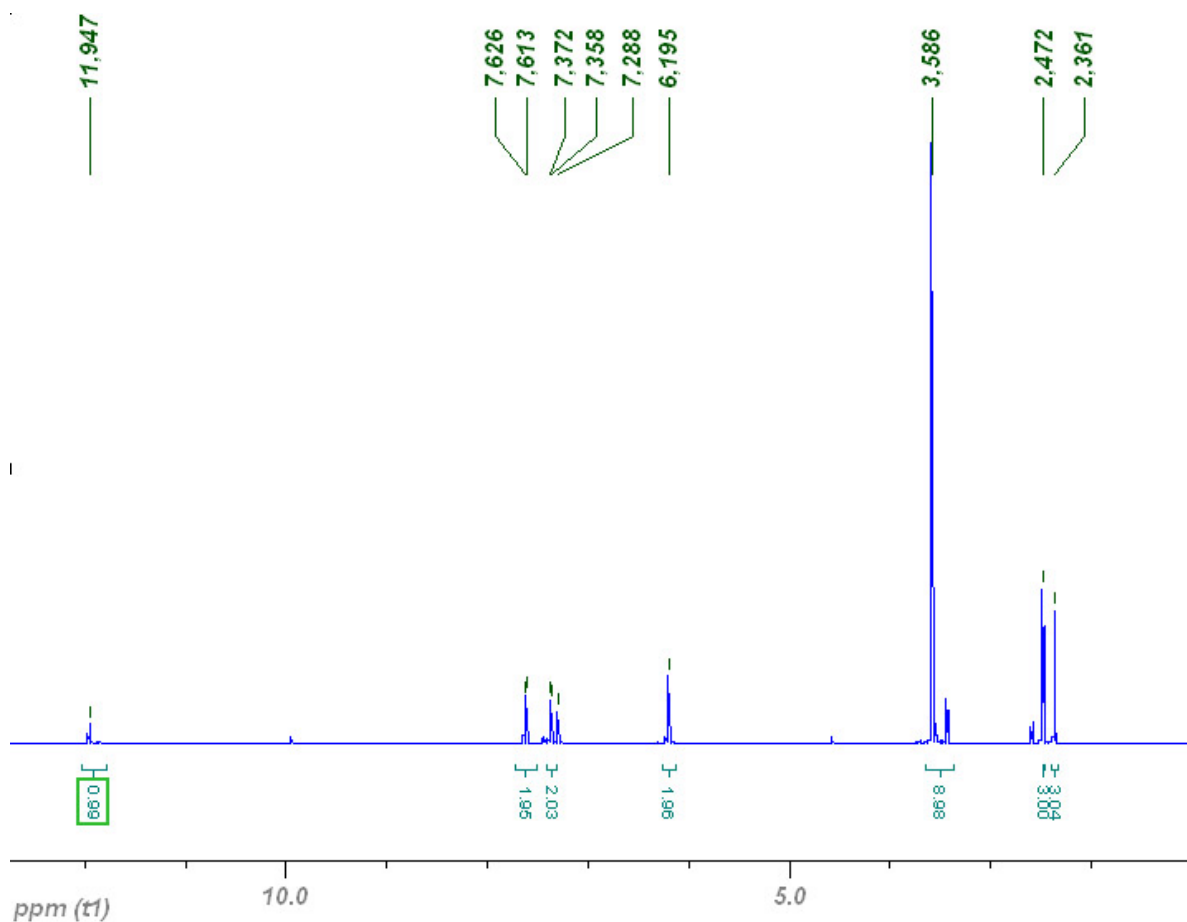
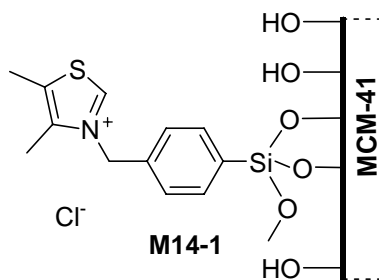


Figure 132.  $^{13}\text{C}$  NMR spectrum of **14**.

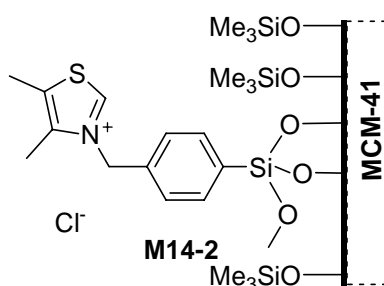
### 2.3.24 Preparation of the supported catalyst using pure silica MCM-41 as the substrate (**M14-1**)



Before functionalization, 3.00 g of pure siliceous MCM-41, which were previously degassed at 200 °C to remove the physisorbed water molecules, were suspended in 150 mL of dry toluene. 0.66 g (1.80 mmol) of **14** dissolved in 5 ml of dry acetonitrile were added and the mixture was heated to reflux for 24 h. The remaining solids were filtered off, washed with

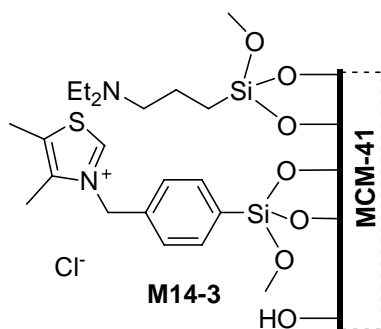
ethanol, subsequently extracted with ethanol in a Soxhlet extractor for further 12 h and then dried in vacuum at room temperature to obtain the hybrid catalyst. Elemental analysis: found C 9.35, H 1.86, N 0.48.

#### 4.3.25 Preparation of the silylated supported catalyst (**M14-2**)

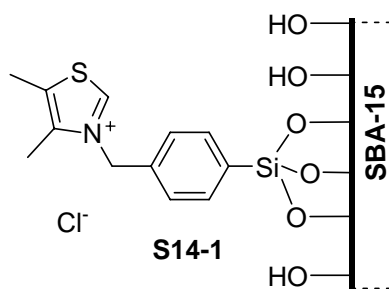


To enhance the hydrophobicity of the heterogenized solid catalyst, a further surface silylation strategy was selected. In a typical silylation experiment 1.00 g of **M14-1**, previously vacuum dehydrated at 80°C, was suspended in 30 ml of toluene and treated with 1.00 g (9.2 mmol) of Me<sub>3</sub>SiCl at room temperature under continuous stirring for 24 h. The solids were filtered off, washed with ethanol and dichloromethane and dried in vacuum. Elemental analysis: found C 12.41, H 2.37, N 0.34.

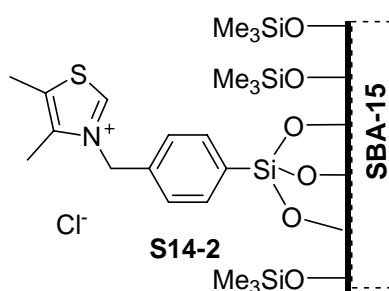
#### 4.3.26 Preparation of the amine base modified supported catalyst (**M14-3**)



1.00 g of **M14-1** was previously dried under vacuum at 80°C, then soaked in a solution of 30 ml of toluene with 1.2 g (5 mmol) of [3-(diethylamino)propyl] trimethoxysilane at 110°C for 24 h. The resulting solid was filtered off, washed with ethanol and dichloromethane and dried in vacuum. Elemental analysis: found C 18.17, H 3.42, N 2.31.

4.3.27 Preparation of the uniform catalyst by co-condensation method with SBA-15 (**S14-1**)

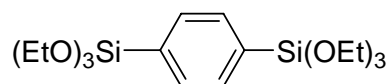
The heterogenous catalyst with a SBA-15 structure was synthesized by a one pot co-condensation method. In a typical preparation, 2 g of Pluronic 123 were dissolved under stirring in 63 g of 1.9 M HCl at room temperature. The solution was heated to 40 °C and kept stirring for 30 min. Then 0.25 g (0.70 mmol) of **14** mixed with 3.90 g (18.6 mmol) of TEOS were dropped into the solution. The resultant mixture was stirred for 20 h at 40 °C, followed by aging at 100 °C for 24 h under static conditions. The solid product was recovered by filtration and dried at 50 °C under vacuum. The template was removed from the as-synthesized material by extraction with ethanol under reflux conditions. Elemental analysis for **S14-1**: C, 15.67; H, 3.15; N, 0.62; which corresponds to a loading of 0.44 mmol/g.

4.3.28 Preparation of the silylated supported catalyst (**S14-2**)

To enhance the hydrophobicity of the heterogenized solid catalyst **S14-1**, a further surface silylation was carried out. In a typical silylation experiment 1.00 g of **S14-1**, previously vacuum dehydrated at 80°C, was suspended in 30 ml of dry toluene and treated with 1.00 g (9.2 mmol) of Me<sub>3</sub>SiCl at room temperature under continuous stirring for 24 h. The solids

were filtered off, washed with ethanol and dichloromethane and dried in vacuum. Elemental analysis: found C 18.46, H 3.99, N 0.48.

#### 4.3.29 Synthesis of 1,4-bis(triethoxysilyl)benzene.



In a three-necked flask, a mixture of TEOS (88.6 g, 426 mmol), dry THF (65 ml), magnesium turnings (3.1 g 0.129 mol), and a small crystal of iodine was slightly heated under an nitrogen atmosphere, and then a solution of 1,4-dibromobenzene (10.0g, 42.5 mmol) in THF (22 ml) was added dropwise over two hours. After the mixture had been refluxed overnight, THF was evaporated in vacuum and hexane (150 ml) was added. The precipitated magnesium salts were removed by filtration and the residual TEOS and hexane were evaporated. The remaining crude product was distilled under reduced pressure (3 mbar, 110 °C) giving the product as a colorless liquid (42%). Anal. calc. for C<sub>18</sub>H<sub>34</sub>O<sub>6</sub>Si<sub>2</sub> (402.65): C 53.70, H 8.51; found: C 53.96, H 8.37. <sup>1</sup>H NMR (CDCl<sub>3</sub>, 600 MHz): δ = 1.13 (t, *J* = 7.2 Hz, 9 H), 3.77 (q, *J* = 7 Hz, 6 H), 7.58 (4 H). <sup>13</sup>C NMR (CDCl<sub>3</sub>, 75 MHz): δ = 18.0 (CH<sub>3</sub>), 58.5 (CH<sub>2</sub>), 133.2 (CH), 133.8 (C).

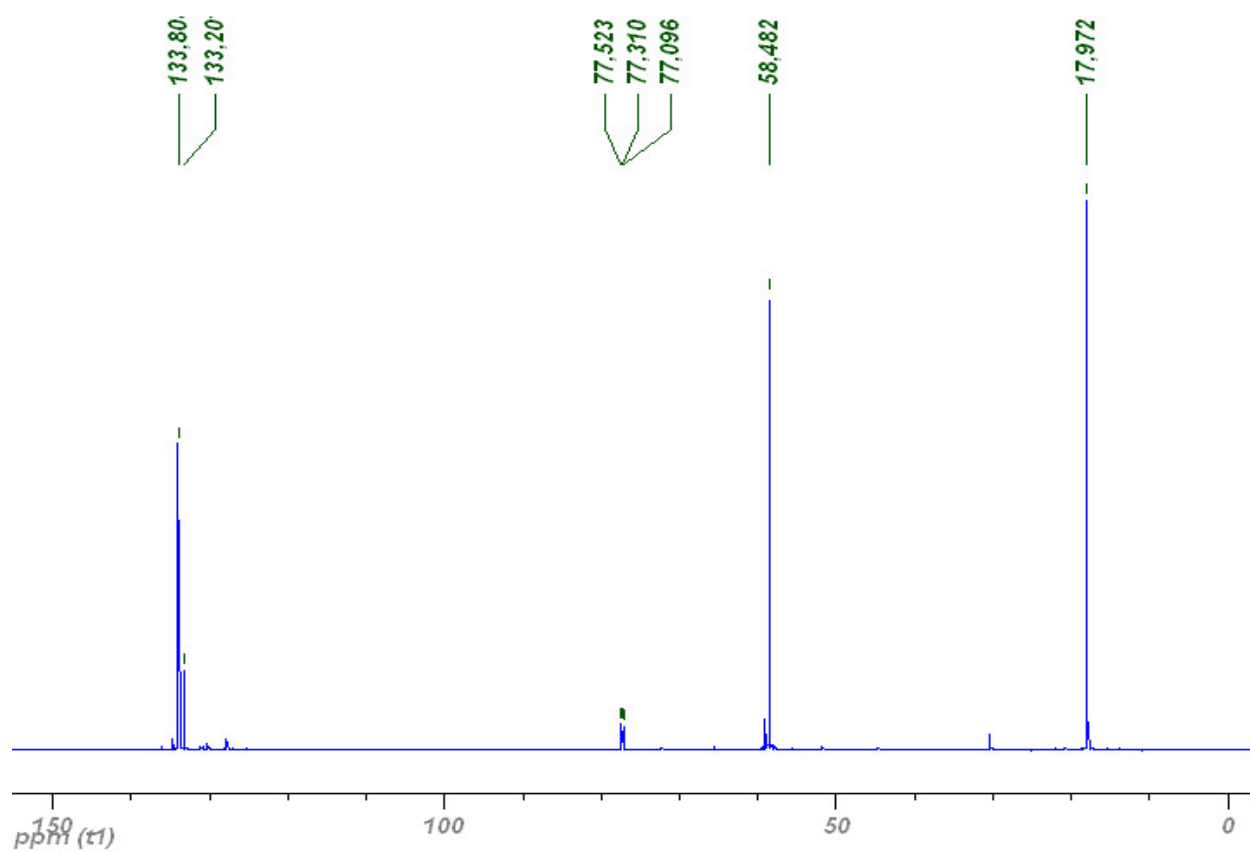


Figure 133.  $^{13}\text{C}$  NMR spectrum of 1,4-bis(triethoxysilyl)benzene.

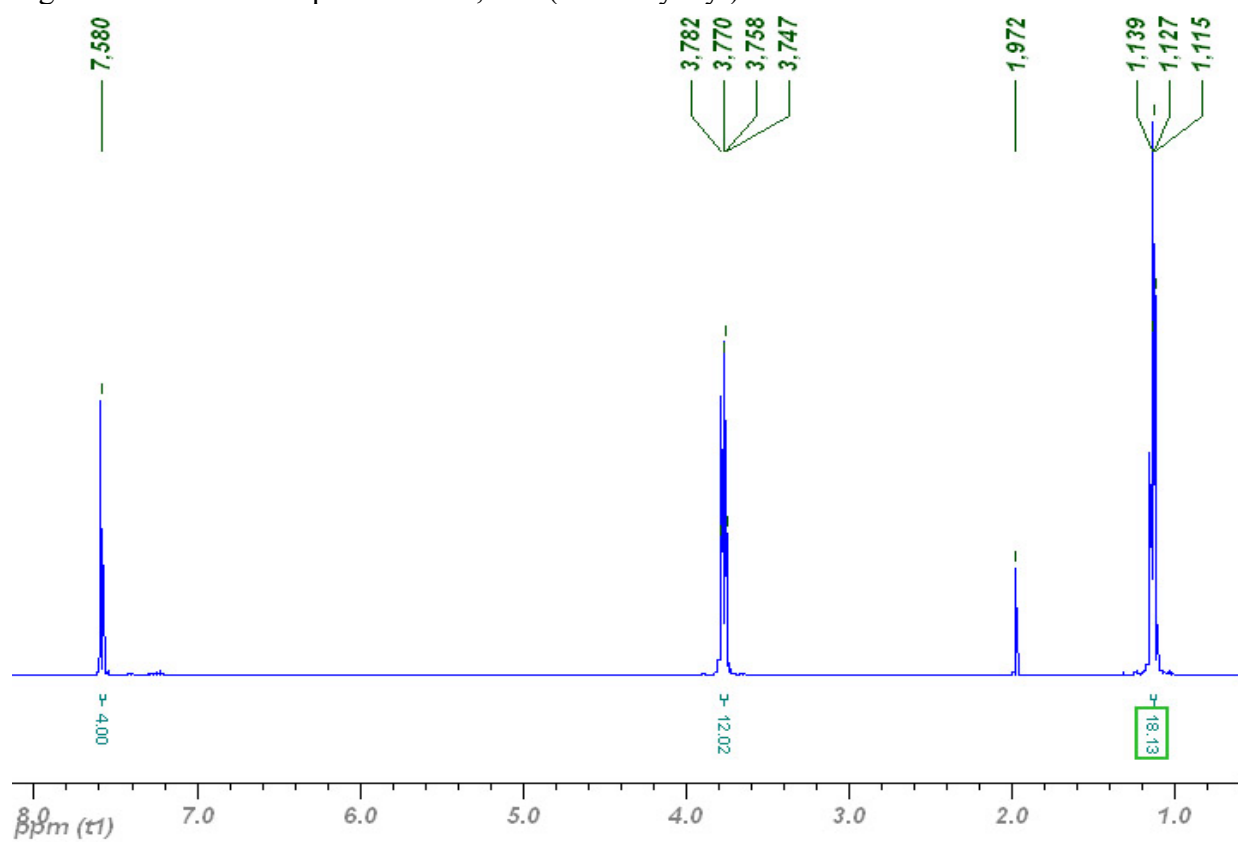
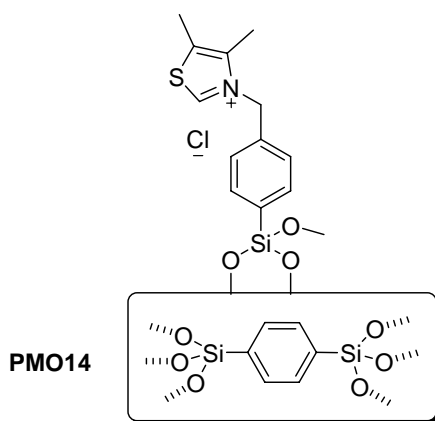


Figure 134.  $^1\text{H}$  NMR spectrum of 1,4-bis(triethoxysilyl)benzene.

4.3.30 Synthesis of periodical mesoporous organosilicas (**PMO**)

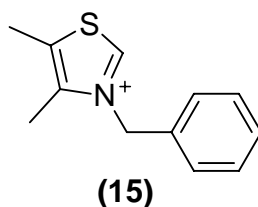
The synthesis of PMO was performed using a mixture with the following molar ratio: BTEB : surfactant : NaOH : H<sub>2</sub>O of 1 : 0.78 : 3.85 : 570. In a typical synthesis, 2.4 g (17 mmol) of octadecyltrimethylammonium bromide (OTAB) were dissolved in a mixture of 80.0 g (4.4 mol) of distilled water and 1.2 g (30 mmol) of sodium hydroxide at room temperature. 3.15 g (8 mmol) of 1,4-bis(triethoxysilyl)benzene (BTEB) were added to the above solution and the suspension was kept for 24 h stirring at room temperature. Then aging at 95 °C for 24 h was carried out. The resulting precipitate was recovered by filtration and dried at 80 °C. The surfactant was removed through solvent extraction: 1.0 g of the as-synthesised sample was stirred in a solution of 1.0 ml 37% HCl and 100 ml ethanol at reflux temperature for 8 hours. The final powder was filtered off, washed with ethanol and dried at 80 °C overnight. Elemental analysis: found C 36.87, H 3.23.

4.3.31 Preparation of the supported catalyst using PMOs as the substrate (**PMO14**)

0.7 g of pure PMOs, which were previously degassed at 150 °C, were suspended in 50 ml of dry toluene. 0.25 g (0.7 mmol) of 4,5-dimethyl-3-(4-trimethoxysilylphenylmethyl)-thiazoliumchloride dissolved in 5 ml of dry CH<sub>2</sub>Cl<sub>2</sub> were added and the mixture was heated to reflux for 24 h. The remaining solids were filtered off, washed with ethanol and methylene chloride then dried in vacuum at room temperature to obtain the hybrid catalyst. Elemental

analysis: found C 37.68, H 3.15, N 0.47, which corresponds to a catalyst loading of 0.34 mmol/g.

#### 4.3.32 Preparation of the homogenous catalyst 4,5-dimethyl-3-benzylthiazolium chloride (**15**)



For comparison, the pure homogenous catalyst 4,5-dimethyl-3-benzylthiazolium chloride was synthesized: 1.13 g (10 mmol) of 4,5-dimethylthiazole and 1.26 g (10 mmol) of benzylchloride were dissolved in 15 ml of dry acetonitrile and heated under an atmosphere of N<sub>2</sub> to reflux for 24 h. All volatiles were removed in vacuum. Washing the solid residue with diethylether resulted in **5** as a yellow powder (yield 85%). Elemental analysis: calcd. C 60.11, H 5.89, N 5.84; found: C 60.04, H 5.75, N 5.74. <sup>1</sup>H NMR (600 MHz, CDCl<sub>3</sub>) δ = 11.84 (s, H<sup>2</sup>), 7.35 – 7.28 (m, H<sup>10</sup>, H<sup>11</sup>, H<sup>12</sup>), 6.12 (s, H<sup>8</sup>), 3.61 (s, H<sup>13</sup>), 2.45 (s, H<sup>6</sup>), 2.37 (s, H<sup>7</sup>). <sup>13</sup>C NMR (600 MHz, CDCl<sub>3</sub>) δ = 158.1 (C<sup>2</sup>), 142.0 (C<sup>4</sup>), 133.0 (C<sup>5</sup>), 132.2 (C<sup>9</sup>), 129.3 (C<sup>10</sup>), 129.1 (C<sup>11</sup>), 128.2 (C<sup>12</sup>), 57.2 (C<sup>8</sup>), 12.5 (C<sup>6</sup>), 12.0 (C<sup>7</sup>).



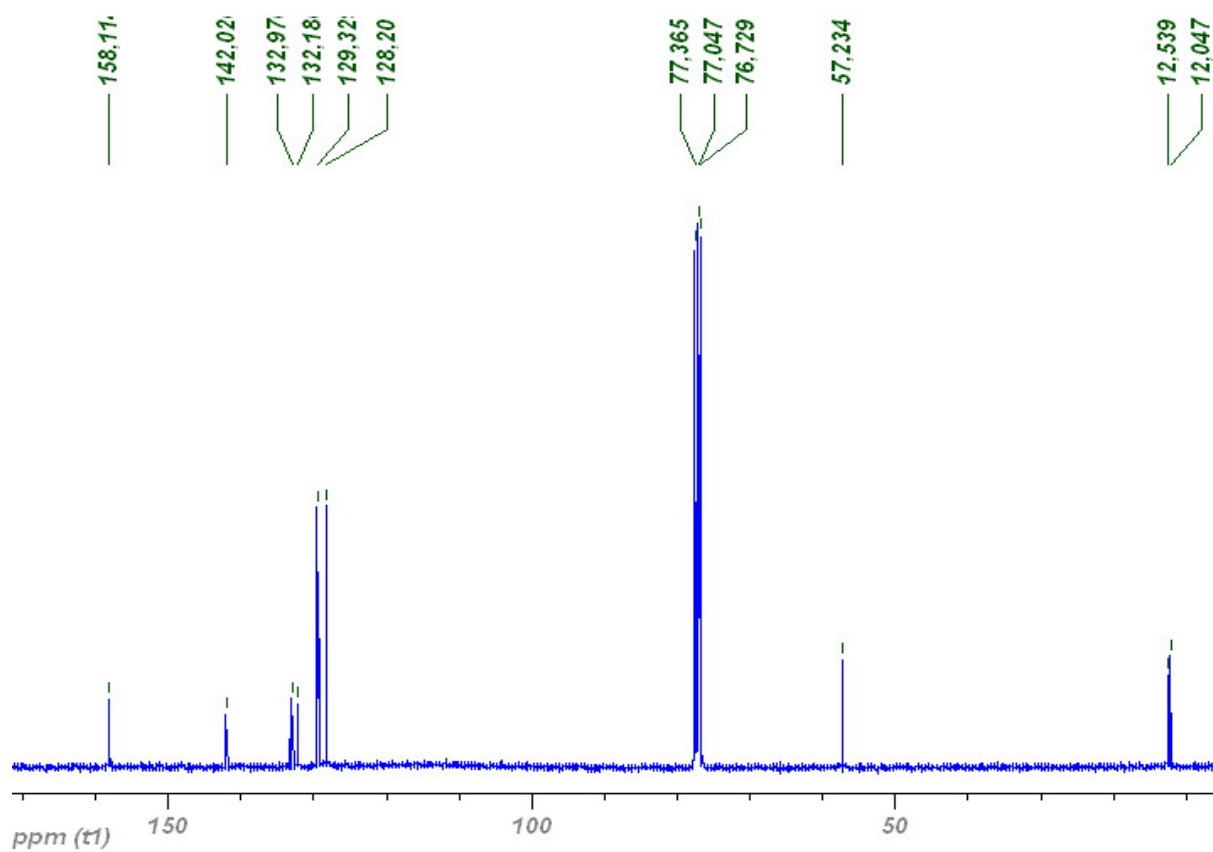


Figure 135.  $^{13}\text{C}$  NMR spectrum of **15**.

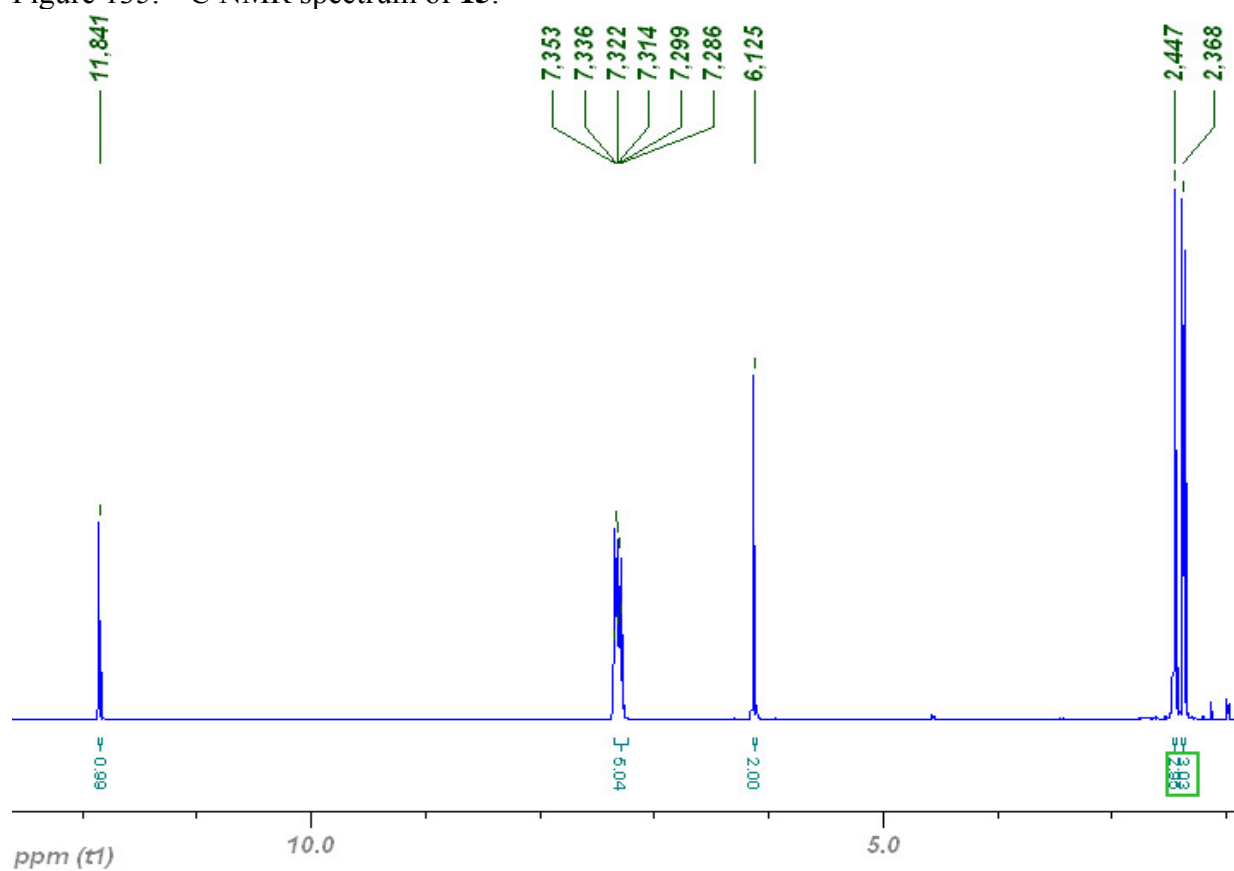
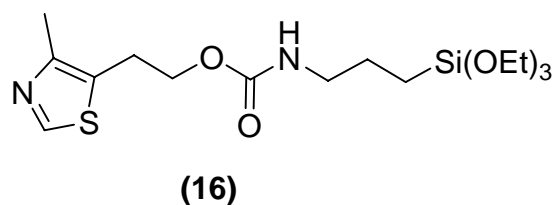


Figure 136.  $^1\text{H}$  NMR spectrum of **15**.

4.3.33 Synthesis of (4-methyl-5-thiazole-5-yl)ethyl-3-(triethoxysilyl)propylcarbamate (**16**)

1.43 g (10 mmol) of 4-methyl-5-thiazolyethanol were mixed with 5.60 g (10 mmol) of 3-(isocyanatopropyl)triethoxysilane under stirring in a screw-cap pressure vessel. A catalytic amount of dibutyltin diacetate was injected into the mixture (0.002 equiv.). The reaction was performed at 80 °C and stirred overnight under a nitrogen atmosphere. After drying in vacuum, the thiazole substituted carbamate **16** was isolated as a colorless viscous oil.

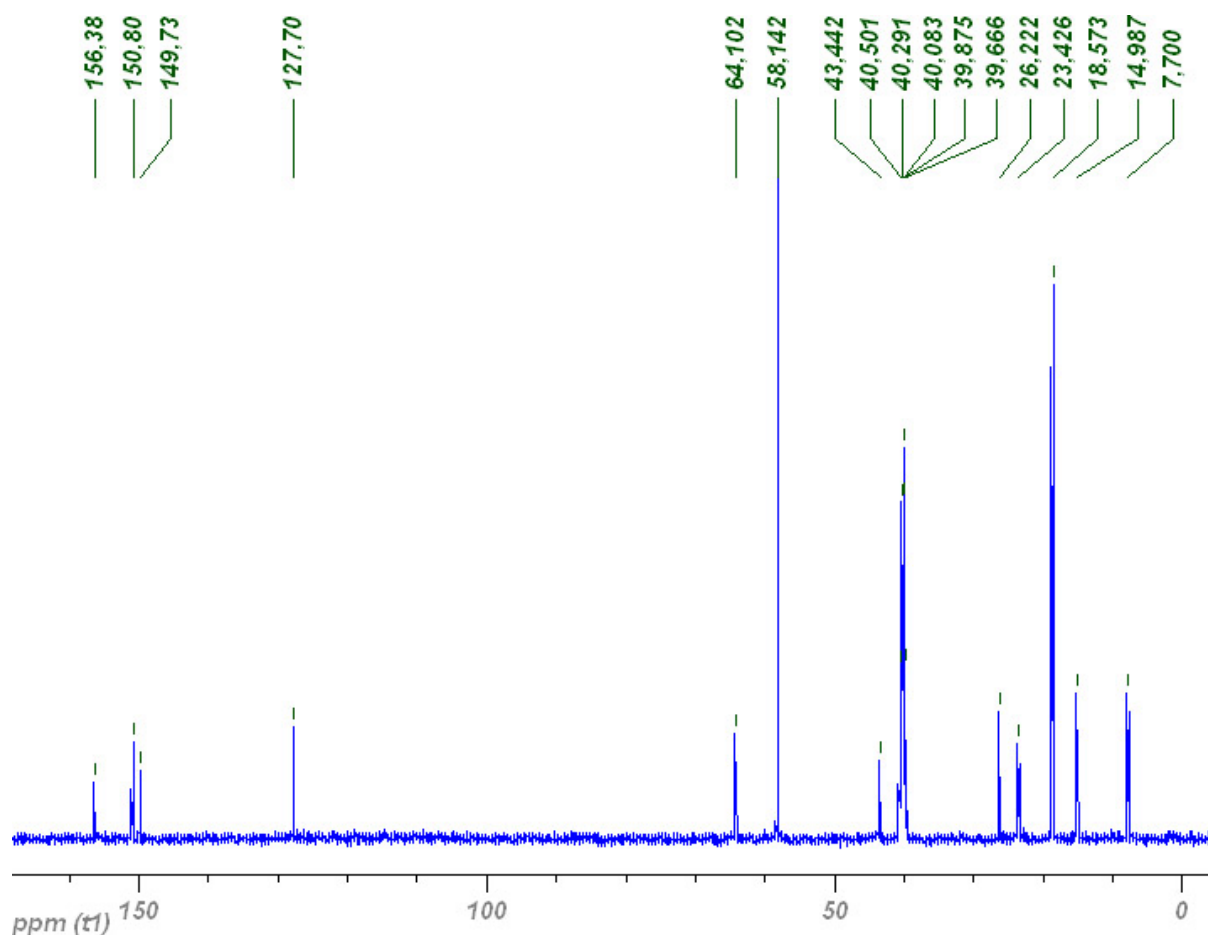
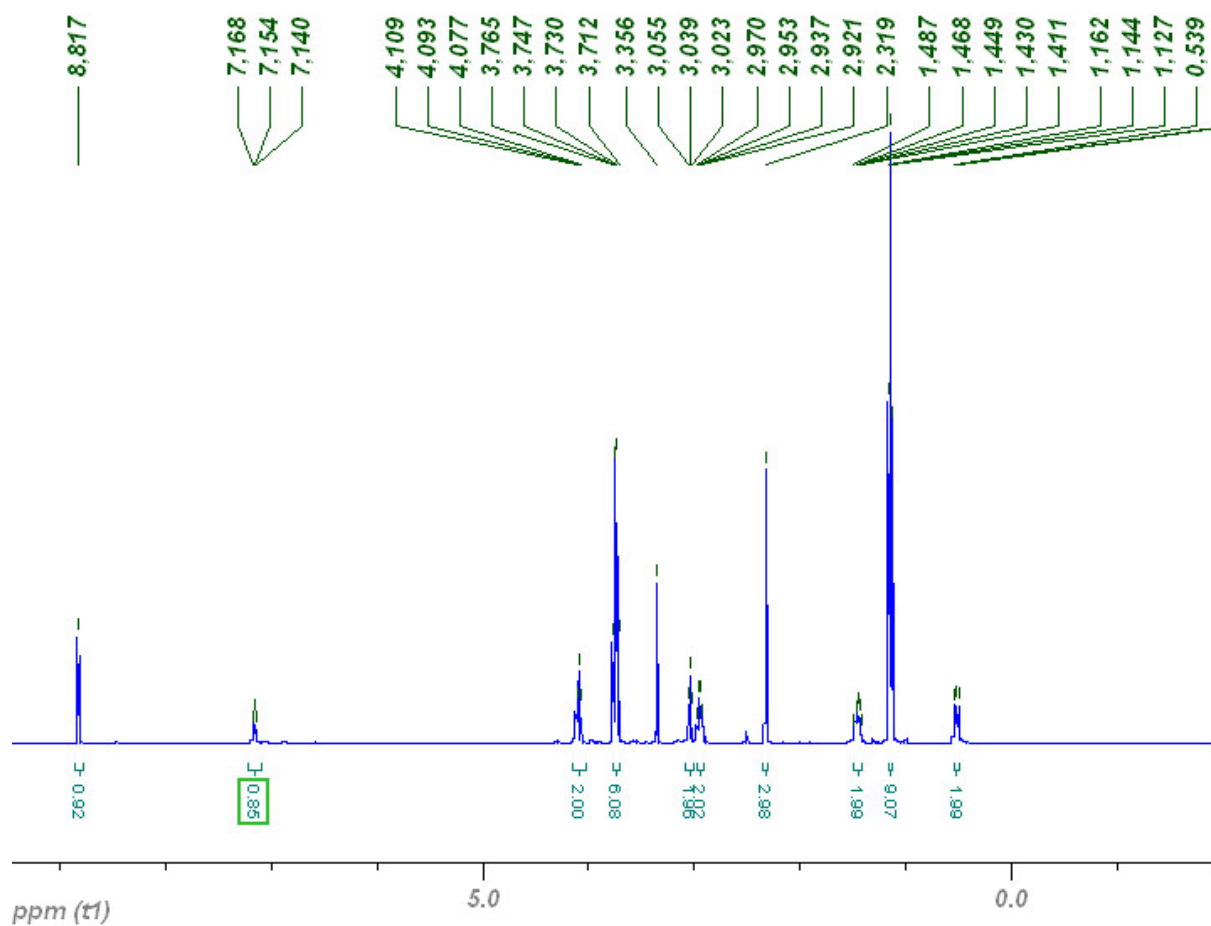
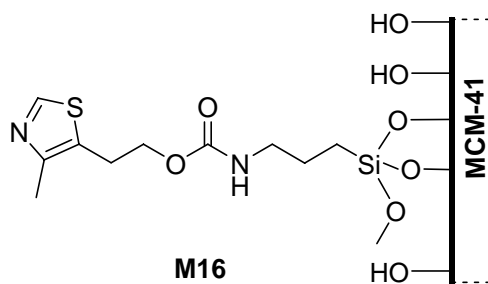


Figure 137.  $^{13}\text{C}$  NMR spectrum of **16**.

Figure 138.  $^1\text{H}$  NMR spectrum of **16**.

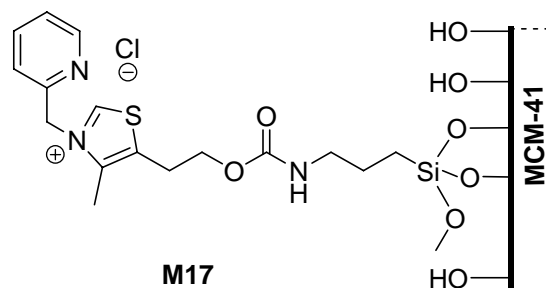
#### 4.3.34 Synthesis of (4-methyl-5-thiazole-5-yl)ethyl-3-(triethoxysilyl)propylcarbamate modified mesoporous MCM-41 (**M16**)



3.00 g of pure siliceous MCM-41, which was previously degassed at 150 °C for 4 h, were suspended in 150 ml of dry toluene. 1.2 g (3.0 mmol) of **16**, dissolved in 5 ml of dry toluene were added. The mixture was heated to reflux for 24 h under a nitrogen atmosphere. The solids were filtered off, washed with ethanol and dichloromethane and subsequently

transferred to a Soxhlet extraction equipment to be extracted with ethanol for 24 h. After being dried under vacuum at 50 °C, the product **M16** was obtained as a colorless powder. Elemental analysis for **M16**: found C, 8.99; H, 2.36; N, 0.88, which corresponds to a loading of 0.31 mmol/g.

#### 4.3.35 Synthesis of the picolyl group substituted thiazolium catalyst on the modified mesoporous MCM-41 (**M17**)



1.23 g (7.5 mmol) of 2-picolylchloride hydrochloride mixed with 15 mmol of Et<sub>3</sub>N in 30 ml CH<sub>3</sub>CN were stirred for 30 min. 3.0 g **M16** were added and the reaction was performed under reflux for 12 h. The solid was filtered off, washed with CH<sub>2</sub>Cl<sub>2</sub> and ethanol and dried under vacuum at 40 °C. The product was a yellow powder. Elemental analysis for **M17**: found C, 9.85; H, 1.85; N, 1.43, which corresponds to a loading of 0.34 mmol/g.

#### 4.3.36 Benzoin condensation

Benzaldehyde was distilled in vacuum and triethylamine was distilled under ambient pressure before use. The heterogenised catalyst was suspended in the solvent under an atmosphere of nitrogen and benzaldehyde was added followed by the dropwise addition of Et<sub>3</sub>N. The reactions were performed in refluxing solvents under stirring. After the reaction, the mixture was filtered under an atmosphere of N<sub>2</sub> to separate the solid state catalyst, the yield of benzoin was determined by GC-MS analysis.

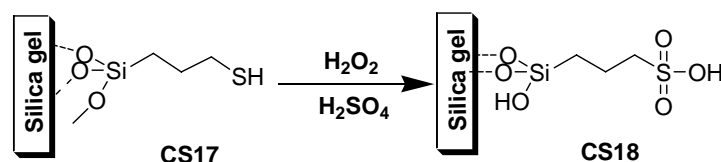
#### 4.3.37 Synthesis of *N*-[(4-methylphenylsulfonyl)(phenyl)methyl]cyclohexanecarboxamide

The preparation was according to the literature<sup>246</sup>. Anal. calc. for C<sub>21</sub>H<sub>25</sub>NO<sub>3</sub>S (371.16): C 67.89, H 6.78, N 3.77; found: C 67.53, H 6.92, N 3.64. <sup>1</sup>H NMR (CDCl<sub>3</sub>, 400 MHz): δ = 1.19 (m, 6 H), 1.68 (m, 4 H), 2.10 (1 H), 2.46 (3 H), 6.35 (d, *J* = 7.2, 1 H), 6.83 (1 H), 7.33 (d, *J* = 5.2, 2 H), 7.44 (m, 5 H), 7.77 (d, *J* = 5.2 2 H). <sup>13</sup>C NMR (CDCl<sub>3</sub>, 75 MHz): δ = 21.8 (CH<sub>3</sub>), 25.4 (CH<sub>2</sub>), 25.6 (CH<sub>2</sub>), 29.3 (CH<sub>2</sub>), 45.2 (CH), 71.6 (CH), 128.9 (CH), 129.0 (CH), 129.3 (CH), 129.7 (CH), 129.8(CH), 130.4 (C), 133.7 (C), 145.4 (C), 174.8 (C=O).

#### 4.3.38 Cross-coupling reaction for the synthesis of α-amido ketones

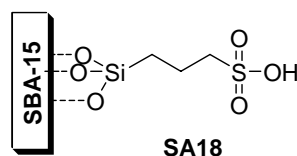
The reaction was carried out in a 25 mL flask under an atmosphere of N<sub>2</sub>. 0.55 g (1.5 mmol, 1.0 eq) of the carboxamide and 300 mg of the heterogenized catalyst (containing 0.01 mmol of thiazolium catalyst, 0.07 eq) were set under vacuum at 35 °C for 1 h. Then 15 mL of the appropriate solvent were added followed by 0.17 g (1.6 mmol, 1.1 eq) of 4-pyridinecarbaldehyde. The resulting mixture was stirred and heated to the desired temperature. An appropriate amount of distilled triethylamine was added in one portion via a syringe to start the reaction. After the reaction, the catalyst was filtered off and the product was isolated from the filtered solution by flash chromatography over silica (70% ethyl acetate and 30% hexane) as a white powder. Anal. calc. for C<sub>20</sub>H<sub>22</sub>N<sub>2</sub>O<sub>2</sub> (322.40): C 74.51, H 6.88, N 8.69; found: C 74.38, H 6.96, N 8.64. <sup>1</sup>H NMR (CDCl<sub>3</sub>, 400 MHz): δ = 8.74 (d, *J* = 6 Hz, 2 H), 7.71 (d, *J* = 6 Hz, 2 H), 7.35 (m, 5 H), 6.80 (d, *J* = 6.8 Hz, 1 H), 6.48 (d, *J* = 7.2, 1 H), 2.2 (tt, *J* = 11.6 Hz, *J* = 3.2 Hz, 1 H), 1.82 (m, 5 H), 1.44 (m, 2 H), 1.25 (m, 3 H). <sup>13</sup>C NMR (CDCl<sub>3</sub>, 75 MHz): δ = 25.6 (CH<sub>2</sub>), 25.7 (CH<sub>2</sub>), 29.4 (CH<sub>2</sub>), 29.4 (CH<sub>2</sub>), 45.0 (CH), 59.0 (CH), 121.7 (CH), 128.3 (CH), 128.9 (CH), 129.5(CH), 135.8 (C), 140.7 (C), 150.9 (C), 175.4 (C=O), 196.0 (C=O).

#### 4.3.39 Propylsulfonic acid functionlized commercial silica gel by grafting method (CS18)



A commercial silica gel having a surface area of  $500 \text{ m}^2\text{g}^{-1}$  (pore size 6.0 nm, pore volume  $0.75 \text{ cm}^3/\text{g}$ ) was used for the incorporation of (3-mercaptopropyl)trimethoxysilane (MPTMS). In a typical synthesis procedure, 3.0 g of silica gel, previously degassed at  $150 \text{ }^\circ\text{C}$ , were suspended in 80 ml of dry toluene. 1.2 g (6.11 mmol) of (3-mercaptopropyl)trimethoxysilane were added and the mixture was refluxed under stirring for 24 h in a  $\text{N}_2$  atmosphere. The solids were filtered off, washed with dichloromethane and ethanol and dried under vacuum (**CS17**). Then oxidation of the thiol groups was performed by reaction with  $\text{H}_2\text{O}_2$ , which leads to sulfonic acid functionalised powders. In a typical reaction 2.0 g of thiol functionalised powder were suspended in 50 ml of  $\text{H}_2\text{O}_2$  (30 wt%) and stirred for 12 h at room temperature. The product was filtered and washed with ethanol and water. Subsequently, the solid was transferred to a flask with 50 ml 0.05 M  $\text{H}_2\text{SO}_4$ , and stirred for 2 h at RT. The final step was filtration and washing with ethanol and water and drying at  $80 \text{ }^\circ\text{C}$  overnight.

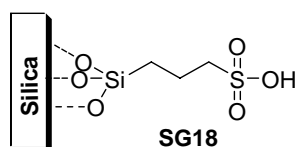
#### 4.3.40 Propylsulfonic acid functionalized SBA-15 materials by co-condensation method (**SA18**)



The preparation is according to the literature<sup>288</sup>. In a typical process, 4 g of Pluronic 123 (Aldrich) were dissolved with stirring in 125 g of 1.9 M HCl at room temperature. Then the solution was heated to  $40 \text{ }^\circ\text{C}$  and 7.8 g (37 mmol) TEOS were added to the mixture. After prehydrolysis of TEOS for 45 min, 0.8 g (4.1 mmol) of (3-mercaptopropyl)trimethoxysilane and 4.2 g (37 mmol) of  $\text{H}_2\text{O}_2$  (30% in aqueous solution) were slowly added. The resultant

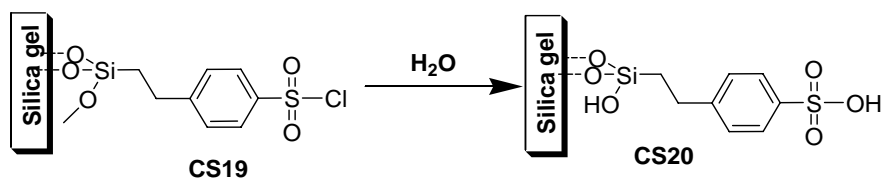
solution was stirred for 20 h at 40 °C and then the mixture was aged at 100 °C for 24 h under static conditions. The solids were filtered off, washed with water and dried at 80 °C overnight. The template was removed from the as-synthesised materials by a Soxhlet extraction with ethanol for 2 d and dried at 80 °C overnight.

#### 4.3.41 Propylsulfonic acid functionalized materials by one-pot template free sol-gel method (SG18)



In a typical procedure, 7.8 g of TEOS were added to 150 ml of a 1.8 M HCl aqueous solution and kept stirring for one day at room temperature under a nitrogen atmosphere. Then 0.8 g (4.1 mmol) of (3-mercaptopropyl)trimethoxysilane were slowly added. At the same time an aqueous solution of 4.6 g (41 mmol) of H<sub>2</sub>O<sub>2</sub> (30%) was also slowly added in the flask. The mixture was kept stirring at room temperature overnight and heated to 40 °C with stirring in an open bottle to dry out the water. The final solid was dried at 80 °C overnight and grounded to powder.

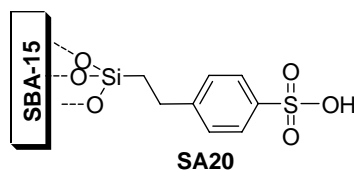
#### 4.3.42 Arenesulfonic acid functionalized commercial silica gel by grafting method (CS20)



The same silica gel was used as in the preparation of **CS18**. In a typical synthesis procedure, 3.0 g of silica gel were previously degassed at 150 °C and suspended in 50 ml of dry dichloromethane. 1.0 g (3.0 mmol) of 2-(4-chlorosulfonylphenyl)ethyltrimethoxysilane was added, and the mixture was stirred for 2 d at room temperature. The solids were filtered

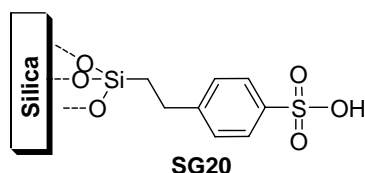
off, washed with dichloromethane and dried under vacuum. To hydrolyze the chlorosulfonyl groups to the sulfonic acid, the samples were suspended in 300 ml of distilled water and stirred for 2 h. The product was filtered off, washed with water until pH = 7 and dried at 80 °C overnight.

#### 4.3.43 Arenesulfonic acid functionalized SBA-15 materials by direct synthesis method (**SA20**)



The preparation is according to the literature <sup>147</sup>. In a typical synthesis, 4 g of Pluronic 123 (Aldrich) were dissolved with stirring in 125 g of 1.9 M HCl at room temperature. Then the solution was heated to 40 °C before the addition of the silica source. 7.8 g (37 mmol) TEOS were added to the mixture. After prehydrolysis of TEOS for 45 min, 1.3 g (4.1 mmol) of 2-(4-chlorosulfonylphenyl)ethyltrimethoxysilane were added. The resulting solution was stirred for 20 h at 40 °C. After this time, the mixture was aged at 100 °C for 2 d under static conditions. The solid was filtered off, washed with water and dried at 80 °C overnight. The template was removed from the as-synthesised materials by a Soxhlet extraction with ethanol for 2 d. In general, the amount of functional groups from the precursor can be adjusted from 2 mol% to 15 mol% (respect to the total mass of Si).

#### 4.3.44 Arenesulfonic acid functionalized materials by a template free sol-gel method (**SG20**)



In a typical procedure, 7.8 g of TEOS were added to 150 ml of a 1.8 M HCl aqueous solution and kept stirring for 1 d at room temperature. Then 1.3 g (4.1 mmol) of 2-(4-



chlorosulfonylphenyl)ethytrimethoxysilane were slowly added to the solution. The mixture was kept stirring at 40°C overnight and then the bottle was opened for drying out the water. The final solid was dried at 80 °C overnight and grounded to powder. The concentration of the organosilane can be changed. The structure of final product is significantly influenced by it.

### 4.3.45 Acid-base titration

The titration technique was used to determine the number of H<sup>+</sup> on the solid acid materials. In typical process, about 0.05 g of the sample was added to 10 ml of water and 5 ml of NaCl (2M). The mixture was stirring overnight, and the liquid was titrated by dropwise addition of 0.01 M NaOH (aq) using phenolphthalein as indicator.

### 4.3.46 Acetalization reaction

The reaction was performed in toluene under reflux with a condenser for the azeotropic removing of water. In typical reaction, 10 mg of the solid acid catalyst or a proper weight of a catalyst containing 0.1 mmol% of acidic sites (with respect to the carbonyl compound) was dried at 80 °C under vacuum for 4h. About 5 mmol of the carbonyl compound and 6 mmol of ethylene glycol mixing with toluene (5 ml) were added into the bottle. The conversions and yields were determined by GC with dibutylether as an internal standard.

### 4.3.47 Gas-phase dehydration reaction of glycerol to acrolein

The gas-phase reaction was carried out at 200 °C under atmospheric pressure in a vertical fixed-bed glass reactor (i.d. 10 mm). The catalyst with a weight of ca. 0.50 g and with a particle size 250–355 μm was charged in the middle section of the reactor. Prior to the reaction, the catalyst was preheated to 200 °C for 30 min in a flow of nitrogen (40 ± 0.2 ml/min). The reaction feed an aqueous solution containing 36.2% of glycerol (molar ratio of glycerol/water = 1/9), was fed into the reactor by a saturator. Methane as internal standard

streams under atmospheric pressure in a mixing unit together with N<sub>2</sub> in the speed of 0.50 ± 0.03 ml/min. The product was analyzed by an on-line Hewlett Packard 6890 GC equipped with a CHROMPACK 7502 capillary column and a FID detector. The on-line reaction and analysis system are illustrated in Figure 139.

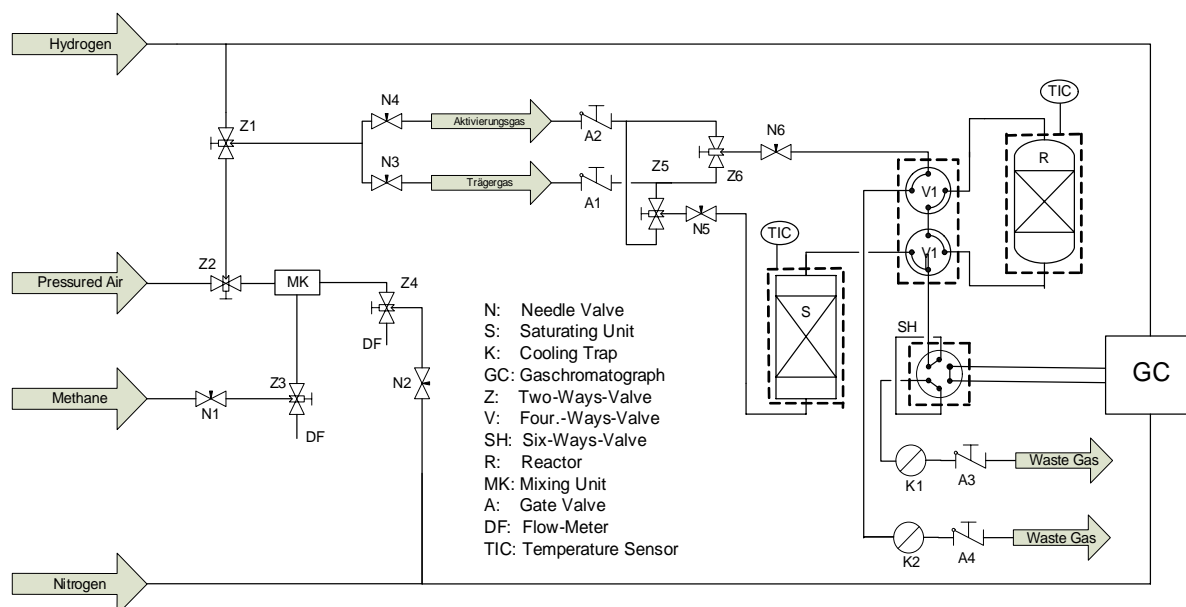


Figure 139. The reaction and analysis system for the gas-phase dehydration reaction of glycerol to acrolein

#### 4.3.48 A $\mu$ -oxo-bridged diferric complex incorporated in an arenesulfonic acid functionalized commercial silica gel (**CS21**) and a SBA-15 structured silica material (**SA21**)

0.22 g (0.55 mmol) of Fe(NO<sub>3</sub>)<sub>3</sub>·9H<sub>2</sub>O was dissolved in 0.5 ml H<sub>2</sub>O and added into a solution of 0.18 g (1.10 mmol) of bipyridine in 4.5 ml of CH<sub>3</sub>CN. After 30 min of stirring, 0.5 g of CS21 or SA21 (suspended in 15 ml of CH<sub>3</sub>CN) were added under stirring. The mixture was kept stirring for 24 h, the product was separated by filtration and was sufficiently washed with ethanol. After drying in vacuum, the products **CS21** and **SA21** were obtained as a slightly brown and a yellow powder, respectively.

#### 4.3.49 Epoxidation of *cis*-cyclooctene

A CH<sub>3</sub>CN (7.0 ml) solution of *cis*-cyclooctene 0.58 g (5.0 mmol) was mixed with a proper amount of **SA21** or **CS21** (0.25 mol%) in a 25 ml flask at 0 °C. 0.06 g of decane as the internal standard were added. Two equivalents of 32% peracetic acid (10.0 mmol) dissolved in 3.0 ml of CH<sub>3</sub>CN were added dropwise over 2 min. The GC analysis of the solution provides the substrate conversion and product yield relative to the internal standard integration.

The epoxidation of *cis*-cyclooctene was also performed using tBuOOH as the oxygen source. In a typical process, a CHCl<sub>3</sub> (5.0 ml) solution of *cis*-cyclooctene (1.0 mmol), **SA21** (0.5 mol%) and decane (internal standard, 0.03 g) was prepared in 25 ml flask under reflux with a stirring bar. 1.1 equivalents of tBuOOH were injected to the mixture. The GC analysis of the solution provides the substrate conversion and product yield relative to the internal standard integration.

#### 4.3.40 Epoxidation of methyl oleate

To 1.0 g of methyl oleate dissolved in 2 ml of CH<sub>3</sub>CN, a proper amount of **SA21** or **CS21** (0.25 mol%) was added. The mixture was kept stirring at 0°C, then two equivalents of peracetic acid (32%) in 1.4 ml CH<sub>3</sub>CN were added dropwise over 30 minutes. The reaction was stirred for 1h, filtered, and extract with pentane. The product was identified by NMR spectroscopy.

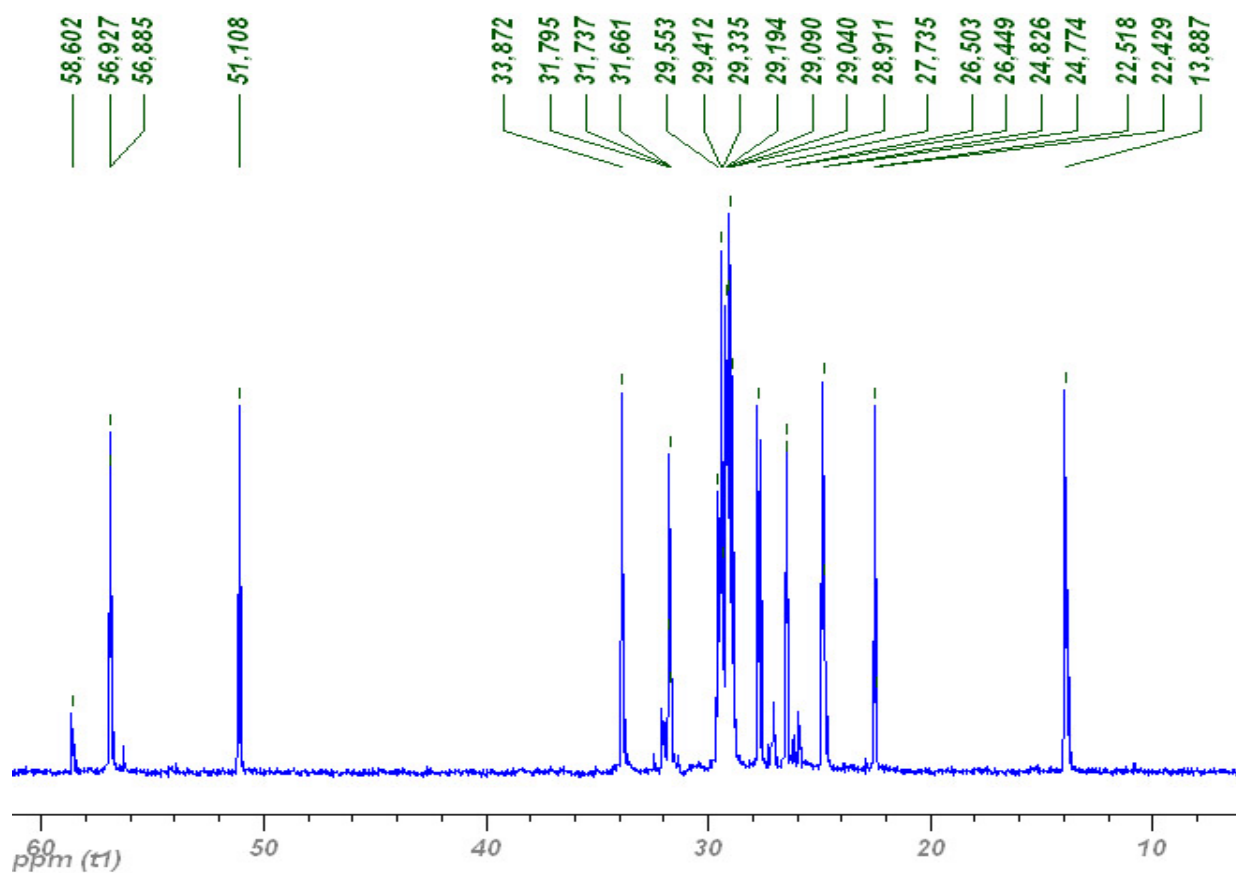


Figure 140.  $^{13}\text{C}$  NMR spectrum of the product of epoxidation of methyl oleate.

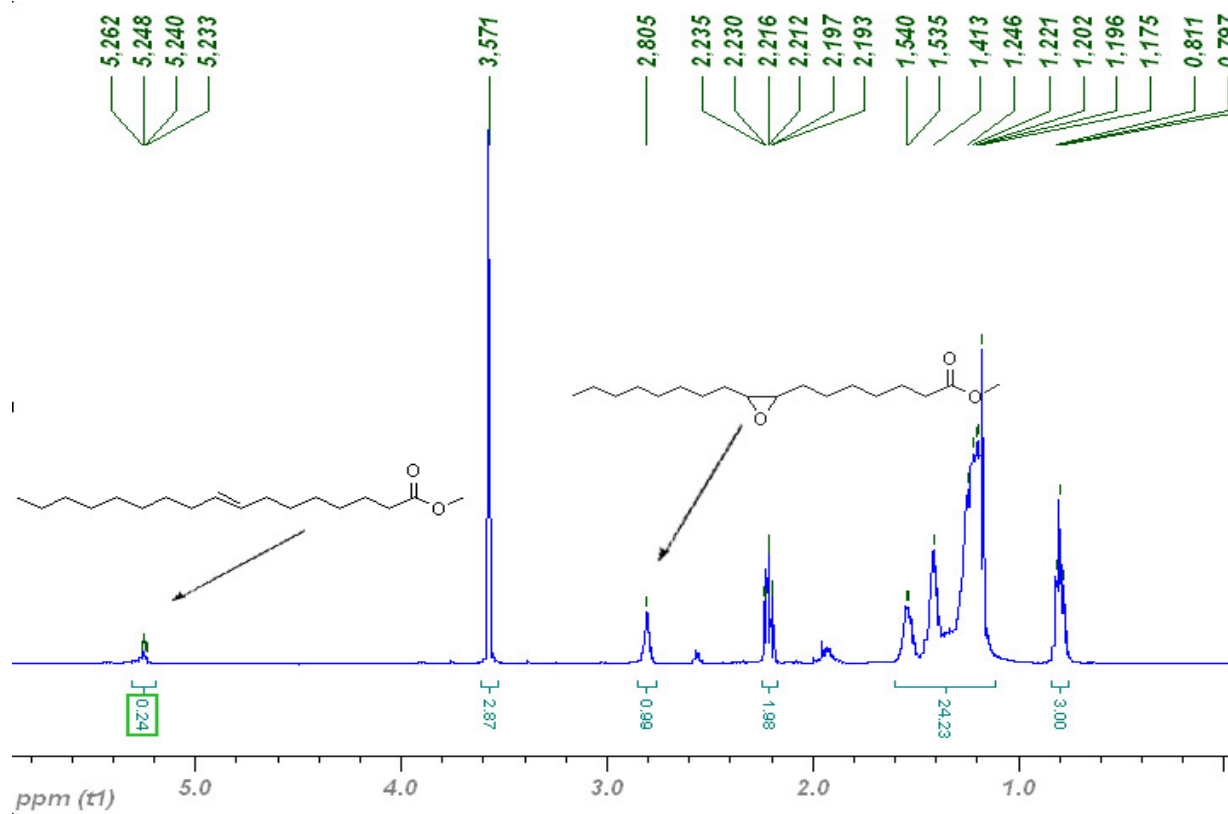


Figure 141.  $^1\text{H}$  NMR spectrum of the product of epoxidation of methyl oleate.

## References

1. IUPAC, *Pure Appl. Chem*, 1978, **31**, 578.
2. D. W. Breck, *Zeolite Molecular Sieves*, Wiley, New York, 1974.
3. R. Szostak, *Molecular Sieves: Principles of Synthesis and Identification*, Van Nostrand Reinhold, New York, 1989.
4. C. T. Kresge, M. E. Leonowicz, W. J. Roth, J. C. Vartuli and J. S. Beck, *Nature*, 1992, **359**, 710-712.
5. T. S. T. Yanagisawa, K. Kuroda, C. Kato, *Bull. Chem. Soc. Jn.*, 1990, **63**, 988.
6. Q. Huo, D. I. Margolese, G. D. Stucky, *Chem. Mater.*, 1996, **8**, 1147-1160.
7. J. S. Beck, J. C. Vartuli, W. J. Roth, M. E. Leonowicz, C. T. Kresge, K. D. Schmitt, C. T. W. Chu, D. H. Olson, E. W. Sheppard, S. B. McCullen, J. B. Higgins, J. L. Schlenker, *J. Am. Chem. Soc.*, 1992, **114**, 10834-10843.
8. Q. S. Huo, D. I. Margolese, U. Ciesla, P. Y. Feng, T. E. Gier, P. Sieger, R. Leon, P. M. Petroff, F. Schüth, G. D. Stucky, *Nature*, 1994, **368**, 317-321.
9. A. Stein, *Adv. Mater.*, 2003, **15**, 763-775.
10. F. Schüth, *Chem. Mater.*, 2001, **13**, 3184-3195.
11. F. S. A.-H. Lu, *Adv. Mater.*, 2006, **18**, 1793-1805.
12. J. Frasc, B. Lebeau, M. Soudard, J. Patarin, R. Zana, *Langmuir*, 2000, **16**, 9049-9057.
13. C. C. Landry, S. H. Tolbert, K. W. Gallis, A. Monnier, G. D. Stucky, P. Norby, J. C. Hanson, *Chem. Mater.*, 2001, **13**, 1600-1608.
14. J. Y. Ying, C. P. Mehnert, M. S. Wong, *Angew. Chem. Int. Ed.*, 1999, **38**, 56-77.
15. C. T. Kresge, M. E. Leonowicz, W. J. Roth, J. C. Vartuli, *US-A 5098684*, 1992.
16. J. C. Vartuli, C. T. Kresge, M. E. Leonowicz, A. S. Chu, S. B. McCullen, I. D. Johnson, E. W. Sheppard, *Chem. Mater.*, 1994, **6**, 2070-2077.
17. C. Y. Chen, S. L. Burkett, H. X. Li, M. E. Davis, *Microporous Mater.*, 1993, **2**, 27.
18. J. C. Vartuli, W. J. Roth, J. S. Beck, S. B. McCullen, C. T. Kresge, *The Synthesis and Properties of M41S and Related Mesoporous Materials, Molecular Sieves, Springer-Verlag: Berlin*, 1998, **1**, 97.
19. A. Firouzi, D. Kumar, L. M. Bull, T. Besier, P. Sieger, Q. Huo, S. A. Walker, J. A. Zasadzinski, C. Glinka, J. Nicol, et al., *Science*, 1995, **267**, 1138-1143.
20. C. J. Glinka, J. M. Nicol, G. D. Stucky, E. Ramli, D. I. Margolese, Q. Huo, *Adv. Porous Mater.*, 1995, **371**, 47-52.
21. O. Regev, *Langmuir*, 1996, **12**, 4940-4944.
22. Q. S. Huo, D. I. Margolese, U. Ciesla, D. G. Demuth, P. Y. Feng, T. E. Gier, P. Sieger, A. Firouzi, B. F. Chmelka, F. Schüth, G. D. Stucky, *Chem. Mater.*, 1994, **6**, 1176-1191.
23. Q. S. Huo, D. I. Margolese, G. D. Stucky, *Chem. Mater.*, 1996, **8**, 1147-1160.
24. A. Monnier, F. Schüth, Q. Huo, D. Kumar, D. Margolese, R. S. Maxwell, G. D. Stucky, M. Krishnamurty, P. Petroff, A. Firouzi, M. Janicke, B. F. Chmelka, *Science*, 1993, **261**, 1299-1303.
25. P. T. Tanev, T. J. Pinnavaia, *Science*, 1995, **267**, 865-867.
26. D. Zhao, J. Feng, Q. Huo, N. Melosh, G. H. Fredrickson, B. F. Chmelka, G. D. Stucky, *Science*, 1998, **279**, 548-552.
27. K. Cassiers, T. Linssen, M. Mathieu, M. Benjelloun, K. Schrijnemakers, P. Van Der Voort, P. Cool, E. F. Vansant, *Chem. Mater.*, 2002, **14**, 2317-2324.
28. R. Mokaya, *J. Phys. Chem. B*, 1999, **103**, 10204-10208.
29. N. K. Raman, M. T. Anderson, C. J. Brinker, *Chem. Mater.*, 1996, **8**, 1682-1701.
30. S. S. Kim, W. Z. Zhang, T. J. Pinnavaia, *Science*, 1998, **282**, 1302-1305.

31. Z. H. Luan, C. F. Cheng, W. Z. Zhou, J. Klinowski, *J. Phys. Chem.*, 1995, **99**, 1018-1024.
32. D. Y. Zhao, Q. S. Huo, J. L. Feng, B. F. Chmelka, G. D. Stucky, *J. Am. Chem. Soc.*, 1998, **120**, 6024-6036.
33. D. Zhao, J. Sun, Q. Li, G. D. Stucky, *Chem. Mater.*, 2000, **12**, 275-279.
34. C. J. Brinker, G. W. Scherer, *Sol-Gel Science; Academic Press; Boston*, 1990.
35. F. Zhang, Yan, H. Yang, Y. YanMeng, C. Yu, B. Tu, D. Zhao, *J. Phys. Chem.B*, 2005, **109**, 8723-8732.
36. M. Kruk, M. Jaroniec, C. H. Koo, R. Ryoo, *Chem. Mater.*, 2000, **12**, 1961-1968.
37. R. van Grieken, G. Calleja, G. D. Stucky, J. A. Melero, R. A. Garcia, J. Iglesias, *Langmuir*, 2003, **19**, 3966-3973.
38. K. W. Gallis, C. C Landry, *Adv. Mater.*, 2001, **13**, 23-26.
39. A. Hozumi, Y. Yokogawa, T. Kameyama, K. Hiraku, H. Sugimura, O. Takai, M. Okido, *Adv. Mater.*, 2000, **12**, 985-987.
40. J. C. Vartuli, K. D. Schmitt, C. T. Kresge, W. J. Roth, M. E. Leonowicz, S. B. McCullen, S. D. Hellring, J. S. Beck, J. L. Schlenker, *Chem. Mater.*, 1994, **6**, 2317-2326.
41. S. Che, H. Li, S. Lim, Y. Sakamoto, O. Terasaki, T. Tatsumi, *Chem. Mater.*, 2005, **17**, 4103-4113.
42. C. Gao, H. Qiu, W. Zeng, Y. Sakamoto, O. Terasaki, K. Sakamoto, Q. Chen, S. Che, *Chem. Mater.*, 2006, **18**, 3904-3914.
43. D. Kaneko, U. Olsson, K. Sakamoto, *Langmuir*, 2002, **18**, 4699-4703.
44. J. M. Kim, Y. Sakamoto, Y. K. Hwang, Y.-U. Kwon, O. Terasaki, S.-E. Park, G. D. Stucky, *J. Phys. Chem. B*, 2002, **106**, 2552-2558.
45. J. C. Vartuli, Kresge, C. T., Roth, W. J., McCullen, S. B., Beck, J. S., Schmitt, K. D., Leonowicz, M. E., Lutner, J. D., Sheppard, E. W., *Advanced Catalysts and Nanostructured Materials: Modern Synthesis Methods (Ed.: W. R. Moser)*, Academic Press, New York, 1996, 1.
46. H. V. Olphen, *Science*, 1966, **154**, 645.
47. G. Kickelbick, *Angew. Chem.-Int. Ed.*, 2004, **43**, 3102-3104.
48. C. Sanchez, B. Lebeau, F. Chaput, J. P. Boilot, *Adv. Mater.*, 2003, **15**, 1969-1994.
49. A. P. Wight, M. E. Davis, *Chem. Rev.*, 2002, **102**, 3589-3614.
50. M. Vallet-Regi, F. Balas, D. Arcos, *Angew. Chem. Int. Ed.*, 2007, **46**, 7548-7558.
51. X. S. Zhao, G. Q. Lu, *J. Phys. Chem. B*, 1998, **102**, 1556-1561.
52. T. Kimura, S. Saeki, Y. Sugahara, K. Kuroda, *Langmuir*, 1999, **15**, 2794-2798.
53. D. Brunel, *Microporous Mesoporous Mater.*, 1999, **27**, 329-344.
54. F. Hoffmann, M. Cornelius, J. Morell, M. Fröba, *Angew. Chem. Int. Ed.*, 2006, **45**, 3216-3251.
55. S. L. Burkett, S. D. Sims, S. Mann, *Chem. Commun.*, 1996, 1367-1368.
56. M. H. Lim, A. Stein, *Chem. Mater.*, 1999, **11**, 3285-3295.
57. K. Moller, T. Bein, R. X. Fischer, *Chem. Mater.*, 1999, **11**, 665-673.
58. L. Mercier, T. J. Pinnavaia, *Chem. Mater.*, 2000, **12**, 188-196.
59. J. Brown, R. Richer, L. Mercier, *Microporous Mesoporous Mater.*, 2000, **37**, 41-48.
60. M. Jia, A. Seifert, M. Berger, H. Giegengack, S. Schulze, W. R. Thiel, *Chem. Mater.*, 2004, **16**, 877-882.
61. D. A. Loy, K. J. Shea, *Chem. Rev.*, 1995, **95**, 1431-1442.
62. K. J. Shea, D. A. Loy, *Chem. Mater.*, 2001, **13**, 3306-3319.
63. S. Inagaki, S. Guan, Y. Fukushima, T. Ohsuna, O. Terasaki, *J. Am. Chem. Soc.*, 1999, **121**, 9611-9614.

64. B. J. Melde, B. T. Holland, C. F. Blanford, A. Stein, *Chem. Mater.*, 1999, **11**, 3302-3308.
65. S. Inagaki, S. Guan, T. Ohsuna, O. Terasaki, *Nature*, 2002, **416**, 304-307.
66. K. A. Koyano, T. Tatsumi, Y. Tanaka, S. Nakata, *J. Phys. Chem. B*, 1997, **101**, 9436-9440.
67. V. Antochshuk, M. Jaroniec, *J. Phys. Chem. B*, 1999, **103**, 6252-6261.
68. A. Walcarius, *Electroanalysis*, 2008, **20**, 711-738.
69. S. A. El-Safty, D. Prabhakaran, A. A. Ismail, H. Matsunaga, F. Mizukami, *Chem. Mater.*, 2008, **20**, 2644-2654.
70. R. Marschall, I. Bannat, J. Caro, M. Wark, *Microporous Mesoporous Mater.*, 2007, **99**, 190-196.
71. G. Soler-Illia, P. Innocenzi, *Chem. Eur. J.*, 2006, **12**, 4478-4494.
72. E. L. Margelefsky, R. K. Zeidan, M. E. Davis, *Chem. Soc. Rev.*, 2008, **37**, 1118-1126.
73. M. J. Jia, A. Seifert, M. Berger, H. Giegengack, S. Schulze, W. R. Thiel, *Chem. Mater.*, 2004, **16**, 877-882.
74. H. Sun, A. M. Scharff-Poulsen, H. Gu, K. Almdal, *Chem. Mater.*, 2006, **18**, 3381-3384.
75. R. A. Sheldon, *Adv. Synth. Catal.*, 2007, **349**, 1289-1307.
76. X. Feng, G. E. Fryxell, L. Q. Wang, A. Y. Kim, J. Liu, K. M. Kemner, *Science*, 1997, **276**, 923-926.
77. Z. Yan, G. T. Li, L. Mu, S. Y. Tao, *J. Mater. Chem.*, 2006, **16**, 1717-1725.
78. J. F. Diaz, K. J. Balkus, F. Bedioui, V. Kurshev, L. Kevan, *Chem. Mater.*, 1997, **9**, 61-67.
79. J. A. Melero, R. van Grieken, G. Morales, *Chem. Rev.*, 2006, **106**, 3790-3812.
80. M. Sohmiya, Y. Sugahara, M. Ogawa, *J. Phys. Chem. B*, 2007, **111**, 8836-8841.
81. K. Klier, A. C. Miller, L. L. Zhang, M. K. Hatalis, *Chem. Mater.*, 2008, **20**, 1359-1366.
82. S. Hamoudi, S. Royer, S. Kaliaguine, *Microporous Mesoporous Mater.*, 2004, **71**, 17-25.
83. W. J. Albery, A. W. Foulds, K. J. Hall, A. R. Hillman, R. G. Edgell, A. F. Orchard, *Nature*, 1979, **282**, 793-797.
84. M. Sainsbury, *Comprehensive Heterocyclic Chemistry*, Pergamon, Oxford, 1984.
85. G. Karreman, I. Isenberg, A. Szent-Györgyi, *Science*, 1959, **130**, 1191-1192.
86. J. P. Billon, *Bul. Soc. Chim. France*, 1960, 1784-1785.
87. G. Cauquis, A. Deronzier, D. Serve, *Bull. Soc. Chim. France*, 1976, 295-302.
88. D. Clarke, B. C. Gilbert, P. Hanson, C. M. Kirk, *J. Chem. Soc., Perkin Trans. 2*, 1978, 1103-1110.
89. E. Bosch, J. K. Kochi, *J. Chem. Soc., Perkin Trans. 1057*, 1995.
90. R. E. Hester, K.P. J. Williams, *J. Chem. Soc., Perkin Trans. 2*, 1981, 852-859.
91. I. Forrester, F. Forrester, *Biochim. Biophys. Acta*, 1958, **29**, 441.
92. E. Nishiwaki, H. Nakagawa, M. Takasaki, T. Matsumoto, H. Sakurai, M. Shiuya, *Heterocycles*, 1990, **31**, 1763-1767.
93. R. Duesing, G. Tapolsky, T. J. Meyer, *J. Am. Chem. Soc.*, 1990, **112**, 5378-5379.
94. A. M. Brun, A. Harriman, V. Heitz, J. P. Sauvage, *J. Am. Chem. Soc.*, 1991, **113**, 8657-8663.
95. J. Daub, R. Engl, J. Kurzawa, S. E. Miller, S. Schneider, A. Stockmann, M. R. Wasielewski, *J. Phys. Chem. A*, 2001, **105**, 5655-5665.
96. R. C. Wheland, J. L. Gillson, *J. Am. Chem. Soc.*, 1976, **98**, 3916-3925.
97. J. D. Hubert Spreitzer, *Chem. Eur. J.*, 1996, **2**, 1150-1158.
98. J. D. Andreas Knorr, *Angew. Chem. Int. Ed.*, 1996, **34**, 2664-2666.

99. N. Limited, in *EP 1443090 A1 2040804*, ed. E. P. Application, 13, Ireland, 2004.
100. R. Y. Lai, X. Kong, S. A. Jenekhe, A. J. Bard, *J. Am. Chem. Soc.*, 2003, **125**, 12631-12639.
101. R. Y. Lai, E. F. Fabrizio, L. Lu, S. A. Jenekhe, A. J. Bard, *J. Am. Chem. Soc.*, 2001, **123**, 9112-9118.
102. D. H. Hwang, S. K. Kim, M. J. Park, J. H. Lee, B. W. Koo, I. N. Kang, S. H. Kim, T. Zyung, *Chem. Mater.*, 2004, **16**, 1298-1303.
103. Y. S. Han, S. D. Kim, L. S. Park, D. U. Kim, Y. W. Kwon, *J. Polym. Sci. Part A: Polym. Chem.*, 2003, **41**, 2502-2511.
104. J. D. Bell, J. F. Blount, O. V. Briscoe, H. C. Freeman, *Chem. Commun.*, 1968, 1656-1657.
105. J. J. H. McDowell, *Acta Cryst. Sec. B*, 1976, **32**, 5-10.
106. T. Uchida, M. Ito, K. Kozawa, *Bull. Chem. Soc. Jpn*, 1983, **56**, 577-582.
107. D. Pan, D. L. Phillips, *J. Phys. Chem. A*, 1999, **103**, 4737-4743.
108. L. Yang, J. K. Feng, A. M. Ren, *J. Org. Chem.*, 2005, **70**, 5987-5996.
109. G. P. Brown, S. Aftergut, *Nature*, 1962, **193**, 361-362.
110. D. R. Kearns, M. Calvin, *J. Chem. Phys.*, 1961, **34**, 2022-&.
111. Y. Sato, M. Kinoshita, M. Sano, H. Akamatu, *Bull. Chem. Soc. Jpn*, 1969, **42**, 548-550.
112. D. Sun, S. V. Rosokha, J. K. Kochi, *J. Am. Chem. Soc.*, 2004, **126**, 1388-1401.
113. R. Anthonj, N. Karl, E. R. Beverly, J. S. John, *J. Chem. Phys.*, 1980, **72**, 1244-1255.
114. B. Claudia, M. Lee, W. Richard Liangchen, J. R. Dahn, *J. Electrochem. Soc.*, 2006, **153**, A288-A294.
115. X. Kong, A. P. Kulkarni, S. A. Jenekhe, *Macromolecules*, 2003, **36**, 8992-8999.
116. Y. Zou, W. Wu, G. Sang, Y. Yang, Y. Liu, Y. Li, *Macromolecules*, 2007, **40**, 7231-7237.
117. T. J. Meyer, G. J. Meyer, B. W. Pfennig, J. R. Schoonover, C. J. Timpson, J. F. Wall, C. Kobusch, X. H. Chen, B. M. Peek, C. G. Wall, W. Ou, B. W. Erickson, C. A. Bignozzi, *Inorg. Chem.*, 1994, **33**, 3952-3964.
118. R. Argazzi, C. A. Bignozzi, T. A. Heimer, F. N. Castellano, G. J. Meyer, *J. Am. Chem. Soc.*, 1995, **117**, 11815-11816.
119. J. Huang, Z. Huang, S. Jin, T. Lian, *J. Phys. Chem. C*, 2008, **112**, 19734-19738.
120. R. M. Krishna, A. M. Prakash, L. Kevan, *J. Phys. Chem. B*, 2000, **104**, 1796-1801.
121. Z. H. Luan, J. Y. Bae, L. Kevan, *Chem. Mater.*, 2000, **12**, 3202-3207.
122. S. Sinlapadech, R. M. Krishna, Z. H. Luan, L. Kevan, *J. Phys. Chem. B*, 2001, **105**, 4350-4355.
123. L. Stryer, *Biochemistry*, Freedman, New York, 1995.
124. Y. Tachibana, N. Kihara, T. Takata, *J. Am. Chem. Soc.*, 2004, **126**, 3438-3439.
125. M. S. Kerr, J. Read de Alaniz, T. Rovis, *J. Am. Chem. Soc.*, 2002, **124**, 10298-10299.
126. A. E. Mattson, A. R. Bharadwaj, K. A. Scheidt, *J. Am. Chem. Soc.*, 2004, **126**, 2314-2315.
127. J. A. Murry, D. E. Frantz, A. Soheili, R. Tillyer, E. J. J. Grabowski, P. J. Reider, *J. Am. Chem. Soc.*, 2001, **123**, 9696-9697.
128. D. E. Frantz, L. Morency, A. Soheili, J. A. Murry, E. J. J. Grabowski, R. D. Tillyer, *Org. Lett.*, 2004, **6**, 843-846.
129. R. Breslow, *J. Am. Chem. Soc.*, 1958, **80**, 3719-3726.
130. D. Enders, O. Niemeier, A. Henseler, *Chem. Rev.*, 2007, **107**, 5606-5655.
131. H. Stetter and G. Dambkes, *Synthesis-Stuttgart*, 1980, 309-310.
132. X. Linghu, C. C. Bausch, J. S. Johnson, *J. Am. Chem. Soc.*, 2005, **127**, 1833-1840.



133. H. Takikawa, Y. Hachisu, J. W. Bode, K. Suzuki, *Angew. Chem.*, 2006, **118**, 3572-3574.
134. H. Stetter, H. Kuhlmann, *Org. React*, 1991, **40**, 407.
135. Y. Hachisu, J. W. Bode, K. Suzuki, *J. Am. Chem. Soc.*, 2003, **125**, 8432.
136. C. C. Galopin, *Tetrahedron Lett.*, 2001, **42**, 5589-5591.
137. G. W. Nyce, T. Glauser, E. F. Connor, A. Mock, R. M. Waymouth, J. L. Hedrick, *J. Am. Chem. Soc.*, 2003, **125**, 3046-3056.
138. U. Nilsson, L. Meshlkina, Y. Lindqvist, G. Schneider, *J. Biol. Chem.*, 1997, **272**, 1864.
139. W. Tagak, Y. Tamura, Y. Yano, *Bull. Chem. Soc. Jpn.*, 1980, **53**, 478.
140. A. G. M. Barrett, A. C. Love, L. Tedeschi, *Org. Lett.*, 2004, **6**, 3377-3380.
141. O. Kennedy, T. Smyth, *J. Chem. Res., Synopses*, 1993, 188.
142. J. S. Yadav, K. Anuradha, B. V. S. Reddy, B. Eeshwaraiah, *Tetrahedron Lett.*, 2003, **44**, 8959-8962.
143. S. Raghavan, K. Anuradha, *Tetrahedron Lett.*, 2002, **43**, 5181-5183.
144. S. Shylesh, S. Sharma, S. P. Mirajkar, A. P. Singh, *J. Mol. Catal. A-Chem.*, 2004, **212**, 219-228.
145. S. Shylesh, P. P. Samuel, C. Srilakshmi, R. Parischa, A. P. Singh, *J. Mol. Catal. A-Chem.*, 2007, **274**, 153-158.
146. S. Inagaki, S. Guan, T. Oshuna, O. Terasaki, *Nature*, 2002, **416**, 304.
147. J. A. Melero, G. D. Stucky, R. v. Grieken, G. Morales, *J. Mater. Chem.*, 2002, **12**, 1664-1670.
148. M. Alvaro, A. Corma, D. Das, V. Fornes, H. Garcia, *Chem. Commun.*, 2004, 956-957.
149. J. M. Fraile, J. I. Garcia, J. A. Mayoral, T. Tarnai, M. A. Harmer, *J. Catal.*, 1999, **186**, 214-221.
150. D. J. Macquarrie, S. J. Tavener, M. A. Harmer, *Chem. Commun.*, 2005, 2363-2365.
151. I. K. Mbaraka, D. R. Radu, V. S. Y. Lin, B. H. Shanks, *J. Catal.*, 2003, **219**, 329-336.
152. K. Shimizu, E. Hayashi, T. Hatamachi, T. Kodama, T. Higuchi, A. Satsuma, Y. Kitayama, *J. Catal.*, 2005, **231**, 131-138.
153. R. v. Grieken, J. A. Melero, G. Morales, *App. Catal. A: General*, 2005, **289**, 143-152.
154. M. Siler, A. Franz, T. J. J. Müller, *Chem. Eur. J.*, 2008, **14**, 2602-2614.
155. A. Walcarius, M. Etienne, B. Lebeau, *Chem. Mater.*, 2003, **15**, 2161-2173.
156. R. Anwander, I. Nagl, M. Widenmeyer, G. Engelhardt, O. Groeger, C. Palm, T. Roser, *J. Phys. Chem. B*, 2000, **104**, 3532-3544.
157. M. H. Lim, C. F. Blanford, A. Stein, *J. Am. Chem. Soc.*, 1997, **119**, 4090-4091.
158. X. S. Zhao, G. Q. Lu, X. Hu, *Microporous and Mesoporous Mater.*, 2000, **41**, 37-47.
159. A. Jentys, K. Kleestorfer, H. Vinek, *Microporous and Mesoporous Mater.*, 1999, **27**, 321-328.
160. J. S. Beck, J. C. Vartuli, G. J. Kennedy, C. T. Kresge, W. J. Roth, S. E. Schramm, *Chem. Mater.*, 1994, **6**, 1816-1821.
161. A. Corma, Q. B. Kan, M. T. Navarro, J. P. Pariente, F. Rey, *Chem. Mater.*, 1997, **9**, 2123-2126.
162. M. Kruk, M. Jaroniec, Y. Sakamoto, O. Terasaki, R. Ryoo, C. H. Koo, *J. Phys. Chem. B*, 2000, **104**, 292-301.
163. B. Marler, U. Oberhagemann, S. Vortmann, H. Gies, *Microporous Materials*, 1996, **6**, 375-383.
164. S. J. Gregg, W. K. Sing, *Adsorption, Surface Area and Porosity, 2nd ed.*; Academic Press: London, 1982.
165. A. V. Neimark, P. I. Ravikovitch, M. Grun, F. Schüth, K. K. Unger, *J. Colloid Interface Sci.*, 1998, **207**, 159-169.

166. P. I. Ravikovitch, S. C. Odomhnaill, A. V. Neimark, F. Schüth and K. K. Unger, *Langmuir*, 1995, **11**, 4765-4772.
167. A. Fidalgo and L. M. Ilharco, *Chem. Eur. J.*, 2004, **10**, 392-398.
168. N. B. Colthup, *An Introduction to Infrared and Raman Spectroscopy*, Academic Press, Boston., 1990.
169. R. S. Macomber, *A Complete Introduction to Modern NMR Spectroscopy*, John Wiley & Sons, 1998.
170. X. S. Zhao, G. Q. Lu, A. K. Whittaker, G. J. Millar, H. Y. Zhu, *J. Phys. Chem. B*, 1997, **101**, 6525-6531.
171. R. Simonutti, A. Comotti, S. Bracco, P. Sozzani, *Chem. Mater.*, 2001, **13**, 771-777.
172. P. A. Leermakers, H. T. Thomas, L. D. Weis, F. C. James, *J. Am. Chem. Soc.*, 1966, **88**, 5075-5083.
173. B. Valeur, *Molecular Fluorescence*, 2002.
174. H. Oka, *J. Mater. Chem.*, 2008, **18**, 1927-1934.
175. W. A. Pryor, *Organic Free Radicals; American Chemical Society: Washington, DC*, 1978.
176. T. Okamoto, M. Kuratsu, M. Kozaki, K. Hirotsu, A. Ichimura, T. Matsushita, K. Okada, *Org. Lett.*, 2004, **6**, 3493-3496.
177. S. van der Laan, B. L. Feringa, R. M. Kellogg, J. van Esch, *Langmuir*, 2002, **18**, 7136-7140.
178. J. J. E. Moreau, B. P. Pichon, C. Bied, M. W. C. Man, *J. Mater. Chem.*, 2005, **15**, 3929-3936.
179. F. P. Schmidtchen, M. Berger, *Chem. Rev.*, 1997, **97**, 1609-1646.
180. E. J. Cho, J. W. Moon, S. W. Ko, J. Y. Lee, S. K. Kim, J. Yoon, K. C. Nam, *J. Am. Chem. Soc.*, 2003, **125**, 12376-12377.
181. K. Moller, T. Bein, R. X. Fischer, *Chem. Mater.*, 1999, **11**, 665-673.
182. M. T. Anderson, J. E. Martin, J. G. Odinek, P. P. Newcomer, *Chem. Mater.*, 1998, **10**, 1490-1500.
183. M. Kruk, M. Jaroniec, A. Sayari, *J. Phys. Chem. B*, 1999, **103**, 4590-4598.
184. Q. Huo, D. I. Margolese, U. Ciesla, D. G. Demuth, P. Feng, T. E. Gier, P. Sieger, A. Firouzi, B. F. Chmelka, *Chem. Mat.*, 1994, **6**, 1176-1191.
185. R. Huq, L. Mercier, P. J. Kooyman, *Chem. Mater.*, 2001, **13**, 4512-4519.
186. M. C. Holmes, *Curr Opin Colloid Interface Sci.*, 1998, **3**, 485-492.
187. U. Henriksson, E. S. Blackmore, G. J. T. Tiddy, O. Soederman, *J. Phys. Chem.*, 1992, **96**, 3894-3902.
188. Z. Zhang, Y. Han, F.-S. Xiao, S. Qiu, L. Zhu, R. Wang, Y. Yu, Z. Zhang, B. Zou, Y. Wang, H. Sun, D. Zhao, Y. Wei, *J. Am. Chem. Soc.*, 2001, **123**, 5014-5021.
189. R. K. Iler., *The Chemistry of Silica*, Wiley, New York., 1971.
190. X. Liu, B. Tian, C. Yu, F. Gao, S. Xie, B. Tu, R. Che, L. M. Peng, D. Y. Zhao, *Angew. Chem. Int. Ed.*, 2002, **41**, 3876-3878.
191. J. J. E. Moreau, B. P. Pichon, M. W. C. Man, C. Bied, H. Pritzkow, J. L. Bantignies, P. Dieudonne, J. L. Sauvajol, *Angew. Chem. Int. Ed.*, 2004, **43**, 203-206.
192. K. S. W. Sing, D. H. Everett, R. A. W. Haul, L. Moscou, R. A. Pierotti, J. Rouquerol, T. Siemieniewska, *Pure Appl. Chem.*, 1985, **57**, 603-619.
193. F. Rojas, I. Kornhauser, C. Felipe, J. M. Esparza, S. Cordero, A. Dominguez, J. L. Riccardo, *Phys. Chem. Chem. Phys.*, 2002, **4**, 2346-2355.
194. E. P. Barrett, L. G. Joyner, P. P. Halenda, *J. Am. Chem. Soc.*, 1951, **73**, 373-380.
195. M. H. Lim, C. F. Blanford, A. Stein, *Chem. Mater.*, 1998, **10**, 467-+.
196. C. E. Fowler, S. L. Burkett, S. Mann, *Chem. Commun.*, 1997, 1769-1770.
197. C. E. Fowler, S. Mann, B. Lebeau, *Chem. Commun.*, 1998, 1825-1826.

198. A. Corma, *Chem. Rev.*, 1997, **97**, 2373-2419.
199. R. Richer, L. Mercier, *Chem. Mater.*, 2001, **13**, 2999-3008.
200. S. M. Gruner, *J. Phys. Chem.*, 1989, **93**, 7562-7570.
201. J. S. Beck, *Patent, U. S. 5, 057*, 296, 1991.
202. M. H. Lim, A. Stein, *Chem. Mater.*, 1999, **11**, 3285-3295.
203. H. Tüysüz, C. W. Lehmann, H. Bongard, B. Tesche, R. Schmidt, F. Schüth, *J. Am. Chem. Soc.*, 2008, **130**, 11510-11517.
204. Q. Huo, R. Leon, P. M. Petroff, G. D. Stucky, *Science*, 1995, **268**, 1324-1327.
205. S. Huh, J. W. Wiench, J. C. Yoo, M. Pruski, V. S. Y. Lin, *Chem. Mater.*, 2003, **15**, 4247-4256.
206. S. Huh, J. W. Wiench, B. G. Trewyn, S. Song, M. Pruski, V. S. Y. Lin, *Chem. Commun.*, 2003, 2364-2365.
207. L. P. Kuhn, *J. Am. Chem. Soc.*, 1952, **74**, 2492-2499.
208. J. Jadzyn, M. Stockhausen, B. Zywuicki, *J. Phys. Chem.*, 1987, **91**, 754-757.
209. R. B. Laughlin, J. D. Joannopoulos, *Phys. Rev. B*, 1977, **16**, 2942.
210. M. Fröba, P. Behrens, J. Wong, G. Engelhardt, C. Haggemuller, G. Vandegoor, M. Rowen, T. Tanaka, W. Schwieger, *Advances in Porous Materials*, eds. S. Komarneni, D. M. Smith and J. S. Beck, Materials Research Soc, Pittsburgh, 1995, pp. 99-104.
211. D. W. Sindorf, G. E. Maciel, *J. Am. Chem. Soc.*, 1981, **103**, 4263-4265.
212. S. M. De Paul, J. W. Zwanziger, R. Ulrich, U. Wiesner, H. W. Spiess, *J. Am. Chem. Soc.*, 1999, **121**, 5727-5736.
213. S. Ek, E. I. Iiskola, L. Niinisto, J. Vaittinen, T. T. Pakkanen and A. Root, *J. Phys. Chem. B*, 2004, **108**, 11454-11463.
214. C. S. Kramer, K. Zeitler, T. J. J. Muller, *Org. Lett.*, 2000, **2**, 3723-3726.
215. C. S. Kramer, T. J. J. Muller, *Eur. J. Org. Chem.*, 2003, 3534-3548.
216. M. Hauck, J. Schonhaber, A. J. Zuccherro, K. I. Hardcastle, T. J. J. Muller, U. H. F. Bunz, *J. Org. Chem.*, 2007, **72**, 6714-6725.
217. C. S. Kramer, K. Zeitler, T. J. J. Muller, *Tetrahedron Lett.*, 2001, **42**, 8619-8624.
218. A. W. Franz, L. N. Popa, T. J. J. Muller, *Tetrahedron Lett.*, 2008, **49**, 3300-3303.
219. D. Fattakhova Rohlfing, J. Rathousky, Y. Rohlfing, O. Bartels, M. Wark, *Langmuir*, 2005, **21**, 11320-11329.
220. A. J. Bard, L. R. Faulkner, *Electrochemical Methods Fundamentals and Applications*, John Wiley & Sons., New York Chichester Weinhei Brisbane Singapore Toronto, 2001.
221. R. W. Murray, *Chemically Modified Electrodes in Electroanalytical Chemistry, A Series of Advances*, New York, 1984, Vol.13.
222. Y. Guo, A. Mylonakis, Z. Zhang, G. Yang, P. Lelkes, S. Che, Q. Lu, Yen. Wei, *Chem. Eur. J.*, 2008, **14**, 2909-2917.
223. A. Domenech, M. Alvaro, B. Ferrer, H. Garcia, *J Phys. Chem. B*, 2003, **107**, 12781-12788.
224. R. McIntyre, H. Gerischer, *Ber. Bunsen-Ges. Phys. Chem.*, 1984, **88**, 963.
225. N. C. Maiti, S. Mazumdar, N. Periasamy, *J. Phys. Chem. B*, 1998, **102**, 1528-1538.
226. G. R. Hutchison, M. A. Ratner, T. J. Marks, *J. Am. Chem. Soc.*, 2005, **127**, 16866-16881.
227. E. H. A. Beckers, S. C. J. Meskers, A. P. H. J. Schenning, Z. Chen, F. Wurthner, P. Marsal, D. Beljonne, J. Cornil, R. A. J. Janssen, *J. Am. Chem. Soc.*, 2006, **128**, 649-657.
228. M. Sailer, A. W. Franz, T. J. J. Muller, *Chem.Eur. J.*, 2008, **14**, 2602-2614.
229. P. L. Magueres, S. V. Lindeman, J. K. Kochi, *J. Chem. Soc., Perkin Trans. 2*, 2001, 1180-1185.

230. B. Badger, Brocklehurst, *Nature*, 1968, **219**, 263-&.
231. J. K. Kochi, R. Rathore, P. L. Magueres, *J. Org. Chem.*, 2000, **65**, 6826-6836.
232. Z. X. Chang, R. M. Krishna, J. Xu, R. Koodali, L. Kevan, in *33rd International Meeting of the ESR Group of the Royal-Society-of-Chemistry*, Norwich, England, 2000, pp. 1699-1704.
233. T. Asefa, M. J. MacLachlan, N. Coombs, G. A. Ozin, *Nature*, 1999, **402**, 867-871.
234. T. Asefa, C. Yoshina-Ishii, M. J. MacLachlan, G. A. Ozin, *J. Mater. Chem*, 2000, **10**, 1751-1755.
235. S. Inagaki, S. Guan, Q. Yang, M. P. Kapoor, T. Shimada, *Chem. Commun.*, 2008, 202-204.
236. P. Van der Voort, C. Vercaemst, D. Schaubroeck, F. Verpoort, *Phys. Chem. Chem. Phys.*, 2008, **10**, 347-360.
237. G. J. d. A. Soler-Illia, C. Sanchez, B. Lebeau, J. Patarin, *Chem. Rev.*, 2002, **102**, 4093-4138.
238. H. M. A. Hunter, A. E. Garcia-Bennett, I. J. Shannon, W. Zhou, P. A. Wright, *J. Mater. Chem.*, 2002, **12**, 20-23.
239. J. Feng, Q. Huo, P. M. Petroff and G. D. Stucky, *App. Phys. Lett.*, 1997, **71**, 620-622.
240. M. J. Jia, A. Seifert, W. R. Thiel, *Chem. Mater.*, 2003, **15**, 2174-2180.
241. X. S. Zhao, G. Q. Lu, A. K. Whittaker, G. J. Millar and H. Y. Zhu, *J. Phys. Chem. B*, 1997, **101**, 6525-6531.
242. R. J. P. Corriu, A. Mehdi, C. Reye, C. Thieuleux, *New J. Chem.*, 2003, **27**, 905-908.
243. P. I. Dalko, L. Moisan, *Angew. Chem. Int. Ed.*, 2004, **43**, 5138-5175.
244. E. G. Doyaguez, F. Calderon, F. Sanchez, A. Fernandez-Mayoralas, *J. Org. Chem.*, 2007, **72**, 9353-9356.
245. Y. Zhang, L. Zhao, S. S. Lee, J. Y. Ying, *Adv. Synth. Catal.*, 2006, **348**, 2027-2032.
246. J. A. Murry, D. E. Frantz, A. Soheili, R. Tillyer, E. J. J. Grabowski, P. J. Reider, *J. Am. Chem. Soc.*, 2001, **123**, 9696-9697.
247. T. Joseph, S. S. Deshpande, S. B. Halligudi, A. Vinu, S. Ernst, M. Hartmann, *J. Mol. Catal. A: Chemical*, 2003, **206**, 13-21.
248. W. Hammond, E. Prouzet, S. D. Mahanti, T. J. Pinnavaia, *Microporous Mesoporous Mater.*, 1999, **27**, 19-25.
249. S. Angloher, T. Bein, *J. Mater. Chem.*, 2006, **16**, 3629-3634.
250. S. J. Gregg, K. S. W. Sing, *Adsorption, Surface Area and Porosity*, 2nd ed.; Academic Press, London, 1982.
251. B. J. Melde, B. T. Holland, C. F. Blanford, A. Stein, *Chem. Mater.*, 1999, **11**, 3302-3308.
252. Q. H. Yang, H. Liu, H. Yang, L. Zhang, Z. C. Feng, J. Zhang, C. Li, *Microporous Mesoporous Mater.*, 2005, **77**, 257-264.
253. R. van Grieken, J. A. Melero, G. Morales, *Appl. Catal. A-Gen.*, 2005, **289**, 143-152.
254. H. K. Stetter, H., *Org. React*, 1991, 407-496.
255. S. M. Mennen, J. D. Gipson, Y. R. Kim, S. J. Miller, *J. Am. Chem. Soc.*, 2005, **127**, 1654-1655.
256. F. Kleitz, W. Schmidt, F. Schüh, *Microporous Mesoporous Mater.*, 2003, **65**, 1-29.
257. R. C. T. Slade, C. M. Bambrugh, R. T. Williams, *Phys. Chem. Chem. Phys.*, 2002, **4**, 5394-5399.
258. L. D. Perez, J. F. Lopez, V. H. Orozco, T. Kyu, B. L. Lopez, *J. Appl. Polym. Sci.*, 2009, **111**, 2229-2237.
259. X. S. Zhao, G. Q. Lu, *J. Phys. Chem. B*, 1998, **102**, 1556-1561.
260. S. Fujita, S. Inagaki, *Chem. Mater.*, 2008, **20**, 891-908.
261. O. Olkhoviyk, S. Pikus, M. Jaroniec, *J. Mater. Chem.*, 2005, **15**, 1517-1519.

262. A. Sayari, W. Wang, *J. Am. Chem. Soc.*, 2005, **127**, 12194-12195.
263. M. Cornelius, F. Hoffmann, M. Fröba, *Chem. Mater.*, 2005, **17**, 6674-6678.
264. M. P. Kapoor, Q. Yang, S. Inagaki, *J. Am. Chem. Soc.*, 2002, **124**, 15176-15177.
265. J. Liu, Q. H. Yang, M. P. Kapoor, N. Setoyama, S. Inagaki, J. Yang, L. Zhang, *J. Phys. Chem. B*, 2005, **109**, 12250-12256.
266. M. C. Burleigh, M. A. Markowitz, S. Jayasundera, M. S. Spector, C. W. Thomas, B. P. Gaber, *J. Phys. Chem. B*, 2003, **107**, 12628-12634.
267. G. R. Zhu, Q. H. Yang, D. M. Jiang, J. Yang, L. Zhang, Y. Li, C. Li, *J. Chromatography A*, 2006, **1103**, 257-264.
268. O. Olkhovyyk, M. Jaroniec, *J. Am. Chem. Soc.*, 2005, **127**, 60-61.
269. H. Peng, J. Tang, L. Yang, J. Pang, H. S. Ashbaugh, C. J. Brinker, Z. Yang, Y. Lu, *J. Am. Chem. Soc.*, 2006, **128**, 5304-5305.
270. S. Y. Kim, J. W. Lee, J. H. Jung, J. K. Kang, *Chem. Mater.*, 2007, **19**, 135-137.
271. J. Alauzun, A. Mehdi, C. Reye, R. J. P. Corriu, *J. Am. Chem. Soc.*, 2006, **128**, 8718-8719.
272. Q. H. Yang, J. Liu, J. Yang, M. P. Kapoor, S. Inagaki, C. Li, *J. Catal.*, 2004, **228**, 265-272.
273. Q. Yang, M. P. Kapoor, N. Shirokura, M. Ohashi, S. Inagaki, J. N. Kondo, K. Domen, *J. Mater. Chem.*, 2005, **15**, 666-673.
274. D. M. Jiang, Q. H. Yang, J. Yang, L. Zhang, G. R. Zhu, W. G. Su, C. Li, *Chem. Mater.*, 2005, **17**, 6154-6160.
275. C. Baleizao, B. Gigante, D. Das, M. Alvaro, H. Garcia, A. Corma, *J. Catal.*, 2004, **223**, 106-113.
276. M. P. Kapoor, A. Bhaumik, S. Inagaki, K. Kuraoka, T. Yazawa, *J. Mater. Chem.*, 2002, **12**, 3078-3083.
277. Q. Yang, J. Yang, Z. Feng, Y. Li, *J. Mater. Chem.*, 2005, **15**, 4268-4274.
278. S. Hudson, J. Cooney, B. K. Hodnett, E. Magner, *Chem. Mater.*, 2007, **19**, 2049-2055.
279. S. Shylesh, M. Jia, A. Seifert, S. Adappa, S. Ernst, W. R. Thiel, *New J. Chem.*, 2009, in print.
280. K. J. Shea, D. A. Loy, O. Webster, *J. Am. Chem. Soc.*, 1992, **114**, 6700-6710.
281. T. Asefa, M. J. MacLachlan, *Nature*, 1999, **402**, 867.
282. N. Bion, P. Ferreira, A. Valente, I. S. Goncalves, J. Rocha, *J. Mater. Chem.*, 2003, **13**, 1910-1913.
283. R. D. Badley, W. T. Ford, *J. Org. Chem.*, 1989, **54**, 5437-5443.
284. Wim M. Van Rhijn, Dirk E. De Vos, Bert F. Sels, W. D. Bossaert, *Chem. Commun*, 1998, 317-318.
285. W. V. Rhijn, D. D. Vos, W. Bossaert, J. Bullen, B. Wouters, P. Grobet, P. Jacobs, F. B. C. D. S. G. L. Bonneviot, S. Kaliaguine, in *Studies in Surface Science and Catalysis*, Elsevier, 1998, pp. 183-190.
286. M. Boveri, J. Aguilar-Pliego, J. Pérez-Pariente, E. Sastre, *Catal. Today*, 2005, **868**, 107-108.
287. M. H. Lim, C. F. Blanford, A. Stein, *Chem. Mater.*, 1998, **10**, 467-470.
288. D. Margolese, J. A. Melero, S. C. Christiansen, B. F. Chmelka, G. D. Stucky, *Chem. Mater.*, 2000, **12**, 2448-2459.
289. W. M. Van Rhijn, D. E. De Vos, B. F. Sels, W. D. Bossaert, P. A. Jacobs, *Chem. Commun*, 1998, 317-318.
290. Ken-ichi Shimizu, Eidai Hayashi, Tsuyoshi Hatamachi, Tatsuya Kodamab, Yoshie Kitayama, *Tetrahedron Letters*, 2004, **45**, 5135-5138.
291. A. Corma, S. Iborra, A. Velty, *Chem. Rev.*, 2007, **107**, 2411-2502.

292. M. Pagliaro, R. Ciriminna, H. Kimura, M. Rossi, C. Della Pina, *Angew. Chem. Int. Ed.*, 2007, **46**, 4434-4440.
93. P. Sreekanth, S. W. Kim, T. Hyeon, B. M. Kim, *Adv. Synth. Catal.*, 2003, **345**, 936-938.
294. Y. Gu, C. Ogawa, J. Kobayashi, Y. Mori, S. Kobayashi, *Angew. Chem. Int. Ed.*, 2006, **45**, 7217-7220.
295. Y. Gu, A. Karam, F. Jerome, J. Barrault, *Org. Lett.*, 2007, **9**, 3145-3148.
296. V. Ganesan, A. Walcarius, *Langmuir*, 2004, **20**, 3632-3640.
297. D. M. Kurtz, *Chem. Rev.*, 1990, **90**, 585-606.
298. R. E. Norman, R. C. Holz, S. Menage, L. Que, J. H. Zhang, C. J. O'Connor, *Inorg. Chem.*, 1990, **29**, 4629-4637.
299. C. G. Wu, T. Bein, *Science*, 1994, **264**, 1757-1759.
300. H. G. O. Becker, R. Beckert, G. Domschke, E. Fanghänel, W. D. Habicher, P. Metz, D. Pavel and K. Schwetlick, *Organikum*, Wiley-VCH, Weinheim, 2001.
301. A. T. P. Zanello, T. Hayashi, *Ferrocenes*, 1995, 317.
302. W. Y. Lin, Q. Cai, W. Q. Pang, Y. Yue, *Chem. Commun.*, 1998, 2473-2474.

## Acknowledgements

First and foremost I would like to warmly thank my supervisor Prof. Werner R. Thiel for giving me an opportunity to study in his group. His abundant knowledge, constant support, extreme patience and invaluable guidance helped me a lot throughout my work. I also will never forget his timely helps and strong personal support, from the first day I arrived here and throughout all the stages of these three years. I take this opportunity to express my most intense thanks and deepest regards to him. I am also special thankful to Prof. Mingjun Jia and Prof. Wenxiang Zhang, who recommended me to this group and who received me as a graduate student to continue my study. Their help considered to me never stopped even when I was so far away. I am very lucky to have these three kind supervisors. Without them I could not even believe to write a PhD thesis and particularly in English.

I am also very grateful to Prof. Thomas J. J. Müller and Adam W. Franz (Institut für organische Chemie und Makromolekulare Chemie, Heinrich Heine Universität Düsseldorf) for their helpful discussions and our successful cooperation on the work of phenothiazine functionalized hybrid materials, as well as the very pleasant time during my visit in their group.

I would like to thank Dr. Qingguo Meng for his initial work on thiazolium salt catalysts and discussions, which guided me to a fast progress in this part of my work.

Special thanks are given to Dr. Yu Sun for his valuable helps in organic synthesis and timely advice of my personal life.

I would also like to thank Anett Schubert for her help in the synthesis of the  $\mu$ -oxo-bridged diferric complex and the epoxidation reaction.

I also acknowledge Dr. Shylesh Sankar, who introduced me to the PMOs system, as well as the valuable discussions with him.

I am indebted to the group of Technische Chemie for allowing me to use the facilities in their lab, especially to Prof. Stefan Ernst, Alex Wagener and Gunder Dörr due to their valuable helps in the characterizations and the cooperation in the glycerol-to-acrolein reaction.

My heartfelt thank is also given to Ms Christiane Müller for her efficient measurements of large numbers of my NMR samples.


This was a very interdisciplinary project and I also would like to thank Dr. Andreas Seifert (Institut für Chemie, Technische Universität Chemnitz), Prof. Martin Hartmann (Institut für Physik, Universität Augsburg), Dr. Markus Pagels (Schlumberger Cambridge Research Ltd.), Dr. Biprajit Sarkar (Institut für Anorganische Chemie, Universität Stuttgart), and Dr. Piaoping Yang (Changchun Institute of Applied Chemistry, Chinese Academy of Sciences) for their help in the measurements of solid state NMR, EPR, solid state CV and TEM.

I also acknowledge Dr. Gotthelf Wolmershäuser, Jie, Frank, Christoph, Stephanie, Lisa, and Anke for their help during the AC Praktikum.

I am very grateful to Claudia and Susi, who had been in the same lab with me since the beginning of my work and given me a lot of help 🙌. I am also very thankful to Kevin and Katrin, who joined in our big lab later, and the time in the laboratory was never dull due to their happiness and energy ☀️. I thank my ‘badminton colleagues’ 🏸 my ‘cooking testers’ 🍷 Andy, Daniel, and Lei. They brought a lot of fun to me during the break of work. I thank Andreas Reis for his self-giving work of repairing our computers and helping my computer get rid of the viruses 🍏. I thank Dirk for helping me fix the dirty, oily and heavy pump 🙌. I would like to give my faithful thanks to everyone in this group for the friendly working atmosphere, the home feeling you provide to me 😊, and the happy hours of hike, BBQ, dinner and so on, as well as the most important beer drinking 🍺.



There are many of my teachers, friends and acquaintances, who always help me and inspired me. I would like to give my sincere thanks and best wishes to all of them. Thanks! A special thank and admiration are given to Prof. Dazhen Jiang, who can not read this anymore. I really regret my inarticulate and late thank to him. I will always remember him in a picture of a very kind, generous, and knowledgeable senior cycled with a group of young students.

Finally, I give my special thank to Bao, who consecutive encouraged and supported me in these years. I am forever indebted to my parents and brother for their understanding, encouragement and supporting. Their love is always motivating me to keep going and they are the treasure of my whole life  .

## **Curriculum Vitae**

- Name: Zhou Zhou
- Date of birth: 08.08.1979
- Place of birth: Changchun, Jilin province, China
- Status of marriage: Single

### **EDUCATION:**

- 02/2006–04/2009 Technische Universität Kaiserslautern, Kaiserslautern, Germany  
Ph.D. study in Inorganic Chemistry.
- 09/2002–07/2005 Jilin University, Jilin, China  
M. A. degree in Physical Chemistry.
- 09/1998–07/2002 Jilin University, Jilin, China  
B. A. degree in Chemistry.

### **OTHER EXPERIENCES:**

- 03/2002 – 06/2002 "Analyze effective components of various nutrients by high performance liquid chromatography" Jilin Municipal center for hygiene and epidemic control.
- 06/2001–08/2001 Practice in industry, China National Petroleum Corporation Jilin Chemical.